Dissertation zur Erlangung des Doktorgrades der Fakultät für
Chemie und Pharmazie an der Ludwig-Maximilians-Universität München

Molecular Force Measurements in Desmosomes

Anna-Lena Cost
aus Bad Homburg vor der Höhe, Deutschland

2019

Erklärung

Diese Dissertation wurde im Sinne von §7 der Promotionsordnung vom 28. November 2011 von Herrn Prof. Dr. Reinhard Fässler betreut.

Eidesstattliche Versicherung

Diese Dissertation wurde eigenständig und ohne unerlaubte Hilfe erarbeitet.

München, den 02. Mai 2019

(Anna-Lena Cost)

Dissertation eingereicht am 25. März 2019
Erstgutachter: Prof. Dr. Reinhard Fässler
Zweitgutachter: Prof. Dr. Andreas R. Bausch
Mündliche Prüfung am 29. April 2019

Summary

Desmosomes are cell–cell adhesion sites especially important in heart and skin tissues. Both tissues are exposed to mechanical stress and desmosomes are essential for stable cell–cell adhesion but whether and how forces act on desmosomes was unclear. Here, a desmoplakin tension sensor was developed reporting on molecular forces experienced by desmoplakin, which is essential for the connection to the intermediate filament cytoskeleton. Tension measured with the desmoplakin tension sensor can therefore also serve as a proxy for forces transduced across desmosomes towards the intermediate filament cytoskeleton. Fluorescence lifetime imaging microscopy (FLIM)-based Förster resonance energy transfer (FRET) measurements of the desmoplakin tension sensor revealed the absence of desmoplakin forces during the formation of desmosomes in keratinocytes. Forces are experienced by desmoplakin, however, on very soft substrates, where the substrate stiffness is in the range of the intermediate filament stiffness. Furthermore, desmosomes are transiently loaded in response to external mechanical stress. The stress-induced loading depends on the magnitude and orientation of the applied tissue deformation. These observations suggest that desmosomes act as stress absorbers and evolved in mammalian tissues to complement adherens junctions especially in more extreme situations.

Next to the development and experiments with the desmoplakin tension sensor, the fluorescence lifetime analysis and merge software (FLAMES) was developed. The software provides an automated data analysis pipeline for FRET-based tension sensor experiments measured with FLIM. FLAMES thereby improves the estimation of lifetimes from photon count curves for the signal of interest. Moreover, FLAMES also allows the determination of the relative amount of molecules under tension, which provides a new way for the analysis of tension sensor experiments.

Zusammenfassung

Desmosomen sind Zellkontakte zwischen benachbarten Zellen und besonders wichtig im Herzen und in der Haut, die starker mechanischer Belastung ausgesetzt sind. Für eine stabile Zelladhäsion sind Desmosomen unerlässlich, aber es war bisher nicht bekannt ob Desmosomen direkt an der Kraftweiterleitung beteiligt sind. In dieser Arbeit wurde ein Desmoplakin-Kraftsensor entwickelt, der die Kraft über Desmoplakin ausliest. Desmoplakin ist ein essentieller Bestandteil von Desmosomen und bindet an Intermediärfilamente, welche ein wesentlicher Bestandteil des Zytoskeletts sind. Die Kraft über Desmoplakin kann daher auch als Näherung dienen für die Kraft, die über Desmosomen zum Zytoskelett weitergeitet wird. Um den Kraftsensor auszulesen, wurde die Effizienz des Förster-Resonanzenergietransfers (FRET) mit Hilfe von Fluoreszenzlebensdauermessungen (engl. FLIM) bestimmt. Diese Experimente zeigten, dass bei der Bildung von Desmosomen keine Kraft über Desmosomen ans Zytoskelett weitergeleitet wird. Wenn sich die Keratinozytenzellschicht allerdings auf einem sehr weichen Untergrund befindet, wird Kraft an Desmosomen gemessen. Im Unterschied zu den Experimenten auf festeren Untergründen ist die Umgebung in dieser Situation etwa genauso weich wie die Intermediärfilamente. Außerdem sind Desmosomen unter Kraft, wenn sie akut extern mechanisch belastet werden und zwar in Abhängigikeit von der Stärke und Orientierung der externen Belastung. Diese Beobachtungen unterstützen ein Model in dem Desmosomen in Säugetieren als weitere Zellkontakte neben Adhäsionsverbindungen entstanden sind, um zusätzliche Belastungen in extremeren Situationen abzufedern.

Neben der Entwicklung und Experimenten mit dem Desmoplakin-Kraftsensor, wurde auch FLAMES (engl. fluorescence lifetime analysis and merge software) zur Analyse von Fluoreszenzlebensdauern und zum Zusammenführen von Daten entwickelt. Das Programm ermöglicht eine automatisierte Auswertung von Kraftsensorexperimenten, in denen FRET in verschiedenen Konstrukten mit Hilfe von FLIM bestimmt wird. Mit FLAMES können dabei die Fluoreszenzlebensdauern aus den Ankunftszeiten von Photonen innerhalb des spezifischen Signals bestimmt werden. Zudem kann auch der relative Anteil der Moleküle berechnet werden, die unter ausreichend Kraft stehen um den Kraftsensor zu öffnen, was einen neuen Weg darstellt die Daten eines Kraftsensorexperiments auszuwerten.

List of Publications

Andrew J. Price*, **Anna-Lena Cost***, Hanna Ungewiß, Jens Waschke, Alexander R. Dunn§, and Carsten Grashoff§. "Mechanical loading of desmosomes depends on the magnitude and orientation of external stress". *Nature Communications* 9.1 (2018), e5284.

Pia Ringer, Andreas Weißl, **Anna-Lena Cost**, Andrea Freikamp, Benedikt Sabass, Alexander Mehlich, Marc Tramier, Matthias Rief, and Carsten Grashoff§. "Multiplexing molecular tension sensors reveals piconewton force gradient across talin-1". *Nature Methods* 14.11 (2017), pp. 1090–1096.

Sandra B. Lemke§, Thomas Weidemann, **Anna-Lena Cost**, Carsten Grashoff§, and Frank Schnorrer§. "A small proportion of Talin molecules transmit forces at developing muscle attachments in vivo". *PLOS Biology* 17.3 (2019), e3000057.

Anna-Lena Cost§, Samira Khalaji, and Carsten Grashoff§. "Genetically encoded FRET-based tension sensors". *Current Protocols in Cell Biology* (2019), e85.

Andrea Freikamp*, **Anna-Lena Cost***, and Carsten Grashoff§. "The piconewton force awakens: Quantifying mechanics in cells." *Trends in Cell Biology* 26.11 (2016), pp. 838–847.

Anna-Lena Cost*, Pia Ringer*, Anna Chrostek-Grashoff, and Carsten Grashoff§. "How to measure molecular forces in cells: A guide to evaluating genetically-encoded FRET-based tension sensors". *Cellular and Molecular Bioengineering* 8.1 (2015), pp. 96–105.

*These authors contributed equally.
§Corresponding author

Contents

List of Figures

List of Tables

1 Desmosomes

1.1 Cell Adhesions in the Skin

To preserve tissue, organ, and ultimately animal integrity, cells need to adhere to and interact with their surrounding. In the stratified epithelium of the epidermis, for example, keratinocytes are the predominant cell type and their adhesion is essential to preserve skin integrity. Basal keratinocytes adhere to the underlying basement membrane using focal contacts to connect to the filamentous actin (F-actin) and hemidesmosomes (HDs) to connect to the keratin intermediate filament (IF) cytoskeletons, respectively. To neighboring cells, basal keratinocytes connect on one hand via gap junctions that allow cell–cell communication by the exchange of ions and small molecules [2] and on the other hand via adhesive adhesions: adherens junctions (AJs) connecting to the F-actin cytoskeleton and desmosomes (DSMs) connecting to the keratin IF [3].

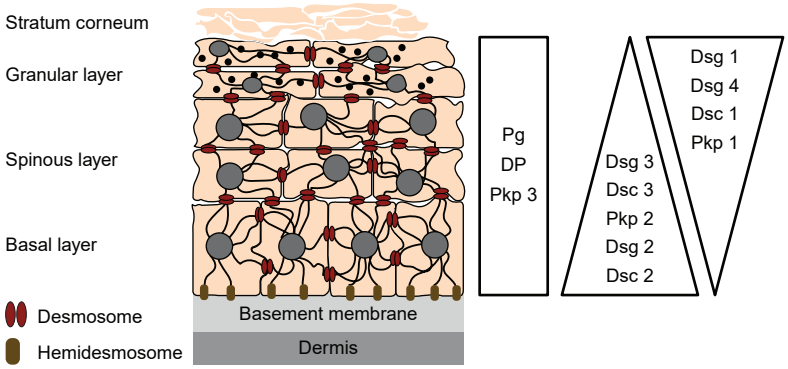

Figure 1.1: Epidermal layers express distinct desmosomal proteins. Keratinocytes in the basal layer adhere with hemidesmosomes (HDs) to the underlying basement membrane and with desmosomes (DSMs) to neighboring cells, which are both connected to the keratin intermediate filament (IF). Next to the ubiquitously expressed plakoglobin (Pg), desmoplakin (DP), and plakophilin (Pkp)3, basal keratinocytes express Pkp2 as well as desmocollin (Dsc)2 and 3 and desmoglein (Dsg)2 and 3. While Dsg2 expression is strictly limited to basal keratinocytes, Dsc3 and Dsg3 are expressed in the spinous and Pkp2 and Dsc2 even in the granular layer, albeit with reduced levels. Similarly, the expression of Dsc1 and Dsg4 is strictly limited to suprabasal layers but low levels of Dsc1 and Pkp1 isoforms, which are mainly expressed in suprabasal layers, are also detected in basal layers. The modified figure is reproduced with permission from [1].

Upon terminal differentiation, keratinocytes move upwards through spinous and granular layers until they end up as enucleated, flattened cells in the stratum corneum [4]. During this process, keratinocytes change their desmosomal components and keratin composition, which therefore differs throughout the epidermal layers (Fig. 1.1) [4, 5]. In the granular layer, tight junctions (TJs) appear as additional cell–cell adhesion structure and establish a diffusion barrier for molecules between neighboring cells, which is essential for skin barrier function [6]. The restriction of TJ to the uppermost viable layer in the epidermis is thereby likely dependent on the AJ protein E-cadherin [7].

1.2 Desmosome Architecture

DSMs were first described in 1864 by Guilio Bizzozero, who already inferred that the dense nodes at cell–cell contacts in the epidermis are adhesive structures. The term DSM was then coined by Josef Shaffer from the Greek *desmos* meaning bond and *soma* meaning body in the 1920s [4]. Electron-microscopic images allowed in the 1960s to describe the general desmosomal architecture: the extracellular core domain (ECD) or *desmoglea* between neighboring cells is divided in two parts by a central electron-dense region, termed dense midline (DM). The symmetric electron-dense regions at the inner side of the plasma membrane (PM), called outer dense plaque (ODP), is followed by a small electron-lucent region and another electron-dense region termed inner dense plaque (IDP) [4, 8–10] (Fig. 1.2a).

The protein composition of DSMs became biochemically accessible after Christine J. Skerrow and A. Gedeon Matoltsy isolated DSMs from bovine nasal epidermis in 1974 [12]. Isolated DSMs were then used to separate proteins with gel electrophoresis. These bands were either used to generate antibodies and characterize protein localization by immunofluorescence, e.g. for desmosomal cadherins [13] or DP [14], and immuno-electron microscopy (EM) [15] or to biochemically characterize amino acid (aa) composition and sugar content [16], which for example allowed the characterization of DP bands as intracellular plaque proteins [17]. Interaction studies and sequence comparisons were used for initial protein arrangement [18]. Immunogold labeling was later used to combine antibody labeling with transmission electron microscopy (TEM) images and allowed for a first low resolution map of the DSM in 1999 [9] (Fig. 1.2b), which was refined later using cryoelectron tomography (cryo-ET) [19] and direct stochastical optical reconstruction microscopy (dSTORM) [20].

Taken information from many studies together, the ECD consists of desmosomal cadherins, the IDP of armadillo family protein members and the N-terminal region of DP, and the ODP of DP that connects to the keratin IF [4, 10, 21].

1.3 Desmosomal Proteins

1.3.1 Desmosomal Cadherins

The desmosomal cadherins, desmogleins (Dsgs) and desmocollins (Dscs), establish a direct linkage between neighboring cells. They belong to the same family as classical cadherins that mediate cell–cell adhesion in AJs and comprises five extracellular domains, a single-pass transmembrane domain, and an intracellular tail domain of variable length, which mediates interaction with desmosomal plaque proteins (Fig. 1.3a) [4, 10, 22]. Similar to classical cadherins also desmosomal cadherins require calcium ions (Ca^{2+})

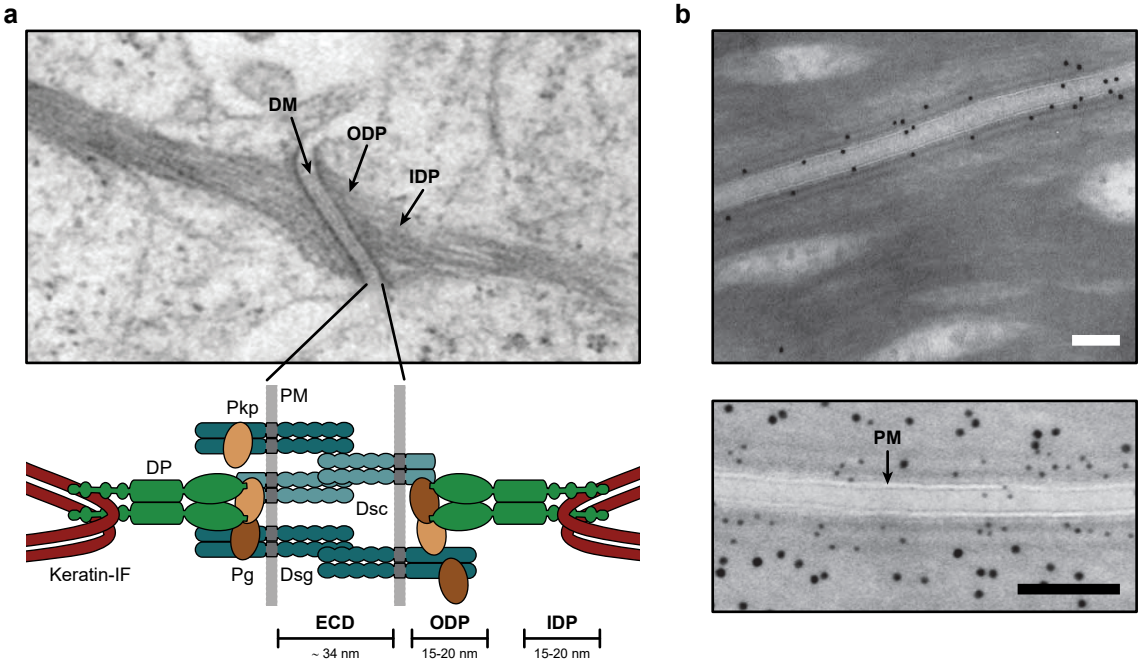

Figure 1.2: Desmosomes (DSMs) connect the keratin intermediate filaments (IFs) of neighboring cells. (**a**) The extracellular core domain (ECD) with the dense midline (DM) comprises of the extra-cellular domains of the desmosomal cadherins desmocollins (Dscs) and desmogleins (Dsgs). At the inner side of the plasma membrane (PM), desmosomal cadherins are bound by the outer dense plaque (ODP) proteins, i.e. the armadillo family proteins plakophilins (Pkps) and plakoglobin (Pg) and the N-terminus of desmoplakin (DP). DP also establishes the connection to the keratin-intermediate filament (IF), which is the inner dense plaque (IDP) in electron microscopic images. (**b**) *Top* Cryo-section shows specific labeling of DSMs with immunogold particles against DP N-terminus. *Bottom* Distance distributions of 5 nm and 10 mn gold particles against the DP N-terminus and C-terminus, respectively, show that DP is oriented perpendicular to the cell–cell contact. Scale bars: 100 nm. The modified figures are adapted with permissions from [1] (**a**) and [9] (**b**). The schematic is published [11].

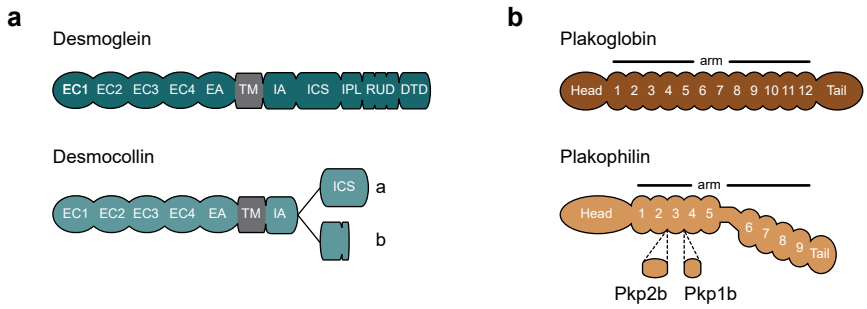

Figure 1.3: Desmosomal cadherins and armadillo family protein members have several domains. (**a**) The desmosomal cadherins desmocollin (Dsc) and desmoglein (Dsg) comprise of four extracellular domains (ECs) followed by an extracellular anchor (EA), a transmembrane domain (TM), an intracellular anchor (IA), and differ in the subsequent intracellular domains. In Dsg, the ICS is followed by a short intracellular proline-rich linker (IPL), a variable amount of repeat unit domains (RUDs) (Dsg1,2,3,4: 5, 6, 2, 3 repeats) and a desmoglein terminal domain (DTD). Dsc "a" contains an intracellular cadherin-like sequence (ICS) lacking in the shorter "b" isoform. (**b**) In plakoglobin (Pg) terminal head and tail domains are connected by 12 arm repeats. Plakophilins (Pkps) have 9 arm repeats with an additional insert between arm repeat 5 and 6 that induces a kink. For Pkp1 and Pkp2 "a" and longer "b" isoforms exist. The domain architecture is adapted from [4, 10].

to form adhesions [23]. In mature tissues, however, DSMs adopt a more stable, Ca^{2+}-independent, hyper-adhesive state [24, 25], while AJs always remain Ca^{2+}-dependent. The hyper-adhesive state is regulated by protein kinase C (PKC)-α and quickly reverted upon wounding [25]. Other unique features of desmosomal cadherins are the highly ordered structure that only DSM adopt and the *trans* or heterophilic binding of different cadherins [26, 27]. On a structural level, an increased flexibility of the extracellular domains even in the Ca^{2+}-bound state might explain the remarkable increase of DSM as compared to AJ adhesion strength [28].

Dsg and Dsc isoforms are expressed in a tissue- and differentiation-specific fashion (Fig. 1.1). In line with strong isoform specific effects, knockout mice exhibit a broad range of phenotypes ranging from embryonic lethality (Dsg2, [29]), clearly weakened cell–cell adhesion (Dsg3, [30]), to only mild phenotype (Dsc2, [31]). Remarkably, ectopically expressing Dsg3 in the suprabasal layers of the epidermis causes early postnatal lethality due to extensive water loss [32]. The impaired adhesion by expression of Dsg3 in suprabasal layers fits with the observation that the binding affinity of Dsg3:Dsc3, prevalent in basal layers, is a factor of ten weaker than the binding affinity of Dsg1:Dsc1, which is expressed in the suprabasal layers [27]; thereby confirming the importance of regulated expression patterns.

1.3.2 Armadillo Family Protein Members

The armadillo family protein members plakoglobin (Pg) and plakophilins (Pkps) bind to the cytoplasmic tail of desmosomal cadherins. The structural basis of the armadillo family proteins are units of 42 aa arm repeats [33] (Fig. 1.3b), which Pg and Pkps share among others with their AJ analogues β-catenin and p120-catenin [4]. In the skin, Pg expression only slightly increases towards the suprabasal layers, while Pkp isoform expression strongly depends on the epidermal layers (Fig. 1.1) providing another regulatory level for DSM adhesion.

Functionally, Pg and Pkps establish the connection between desmosomal cadherins and DP and regulate the clustering of desmosomal components [4, 10, 34]. Furthermore, Pkps have been proposed to help positioning of PKC and Ras homologue (Rho) GTPases, which for example are required to promote juncion assembly [10], interact with the F-actin cytoskeleton [34], whereas Pg can not only bind to desmosomal but also to classical cadherins, albeit with less affinity [35]. Next to their localization to DSMs, Pg and Pkp isoforms are also found in the nucleus [10, 34], where Pg acts as regulator of transcription factors and wingless/integrated (Wnt) growth factor signaling important in hair follicle development [4, 36], while the role of Pkps remains to be elucidated.

1.3.3 Plakins

Plakins are a family of modular cytolinkers that connect the F-actin, microtubule (MT), and IF cytoskeletons and act as scaffolds and adapters for signaling proteins [37]. In DSMs, DP is an obligate component, the most abundant protein, and consequently expressed in all epidermal layers (Fig. 1.1; Sec. 1.7). In the granular layer, the non-essential plakins envoplakin, periplakin, and epiplakin are additionally expressed and assist in the formation of the cornified envelope [37].

1.4 Keratin Intermediate Filament

1.4.1 Intermediate Filament Superfamily

DSMs connect the IF cytoskeletons of neighboring cells. The IF is a diverse superfamily of structurally similar proteins encoded on approximatley 70 human genes [38] and broadly classified in six types based on sequence homologies, of which five are cytoskeletal and one comprises of nuclear lamins [39–41]. IF expression is cell type-dependent (Fig. 1.4) and regarded as a mechanical footprint [40].

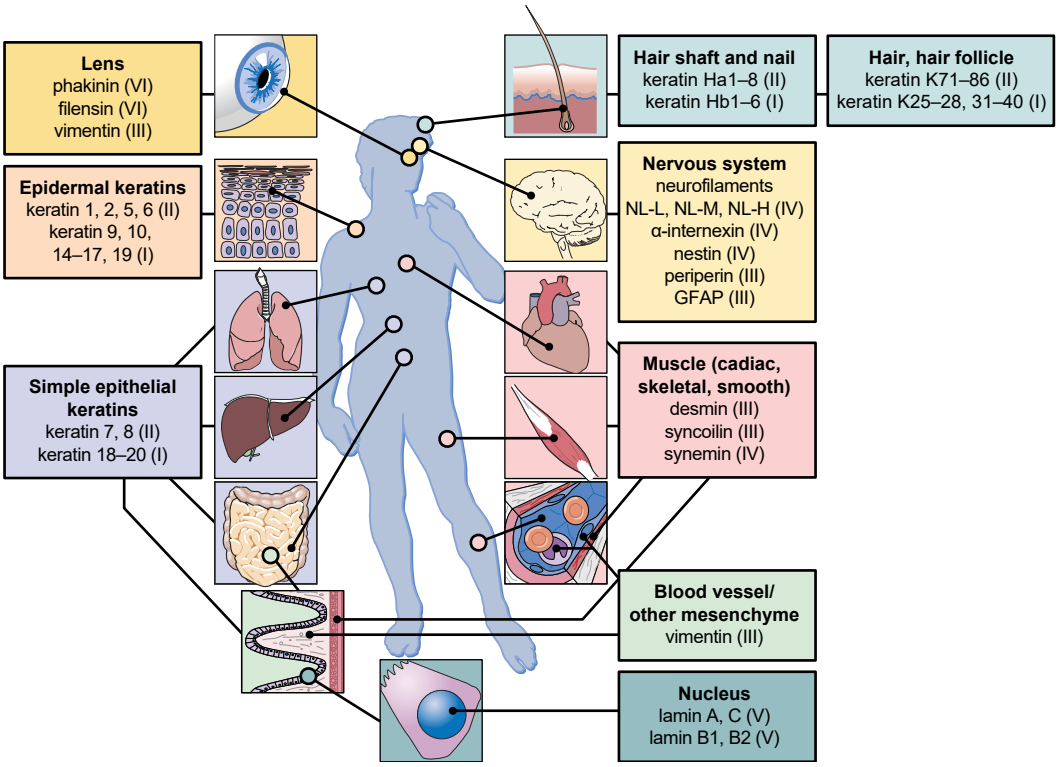

Figure 1.4: The intermediate filament (IF) expression is cell type-dependent. The IF proteins are classified in six classes. Lamins (type V) are ubiquitously expressed, while all other IF proteins are restricted to specific cell types and thought to determine their mechanical properties [40]. GFAP: glial fibrillary acidic protein. The modified figure is reproduced with permission from [39].

Keratinocytes in the stratified epithelium of the epidermis express acidic type I and basic type II keratins that form obligate heterodimers [5, 42]. Similar to the expression pattern throughout the body, expression of specific keratins is tightly regulated and for example differentiation-dependent: Basal keratinocytes predominantly express keratin (K)5/K14, while suprabasal keratinocytes express K1/K10; on epidermal injury, however, K6/K17 are up-regulated [5].

1.4.2 Structure and Mechanical Properties of the IF

All IF proteins are characterized by a central α-helical rod surrounded by unstructured head and tail domains (Fig. 1.5a). Type I and II keratins form obligate, parallel coiled-coil heterodimers, which then assemble into anti-parallel, non-polar tetramers (Fig. 1.5b). These tetramers self-assemble via lateral interactions into unit length filaments of approximately 65 nm length that further elongate via longitudinal interactions to µm-long filaments [5, 40, 43]. The resulting 10 nm wide non-polar fibers have an intermediate

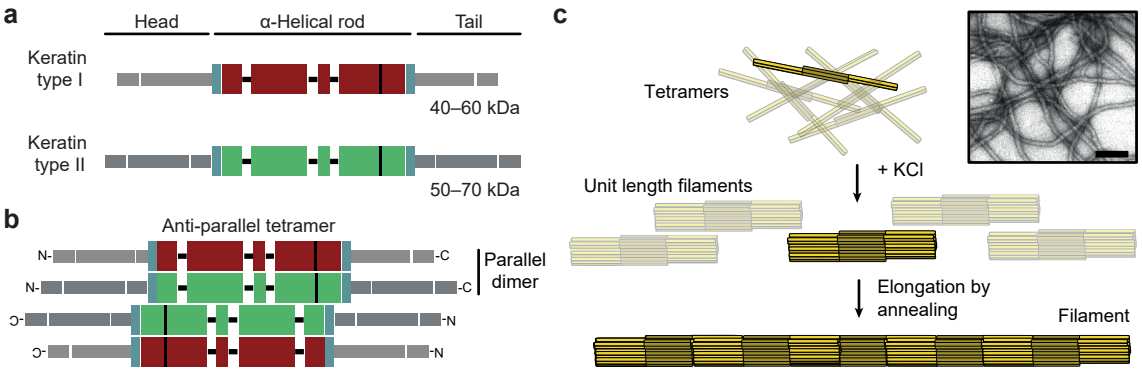

Figure 1.5: Non-polar keratin IFs assemble from tetramers. (**a**) Keratins have a central α-helical coiled-coil rod flanked by unstructured head and tail domains. (**b**) Keratins form parallel dimers of acidic type I and basic type II molecules that then assemble to anti-parallel tetramers. (**c**) *In vitro* tetramers assemble in the presence of ions to unit length filaments that elongate by annealing to long non-polar filaments, which can grow on either side by end-to-end annealing. The resulting filaments, e.g. containing K5/K14, can then be imaged using transmission electron microscopy (TEM). Scale bar: 100 nm. The modified figures are reproduced with permissions from [5] (**a, b**), [40] (schematic) and [47] (TEM image) (**c**).

diameter as compared to the other two cytoskeletons: F-actin-based microfilaments have 5−8 nm and MTs 25 nm, thus explaining the term *intermediate filaments* (originally *intermediate* related to actin and myosin fibers [44]) [39, 45] (Fig. 1.5c). Of note, the diameter of IF is sometimes variable across the filament length [40] and also varies between different filaments, e.g. lamin-based filaments have with 3.5 nm a comparably small diameter [46].

The mechanical properties set the IF apart from F-actin and MT cytoskeletons [40]. The mechanical stiffness of a polymer can be described using the persistence length L_P, i.e. the distance along which correlations in the orientation persist, which is in the range of a few μm for the F-actin cytoskeleton and up to mm for MTs [48] but with only a few 100 nm considerably shorter for different IF proteins [40, 49, 50]. The shorter L_P reflects increased flexibility and interestingly, neurofilaments expressed in the soft brain environment are also more flexible than other IF proteins expressed in stiffer environments [40]. Notably, individual IF fibers including K5/K14 can extend by more than two-fold [51], a remarkable extensibility that might be explained by an α-helix-to-β-sheet transition of the coiled-coil rod potentially combined with unfolding of the N- and C-terminal domains and/or sliding of the subunits on the filament relative to each other [40, 51–53].

IF networks show visco-elastic responses when exposed to external mechanical stress and keratin but not vimentin IF stiffens in response to repeated small deformations [54, 55]. K8/K18 networks self-assemble *in vitro* without any crosslinkers within seconds; during the first hour, the elasticity still increases until mature networks are formed [56].

These mature networks are then characterized by a high elastic modulus G_0 mediated by a weak interaction of hydrophobic amino acids in the central rod and strain stiffening mediated by strong attractive interactions between filaments located in the C-terminal tail [56]. Similarly, the tail domain of K14 induces bundling of K5/K14 filaments *in vitro* resembling the large bundles formed *in vivo* that mediate mechanical resilience [57].

The important role of the IF on the mechanical resilience of cells is further underlined by experiments with cells depleted of the keratin IF [58], which show decreased cell stiffness and increased viscosity [59]. Furthermore, cells lacking keratins have an about 60 % higher cell deformability than wild type cells [59], which is strikingly more than caused by latrunculin A-mediated depolarization of the F-actin cytoskeleton [60]. Interestingly, re-expression of K5/K14 rescues the mechanical defects of keratin-deficient cells [59].

1.4.3 Keratin IF *in vivo*

The first direct evidence that keratin IF regulates the mechanical properties of keratinocytes came from mice expressing dominant negative keratin mutants disturbing IF assembly and resembling epidermolysis bullosa simplex (EBS) patients [61]. With theses mice, mechanical stress was also identified as one of the key factors to cell rupture [61]. The mechanical properties of keratinocytes are largely regulated by the expressed keratins [5]. While K5/K14 in basal keratinocytes organize into loose bundles connecting DSMs and HDs (Fig. 1.6a), the expression of K1/K10 in suprabasal layers leads to tight bundles of keratin fibers that arrange parallel to the cell surface and cause flattening of the afore prismatic cells [5, 62]. At sites of high mechanical strain at the palms and soles, K9 is additionally expressed [63].

Despite the crucial role of keratins in cell shape and mechanical stability, individual keratin knockout mice do not show dramatic phenotypes because of the compensatory effects of different keratin isoforms [5, 42, 66]. Mice entirely lacking keratin type II expression, however, die early during embryonic development presumably due to disruptions in mammalian target of rapamycin (mTOR) signaling [67]. The re-expression of the simple epithelial keratin K8 alone is sufficient to rescue the embryonic phenotype but still leads to keratinocytes depleted of type II keratins (KtyII$^{-/-}$) because K8 is not expressed in stratified epithelia [58].

In the KtyII$^{-/-}$ keratinocytes, DSMs are destabilized due to PKC-α mediated phosphorylation of DP [58]. In the skin of these keratin-deficient mice, the impaired desmosomal adhesion manifests by cytosolic expression of desmosomal components and inter-cellular splits [64] (Fig. 1.6b). Conversely, the disruption of DSMs by depletion of DP leads to disorganized keratin IFs [68, 69]. The interdependence of DSMs and keratin IF, which allows stable cell–cell adhesion, is also manifested in cell culture experiments, in which

at least 60 % of wt keratinocytes in a mixture with KtyII$^{-/-}$ are required for cell sheet stabilization [64].

On the cellular level, DSM formation changes the keratin dynamics (Fig. 1.6c) [65]. In cultured keratinocytes without cell–cell contacts, F-actin [70], MT [71, 72], and keratin IF [73] formation are initiated close to focal adhesions (FAs) [65]. Keratin filaments then elongate by end-to-end fusion of oligomers, integrate in the keratin IF, and are transported towards the nucleus in an actin-dependent manner [65, 74]. Bundling increases mechanical stability, reduces turnover, and is increased around the nucleus [65, 75]. The keratin filaments are then degraded or disassembled providing a diffusible pool [65, 74]. At DSMs, HDs, and in the perinuclear region, keratin filaments are stabilized and turnover is reduced [65]. In living mouse embryos, the movement of keratin particles is random and not organized by the MT and F-actin cytoskeletons as in

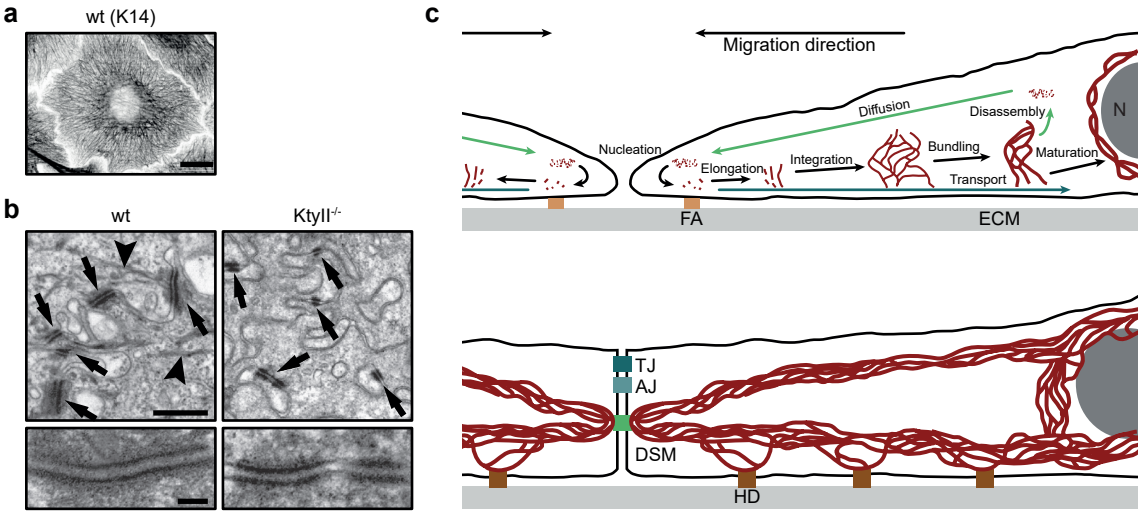

Figure 1.6: The keratin IF is essential for stable cell–cell adhesion. (**a**) The keratin IF shows enhanced bundling in the perinuclear region of cultured keratinocytes. Scale bar: 10 µm. (**b**) Keratinocytes depleted of type II keratins (KtyII$^{-/-}$) have less and smaller DSMs than wt keratinocytes. Arrows: desmosomes, arrow heads: keratin IF. Scale bars: 500 nm, 100 nm. (**c**) *Top* In epithelial cells migrating to close a wound, keratin (red) turnover is high to allow migration. Keratin filaments are nucleated close to focal adhesions (FAs) at the leading edge, then individual filaments elongate and integrate in the keratin network, which bundles more towards the nucleus. Bundled filaments either mature by post-translational modifications and integrate in the perinuclear cage, which protects the nucleus, or disassemble. While transport in the cell is F-actin-dependent, disassembled fragments diffuse back to the leading edge. *Bottom* In static epithelia, the keratin IF is mature and forms stable, thick filaments connecting desmosomes (DSMs), hemidesmosomes (HDs), and the perinuclear cage. Furthermore, the keratin cycling is low. N: nucleus, ECM: extracellular matrix, TJ: tight junction, AJ: adherens junction. The modified figures are reproduced with permissions from [5] (**a**), [64] (**b**), and [65] (**c**).

cultured keratinocytes [76]. DSMs, however, act also in the living system as organizing centers for the keratin IF [76]. Even though the detailed mechanism of the stabilization of the IF at DSMs remains to be elucidated, it highlights the importance of mechanical strength in cell–cell adhesions even at the cost of reduced dynamics.

1.5 Desmosomes and Disease

DSMs are targeted by auto-immune diseases as well as bacterial or endogenous toxins [1, 26, 77]. In Pemphigus, for example, auto-antibodies against desmosomal cadherins result in impaired cell adhesion [1]. While targeting Dsg3 affects mucous membranes around inner organs [1], targeting Dsg1 leads to skin blistering [78]. Similar symptoms are also observed if instead of auto-antibodies bacterial proteases in *Staphylococcus* scalded-skin syndrome or bullous impetigo disrupt Dsg1 function [1, 79]. Despite the appealing theory that auto-antibodies and proteases directly prevent cadherin adhesion, downstream events seem to be involved in diseases phenotypes. For example, Dsg1 regulates mitogen-activated protein kinase (MAPK) signaling [80] and Pg is required for the full disease phenotype of Dsg3 antibodies in cell culture [1, 81].

Genetic mutations targeting desmosomal components lead to heart and skin diseases. Interestingly, other internal organs are not affected, strongly suggesting that DSMs are particularly important in tissues exposed to high mechanical stress [26]. To date, a variety of genetic mutations for all major desmosomal components are reported (Tab. 1.1) [1, 26, 77]. Among the best described diseases are the Naxos-Carvajal syndrome and epidermolysis bullosa (EB). The Naxos-Carvajal syndrome can be caused by mutations in DP or Pg and is characterized by cardiomyopathy, palmoplantar keratoderma, and woolly hair [77, 82]. EB collectively describes a variety of skin blistering diseases caused by impaired cell–matrix or cell–cell adhesion [83], where the specific disease phenotype varies largely ranging from lesions at sites of increased mechanical stress like palm and soles to the lack of epidermis in large areas [84].

Despite the growing knowledge on the genetic cause for DSM-associated diseases, mechanistic insights in how the underlying mutation results in the observed phenotype remain sparse. Disruption of the mechanical DSM–IF linkage is involved in disease development but does not explain all phenotypes [77]. DSMs are for example also important for gap junction formation, which might be the cause of some cardiac phenotypes [86]. Other interesting mechanistic questions center around the tissue-specificity: expression patterns can explain tissue specificity for some desmosomal components but DP, for example, is an obligate component of DSMs in heart and skin tissues. However, skin- and heart-specific DP mutations as well as mutations clinically manifesting in both tissues have been reported [77].

Affected protein	Disease	Heart	Skin	Hair
DP	Carvajal	LV DCM	PPK	Woolly hair
	SFWS	LV DCM	Skin fragility, PPK	Woolly hair
	LAEB	LV DCM	Skin fragility	Hypotrichosis/alopecia
	SPPK		PPK	
Dsg1	SPPK		Skin fragility, PPK, erythoderma	Hypotrichosis/alopecia
	SAM		Skin fragility, PPK, erythoderma	Hypotrichosis/alopecia
Dsg4	ARM			Monilethrix
	LAH			Hypotrichosis/alopecia
Corneo-desmosin	LAH			Hypotrichosis/alopecia
	PSS-B		Erythoderma, skin peeling	
Dsc2	CWP	ARVD/C, LV DCM	PPK	Woolly hair
Dsc3	HRSV		Skin fragility (debated)	Hyptrichosis/alopecia
Pg	LCEB		Skin fragility	Hypotrichosis/alopecia
	Naxos	ARVD/C	PPK	Woolly hair
	CAP	ARVD/C	PPK	Hypotrichosis/alopecia
	AED		Skin fragility, PPK	
Pkp1	EDSFS		Skin fragility, PPK	Hypotrichosis/alopecia

Table 1.1: Genetic DSM disorders (classified as desmosomal genodermatoses) affect heart, skin, and hair. Heart problems can manifest in arrythmogenic right ventricular dysplasia/cardiomyopathy (ARVD/C) or left ventricle dilated cardiomyopathy (LV DCM), skin can be fragile, peeled off, thickened [palmoplantar keratoderma (PPK)] or inflamed (erythoderma), and hairs can be less (hypotrichosis) or absent (alopecia), woolly or appear beaded (monilethix). Most genetic desmosomal disorders are autosomal-recessive with the exception of the autosomal-dominant striate palmoplantar keratoderma (SPPK) and hereditary hypotrichosis simples (HHS) and in rare cases the Carvajal syndrome. SFWS: skin fragility woolly hair syndrome, LAEB: lethal ancantholytic epidermolysis bullosa, SPPK: striate palmoplantar keratoderma, SAM: skin dermatitis, multiple severe allergies and metabolic wasting, ARM: autosomal recessive monilethrix, LAH: localized autosomal recessive hypotrichosis, PSS-B: peeling skin syndrome type B, CWP: cardiomyopathy with woolly hair and palmoplantar keratoderma, HRSV: hypotrichosis with recurrent skin vesicles, LCEB: lethal congenital epidermolysis bullosa, CAP: cardiomyopathy with alopecia and palmoplantar keratoderma, AED: acantholytic ectodermal dysplasia, EDSFS: ectodermal dysplasia skin fragility syndrome. The table content is reproduced with permission from [85].

1.6 Dynamics of the Desmosome

DSMs are very stable structures that are hard to dissolve biochemically because of their resistance to many detergents over a wide pH range [12]. Furthermore, cell–cell adhesion is so stable that DSM are not split in half but reside with one cell upon mechanical stress if the DSM–IF linkage is disrupted [69]. In addition, the mobile fraction of DP is with $< 20\,\%$ very low in both, the epidermis and cultured keratinocytes [87]. Therefore, DSMs were long regarded as stable, static tethers for the keratin IF [22, 88]. Insights from DSM-associated diseases (Sec. 1.5) and mice but mostly cell culture and *in vitro* experiments, have shown in the meantime that the DSM assembly as well as dynamics are tightly regulated [22].

DSM formation is induced by Ca^{2+} [23]. In the presence of extracellular Ca^{2+}, first AJs form but quickly afterwards also DSMs establish [22, 89]. DP in cultured human cells for example is recruited to DSMs in three phases: within the first $3-10\,\text{min}$ new contact zones appear, after about 30 min cytosolic Pkp2-enriched puncta are formed, which are then F-actin cytoskeleton-dependently transported to the cell–cell contacts [90]. The dynamics of this process can be slowed by introducing a point mutation (S2849G) in DP that prevents PKC-α-dependent phosphorylation and thereby enhances DP–IF binding [90]. PKC-α-mediated phosphorylation is thus important for the initial recruitment of DP to DSMs. On the other hand, PKC-α also serves as a negative regulator for the hyper-adhesive state that is assumed to be the predominant adhesive state of DSMs in the adult skin tissue [25] (Fig. 1.7). Note that hyper-adhesion takes days to evolve in cultured cells but upon wounding cells across hundreds of micrometers become Ca^{2+}-dependent within an hour [25, 91], potentially because Pkp3 recruits PKC-α [92].

Next to PKC-α-dependent phosphorylation, other post-translational modifications (PTMs), like glycogen synthase kinase 3 (GSK3)-dependent phosphorylation and protein arginin methyltransferase 1 (PRMT-1)-dependent methylation of DP, modify the strength of the DP–IF linkage [93] and a point mutation, R2834H, is even associated with arrhythmogenic cardiomyopathy (AC) [93, 94]. The regulatory function of most reported desmosomal mutations, however, remains to be elucidated. Furthermore, also p38 MAPK signaling downstream of hepatocyte growth factor activator inhibitor type 1 (HAI1) is involved in regulation of the DSM–IF binding [95]. In addition, the casein kinase (CK)-1α scaffold protein family with sequence similarity 8 member H (FAM83H), which regulates keratin networks by recruitment of CK-1α preferentially around the nucleus, could also be involved in the regulation of the DSM–IF linkage [96].

Not only the DP–IF linkage is regulated by PTMs but also other processes during the formation of DSMs. For instance, Dsc3 is phosphorylated when DSMs are formed [97] and the association of 14-3-3 proteins with Pkps in a phosphorylation- and isoform-dependent manner provides an additional regulatory level [98]. The importance of intact localization

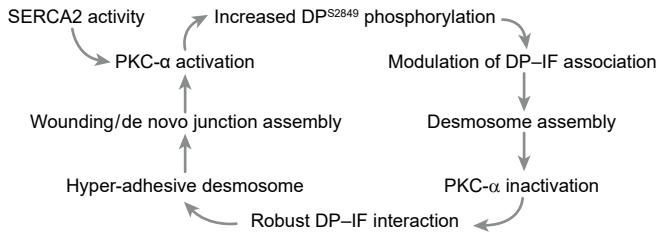

Figure 1.7: DP-related signaling regulates DSM assembly and disassembly. During junction assembly sarcoendoplasmatic reticulum Ca^{2+}-ATPase isoform 2 (SERCA2) activates protein kinase C (PKC)-α, which phosphorylates desmoplakin (DP) and allows for initial desmosome assembly but needs to be inactivated for the robust DP–intermediate filament (IF) interaction in hyper-adhesive desmosomes. The figure is reproduced with permission from [22].

pathways is underlined by diseases that do not affect desmosomal components directly but impair their localization like Darier's disease, where sarcoendoplasmatic reticulum Ca^{2+}-ATPase isoform 2 (SERCA2) is lost, or Hailey-Hailey disease, where the Golgi-resident secretory pathway Ca^{2+}-ATPase isoform 1 (SPCA1) is defective, both leading to cytosolic accumulation of desmosomal components and loss of adhesion [22, 99].

Finally, the dynamics of desmosomal proteins depend on all three cytoskeletal networks. The dependence of the keratin IF is obvious and detailed above, F-actin-driven formation of AJ precedes formation of DSM [89] and some parts of the localization of DP to DSM is F-actin dependent [90]. In addition, the lack of the centrosomal protein Lis1 leads to reduced protein expression and localization of desmosomal components and increased DP turnover [100] demonstrating a role of the MT cytoskeleton in DSM regulation.

1.7 Desmoplakin

DP is the major linkage of the ODP proteins to the keratin IF and an obligate component of all DSMs. DP recruitment to DSMs as well as its PTMs are tightly regulated (Sec. 1.6) and disturbances lead to heart and/or skin diseases (Sec. 1.5). The role of DP is, however, not only limited to DSMs but DP is also involved in the regulation of differentiation-specific MT arrangement in the epidermis [101].

1.7.1 Domain Structure

The tripartite structure of DP was revealed already in the first biochemical analysis of the two major DP splice isoforms, DPI and DPII: a central elongated rod with terminal coiled or folded domains [102]. This assignment was confirmed by the isolation and characterization of complementary deoxyribonucleic acid (cDNA) [18].

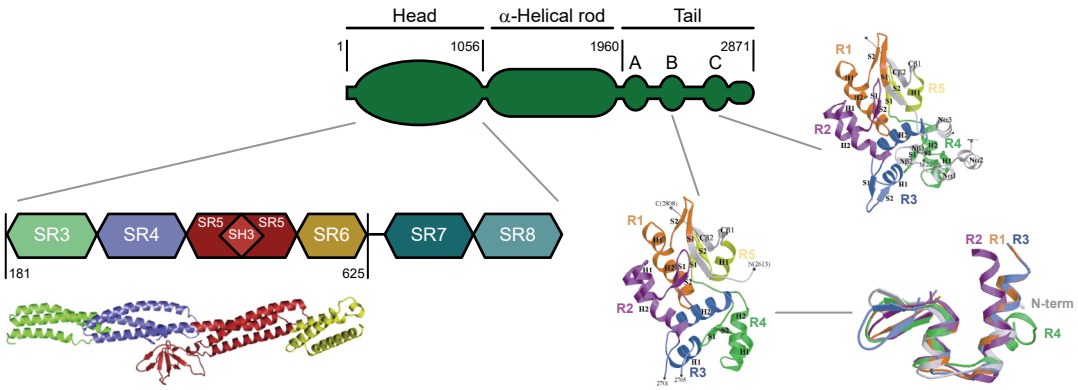

Figure 1.8: Desmoplakin (DP) has a tripartite structure with globular head and tail domains connected by an elongated α-helical coiled-coil rod. In the DP head a short unstructured N-terminal region is followed by a plakin domain comprising of six spectrin repeats (SRs). Note the unusual long linker between SR6 and SR7 and the Scr-homology 3 (SH3) domain in the middle of SR5. The C-terminal tail domain has three intermediate filament binding domains, A, B, and C, which consist of 4.5 plakin repeats (R). The high similarity of the individual repeats and the N-terminus is visualized in the overlay of individual repeats from domain B. Indicated domain boundaries correspond to amino acids in DPI. The modified figures are reproduced with permissions from [103] (plakin domain) and [104] (intermediate filament binding domains).

Next to structural information, localization of truncated DP constructs provided first insights in domain functions: the N-terminal region is required for desmosomal localization but is dispensable for IF interaction, while the C-terminal region interacts with keratin and vimentin IF differential but is not involved in desmosomal localization [105–107]. Overexpression of a dominant-negative N-terminal truncation mutant then provided the first direct evidence that the C-terminal region of DP is indeed required for the DSM–IF linkage and also revealed a role of DP in the proper segregation of AJs and DSMs [108].

The periodicity of acidic and basic residues in the sequence of the central coiled-coil rod suggests the formation of dimers or oligomers for DPI and DPII [18], while *in vitro* dimerization is only observed for the longer splice isoform DPI [102]. This long, flexible rod domain extends up to approximatley 130 nm [18] and is next to the overall protein size one reason why to date no crystal structure of full-length DP exists. Individual domains of DP head and tail, however, have been resolved (Fig. 1.8).

The N-terminal domain comprises of six spectrin repeats (SRs), termed SR3 to SR8 based on sequence homologies to other plakin family members, which form tandem pairs [109]. An extended linker region between SR6 and SR7 provides flexibility between the rather inflexible SR domains and could also act as a spring in response to mechanical force [110]. Furthermore, this linker region is the predicted hinge point for an overall *L*-shape of the plakin domain [111] providing a remarkable difference to the highly similar but linear arrangement of plectin's plakin domain [112]. Another striking feature of the N-terminal

domain is a single Scr-homology 3 (SH3) domain that is inserted in the middle of SR5 [103], a feature also seen in other plakins [113]. Upon unfolding, i.e. in response to mechanical stress, the SH3 domain is predicted to shift from an auto-inhibited into a fully functional state [114].

The C-terminal domain contains three regions with 4.5 repeats of a 38 aa motif already identified in the cDNA sequence [18], which fold into discrete subdomains termed IF-binding domains A, B, and C [104]. IF proteins possess many negatively charged patches, while the resolved structures of IF-binding domains B and C contain positively charged grooves, suggesting an electrostatic-driven interaction between DP and IF [104]. *In vitro* experiments confirmed that individual domains are capable of binding the IF protein vimentin but cooperativity of two domains requires a flexible linker region, which is present for BC but not AB [104].

In summary, DP has a tripartite structure with the head domain binding to desmosomal plaque and the tail domain binding to IF connected by a central coiled-coil rod of isoform-specific length (Fig. 1.8).

1.7.2 Splice-isoforms

Even before DP was named, the two major isoforms, DPI and DPII, were identified as highly similar proteins distinct from all other desmosomal components and expressed in similar high levels in the epidermis [115], but it took three decades to also identify a third minor isoform, DPIa, which is expressed in much lower levels [116]. All DP isoforms are splice variants differing in the length of the central coiled-coil rod with DPII lacking about 2/3 of the rod present in DPI [18], while DPIa has an intermediate rod length [116] (Fig. 1.9a).

DPI is ubiquitously expressed in DSM forming tissues. Levels of DPII, however, are comparable to DPI in simple and stratified epithelial cells, but no DPII is expressed in cardiac muscle cells [117]. The overall expression levels of DPIa are much lower than for the two major splice isoforms and expression patterns seem to follow DPII (Fig. 1.9b) [116].

On a functional level, DPII can compensate partially but not entirely for the loss of DP [118]. A patient with a homozygous truncation of DPI, which impaired stability and caused protein degradation, developed a recessive mild epidermolytic palmoplantar keratoderma as well as woolly hair and died of an early cardiomyopathy at the age of four [118]. This patient thereby showed that DPI was dispensable for the development but required for full functionality, particularly of the heart [118].

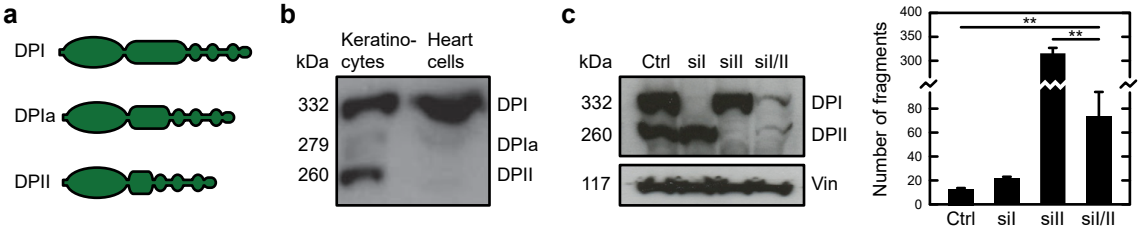

Figure 1.9: Desmoplakin (DP) has two major and one minor splice isoforms. (**a**) DPII and DPIa lack parts of the central coiled-coil rod domain present in DPI. (**b**) In human keratinocytes (HaCaT) all DP isoforms are expressed, while human atrium cells express only DPI. Note that expression levels of DPIa are low compared to DPI and DPII. (**c**) Depletion of DPI only slightly disturbs cell sheet integrity as judged by the number of fragments after rapid movement by tube inversion. In contrast, depletion of DPII dramatically reduces cell sheet stability, which presumably also explains the increased fragment number for reduced levels of both isoforms. Ctrl: siRNA control, siI: siRNA against DPI, siII: siRNA against DPII, siI/II: siRNA against DPI and DPII, Vin: Vinculin. Two-sided student's t-test with ** $p \leq 0.01$. The modified figures are reproduced with permissions from [116] (**b**) and [119] (**c**).

This DPI-deficient patient as well as patients showing skin problems caused by DP haploinsufficiency (Sec. 1.7.4) sparked the analysis of isoform-specific effects on cell stability in cultured keratinocytes [119]. While the keratin IF in wt cells thickens, wrinkles and condensates bundles particularly around the nucleus in response to cyclic mechanical stress, the keratin IF in cells with reduced DP levels is thinner and large intercellular gaps appear. Interestingly, reducing DPI levels but keeping DPII levels unaffected preserves the response of the keratin IF in response to mechanical stress. Along this line, assessing skin sheet stability upon mechanical stress in cells expressing different levels of DPI and DPII shows that DPII is required for cell sheet stability (Fig. 1.9c). Thus, DPII is essential for stable cell–cell adhesion upon mechanical stress in cultured keratinocytes [119].

On a basic level, the difference between DPI and DPII is reflected in their protein lengths. While DPI rod is predicted by sequence data and rotary shadowing to extend up to 130 nm and 180 nm, respectively, DPII could only span 43 nm and 78 − 93 nm [18, 102]. In ultrastructural images combined with immunogold labeling, the distance between DP head and tail domains was determined to 42 nm [9] (Sec. 1.2) matching with the predicted lengths for DPII but provoking the question how DPI is arranged in DSMs. More recent dSTORM measurements confirmed the order of magnitude of measured distances and suggest an orientation of DPI in an angle towards the plaque [20]. Of note, DP seems to be more elongated in basal as compared to suprabasal layers [20].

In some arrythmogenic right ventricular dysplasia/cardiomyopathy (ARVD/C) patients, the DPI specific part of the coiled-coil rod is mutated but their effect is unknown, so phenotypes might also be caused by impairment of the protein stability and not necessarily involve domain specific effects [110]. A functional distinct role of DPI is

the recruitment of Lis1, a centrosomal protein essential for differentiation-specific MT organization in the epidermis [100].

In summary, the differential expression of DPI and DPII is striking and both isoforms can only partially compensate for the loss of the other isoform but mechanistic insights how isoform-specificity is mediated remains sparse.

1.7.3 Knockout Mouse

Mice lacking DP die early during embryonic development at embryonic day (E)6.5 [68], even before keratin-deficient mouse embryos (E9.5) [67] implicating a role of DSMs in embryonic development independent of their attachment to keratins. In the DP-deficient embryos, only few and small DSMs form and the keratin IF remains unstructured demonstrating roles for DP in both, DSM stabilization and IF linkage [68]. Interestingly, proliferation is impaired and embryos fail to elongate the egg cylinder, which requires tight cell–cell adhesion [68]. Growing $DP^{-/-}$-embryos in $DP^{+/+}$-extra-embryonic tissue rescues egg cylinder formation and knockout (KO) embryos are indistinguishable from wt embryos until E7.5, when the heart forms [120], and cell–cell adhesions gain importance due to the increased stress by the heart beat [121]. The small and malformed embryos die because of their drastically slowed heart beat at E10 but also exhibit defects in neural tube formation, skin epithelium development, and capillary formation [121].

Epidermis-specific DP-deficient mice [69] are perinatal lethal because of their inability to withstand even mild mechanical stress (Fig. 1.10a). In the epidermis, DSM number and size is only slightly reduced, while isolated keratinocytes form almost no DSMs (Fig. 1.10b, c). Most desmosomal proteins, however, are expressed in skin and isolated keratinocytes to comparable levels in wt and KO background (Fig. 1.10d). In contrast to the hardly reduced number of DSMs, significantly less AJs form in basal and spinous layers of DP-deficient epidermis. Upon Ca^{2+}-driven induction of cell–cell contact formation in cultured keratinocytes, KO cells form initial cell contacts but fail to arrange adhesion zippers or re-organize the F-actin cytoskeleton; an observation matching with disturbed F-actin appearance in the epidermis [69]. The localization defect observed in cultured DP-deficient keratinocytes can be rescued with the expression of DP constructs containing the DP head domain, while the binding to the keratin IF requires the tail domain (Fig. 1.10e) [69], which confirms the distinct functions of head and tail domains (Sec. 1.7.1).

Cardiac-specific DP-deficient mice [122] are viable but have defects in desmosomal integrity, which are ultrastructurally detectable and lead to cardiomyopathy and premature death within the first five months. Next to impaired desmosomal adhesion also gap junctions are affected, which indicates a role of DP in the stabilization of connexins.

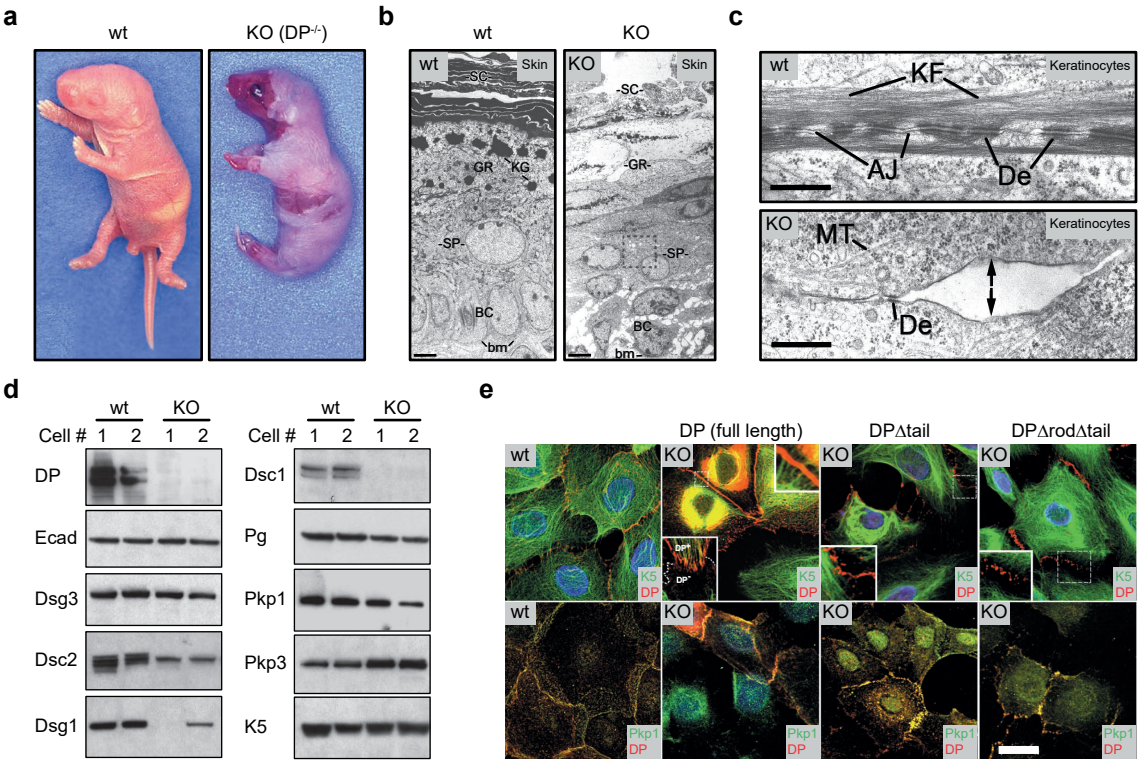

Figure 1.10: The epidermis-specific desmoplakin (DP) knockout (KO) is perinatal lethal. (**a**) Newborn pups denude upon mild mechanical stress. (**b**) Electron microscopy images of the skin of E18.5 wild type and DP-KO mice show disruption of the stratum corneum (SC) in some parts. Furthermore, cells in the granular layer (GR) show reduced keratohyalin granules (KG) and in some parts, basal cells (BC) and spinous layer (SP) are separated. bm: basement membrane. Scale bar: 5 µm. (**c**) Ultrastructural images of wt keratinocytes show alternate patterns of adherens junctions (AJ) and desmosome (De) connected to keratin filament (KF), while KO keratinocytes fail to seal the cell–cell contact (arrows). MT: microtubule. Scale bar: 0.5 µm. (**d**) The expression of E-cadherin (Ecad), most desmosomal components and keratin (K)5 are unaffected but desmoglein (Dsg)1 and desmocollin (Dsc)1 are reduced in cultured keratinocytes. Pg: plakoglobin, Pkp: plakophilin. (**e**) Re-expression of full-length DP rescues the KO phenotype as judged by localization of Pkp1 to cell–cell adhesions instead of the nucleus and attachment of the keratin filaments. Truncated protein versions lacking either the tail domain or tail and rod domains, rescue Pkp1 localization but only partially the attachment of keratin filaments. Scale bar: 20 µm. The modified figures are reproduced with permission from [69].

Similarly, depleting DP from the cardiac conduction system [123] showed that DP is involved in the beat-to-beat regulation probably via its role in stabilizing the gap junction proteins connexins. The stabilization of connexins by DP might thereby be indirect via the stabilization of MT trough an interaction with end-binding protein 1 (EB1) [124, 125].

In contrast to heart and skin cells, loss of DP in the simple epithelium of the intestine does not cause adhesion defects [126]. Furthermore, the assembly of the keratin IF remains unaffected by the loss of the DSM–IF connection in the intestine. Instead the formation of the F-actin-based microvilli is impaired [126], which underlines the apparently different roles of DP in simple and stratified epithelia.

1.7.4 Clinically-manifested Mutations

Mutations in DP lead to heart and skin diseases (Sec. 1.5). The pathogenic mechanisms of these mutations are only beginning to be understood. Two point mutations, V30M and Q90R, in the very N-terminal part of DP abolish the localization to DSMs and *in vitro* binding to Pg [94]. Several point mutations in the following plakin domain have been associated with ARVD/C [85, 127]. Many of these pathogenic mutations associated with ARVD/C are located in or around the SH3 domain (Fig. 1.8), targeting both core residues, which are presumably important for structural stability, and surface-exposed residues, which are potentially involved in protein–protein interactions [103, 110]. Other ARVD/C-causing mutations affect the flexible linker between SR6 and SR7, while mutations affecting surface residues of SR7/8 are not pathogenic [112]. Additional mutations in the coiled-coil rod and C-terminus associated with ARVD/C are assumed to decrease protein stability and promote aggregation [110].

Patients suffering from a DP haploinsufficiency are viable and show palmoplantar thickening, increased susceptibility to fissures, and normal DSMs coexisting with DSM-like structures lacking the keratin IF attachment [128]. Of note, skin integrity is preserved at most sites and only disturbed at palms and soles, which are sites of intense and repetitive mechanical stress. Furthermore, the clinical phenotype is stronger in patients performing manual labor [128, 129]. The observation that the severeness of the symptoms correlates with mechanical labor is consistent with the observation that haploinsufficiency of DP can also remain without clinical symptoms [130]. Patients that combine the haploinsufficient background with point mutations either in the plakin region, N287K presumably important for Pkp1 binding, or in the IF-binding B domain, R2366C, suffer from palmoplantar keratoderma, hyperkeratotic plaques, and alopecia [130].

Truncated versions of DP are sufficient to allow heart and skin development but impair the resistance to mechanical stress. Loss of the C domain causes striate keratoderma especially at sites of high mechanical exposure, woolly hair, and dilated left ventricular

cardiomyopathy [131]. A more drastic truncation of the entire tail domain causes lethal acantholytic EB, which is neonatal lethal due to extensive water loss caused by skin and mucous membrane fragility because DSM form but lack their IF-connection [132].

Taken together, DP mutants show that the N-terminal regions are sufficient for tissue development but full-length DP is required to withstand mechanical stress.

1.8 Desmosomes and Mechanical Stress

1.8.1 Impaired Tissue Integrity

DSMs are prevalent in tissues exposed to mechanical stress like the heart and the skin tissues [10, 26] suggesting a role of DSMs in coping with mechanical stress. A common theme in many desmosomal mutant mice and patients suffering from DSM-associated diseases is the reduced ability to withstand mechanical stress (Sec. 1.5, 1.7.3, 1.7.4). In DP-deficient mice, for example, mice die when stress increases either because the heart starts to beat or in epidermis-specific KO mice, when pups are exposed to the mechanical stress of birth [69, 121]. Similarly, mechanically challenged palms and soles are the skin areas affected in all patients that survive early childhood (Sec. 1.5). Remarkably, for diseases with comparatively mild symptoms, patients performing manual labor suffer from more severe symptoms [129] (Sec. 1.7.4). Mouse and patient data therefore demonstrate a role of DSMs in tissue integrity upon mechanical stress.

1.8.2 Transcriptional Regulation

Little is known about stress-induced regulation of DSM composition and number by signaling pathways [133]. In general, serum-response factor (SRF) and Yes-associated protein (YAP)/transcriptional coactivator with PDZ-binding motif (TAZ) shuttle between the cytoplasm and the nucleus in keratinocytes. The translocation of SRF to the nucleus is regulated by actin, RhoA and myocardin-related transcription factor (MRTF)-A. Because MRTF-A in the nucleus promotes expression of Dsg1 and Pkp2 a role of the SRF pathway in DSM regulation is plausible [133]. The modification of RhoA by Pkps [134] and the up-regulation of the SRF/MRTF-activated transcription factor activator protein (AP)1 in stretched skin [135] provide the basis for speculations about mechanical stress-induced regulation but direct evidence is missing [133].

In the Hippo signaling pathway, the transcriptional coactivators YAP and TAZ are well-described to localize to the nucleus in response to a broad variety of stimuli including e.g. an increase in cell area, stiffening of the extracellular matrix (ECM) or disruptive flow (Sec. 2.1.2) [136]. In the nucleus, YAP/TAZ bind to transcription enhanced associate

domain (TEAD) proteins to stimulate transcription [136]. Desmosomal components are to date not directly associated with the YAP/TAZ pathway but identified as putative targets of Tead4 [133, 137].

1.8.3 Stiffening of the Keratin IF

On a molecular level, the keratin IF forms non-polar fibers that in contrast to F-actin and MT cytoskeletons do not provide the polarity required for directional movement of motor proteins [138–140]. Thus, motor-protein activity, which is important for intracellular generated tension across FAs and AJs, cannot contribute directly to tension across DSMs. Increased actomyosin activity, however, leads to reduced keratin IF motion, which is likely caused by prestressed filaments [141]. Furthermore, the keratin IF is essential for cell integrity even upon mild external stress [133, 142]. Mutations affecting keratin IF stability in cells, still form normal filaments *in vitro* [143] suggesting that bundling, dynamics or the association with other proteins, e.g. DP, is affected [133]. In line with this observation, the keratin IF responds to external stress *in vitro* by stiffening and increased bundling [55–57] and shows also in cells subjected to mechanical stress increased bundling and concentration around the nucleus (Fig. 1.11a) [144], which might be regulated by enhanced disulfide crosslinks [145]. The bundling is lost, if either the keratin IF is mutated, e.g. in EBS [144], or if the attachment to the DSM is impaired, e.g. by depletion of DPII (Sec. 1.7.2) [119]. This loss of bundling further supports a crucial role of an intact DSM–IF linkage for cell stability upon mechanical stress. Taken these observations together with the complex interplay of the IF with other cytoskeletons in multi-cellular processes like migration and embryonic development and the broad range of expression patterns as well as PTMs, the IF is postulated to be a load-bearing structure important for cell signaling in response to mechanical stimuli [146].

1.8.4 Stretching of Proteins

In *in vitro* experiments the IF resists breakage of the filament also at much higher strains than the more rigid MT and F-actin cytoskeletons (Fig. 1.11b) [148]. For low strains, the IF is very soft but hardens at higher strains [148] (Sec. 1.4), which contributes to the high stiffness of keratinocytes [59, 150]. The IF is also very extensible with at least 200 % extension of K5/K14 filaments *in vitro* lending support to the hypothesis that tension might be transduced through the DSM and buffered at the IF [51]. Stretch-induced conformational changes might then open binding sites that modify cellular behavior. Simulations of the DP plakin domain, for example, suggest that binding sites at the SH3 might become accessible upon tension [114] and recruitment of FAM83H to DSMs as a result of force-induced conformational changes is hypothesized [133].

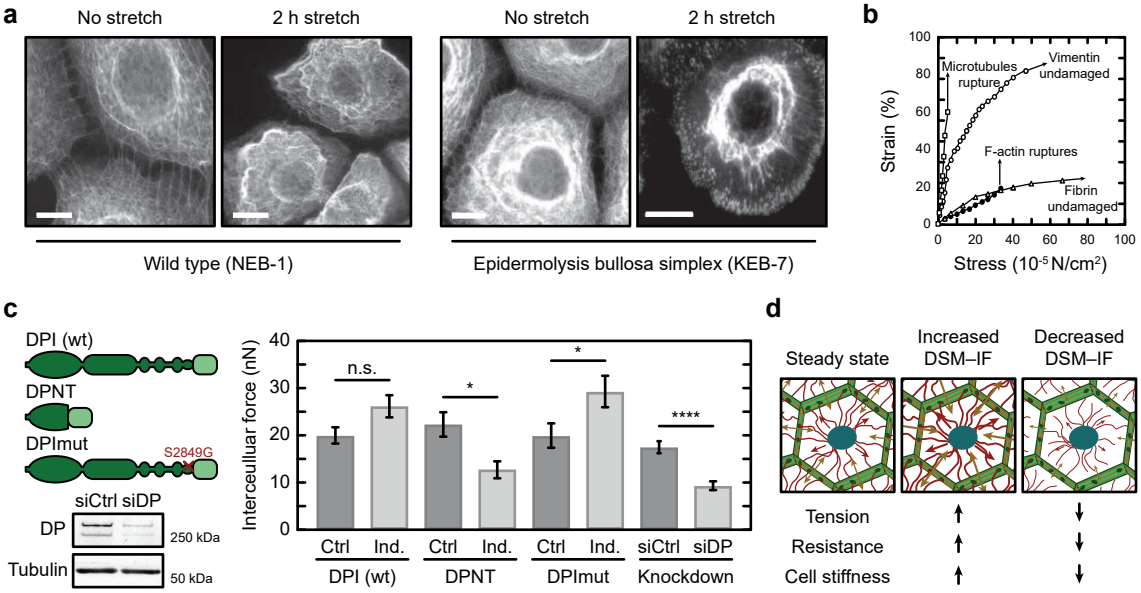

Figure 1.11: The intermediate filament (IF) and the desmosomes (DSMs) modulate cellular response to and generation of force. (**a**) The keratin IF compacts and wrinkles in keratinocytes upon oscillating stretch (4 Hz and 12 % amplitude). If DSMs or IFs are modified, the response to mechanical stress is modulated, e.g. lack of DPII leads to thinner IFs [119] and a single point mutation (R125P) in K14 leads to keratin aggregates. NEB-1: keratinocytes from normal relative of epidermolysis bullosa simplex patient, KEB-7: keratinocytes with keratin mutation in case of epidermolysis bullosa simplex. Scale bars: 10 µm. (**b**) Polymers of the IF protein vimentin have *in vitro* distinct mechanical properties than polymers of the other two main cytoskeletons supporting a role of the IF in maintaining cell integrity. Vimentin is deformable at low stresses similar to microtubules (MTs) but preserves this elasticity also at larger stresses and strains, where MTs rupture. The F-actin polymers are more resistant to deformation than MTs and vimentin but rupture like MTs at higher stress. Next to the IF cytoskeleton also the blood clotting factor fibrin, which forms extracellular networks, resists high stress but shares the high strain resistance with F-actin. (**c**) The average intercellular forces are modulated by the DSM–IF linkage. Intercellular forces are determined with a micropillar assay in A431 cells with and without induction of GFP-tagged DP variants or siRNA-mediated DP knockdown. Decreasing the DSM–IF linkage by the dominant-negative N-terminal 584 aa of DP (DPNT) or knockdown of the endogenous protein, reduces intercellular forces. In contrast, increasing the DSM–IF linkage by overexpression of wild type DPI or S2849G-mutated DPI, which enhances IF binding [90, 93, 147], increases intercellular forces. The error bars represent the SEM from at least 18 cells for induction experiments and 30 cells for the knockdown experiment from three independent experiments. Two-sided student's t-test with **** $p < 0.0001$, * < 0.05, n.s. (not significant), $p \geq 0.05$. (**d**) A model proposes that the keratin IF resists the tension generated by actomyosin contractions. The modified figures are reproduced with permissions from [144] (**a**), [148] (**b**), and [149] (**c, d**).

1.8.5 Force Transduction

Desmosomal proteins, particularly DP, have the theoretical capacity to respond to mechanical cues by conformational changes and opening of binding sites. Experimental evidence for a role of DSMs in force transduction, however, remains sparse. The apparent stiffness of reforming Madine Darby canine kidney (MDCK) monolayers, for example, coincides with the formation of AJs but not with the formation of DSMs [151]. In keratinocytes, tension across AJs, however, increases in the absence of DP as judged by a conformation-specific α-catenin antibody α18 [152], which indicates that DSMs shared the load in the wild type keratinocytes. The open conformation of α-catenin might, however, not necessarily report force but could also reflect increased clustering in the more punctate AJs [153]. Similarly, disrupting the DSM with the dominant-negative acting N-terminal 584 aa of DP (DPNT), leads to increased α18 binding in regions of increased clustering [149].

Cell-generated forces at cell–substrate and cell–cell interfaces as determined by micropillar arrays, however, decrease when the DSM–IF linkage is disrupted by the expression of DPNT or the reduction of DP expression levels [149] (Fig. 1.11c). The effect of both DP depletion methods on the reduction of intracelluar forces is comparable, while cell–substrate forces are stronger affected by reduction of protein levels suggesting a role of non-junctional DP in generation of cell–substrate forces. In line with this hypothesis, increasing the level of DP increases forces at the cell–substrate interface. A more dramatic increase in both, forces at cell–substrate and cell–cell interfaces, however, results from the expression of the S2849G DP [149], which shows enhanced IF-binding [90].

The modulation of the DSM–IF linkage not only impacts cell-generated forces but also cellular stiffness as measured by atomic force microscopy (AFM) [149]. The stronger, the DSM–IF linkage, the stiffer the cells, i.e. lowest stiffness for DPNT-expressing cells and highest for S2849G expressing cells in hyper-adhesive cell sheets. The modification of cellular stiffness depends on the F-actin cytoskeleton lending support to a model, in which the keratin IF provides resistance counter-acting tension generated by actomyosin contractions (Fig. 1.11d) [149]. In accordance with this model, a truncated mutant lacking the keratin IF binding domain C shows on as a short-term reaction reduced cellular stiffness probably because the keratin network collapsed [131] and greater adhesive area. In addition to the short-term response, the DSM–IF interaction also influences the long-term stress response and cells with truncated DP relax more [154]. Furthermore, the impaired formation of microvilli structures in simple epithelia cells of the intestine lacking DP could be explained by a role of DSMs in counter-balancing the forces required for the long protrusions of the F-actin cytoskeleton in microvilli [126].

In summary, DSMs are involved in the cellular resistance to mechanical stress but how the molecular response is mediated and regulated remains to be elucidated.

2 FRET-based Tension Sensor

2.1 Mechanics in Biology

2.1.1 Mechanobiology

Mechanobiology describes the broad field of mechanics in biological systems and spans the range from whole organisms, over tissues and cells to individual proteins responding to mechanical cues [155, 156]. Already 1874, Wilhelm His postulated that cells obey mechanical principles, a point of view adapted by early cell biologists [156]. The research focus then shifted, however, to the deoxyribonucleic acid (DNA)–ribonucleic acid (RNA)–protein paradigm and signaling based on chemical modifications and protein–protein interactions driving cell fate decisions [156]. In the last years, the importance of mechanics to biology has gained more attention again. For example, cancer cell development and metastasis depend on the mechanical properties of the cell, the surrounding, and their interaction [157, 158]. Furthermore, the stiffness of the underlying substrate is sufficient to guide stem cell differentiation [159]. Tissue stiffness, for instance, varies greatly in the human body (Fig. 2.1), correlates with nuclear stiffness [160, 161] as well as changes in gene expression and mutation rates [162], and has direct implications on cellular functions like the heart beat in mouse embryos [163]. The mechanical properties of the cells are thereby largely defined by the cytoskeleton [164].

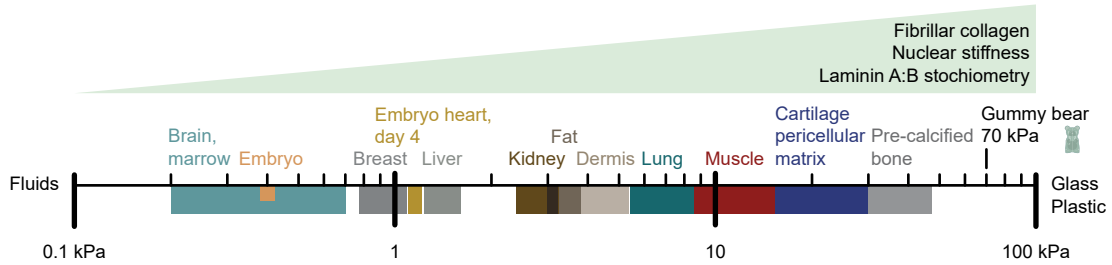

Figure 2.1: The stiffness is a characteristic property of tissues. Increased tissue stiffness correlates with increased fibrillar collagen, nuclear stiffness and laminin A. The modified figure is reproduced with permission from [162].

2.1.2 Mechanotransduction

Mechanotransduction describes the translation of mechanical cues into other signal types such as PTMs and ultimately a cellular response. Mechanical cues include for example tissue stiffness, adhesion, and external forces such as compressive forces on chondrocytes, shear forces on endothelial cells or tensile forces in myocytes or on epidermal cells. The importance of mechanotransduction for cellular biology is supported by the variety of diseases associated with disturbed mechanotransduction. Among the diseases are arteriosclerosis, osteoporosis and developmental disorders [165].

One common theme identified in many mechanotransduction processes is shuttling of transcriptional regulators between the nucleus and the cytoplasm [136, 155, 166, 167]. The best studied examples are YAP and TAZ that localize to the nucleus in response

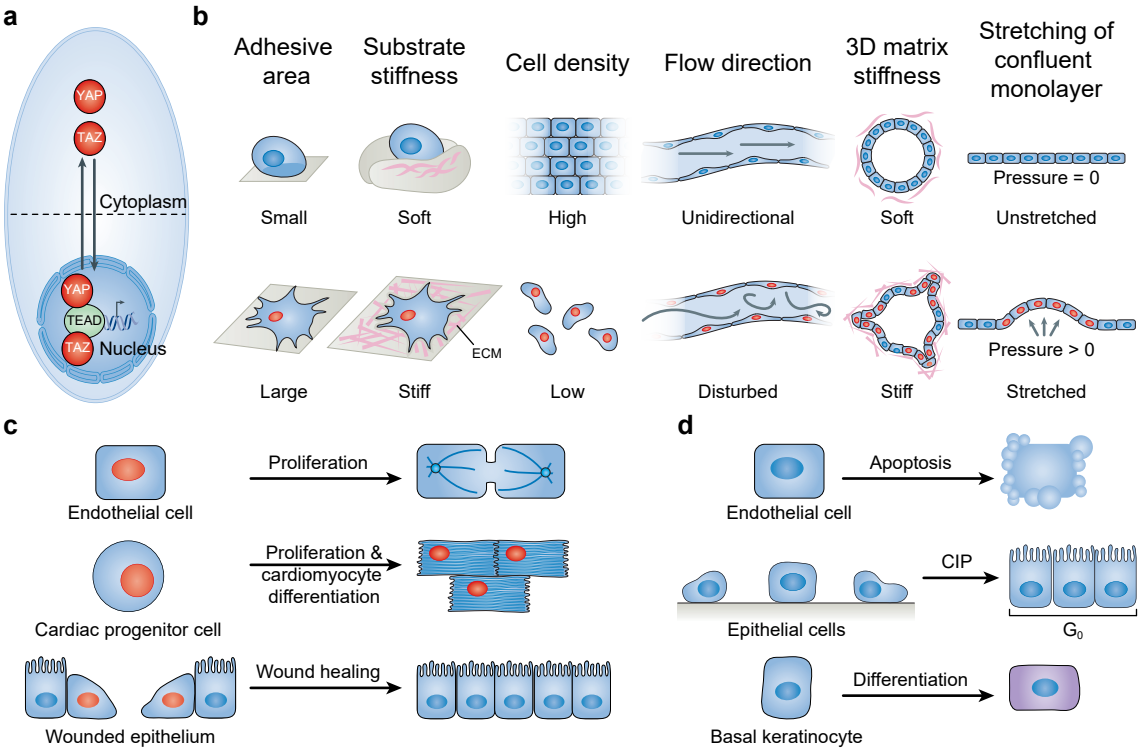

Figure 2.2: Nucleo-cytoplasmic shuttling of Yes-associated protein (YAP) and transcriptional coactivator with PDZ-binding motif (TAZ) depends on mechanical cues. (**a**) YAP and TAZ are either retained in the cytoplasm or localize to the nucleus, where they bind to transcription enhanced associate domain (TEAD)-containing proteins and regulate gene expression. (**b**) The localization of YAP and TAZ depends on external cues. (**c, d**) Nuclear localization and activation of YAP and TAZ (**c**) or cytosolic retention (**d**) cause specific cellular responses. The red nuclei indicate the localization of YAP and TAZ to the nucleus. CIP: contact inhibition of proliferation. The modified figure is reproduced with permission from [136].

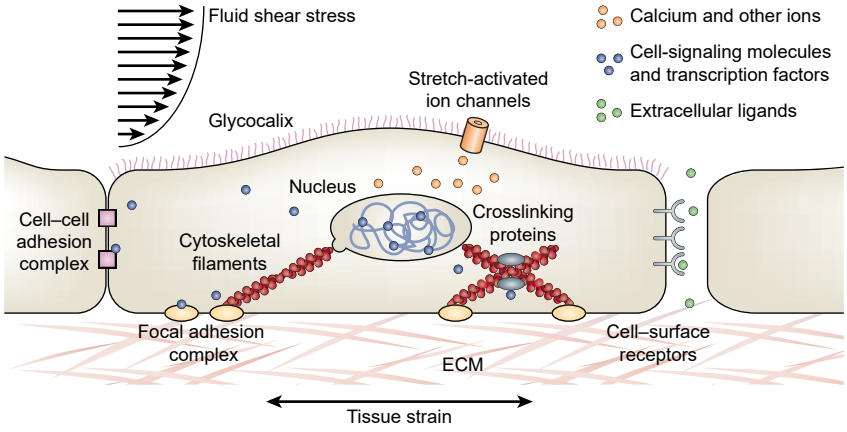

Figure 2.3: Different biological structures act as mechanosensors. Cells probe their environment with cell–matrix and cell–cell adhesions connected to the cytoskeleton, which is also mechanosensitive. Tissue strain can activate signaling pathways by conformation changes in extra- or intracellular proteins like filaments, crosslinkers or motor proteins. Endothelial cells use their glycocalix, carbohydrate-rich proteins at the cell membrane, to detect fluid shear stress, and many cell types possess stretch-activated ion channels selective for e.g. Ca^{2+}. Furthermore, the nucleus might also serve as mechanotransducer and compression of the intercellular space alters effective signaling molecule concentrations, which in turn modifies the cellular response. The modified figure is reproduced with permission from [165].

to a variety of mechanical cues like cell density, substrate stiffness or external stress (Fig. 2.2a, b) [136, 167]. In the nucleus, YAP and TAZ bind to TEAD-containing proteins and cause cell-type specific responses, e.g. wound healing in wounded epithelium or differentiation of progenitor cells to cardiomyocytes, while cytosolic retention leads to inhibition of proliferation and differentiation (Fig. 2.2c, d). In Wnt signaling, the AJ protein β-catenin also serves as a transcriptional regulator. In the steady-state, cytosolic β-catenin is rapidly degraded but Wnt signaling prevents degradation and β-catenin accumulates in the cytoplasm and eventually translocates to the nucleus [166].

The first step in mechanotransduction before transcriptional regulation, however, is the recognition of the mechanical cue. Then, the signal is processed for immediate cellular responses and eventually causes nucleo-cytosolic shuttling and the more long-term transcriptional regulation. In this process, not only individual proteins are involved but many subcellular structures and proteins are mechanosensitive (Fig. 2.3) [165, 168]. During hearing, for example, mechanical signals from sound waves are converted into electrical signals. To this end, hair cells in the inner ear have stereocilia bundles that deform upon the mechanical stimulus of a sound wave, and this motion induces the opening of mechanosensitive ion channels [169]. Another famous example of mechanically activated ion channels are the Piezo proteins, which are evolutionary conserved and expressed in most mechanosensitive cell types [170]. Piezo 1/2 respond to mechanical forces by

channel opening but probably are then inactivated and thus not responding to a following stimulus [170]. Next to ion channels, also the nucleus itself is remodeled in response to mechanical cues [171], cellular adhesion structures probe and sense their environment and are connected to the nucleus via the linker of nucleoskeleton and cytoskeleton (LINC) [171, 172]. Furthermore, conformation changes in extra- or intracellular proteins can reinforce adhesions or activate signaling cascades, and the manipulation of downstream pathways, e.g. MAPK signaling, alters mechanotransduction [165].

2.1.3 Mechanotransduction at Cell Adhesion Sites

Molecular processes involved in mechanotransduction at cell adhesion sites are best studied for the actin-bound adhesion structures FAs [173] and AJs [174]. Integrin-based FAs, for instance, have a well-defined layered structure to which functional roles are assigned, i.e. transmembrane anchorage, signaling, force transduction, and actin regulation [175] (Fig. 2.4a). The cadherin-based AJs are layered similarly [176] (Fig. 2.4b) and even share some of the proteins like vinculin and zyxin [177].

Forces sensed in AJs [178, 179] are not necessarily extrinsic but also intrinsic forces are generated by the contractile actomyosin cytoskeleton [174, 180] as indicated for example by the emergence of tissue-level forces correlated with AJs formation [151]. One molecular building block in generating intrinsic tension when establishing the cell–cell contact might be the catch bond behavior of the cadherin–catenin complex to the F-actin cytoskeleton, i.e. reinforced binding strength with increasing load [174, 181]. In the adhesion strengthening during maturation and upon force, however, additional levels of regulation are involved. The F-actin cytoskeleton is reorganized, the motor-protein non-muscle myosin II is recruited, and potentially even the cadherin adhesion is enhanced [174].

The direct linkage of AJs to the F-actin cytoskeleton is established by α-catenin, which therefore is a prime candidate to sense mechanical tension and initiate a cellular response. Indeed, tension is experienced by α-catenin [182] in the same order of magnitude, approximately 5 pN, required for the unfolding of α-catenin *in vitro* [183] and generated by a single myosin molecule [184]. The presence of the open conformation in cells was confirmed using a conformation-specific antibody [178] and super-resolution microscopy [176]. This open conformation exposes a single cryptic vinculin-binding site and binding of vinculin to α-catenin prevents refolding in the auto-inhibited, closed conformation [183]. Thus, α-catenin might be a classical example for a mechanosensor transducing force into biochemical signals by a conformational change [174]. In addition, α-catenin could also modulate cell signaling via further binding partners, e.g. to activate RhoA signaling or vinculin-dependent changes [174]. For example, vinculin also experiences

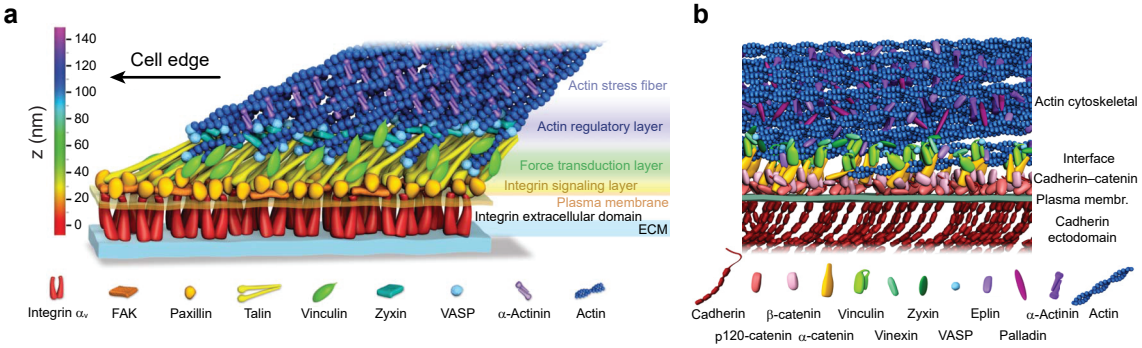

Figure 2.4: Focal adhesion (FA) and adherens junction (AJ) layers have distinct roles in mechanotransduction. (**a**) The transmembrane heterodimeric integrins bind to the extracellular matrix (ECM) and are intracellularly bound by the major integrin-activators talin and kindlin (not depicted). Many proteins including e.g. paxillin and focal adhesion kinase (FAK), are involved in signaling. The talin rod binds to the F-actin cytoskeleton and this connection is reinforced, e.g. by binding of vinculin. Furthermore, the F-actin cytoskeleton is remodeled, e.g. by zyxin, vasodilator-stimualted phosphoprotein (VASP), and α-actinin. (**b**) AJs in MDCK cells are based on the transmembrane protein E-cadherin. The major connection to the F-actin cytoskeleton is established by β- and α-catenin and similar to FAs vinculin is recruited to AJs in a force-dependent manner. Next to vinculin, also many actin-regulatory proteins are found in both, FAs and AJs. The illustrations do not depict protein stoichiometry or lateral organization. The modified figures are reproduced with permissions from [175] (**a**) and [176] (**b**).

forces [179, 185], is specifically phosphorylated upon force in AJs [186], and has many binding partners that influence signaling [187].

Next to α-catenin, also other proteins in the AJ might serve as mechanosensors including α-actinin, filamin or non-muscle myosin that accumulate in response to mechanical stress [188]. Myosin motors, for example, are intrinsically mechanosensitive because the unbinding of the myosin head from the F-actin is delayed if force acts against the direction of movement [189]. Increased tension at AJs therefore leads to increased myosin localization, which stiffens the F-actin cytoskeleton by additional crosslinks and reinforces RhoA signaling [174]. Furthermore, the curvature of the plasma membrane is modified by forces and provides an additional route for signal transduction [174].

To preserve tissue integrity upon stress, junctions are reinforced and stress is dissipated [174]. To strengthen the junction against stress, binding between individual proteins is reinforced upon several pN of stress [190, 191] and more adhesive complexes share the load [174]. Furthermore, the fluid-like behavior of the F-actin cytoskeleton allows stress dissipation on the minutes scale by molecular turnover [174]. For stress dissipation on the hour time scale, the tissue is remodeled with oriented cell divisions or increased proliferation along the stress direction to reduce force by increasing the rest length [174].

2.2 Force Measurement Methods

Measuring forces in biological systems leads to a better understanding of the molecular processes involved in mechanotransduction. Forces act on different length and time scales and therefore many methods are used to determine forces relevant for biological systems.

On the tissue level, for example, junctional forces can be estimated from tissue birefringence or the mechanical equilibrium between cells [192]. Birefringence leads to a difference in refractive index along and opposite to the direction of stress. The mechanical equilibrium, i.e. that forces balance each other, can be used to calculate relative stresses based on cell shapes. Furthermore, tissue-generated forces can be inferred from the deformation of oil droplets [193], or from pushing and pulling cells or cell sheets by a defined force [192]. Alternatively, tissue forces can be detected and qualitatively compared by disrupting tissue integrity, e.g. using laser cutting, and observing the subsequent relaxation [192]. The forces that are generated by a tissue are measured, for example, by external, electronic force sensors [194], bending of cantilevers (Fig. 2.5a) or qualitatively by the deformation of collagen substrates (Fig. 2.5b) [195, 196].

Cell-generated forces are mostly measured by tracking the deformation of an isotropic, linear elastic substrate. Traction force microscopy (TFM) in two dimensions tracks the displacement of fluorescent beads in a chemically-inert silicone or polyacrylamide substrate (Fig. 2.5c) [197] and is the most used method to measure cell-generated forces [198].

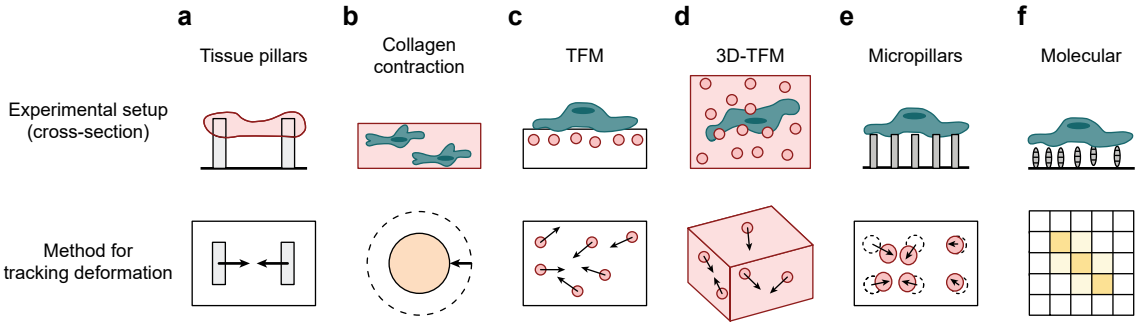

Figure 2.5: Tissue- and cell-generated forces are measured by tracking deformation. (**a**) Tissue-generated forces can be inferred from the deformation of pillars. (**b**) Alternatively, the contraction of a collagen substrate reports on the tension. (**c**) In traction force microscopy (TFM) the movement of beads in a polymer reports deformations caused by cellular adhesion. (**d**) Analyzing the bead-displacement to infer tension is not limited to surfaces but also applied in 3D surroundings. (**e**) To measure forces in 2D environments, micropillars can be used as a read-out for individual cells analog to the pillars used for tissues (**a**). (**f**) Finally, cell-generated forces are also analyzed using molecular tension sensors that are based on binding of a specific ligand (Fig. 2.6d). The modified figure is reproduced with permission from [194].

Pioneering work incorporates more physiologically relevant substrates and also transfers TFM to the 3D environment [199] (Fig. 2.5d). Alternative methods to track cell-generated forces use cells on deformable micropillars (Fig. 2.5e) [200, 201] and on micro-electro-mechanical systems [202]. Next to measuring forces exerted by cells on the environment, also the mechanical properties of the cell itself are characterized, for example by AFM to probe cell stiffness [203] or optical tweezers to deform single cells [204].

To characterize the response of individual proteins on forces, defined forces are exerted on an individual protein *in vitro*. To this end, optical (Fig. 2.6a) and magnetic (Fig. 2.6b) tweezers as well as AFM (Fig. 2.6c) are used [206–208]. To measure forces across individual proteins, extracellular tension sensors are bound to a ligand (Fig. 2.5f). These tension sensors either extend (Fig. 2.6d) or rupture (Fig. 2.6e), if forces acting on the ligand exceed a certain threshold, typically in the low pN range [209–212].

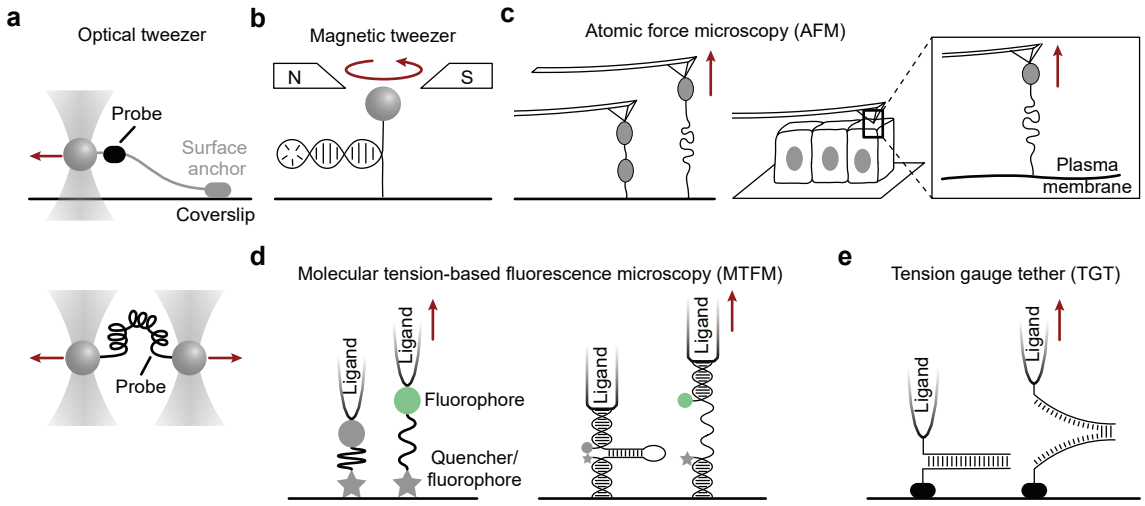

Figure 2.6: Forces across individual molecules can be measured *in vitro* or at the cell surface. (**a**) Optical tweezers are used to study the interaction between proteins. Dual optical traps allow the application of pN forces and therefore the characterization of unfolding properties upon forces applied at defined pulling velocities and holding times. (**b**) Instead of optics, magnetic tweezers use a magnetic field. (**c**) With atomic force microscopy (AFM) individual molecules can be stretched either bound to an artificial or the cell surface. (**d**) In molecular tension-based fluorescence microscopy (MTFM), a cell surface receptor binds to a ligand that in turn is fixed to the surface with a sensor containing a fluorophore, which is in the resting state quenched by FRET or gold particles. Upon force, the fluorescence increases because a force-sensitive linker elongates, which is either a peptide as also used in intracellular tension sensors (Fig. 2.7) or DNA. (**e**) In the tension gauge tether (TGT) approach extracellular ligands are bound to a DNA double-strand that ruptures upon specific forces. Therefore, this sensor reports on a force value that is exceeded at least once. The modified figure is reproduced with permission from [205].

2.3 Genetically Encoded FRET-based Tension Sensors

To measure tension across individual proteins in living cells or organisms, genetically encoded FRET-based tension sensors were developed [185, 213]. The basic design principle of these tension sensors is that a protein of interest (POI) is targeted with a tension sensor module (TSM), which reports on an increase in tension with a decrease in FRET. Therefore, the TSM has to be integrated such that the protein functionality is preserved and tension can be measured.

2.3.1 Tension Sensor Module

The TSM comprises of a FRET pair connected by a force-sensitive linker peptide, which elongates reversibly in response to mechanical force (Fig. 2.7a). In the resting state without tension, the FRET pair is in close proximity and the FRET efficiency is high. Upon force, the linker peptide elongates and thereby the fluorophore separation distance increases. As FRET is a highly distance-dependent process (Sec. 2.4), this increased separation distance leads to a reduced FRET efficiency.

The force response of the TSM therefore depends on the force sensitivity of the linker peptide. To specify the force-dependent unfolding characteristics of the linker peptide, single-molecule calibration can be used [205, 214, 215]. For example, optical tweezers (Fig. 2.7b) were used to determine that the linker peptide flagelliform (F40) opens gradually at $1-6\,\mathrm{pN}$ [185, 216], the ferredoxin-like fold (FL) peptide opens switch-like at $3-5\,\mathrm{pN}$ [216], the villin head piece (HP35) responds to $6-8\,\mathrm{pN}$, and its point-mutated version, stable villin head piece (HP35st), to $9-11\,\mathrm{pN}$ [217] (Fig. 2.7c–e). During calibration, the extension of the TSM is measured in response to force and the FRET–force correlation can be calculated (Fig. 2.7d). The steepness of the FRET–force relationship thereby serves as a marker for the sensitivity of the linker peptides, which is the highest for the FL peptide (Fig. 2.7e). Single-molecule measurements provide also direct access to the contour length increase between closed and elongated linker peptide and to the folding and unfolding curves [205, 214]. These folding and unfolding curves should be equal and free of hysteresis, which describes the difference between folding and unfolding trajectories. In the case of hysteresis, the observed FRET efficiency depends on the force history and thus no exact force value can be assigned to a specific FRET efficiency. Note, folding and unfolding curves are equal for the linker peptides F40, FL, HP35, and HP35st and thus these linker peptides are free of hysteresis [185, 216, 217].

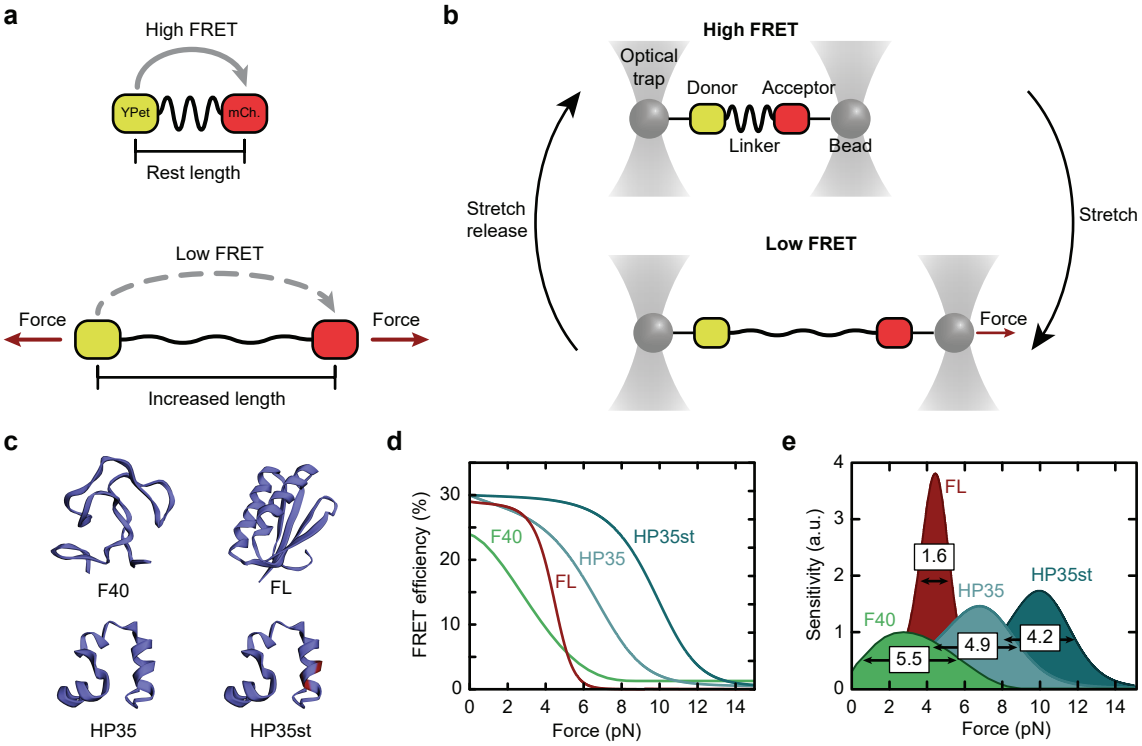

Figure 2.7: The linker peptide determines the force sensitivity of the tension sensor module (TSM). (**a**) In the absence of force, the FRET efficiency in the TSM is high. Upon force the linker peptide elongates, thereby increasing the distance between the FRET pair, e.g. YPet and mCherry, which leads to a reduced FRET efficiency. (**b**) TSMs are calibrated using optical tweezers. (**c**) The flagelliform (F40) linker [185] is unstructured but ferredoxin-like fold (FL) [216], villin head piece (HP35), and stable villin head piece (HP35st), which is derived from HP35 by N27A and K29M mutation [217], linkers have well-defined structures. (**d**) The calibrated linker peptides show a characteristic response to force. While the F40 peptide opens gradually in the range of 1−6 pN, the FL peptide switches almost digitally between 3−5 pN. The HP35 peptide responds to 6−8 pN and HP35st peptide to 9−11 pN. (**d**) The steepness of the FRET change in response to force determines the sensitivity and is highest for the FL peptide. The modified figures are reproduced from [214] (**b**) and [216] (**d, e**). Structures in (**c**) are modeled based on amino acid sequence using Phyre2 [218] and displayed with EzMol [219].

2.3.2 Control Constructs and Experiments

For a tension sensor experiment a set of constructs is required. To identify force-specific effects, the tension sensor is always compared with a no-force control. To this end, the no-force control should closely resemble the tension sensor and localize to the same subcellular structures but must not respond to tension. Three different design principles for such a no-force control can be used (Fig. 2.8a). First, the no-force control can be generated by tagging the protein of interest terminal with the TSM. Terminal-tagging usually preserves protein functionality and the protein is still able to sense and respond to force but the TSM does not experiences tension. The microenvironment of the TSM, however, is changed because the TSM integration site is different from the tension sensor. Second, the no-force control can be a truncated tension sensor construct, in which parts of the protein on either side of the TSM are missing. In this construct, protein functionality is impaired but the TSM has the same integration site as in the tension sensor. Finally, the no-force control can be a mutant that abolishes or strongly reduces binding essential for the establishment of forces. In this construct, the TSM experiences the same microenvironment as in the tension sensor and protein functionality is less impaired than in a truncated mutant. The design of such a no-force control, however, requires in depth knowledge of the protein of interest.

If FRET is measured by fluorescence lifetime imaging microscopy (FLIM), donor-only controls matching tension sensor and no-force control are used to calculate FRET (Sec. 2.4). Regardless of the FRET measurement method, donor-only controls and corresponding acceptor-only constructs are required to determine intermolecular FRET (Fig. 2.8a). Intermolecular FRET, i.e. FRET between neighboring molecules, depends on the protein concentration but also on the relative orientation of the molecules to each other and therefore might depend on the specific constructs. For tension sensor experiments, intermolecular FRET between tension sensor and no-force control should be comparable to exclude differences in intermolecular FRET as cause for changes in overall FRET (Fig. 2.8b).

Importantly, protein functionality has to be validated after TSM integration. To assess protein functionality, the rescue of a KO phenotype is crucial because it excludes compensatory effects of the endogenous protein (Fig. 2.8c). If the tension sensor indeed responds to tension, the FRET efficiency is expected to be lower than the no-force control when forces act but increases to the level of the no-force control under biological no-force conditions (Fig. 2.8b).

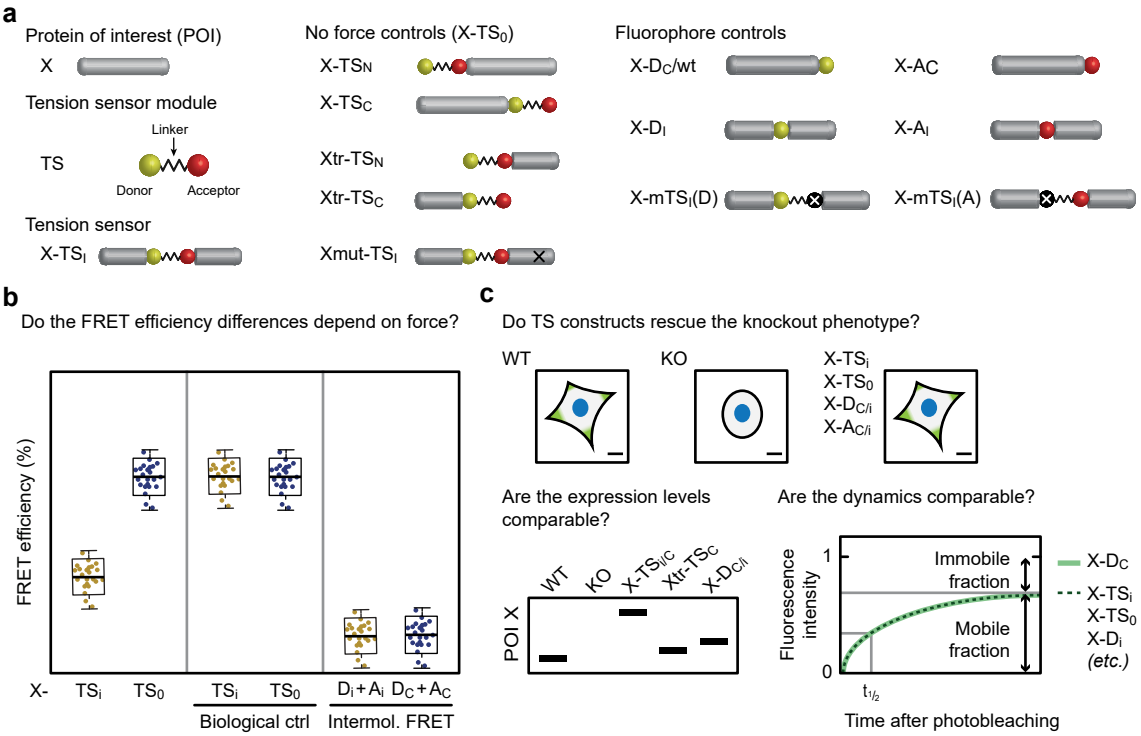

Figure 2.8: Tension sensor experiments require controls. (**a**) The protein of interest (POI) X is internally targeted with a TSM. To detect FRET changes not caused by tension, a no-force control is generated by either terminal tagging, truncating or mutating the protein to abolish one binding site required for the establishment of forces. Fluorophore-only controls have either one fluorophore or a TSM with one mutated non-fluorescent fluorophore. A terminal tagged protein version also serves as wild type (wt) control in functionality assays. (**b**) The FRET efficiency of the tension sensor is lower than the no-force control if tension is experienced by the POI. In biological no-force conditions, e.g. cytosolic adhesion proteins, the FRET efficiency of the tension sensor is expected to elevate to the level of the no-force control. Intermolecular FRET is a confounding factor of the observed overall FRET efficiency. Therefore, intermolecular FRET at the tension sensor and no-force control integration site should be comparable. (**c**) Functionality tests to assess protein functionality after TSM integration could include the rescue of a knockout (KO) phenotype, e.g. a spreading defect. In addition, the expression levels can be assessed, e.g. by Western blot, and protein dynamics can be analyzed, e.g. by fluorescence recovery after photobleaching (FRAP). The modified and extended figure is reproduced from [213].

2.3.3 Interpretation of FRET Efficiencies as Forces

Changes in FRET reflect changes in tension (Sec. 2.3.2) and the TSM is single-molecule calibrated so that the specific force response is characterized (Sec. 2.3.1). Therefore, tension sensor experiments allow insights into molecular forces acting on the POI. The first, and arguably most relevant, information contained in a lower FRET efficiency of the tension sensor compared to the no-force control is that tension is acting across the POI in the experimental condition. Second, a minimal force can be determined depending on the employed linker peptide. While F40-based TSM respond already to very small forces, all other linker peptides have a minimal force threshold that needs to be overcome. The FL-based TSM, for example, does not respond to forces below 3 pN, while the HP35st-based TSM require at least 8−9 pN before a considerable decrease in FRET is observed (Fig. 2.7d, e). Note that an individual linker peptide cannot report on maximal forces because any force outside the force-sensitivity range opens the linker peptide entirely (Fig. 2.9a). The combination of different linker peptides, however, can be used to narrow the force range a POI experiences.

In bulk measurements, the observed FRET efficiency can be caused by all molecules contributing with the same, intermediate FRET efficiency, or by a subpopulation of molecules experiencing sufficient tension to fully elongate the linker while other molecules remain closed or by any combination of these two extremes (Fig. 2.9b). Calculating an average force per molecule from the FRET efficiency assumes that all molecules are partially unfolded to the same degree. If in contrast the second extreme is assumed that all

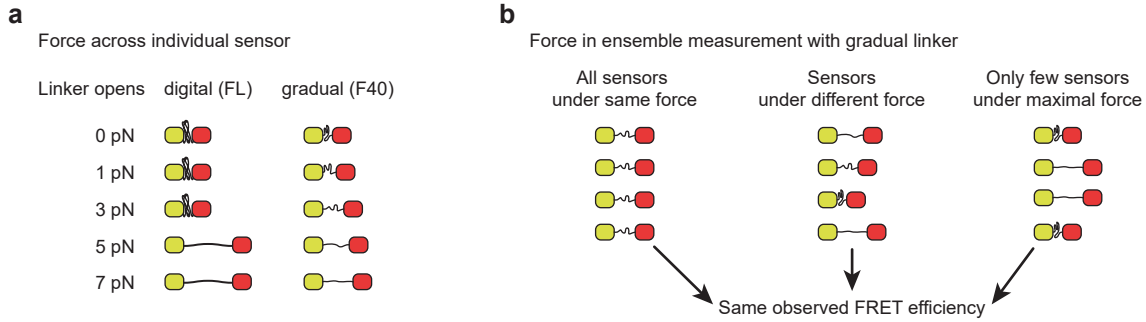

Figure 2.9: Changes in FRET report tension. (**a**) For individual tension sensor molecules, the FRET efficiency reflects the fluorophore separation distance. Therefore, the employed linker peptide determines, whether the distance changes gradually, e.g. F40, or digitally, e.g. FL, in response to force. (**b**) In bulk measurements, an average FRET efficiency of many tension sensor molecules is determined and does not report on the underlying mechanical behavior at a single-molecule level. The same overall FRET efficiency can be caused by all molecules experiencing the same amount of tension, some molecules entirely stretched while others remain folded, or any combination of these scenarios. The modified figure is reproduced from [215].

molecules are either fully elongated or folded, the relative amount of molecules under force can be determined (Sec. 4.8).

2.3.4 Application of Tension Sensors

FRET-based tension sensors are developed for a range of proteins in diverse subcellular structures (Fig. 2.10) [214, 220, 221]. The first tension sensor with a single-molecule calibrated linker, for example, targeted vinculin [185] and variations are now broadly used to analyze forces across vinculin in FAs and AJs [179, 222, 223]. In addition, tension sensors were developed for other adhesion proteins like the FA protein talin [216, 217, 224], which links integrins to the F-actin cytoskeleton, and the transmembrane AJ proteins cadherins [225, 226]. Genetically encoded FRET-based tension sensors, however, are not only limited to various adhesion proteins but also report tension across structural

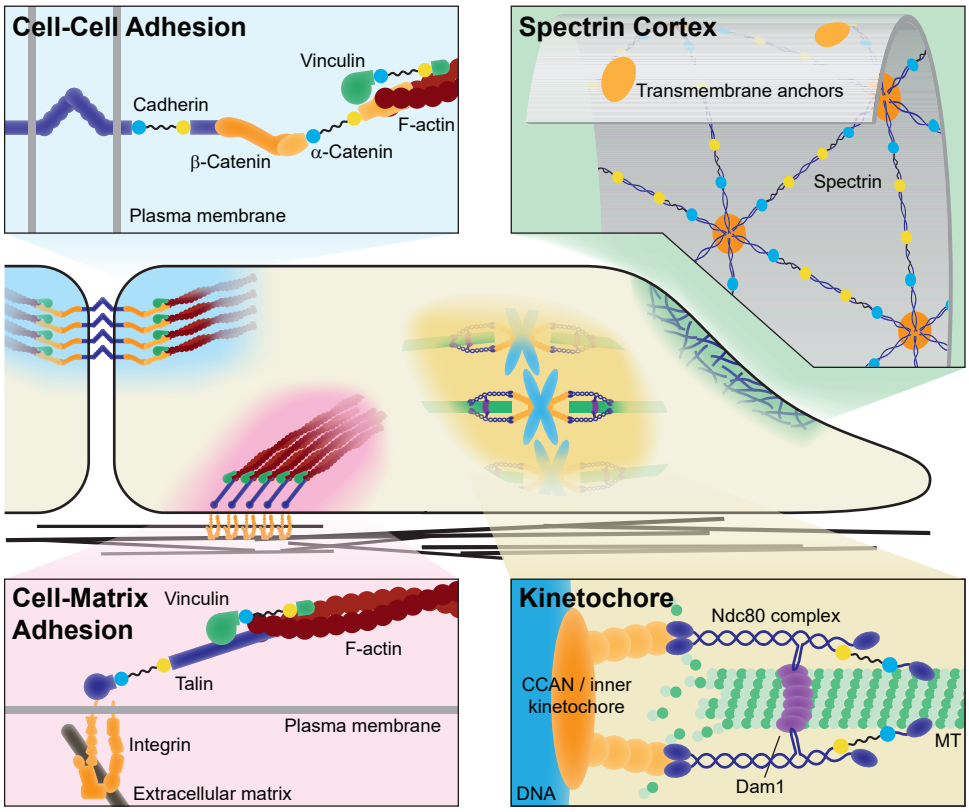

Figure 2.10: Tension sensors are developed for different cellular structures. Most applications target proteins in focal adhesions at the cell–matrix interface or adherens junctions at the cell–cell interface but tension sensors are also developed to measure tension in the kinetochore during cell division or at the spectrin cortex. The modified figure is reproduced from [214].

proteins in the spectrin cortex [227] and a kinetochore protein important during cell division [228].

The tension sensors are genetically encoded and can therefore be expressed in any model system. So far most studies used different types of cultured cells, but tension sensors were also introduced in *Caenorhabditis elegans* [227], *Drosophila* [229, 230], and even zebrafish [226] confirming the broad applicability of the technique.

2.4 Förster Resonance Energy Transfer

2.4.1 FRET Theory

Förster resonance energy transfer (FRET) was originally described by Theodor Förster [231] and is the radiation-free energy transfer from a donor to an acceptor based on long-range dipole-dipole interactions. FRET depends on characteristics of a fluorophore pair and their relative positions. The spectral overlap between donor emission and acceptor absorption $J(\lambda)$ with the wavelength λ (Fig. 2.11a) and the donor quantum yield Q_D are characteristic for a fluorophore pair. The relative orientation of donor and acceptor transition dipole κ^2 (Fig. 2.11b) and fluorophore separation distance r (Fig. 2.11c) describe the relative fluorophore positions.

The distance-dependent transfer rate from a donor to an acceptor is

$$k_T = C\, J(\lambda) \frac{Q_D}{\tau_D} \frac{\kappa^2}{r^6} \tag{2.1}$$

with τ_D the donor lifetime in the absence of an acceptor,

$$C = \frac{9000 \ln(10)}{128\, \pi^5 N_A} \frac{1}{n^4},$$

where N_A is the Avogadro's number and n the refractive index,

$$J(\lambda) = \frac{\int_0^\infty I_D(\lambda) \epsilon_A(\lambda) \lambda^4 \mathrm{d}\lambda}{\int_0^\infty I_D(\lambda) \mathrm{d}\lambda},$$

where $\epsilon_A(\lambda)$ is the wavelength-dependent extinction coefficient of the acceptor and I_D the intensity of the donor, which is normalized to unity [233]. The refractive index for biomolecules in aqueous solutions is typically fixed to $n = 1.4$. The relative orientation of the donor and acceptor transition dipoles is

$$\kappa^2 = (\cos\theta_T - 3\cos\theta_D \cos\theta_A)^2 = (\sin\theta_D \sin\theta_A \cos\phi - 2\cos\theta_D \cos\theta_A)^2 \tag{2.2}$$

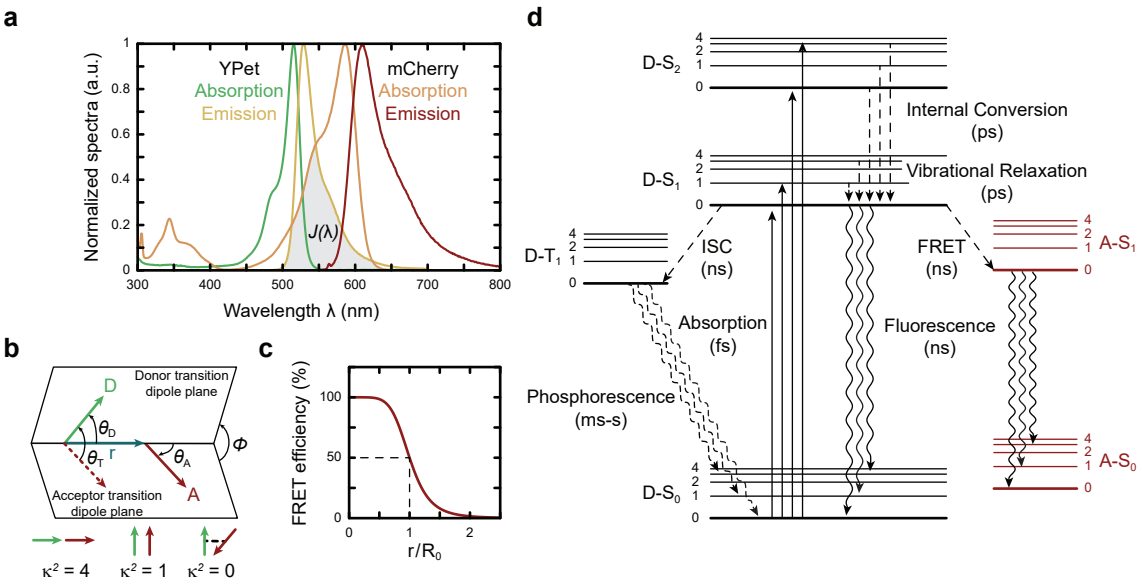

Figure 2.11: Förster resonance energy transfer (FRET) depends on spectral overlap, fluorophore orientation, and distance. (**a**) Emission and absorption spectra of donor and acceptor fluorophores are Stoke's shifted, i.e. emitted photons have less energy. The spectral overlap $J(\lambda)$ between donor emission and acceptor absorption (grey) is characteristic for each FRET pair. (**b**) The FRET efficiency depends on the distance r between donor and acceptor and the their relative orientation, which is reflected in the κ^2-factor. For collinear transition dipoles κ^2 is maximal, while for orthogonal dipoles no FRET takes place. In most applications, fluorophores are assumed to be freely rotating and κ^2 averages to $2/3$. All angles are defined in the graphic. (**c**) The FRET efficiency changes to the power of six around the Förster distance R_0, which is defined as the separation distance for $E = 0.5$. (**d**) Absorption of a photon leads to excitation of an electron from the ground state (singlet, S_0) of the donor (D) to an excited state as illustrated in the Jablonski diagram. The energy is relaxed fast to the ground state of the first singlet (S_1) via internal conversions and vibrational relaxations. From the excited singlet, the electron relaxes either by direct fluorescence or by intersystem crossing (ISC) to a triplet state (T_1) from which it relaxes to the ground state via phosphorescence. FRET offers a third alternative to transfer the energy to an acceptor (A). The acceptor then first relaxes to the ground level of the first singlet via vibrational relaxation and then to the ground state via fluorescence (or phosphorescence). The spectra values are taken from [232] (**a**). The schematics are based on [233] (**b–d**).

with θ_T the angle between transition dipoles, $\theta_{D/A}$ the angles between donor D and acceptor A to the vector connecting both, and ϕ the angle between the dipole transition planes (Fig. 2.11c). For most biological applications, however, rotational freedom is assumed, which results in an average of $\kappa^2 = 2/3$ [233]. For fluorescent proteins rotational freedom is an invalid assumption because rotational diffusion is much slower than the lifetime [234]. The real value of κ^2, however, is typically unknown and therefore $\kappa^2 = 2/3$ is still used for most applications [235].

The FRET efficiency E can be calculated from the transfer rate if all other quenching processes are neglected [233] using

$$E = \frac{k_T}{\tau_D^{-1} + k_T}. \tag{2.3}$$

Photophysically, after excitation of a fluorophore, internal conversions and vibrations rapidly relax the photon to the ground state of the first singlet (Fig. 2.11d). From this first singlet state, the fluorophore can then relax to the ground state via direct photon emission, i.e. fluorescence, or photon emission via the triplet state, i.e. phosphorescence. FRET offers a third relaxation pathway in which energy is transferred to the acceptor. Therefore, in the presence of an acceptor, less photons are emitted from the donor. This can be used to determine the FRET efficiency experimentally, by measuring either the intensity I or the lifetime τ of the donor in the absence (I_D, τ_D) and presence of an acceptor (I_{DA}, τ_{DA})

$$E = 1 - \frac{I_{DA}}{I_D} = 1 - \frac{\tau_{DA}}{\tau_D}. \tag{2.4}$$

Alternatively, the FRET efficiency can also be expressed relative to the Förster distance R_0 at which $E = 0.5$ with

$$E = \frac{R_0^6}{R_0^6 + r^6}. \tag{2.5}$$

This pronounced distance dependency is one hallmark of FRET and because Förster distances are typically in the low nanometer range, it is harnessed as a molecular ruler to observe small distance changes [233].

2.4.2 Fluorophores

The TSM can contain in principle any FRET pair, so that the employed FRET pair can be chosen such that the fluorophore properties suit the used setup and detection method. The first fluorescent protein fused to a protein to monitor its localization was green fluorescent protein (GFP) from *Aequorea victoria* [236, 237]. Protein engineering not only prevented dimerization [238] but also modified the excitation and emission wavelengths

[239], resulting in a broad range of fluorescent proteins [235, 240, 241]. The spectral palette is further extended by fluorophores derived from other proteins, like Discosoma Red (DsRed) from *Discosoma* sp. [242], which also is mutated for monomeric versions and optimized fluorescent properties [243].

YPet, for example, is a yellow GFP variant optimized for FRET with fast maturation, high brightness, good photostability, and comparably low sensitivity to environmental factors like pH [235, 244]. Similarly, the DsRed-derivative mCherry shows high photostability, a fast maturation rate, and high resistance to environmental changes [243]. The YPet/mCherry-FRET pair has a Förster distance of $R_0 = 5.8\,\text{nm}$ [245], which is already in the upper limit for fluorescent protein pairs ($R_0 = 4-6\,\text{nm}$) [235]. Note that large R_0 are favorable because the chromophores are central to a β-barrel structure with approximately 4 nm length and approximately 2 nm diameter [241, 246, 247]. Due to these steric constrictions, the maximal practical FRET efficiency of GFP-like fluorophores is approximately 40 % [241].

The quantum yield of red-shifted fluorophores like mCherry is comparably low, so particularly for FRET detection methods that are based on intensity, more blue-shifted FRET pairs are also employed. Measurements with these combinations suffer from increased autofluorescence and cellular damage but benefit from large quantum yields [235]. The FRET pair monomeric teal fluorescent protein 1 (mTFP1) [248] and enhanced yellow fluorescent protein (EYFP) [246], for example, also has a relatively large Förster distance of $R_0 = 5.9\,\text{nm}$ [235].

While the list of potential FRET pairs is long [235, 240, 241], most fluorophores reside in the same spectral range and therefore prevent simultaneous imaging of two FRET pairs. By combining fluorophores with specific properties, however, dual-color FLIM is feasible [249]. The donors, mTFP1 and Large Stoke Shift monomeric Orange (LSSmOrange) [250], are excited with the same wavelength. Crosstalk of the acceptors is then prevented by using ShadowG as an acceptor for mTFP1. ShadowG has similar acceptor properties as EYFP but a 120-fold reduced quantum yield [251] and therefore emission can be neglected. The long stokes shift of LSSmOrange ensures that no FRET occurs with ShadowG but instead only the far-red fluorophore monomeric Kate2 (mKate2) [252] serves as acceptor.

Next to fluorescent proteins, also organic dyes can be used for FRET measurements. Organic dyes have usually better spectral properties with higher quantum yields, so techniques are developed to specifically target proteins also in cells with organic dyes. One way to label proteins with organic dyes is genetically-tagging the protein with a SNAP-tag, which is a mutant version of the human DNA repair protein O^6-alkylguanine-DNA-alkyltransferase [253]. In the nucleus, the protein functions to repair a specific DNA modification and this specificity for O^6-benzylguanine derivatives is harnessed by

labeling those sugars with organic dyes. Thus, the SNAP-tag itself is non-fluorescent but can be specifically labeled with an organic dye.

2.4.3 FRET Detection

To determine FRET, different methods have been developed detecting changes in intensity, lifetime, polarization or the emission spectrum [235, 240, 241]. In spectral imaging, the complete emission spectrum is imaged after donor excitation. To determine FRET, the emission spectrum is unmixed with a donor-only reference spectrum or even all potentially involved spectra. The use of spectral imaging is limited because it requires specialized equipment, the donor-to-acceptor ratio needs to be known, and the signal-to-noise is low because of the high wavelength resolution that requires separate detection of small wavelength ranges [235, 240]. Measurements of polarization are based on the slow diffusion rotation compared to the lifetime. Therefore, if fluorophores are excited with polarized light, the energy transfer to the differently-oriented acceptor during FRET results in depolarization. Using polarization as a read-out permits the measurement of homo-FRET, i.e. FRET with the same donor and acceptor fluorophore. However, polarization measurements are sensitive to crosstalk and therefore require donor- and acceptor-only controls [235, 241]. In acceptor photobleaching, the change in donor intensity upon bleaching of the acceptor reports FRET. This technique provides a simple method to quantitatively determine FRET efficiencies, but the usage is limited by the extended bleaching times and the fact that bleaching is irreversible and no dynamics can be traced [235, 240, 241].

Sensitized Emission FRET

The term sensitized emission (SE) describes the increase in acceptor emission caused by FRET and provides the technically simplest method to measure FRET. Spectral crosstalk, however, hinders an easy interpretation of the ratio between donor and acceptor. Spectral bleed-through thereby comprises both, direct excitation of the acceptor by the donor excitation wavelength and donor emission signal detected in the acceptor emission channel (Fig. 2.12). Therefore, a variety of correction methods have been developed to determine the spectral bleed-through by measurements of donor-only and acceptor-only controls and then removing these components during the calculation of FRET [241, 254].

Determining FRET from wide-field collected intensity images using SE is fast but requires spectral bleed-through corrections. Furthermore, intensities depend on the details of the microscope setup and therefore relative FRET indices rather than absolute FRET efficiencies are determined.

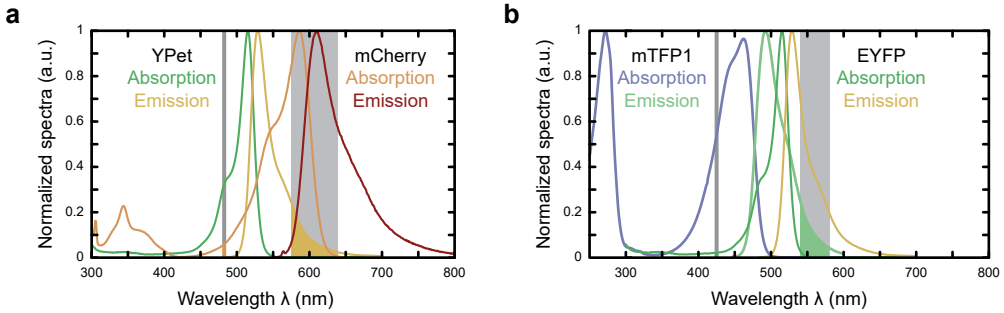

Figure 2.12: Ratiometric FRET requires spectral bleed-through corrections. FRET requires spectral overlap between donor emission and acceptor absorption (Fig. 2.11a). If fluorophore spectra are close, however, spectral bleed-through complicates analysis. Spectral bleed-through describes both, excitation of the acceptor by the donor excitation wavelength (grey line) and emission of the donor in the acceptor emission channel (grey shading). Excitation and detection channels are illustrated as used for sensitized-emission FRET (Sec. 3.6) for YPet/mCherry (**a**) and mTFP1/EYFP (**b**). The spectra values are taken from [232] (YPet, mCherry, EYFP) and [255] (mTFP1).

Fluorescence Lifetime Imaging Microscopy

FRET offers an alternative pathway for the donor fluorophore to relax the excitation energy (Fig. 2.11d) and therefore reduces the average lifetime in the excited state. To determine the FRET efficiency, the lifetime of the donor fluorophore is measured using FLIM with the acceptor and compared to the lifetime without an acceptor (Eq. 2.4). Importantly, the fluorescence lifetime depends on the molecular environment of the fluorophore but not on its concentration and is therefore intensity-independent. Since the first FLIM measurement with a microscope 1959 [256], different techniques have been developed to determine the fluorescence lifetime from biological samples [257, 258].

In time-correlated single photon counting (TCSPC)-FLIM combined with confocal laser scanning microscopy, the arrival times of single photons are detected in pixel-resolved manner, which avoids out-of-focus fluorescence (Fig. 2.13). Alternatively to single-photon counting also analog gating can be used to specifically amplify only those photons, which arrive in the gated time-window. This method collects time information sequentially and is therefore often combined with wide-field microscopy to collect signal from all pixels simultaneously [258].

Measurements in the frequency-domain provide another detection principle for fluorescence lifetimes. The frequency-domain is the Fourier transform of the time-domain and the lifetime can be inferred from a decrease in the modulation angle and a phase shift of the excitation wave [258]. Next to determination of the lifetime, FLIM data can be also graphically analyzed using a phasor plot of each individual image, in which the signal

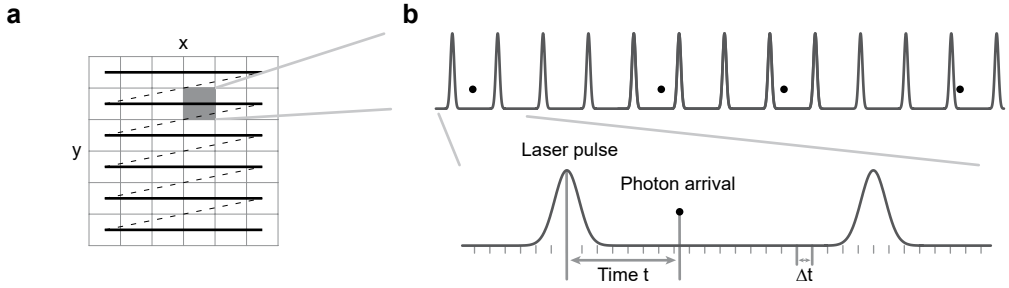

Figure 2.13: Time-correlated single photon counting (TCSPC)-fluorescence lifetime imaging microscopy (FLIM) detects photon arrival times. (**a**) FLIM measurements are performed with a confocal laser scanning microscope, which provides the spatial resolution. (**b**) The photon arrival time t after excitation is detected in time bins of width Δt, which provide the temporal resolution. The modified figure is reproduced from [215].

from each pixel is transferred to a phasor that behaves like a vector and clusters of pixels serve to identify different species [259].

Irrespective of the details in the FLIM protocol, FLIM allows the determination of quantitative FRET efficiencies and is independent of fluorophore intensities. Limiting factors for FLIM in biological systems are mainly the specialized equipment and data analysis procedures as well as the comparatively long acquistion times [241].

3 Material and Methods

3.1 Molecular Biology Methods

DP constructs used in this thesis were generated either by classical restriction enzyme-based cloning or by Gibson assembly. The main templates were human DPI-GFP from Prof. Kathleen J. Green (Addgene 32227) and the TSMs from the Grashoff lab (Addgene 101252 [F40], 101170 [FL], 101250 [HP35] and 101251 [HP35st]). Some cloning intermediates use pBluescript II SK(+) (pBSK) (Agilent Technologies, 212205) as a vector backbone and all other constructs are cloned in the retroviral expression plasmid pLPCX (TaKaRa, 631511). The software SnapGene (version 4.2.1.1) was used to generate plasmid maps and design primers.

3.1.1 Restriction Enzyme-based Cloning

In the restriction enzyme-based cloning, restriction sites are introduced via polymerase chain reaction (PCR), then the DNA is digested, purified from the restriction enzymes, and vector and insert fragments are ligated to assemble the plasmid, which was then transformed into competent bacteria (Sec. 3.1.3).

Polymerase Chain Reaction

A PCR was used to introduce restriction sites and generate overlaps for the ligation. In the PCR mixture (Tab. 3.1), the template DNA was assembled with deoxyribonucleoside triphosphates (dNTPs), the PfuUltra II high fidelity polymerase (Agilent, 600667), and the respective primers (Tab. 3.2). The PCR was performed with a touchdown program, which combines the benefits of high specificity at high temperatures and increased efficiency at low temperatures (Tab. 3.3). The amplified DNA fragments were then purified from an agarose gel.

Component	Stock	Final	Used
Template DNA		5−30 ng	X µl
Reaction buffer	10×	1×	5 µl
dNTP	each 10 mM	each 0.2 mM	1 µl
Forward primer	10 µM	0.2 µM	2 µl
Reverse primer	10 µM	0.2 µM	2 µl
PfuUltra polymerase	2.5 U/µl	0.05 U/µl	1 µl
distilled and purified water (ddH_2O)			ad 50 µl

Table 3.1: PCR reaction mix

Nr.	Name	Sequence
AC074	hDSP_EcoRI_fwd	ATTAAGAATTCACCATGAGCTGCAACGGAGGC
AC075	hDSP_SalI_rev	GGTGGGTCGACAGTCAGCTTCTCATTCCGATGGGG
AC076	hDSP_XhoI_fwd	GCGCGCTCGAGGAAGAGCTGGAAGGCATGAGGAGGTCGCTGAAG
AC085	hDSP_XhoI_rev	TCTTCCTCGAGCTTCTTCCTCTTGCAGGAGTC
AC090	hDSP_Cla_Stop_r	ATAAATCGATTTAGTGCCCAATAGAACTACTGCTAAATGAGTAGG
AC091	hDSP_Sal_Not_r	TAATAGCGGCCGCTATAATAGTCGACGTGCCCAATAGAACTACTGCTAAATGAG
AC092	DSPNT_SalI_NotI_r	ATAAAGCGGCCGCATATATAGTCGACCTCAAGGTCGGCTATCGTCTTCATG
AC098	hDSPII_int584_fwd	AAAAGCGGCCGCTTTACATTACCAAGAGTTCATCAG
AC099	hDSPII_i1592_rev	ATAAGCGGCCGCATAATAGTCGACCTCTCGATG

The number is the inventory number in the Grashoff laboratory.

Table 3.2: Primers used for PCR reaction during enzyme-based cloning

Step	Time	Temperature	Description
1	3 min	95 °C	Initial denaturation
2	20 s	95 °C	Denaturation
3	20 s	68 °C	Primer annealing
4	15 s/kb	72 °C	Elongation
5	20 s	95 °C	Denaturation
6	20 s	60 °C	Primer annealing
7	15 s/kb	72 °C	Elongation
8	5 min	72 °C	Final elongation
9	∞	4 °C	Storage

Steps 2−4 were repeated 8×, each time the annealing temperature in step 3 was reduced by 1 °C. Steps 5−7 were repeated 30×.

Table 3.3: Touchdown PCR program

Mutagenesis PCR

For introducing a point mutation, a PCR reaction was assembled as for a touchdown PCR (Tab. 3.1) with the modification that 125 ng instead of 0.2 µM were used of the overlapping primers, which both contained the intended mutation (Tab. 3.4). The DNA was amplified (Tab. 3.5) and the template DNA was digested by 1 µl DpnI (10 U/µl, NEB, R0176), which specifically digests methylated DNA. Therefore, the mixture was shortly centrifuged and incubated for 1 h at 37 °C. Then, 2 µl of the mutated DNA were transformed into competent bacteria. Note that mutations were introduced with Gibson assembly instead of the mutagenesis PCR once this technique was established in the laboratory.

Nr.	Name	Sequence
AC078	hDSP_dSalI_fwd	GAATGAGAAGCTGACTGTGGACAGTGCCATAGCTC
AC079	hDSP_dSalI_rev	GAGCTATGGCACTGTCCACAGTCAGCTTCTCATTC
AC080	hDSP_dClaI_fwd	GATAGAGATTTGTATCGTTCCCTGAATGATCCCCG
AC081	hDSP_dClaI_rev	CGGGGATCATTCAGGGAACGATACAAATCTCTATC
AC082	hDSP_dXhoI_fwd	CCATCAGTGTCCCACGAGTCCGCAGGG
AC083	hDSP_dXhoI_rev	CCCTGCGGACTCGTGGGACACTGATGG
AC093	pBSK_dSalI_fwd	CCCCCCTCGAGGTGGACGGTATCGATAAG
AC094	pBSK_dSalI_rev	CTTATCGATACCGTCCACCTCGAGGGGGG

The number is the inventory number in the Grashoff laboratory.

Table 3.4: Primers used for mutagenesis PCR

Step	Time	Temperature	Description
1	30 s	95 °C	Initial denaturation
2	30 s	95 °C	Denaturation
3	1 min	55 °C	Primer annealing
4	1 min/kb	68 °C	Elongation
5	∞	4 °C	Store

Steps 2−4 were repeated 12× for a single point mutation, 16× for a single amino acid (aa) change, and 18× for multiple aa changes.

Table 3.5: Mutagenesis PCR program

Overlap Extension PCR

An overlap extension PCR was used to introduce restriction-enzyme recognition sites into DP, which were then later used to introduce the TSM or fluorophores by restriction digest and ligation. In the overlap extension PCR, the two fragments surrounding the future integration site were amplified with long overlapping primers (Tab. 3.6) using touchdown PCR (Tab. 3.1 and Tab. 3.3). These fragments were then separated from the primers and enzymes on an agarose gel, purified, eluted in 30 µl, diluted 1 : 10 with ddH_2O, and mixed in a 1 : 1 ratio. From this mixture of the PCR products, 1 µl was used as template DNA in another touchdown PCR (Tab. 3.1 and Tab. 3.3) using primers over the entire sequence. The PCR product was then purified, digested with restriction enzymes, ligated into a vector, and the assembled DNA was transformed in bacteria.

Nr.	Name	Sequence
AC086	hDSP_TSint1_fwd	GTCGACTATTATGCGGCCGCTTTACATTACCAAGAGTTCATCAGAAATAGCC
AC087	hDSP_TSint1_rev	AGCGGCCGCATAATAGTCGACCTCAAGGTCGGCTATCGTCTTCATGTAATC
AC088	hDSP_TSint2_fwd	GTCGACTATTATGCGGCCGCTACCCAGACTGAGTGTGAGTGGACCGTTGAC
AC089	hDSP_TSint2_rev	AGCGGCCGCATAATAGTCGACCTCTCGATGGGACCCATATGGGCGCTGTCTG
AC095	hDSPII_fwd	GAATATGAAAATGAGCTGGCAAAGGCATCTAATAGGATTCAGGAATCAAAG
AC096	hDSPII_rev	GATTCCTGAATCCTATTAGATGCCTTTGCCAGCTCATTTTCATATTCTCTC
AC097	hDSP_Not_-	AATAGCGGCCGCCCCGTGCCCAATAGAACTACTGCTAAATGAGTAGGAATAA
	dEcoR_r	GAGTAGGAAGAATTGCCTGTGGCGTC
AC106	XhoI_YPet_fwd	CATACTCGAGATGGTGAGCAAAGGC
AC107	mCh_Stop_ClaI_r	GGGGATCGATTTACTTGTACAGCTCGTCCATG
AC108	mCh_Stop_NotI_r	ATAAGCGGCCGCTTACTTGTACAGCTCGTCCATG

The number is the inventory number in the Grashoff laboratory.

Table 3.6: Primers used for overlap extension PCR

DNA Separation and Purification

To separate DNA from enzymes or to analyze the size of restriction bands, DNA was separated on agarose gels. For most purposes, 1 % agarose (Thermo Fisher, 16500500) was cooked in 1×Tris-acetate-EDTA (TAE) buffer (Tab. 3.7) and mixed with 1 : 10,000 ethidium bromide, which intercalates in the DNA and can be visualized with ultraviolet (UV) light. To separate particularly small DNA pieces, 2 % agarose were used. The DNA samples were mixed with 6×loading buffer to visualize the migrating front and sizes were compared with a 1 kilobasepairs (kb) DNA standard (NEB, N3232). Bands of the correct size were isolated and purified with a gel purification kit (Macherey-Nagel, 740412).

Component	Stock	Final	Used
2-amino-2-hyroxymethyl-propane-1,3-diol (Tris)	121 g/mol	2 M	242 g
Acetic acid	1.05 g/l	60 mM	57.1 ml
Ethlyenediaminetetraacetic acid (EDTA), pH = 8.0	0.5 M	5 mM	100 ml
Distilled water (dH_2O)			ad 1 l

For agarose gels ddH_2O, while for the running buffer dH_2O was used.

Table 3.7: Tris-acetate-EDTA (TAE) (10×)

DNA Digestion

Vector and insert templates were digested with the same restriction enzymes to generate overlapping DNA ends (Tab. 3.8). The most frequently used enzymes were ClaI (NEB, R0197), ECoRI (NEB, R0101), ECoRI-high fidelity (HF) (NEB, R3101), NotI (NEB, R0189), NotI-HF (NEB, R3189), PvuI (NEB, R0150), SalI (NEB, R0138), and XhoI (NEB, R0146). In the final DP constructs, an ECoRI recognition site is in front of the DP sequence and a ClaI site follows the DP Stop codon. The TSMs are flanked by XhoI and NotI sites and for the assembly the special situation that XhoI and SalI generate compatible overhangs was harnessed, which leads to a combined sequence of the recognition site in the final DP constructs that neither of the two enzymes can recognize. An additional XhoI site was introduced by a silent point mutation in the DPI specific part to allow separate cloning of the 5′- and 3′-parts of the sequence. The cloning of DPI in two parts was beneficial because the entire sequence of DP spans 8,613 basepair (bp), a TSM is approximately 1.6 kb, and the pLPCX vector contributes with additional 6.3 kb, which results in a total vector size of more than 16 kb. PvuI was used to digest pBSK in smaller fragments if the insert had a comparable size to the vector, which is 2.9 kb.

Component	Stock	Final	Used
DNA		3 µg	X µl
Digest buffer	10×	1×	3 µl
Restriction enzyme 1	10 000 U/ml	333 U/ml	1 µl
Restriction enzyme 2	10 000 U/ml	333 U/ml	1 µl
ddH_2O			ad 30 µl

Table 3.8: Restriction enzyme digest mix

The DNA was digested with the appropriate restriction enzymes for one hour or over night. To prevent religation, the vector was dephosphorylated two times with 1 µl calf

intestine alkaline phosphatase (CiP) (NEB, M0290) for 30 min at 37 °C. The DNA was then purified with an agarose gel separation for the ligation.

Ligation

Vector and insert were ligated with T4 DNA ligase (NEB, M202S) for 4 h at room temperature (RT) (Tab. 3.9). To increase the efficiency of the ligation, only 1 µl of the DNA ligase was added to the initial mixture and the second µl was added after 2 h. The DNA concentration was determined with a spectrophotometer (Thermo Fisher, NanoDrop 1000) and for the vector $m_{\text{vector}} = 1\,\mu\text{g}$ DNA was used and the insert was added in X× molar excess. The required mass of the insert m_{insert} was determined based on the number of nucleotides in both fragments, N_{vector} and N_{insert}, by

$$m_{\text{insert}} = \text{X}\,\frac{N_{\text{insert}}}{N_{\text{vector}}}\,m_{\text{vector}}. \tag{3.1}$$

The starting ligation ratio was X = 3 but because DP constructs are large, the vector-to-insert ratio was varied between 1:1 and 1:5. The entire ligation mix was then used for transformation in competent bacteria (Sec. 3.1.3).

Component	Stock	Final	Used
Vector DNA		0.01 − 0.03 µg	Y µl
Insert DNA		≈ 3 × molar excess	Z µl
T4 DNA ligase buffer	10×	1×	1.5 µl
T4 DNA ligase	400000 U/ml	≈ 500 U/ml	2 µl
ddH_2O			ad 15 µl

Table 3.9: Ligation mix

3.1.2 Gibson Cloning

During the course of this thesis, the Gibson assembly replaced the enzyme-based cloning to assemble the DNA fragments in the Grashoff laboratory. The basic principle is that fragments are generated with single-strand overlaps, which are then annealed [260]. In principle, the Gibson assembly could be seamless but the restriction sites introduced for classical cloning are preserved in all DP constructs to ensure compatibility.

Insert fragments were generated by a PCR reaction (Tab. 3.10) using the Phusion DNA polymerase (Thermo Fisher, F534) and an elongation temperature depending on the melting temperature of the primers (Tab. 3.11). The primers were designed such that approximately 20 bp bind to the gene and also 20 bp overlap to the next fragment, the

3′-end is a G or C, and the melting temperature for the assembly is around 50−60 °C (Tab. 3.12). Note that Gibson primers were also designed to introduce point mutations.

Component	Stock	Final	Used
Template DNA		5−30 ng	X µl
Phusion buffer	5×	1×	5 µl
dNTP	each 10 mM	each 0.2 mM	1 µl
Forward primer	10 µM	0.2 µM	2 µl
Reverse primer	10 µM	0.2 µM	2 µl
Phusion DNA polymerase	2 U/µl	0.02 U/µl	0.5 µl
ddH_2O			ad 50 µl

Table 3.10: PCR reaction mix for Gibson primers

Step	Time	Temperature	Description
1	30 s	98 °C	Initial denaturation
2	10 s	98 °C	Denaturation
3	30 s	$T_{\text{melt}} + 3$ °C	Primer annealing
4	15 s/kb	72 °C	Elongation
5	10 min	72 °C	Final elongation
6	∞	4 °C	Storage

Steps 2−4 were repeated 30×. For $T_{\text{melt}} \geq 69$ °C, steps three and four were combined. The primer melting temperature T_{melt} was determined with the supplier's website; `www.thermofisher.com/tmcalculator`.

Table 3.11: Gibson assembly PCR program

The vector was digested with a classical restriction enzyme-based digest (Sec. 3.1.1). To dephosphorylate the vector, a faster version of the CiP (QuickCiP from NEB, M0508) was used and 1 µl enzyme was incubated with 1 pmol DNA ends for 10 min at 37 °C. The amount of free DNA ends N_{DNAend} can be calculated using the average molecular weight of single nucleotide pair $m_{\text{Nucleotide}} = 660$ g/mol, the number of nucleotides N_{DNA} and the mass of the DNA m_{DNA} to

$$N_{\text{DNAend}} = 2 \frac{m_{\text{DNA}}}{m_{\text{Nucleotide}} N_{\text{DNA}}}. \tag{3.2}$$

The phosphatase was then heat-shock inactivated for 2 min at 80 °C.

The PCR products and the vector were then purified with an agarose gel separation (Sec. 3.1.1). For the assembly, the inserts were used in 2× molar excess compared to the vector if one or two inserts were added into the vector and 3× molar excess if more inserts were added. The amount of DNA was maximized in 5 µl volume, which

Nr.	Name	Sequence
AC131	G_DPIend(mCh)_r	CCATGTCGACGTGCCCAATAGAACTACTGCTAAATG
AC132	G_DPIend(mCh)_f	TGGGCACGTCGACATGGTGAGCAAGGGCGAG
AC133	G_mCh(pLPCX)_r	TCTTTTATTTTATCGATGTATAGGCGGCCGCGGCGGCCGCTTACTTGT
AC134	G_DPfrnt(pLPX)f	GGCCCATAAAGCTTATACGAATTCATGAGCTGCAAC
AC135	G_DPIIend(mCh)r	CATTCCAGCGGCCGCCCCGTG
AC136	G_DPIIend(mCh)f	TGGGCACGGGGCGGCCGCTGGAATGGTGAGCAAGGGCGAG
AC138	G_DPIbck(DSP)f2	CTGCAAGAGGAAGAAGCTCGAGGAAGAGCTG
AC139	G_mC(pLPX)Nt_r2	CTTTTATTTTATCGATGTATAGGCGGCCGCTTACTTGTACAGCTCGTCC
AC144	G_DPend(pLPX)_r	GACTAAATAAAATCTTTTATTTTATCGATTTAGTGCCCAATAGAAC
AC147	DPI(DPI)_f2	GAAGCTCGAGGAAGAGCTGGAAGGCATGAGGAGGTCG
AC148	C(pLPCX)_Not_r2	TTATGCGGCCGCTTACTTGTACAGCTCGTCCATGCCGCC
AC149	Y(pLPCX)_NotI_r	ATAAGCGGCCGCTTAGGCGGCGGTCAGGAACTC
AC172	G_YPet_F40_f	GGAGTTCCTGACCGCCGCCGG
AC173	G_F40_TagBFP_r	CTTAATCAGCTCGCTCATAGCACCACCTGGACCAGC
AC174	G_F40_TagBFP_f	AGGTGGTGCTATGAGCGAGCTGATTAAGGAGAACA
AC175	G_TagBFP_Stop_-pLPCX_r	TAAAATCTTTTATTTTATCGATGTATAGGCGGCCG
AC176	G_TagBFP_DSP_r	TAGCGGCCGCATTAAGCTTGTGCCCCAGTTTG
AC177	G_TagBFP_DSP_f	CAAGCTTAATGCGGCCGCTACCCAGAC
AC178	G_DSP_pLPCX_r	CTGGAGACTAAATAAAATCTTTTATTTTATCGATTTAGTGCCCAAT
AC180	G_F40_SNAP_r	CTTTGTCCATGGATCCAGCACCACCT
AC181	G_F40_SNAP_f	TGCTGGATCCATGGACAAAGACTGCGA
AC182	G_SNAP_Stop_-pLPCX_r	TCTTTTATTTTATCGATGTATAGGCGGCCGCTTAACCCAGCCCAGG
AC183	G_SNAP_DSP_r	TAGCGGCCGCGCGGCCGCACCCAGC
AC184	G_SNAP_DSP_f	GTGCGGCCGCGCGGCCGCTACCCAGACTG
AC185	G_F40_Stop_pLPCX_r	CTTTTATTTTATCGATGTATAGGCGGCCGCTTAAGCACCACCTGGACCAG
AC186	G_F40_DSP_r	CAGTCTGGGTGGATCCAGCACCACCTGGACCAG
AC187	G_F40_DSP_f	TGCTGGATCCACCCAGACTGAGTGTGAGTGGACCG
AC195	G_pLPCX_YPet_f	ATACGAATTCATAGGATCCATACTCGAGATGGTGAGCAAAGGCGAAGAG
AC196	G_YPet_BamHI_r	CCGGCGGCGGTCAGGAACTCC
AC200	G_mCherry_DSP_r2	GCGGCCGCCTTGTACAGCTCGTCCATGCCGC
AC201	G_mCherry_DSP_f2	CATGGACGAGCTGTACAAGGCGG
AC202	G_mCherryY72L_r	GCCTTGGAGCCGAGCATGAACTGAGGG
AC203	G_mCherryY72L_f	CCTCAGTTCATGCTCGGCTCCAAGGC
AC204	G_NotI_pLPCX_r	ATCGATGTATAgGCGGCCGCTATCGATGTTTGGCCGAGGCG
AC206	G_pLPCX_DSP_f	GGGCCCATAAAGCTTATACGAATTCACCATGAGCTGC
AC207	G_YPetY67G_r	ACTGCACGCCGCCGCCCAGGGTGGT
AC208	G_YPetY67G_f	ACCACCCTGGGCGGCGGCGTGCAGT
AC209	G_DPend_NotI_-YPet_f	TATTGGGCACGGGGCGGCCGCAATGGTGA
AC210	G_mCherry_Stop_-pLPCX_r3	GACTAAATAAAATCTTTTATTTTATCGATTTACTTGTACAGCTCGTCCA
AC211	G_DPI_DPI_f	GACTCCTGCAAGAGGAAGAAGCTCGAGGAAGAG

The number is the inventory number in the Grashoff laboratory.

Table 3.12: Primers used to amplify fragments for Gibson assembly

typically resulted in approximately $0.01-0.05$ pmol. The DNA was assembled with 10 µl of a premixed master mix (NEB, E2621) for 1 h at 50 °C. The entire 15 µl of the Gibson assembly mix were then transformed into 100 µl competent bacteria.

3.1.3 Transformation and Amplification

Generation of Competent Bacteria

Escherichia coli (*E. coli*) (OmniMax 2T1, ThermoFisher, C854003) were made heat-shock competent freshly starting from a vial of the last preparation every two months when cloning the large DP constructs and less frequent when cloning smaller intermediate constructs. First, bacteria from the old vial were streaked on a lysogeny broth (LB) agar (Roth, 6675) plate with 10 µg/ml tetracycline (Sigma, 87128) and grown overnight at 37 °C. One colony was then grown in 10 ml LB (Roth, 6673) medium with 10 µg/ml tetracycline shaking overnight but not more than 16 h at 37 °C. From this pre-culture, 2 ml were grown in 100 ml prewarmed, antibiotic-free LB shaking at 37 °C until the optical density (OD) at 550 nm reached $OD_{550} = 0.5$, which were approximately 2 h. The sample was then cooled for 10 min on ice, transferred to precooled, autoclaved centrifugation tubes, and pelleted in a precooled centrifuge for 15 min at 1,100 g at 4 °C. The pellets were then resuspended with a total volume of 10 ml ice-cold transformation and storage solution (TSS) (Tab. 3.13). Next, 2.5 ml sterile glycerol (87 %) were added and the bacteria were aliquoted in 100 µl aliquots. The aliquots were snap-frozen in liquid nitrogen and then stored at −80 °C.

Component	Stock	Final	Used
Tryptone-peptone		1 %	5 g
Yeast extract		0.5 %	2.5 g
Sodium chloride (NaCl)	58.44 g/mol	100 mM	2.5 g
Polyethylen glycol (PEG)	3000−3500 g/mol	10 %	50 g
Dimethyl sulfoxide (DMSO)	100 %	5 %	25 ml
Magnesium chloride ($MgCl_2$)	1 mM	50 mM	25 ml
ddH_2O			ad 500 ml

pH = 6.5, sterile filtered, and stored at 4 °C.

Table 3.13: Transformation and storage solution (TSS)

Transformation of the DNA in Competent *E. Coli*

One aliquot of competent bacteria (100 µl) was thawed on ice and incubated with the assembled DNA from a ligation (Sec. 3.1.1) or a Gibson assembly (Sec. 3.1.2) for 30 min

on ice. The bacteria were heat-shocked for 75 s in a 42 °C water bath, cooled on ice for 3 min, and incubated shaking with 1 ml of antibiotic-free LB medium for 1 h at 37 °C. The bacteria were then pelleted for 3 min at 4,500 g, resuspended with 100 µl LB medium, streaked on a prewarmed agar plate with LB containing 75 µg/µl ampicillin (LB_{amp}) (Sigma, A9518), and grown overnight at 37 °C. Single colonies from the plate were picked and used to amplify and verify the DNA. The plate was stored for the case that more colonies should be picked for up to few weeks at 4 °C. Note that the DP tension sensor constructs were large, i.e. more than 16 kb for DPI and close to 15 kb for DPII. The transformation efficiency for the large constructs was therefore considerably reduced compared to smaller intermediate constructs especially for restriction-enzyme based cloning, where typically $40-80$ clones needed to be picked per construct. The efficiency was remarkably increased when using Gibson assembly, where typically $5-20$ clones were picked.

Amplification of the DNA

To amplify the DNA, a single colony was picked and grown shaking in 4 ml LB_{amp} overnight at 37 °C. The bacteria were then pelleted and the DNA was extracted using a DNA purification kit (Machery-Nagel, 740727). A small amount of the non-pelleted bacteria was kept for up to few weeks stored at 4 °C. If the DNA sequence was verified, this bacteria culture was grown in 250 ml LB_{amp} shaking overnight at 37 °C. From this bacteria solution, 600 µl were mixed with 600 µl glycerol and stored at −80 °C. This glycerol-stock was then later used to start a bacterial culture to amplify more DNA. The majority of the 250 ml bacteria solution was pelleted and the DNA was extracted using a DNA purification kit (Machery-Nagel, 740412).

Verification of the DNA Sequence

To verify the DNA sequence of individual clones, first a restriction digest was performed (Sec. 3.1.1) to identify samples with the expected digestion bands on an agarose gel. To exclude small deletions or inclusions and point mutations, which are not detectable on an agarose gel, typically two samples with the expected digestion pattern were entirely sequenced (Tab. 3.14) using the overnight service of Eurofins. Furthermore, after each purification, at least one primer was used to sequence the DNA to exclude an accidental exchange of samples that were purified simultaneously.

Nr.	Name	Sequence
Nr.020	T7 (pBSK_seq_fwd)	TAATACGACTCACTATAGGG
Nr.021	T3 (pBSK_rev)	AATTAACCCTCACTAAAGGG
Nr.047	pLPCX_seq_fwd	AGCTCGTTTAGTGAACCGTCAGATC
Nr.048	pLPCX_seq_rev	ACCTACAGGTGGGGTCTTTCATTCCC
AC057	hDP_seq_01	GAGCAGCACATTAACAGCCACC
AC067	hDP_seq_01a	CAGAACTGCTCCGACTGCTTG
AC058	hDP_seq_02	TCCTGAAGGACAACAACGAGC
AC059	hDP_seq_03	GCTTGCCAACTTCAGAGGTTCT
AC060	hDP_seq_04	TGCAGATGTTCATGCTCGGTA
AC101	hDP_seq_04a	ATTCAGGAATCAAAGAATCAG
AC068	hDP_seq_05a	GAGATTAACATTACGAAGACCACCATC
AC069	hDP_seq_05b	TGATGATGCTGCCAAAACCAT
AC070	hDP_seq_05c	TGAGGAGGTCGCTGAAGGAG
AC071	hDP_seq_05d	GAAGCGAAGCGGACAGTGAT
AC100	hDP_seq_05e	GATCAAGAGAATTGAAGAGAG
AC062	hDP_seq_06	TTGCCAAAAGATGTCGCCTT
AC063	hDP_seq_07	GGGGCTATTTCAATGAGGAACTC
AC064	hDP_seq_08	GGCATCATCCACCCAACCA
AC192	DSP_tail_seq_r	GTTCGATTCTGCACCGTTCC
A041	Seq_YPet_595_f	CCACTACCTGAGCTACCAGAGCGC
A042	Seq_Cherry590_f	CCTACAACGTCAACATCAAGTTGG
AC102	mCherry_seq_rev	CACGGAGCCCTCCATGTGCAC
AC179	TagBFP_seq_01	CAGAAGAAAACACTCGGCTGGG

The number is the inventory number in the Grashoff laboratory.
The vector sequencing primers are commercially available.
The primer A041 and A042 were designed by Dr. Andrea Freikamp.

Table 3.14: Primers used for sequencing

3.1.4 Generated Constructs

During cloning, intermediate constructs were generated (Tab. 3.15) in pBSK or pLPCX. The expression plasmids (Tab. 3.16 and Tab. 3.17) use all pLPCX as vector.

Nr.	Vector	Name
604	pBSK	hDPI (front)
605	pBSK	hDPI (back) (NoStop)
606	pBSK	hDPI (back).Stop
607	pBSK	hDPI (front) with SalI-NotI linker (int-584)
608	pBSK	hDPI (back) until SalI-NotI linker (int-1952)
609	pBSK	hDPI (back) with SalI-NotI linker (NoStop)
610	pBSK-ΔS	hDPNT (NoStop)-(SalI-NotI linker)
612	pLPCX	hDPI (front)
613	pLPCX	hDPI (back).Stop
651	pLPCX	hDPII (NoStop)
652	pBSK-ΔS	hDPII until SalI-NotI linker (int-1353)

The number is the inventory number in the Grashoff laboratory.

Table 3.15: Constructs generated as cloning intermediates for DP

Nr.	Name	Schematic
614	hDPI-[YPet-HP35-mCherry] (int-584)	
615	hDPI-[YPet-HP35-mCherry] (int-1952)	
616	hDPI-[YPet-HP35-mCherry].Stop	
617	hDPI-YPet.Stop	
618	hDPNT-[YPet-HP35-mCherry].Stop	
619	hDPNT-YPet.Stop	
685	hDPI-[YPet-F40-mCherry] (int-584)	
686	hDPI-[YPet-F40-mCherry] (int-1952)	
687	hDPI-[YPet-F40-mCherry].Stop	
691	hDPI-[YPet-HP35st-mCherry] (int-584)	
692	hDPI-[YPet-HP35st-mCherry] (int-1952)	
720	hDPI-[YPet] (int-584)	
721	hDPI-[mCherry] (int-584)	
722	hDPI-[YPet] (int-1952)	
723	hDPI-[mCherry] (int-1952)	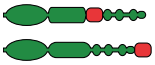
789	hDPI-mCherry.Stop	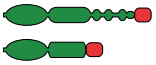
803	hDPI(1-1952)-mCherry.Stop	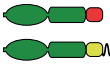
1000	hDPI(1-1952)-[YPet-F40-mCherry].Stop	

The number is the inventory number in the Grashoff laboratory.

Table 3.16: Expression plasmids encoding for desmoplakin (DP)I and DPNT constructs

Nr.	Name	Schematic
620	hDPII-[YPet-HP35-mCherry] (int-584)	
621	hDPII-[YPet-HP35-mCherry] (int-1353)	
622	hDPII-[YPet-HP35-mCherry].Stop	
623	hDPII-YPet.Stop	
688	hDPII-[YPet-F40-mCherry] (int-584)	
689	hDPII-[YPet-F40-mCherry] (int-1353)	
690	hDPII-[YPet-F40-mCherry].Stop	
693	hDPII-[YPet-HP35st-mCherry] (int-584)	
694	hDPII-[YPet-HP35st-mCherry] (int-1353)	
719	hDPII-[YPet-HP35st-mCherry].Stop	
724	hDPII-[YPet] (int-584)	
725	hDPII-[mCherry] (int-584)	
726	hDPII-[YPet] (int-1353)	
727	hDPII-[mCherry] (int-1353)	
790	hDPII-mCherry.Stop	
804	hDPII(1-1353)-YPet.Stop	
805	hDPII(1-1353)-mCherry.Stop	
917	hDPII-[YPet-FL-mCherry] (int-1353)	
918	hDPII-[YPet-FL-mCherry(Y72L)] (int-1353)	
919	hDPII-[YPet-FL-mCherry].Stop	
920	hDPII(1-1353)-[YPet-FL-mCherry(Y72L)].Stop	
921	hDPII(1-1353)-[YPet-FL-mCherry].Stop	
922	hDPII-[YPet-FL-mCherry(Y72L)].Stop	
923	hDPII(1-1353)-[YPet-HP35-mCherry]	
924	hDPII(1-1353)-[YPet-HP35st-mCherry]	
946	hDPII-[YPet-F40-TagBFP] (int-1353)	
947	hDPII(1-1353)-[YPet-F40-TagBFP].Stop	
948	hDPII-[YPet-F40-SNAP] (int-1353)	
949	hDPII(1-1353)-[YPet-F40-SNAP].Stop	
950	hDPII-[YPet-F40] (int-1353)	
951	hDPII(1-1353)-[YPet-F40].Stop	
952	hDPII-[YPet(Y67G)-F40-mCherry] (int-1353)	
953	hDPII(1-1353)-[YPet(Y67G)-F40-mCherry].Stop	
954	hDPII-[YPet-F40-mCherry(Y72L)] (int-1353)	
955	hDPII(1-1353)-YPet-F40-mCherry(Y72L)].Stop	
983	hDPII-[YPet-F7-mCherry] (int-1353)	
984	hDPII(1-1353)-[YPet-F7-mCherry].Stop	
985	hDPII-[YPet-HP35-mCherry(Y72L)] (int-1353)	
986	hDPII(1-1353)-[YPet-HP35-mCherry(Y72L)].Stop	
987	hDPII-[YPet-HP35st-mCherry(Y72L)] (int-1353)	
988	hDPII(1-1353)-[YPet-HP35st-mCherry(Y72L)].Stop	
989	hDPII-[YPet-F7-mCherry(Y72L)] (int-1353)	
990	hDPII(1-1353)-[YPet-F7-mCherry(Y72L)].Stop	

The number is the inventory number in the Grashoff laboratory.

Table 3.17: Expression plasmids encoding for desmoplakin (DP)II constructs

3.2 Cell Preparation

3.2.1 Cell Culture

The murine epidermal keratinocytes (MEKs) used in this thesis are a gift from Prof. Kathleen J. Green (Northwestern University, Chicago). The cells were isolated from neonatal mice, which either had a skin-specific DP depletion resulting in MEKs depleted of desmoplakin (MEK-KO) or a floxed version of DP that does not influence the protein expression, which results in MEKs wild type for desmoplakin (MEK-wt). The keratinocytes were cultured for eight or ten passages, stored frozen, and then finally immortalized by spontaneous immortalization.

Keratinocytes were cultured in T75 flasks with a serum-free, protein-free, animal and human origin-free medium containing amino acids, minerals, vitamins, organic compounds but only a reduced amount of 0.07 mM Ca^{2+} and no antibiotics or antimyotics (CellNTec, CnT-Pr). The medium was exchanged three times per week. When cells reached confluency, they were split in a ratio of 1 : 2 to 1 : 4. For splitting, cells were washed with Dulbecco's phosphate buffered saline (PBS) (Sigma, D8537) and incubated with 4 ml accutase (Sigma, A6964) until cells detached, which was approximately 30 min. Keratinocytes were then pelleted for 5 min at 200 g and resuspended in one ml medium.

To freeze cells, the resuspended cells were mixed in a 1:1-ratio with freezing medium (CellNTec, CnT-Cryo-50) and stored at $-80\,^{\circ}C$. For long-term storage, cells were moved after at least one week at $-80\,^{\circ}C$ to liquid nitrogen.

3.2.2 Transient Transfection

For transient transfection, cells were seeded in the dish required for the desired use, i.e. a microscopy dish for FLIM measurements, a cover slip in a 24-well plate for immunostainings, and a 24-well plate for EM images. The cells were transfected with a lipid-mediated procedure using Lipofectamine 3000 (ThermoFisher, L3000015).

In a microscopy dish, the medium was exchanged to 1 ml fresh medium. In one tube, 125 µl of medium were mixed by gentle vortexing with 4.5 µg DNA, then 9 µl of the P3000-component were added and the sample was mixed again. In a second tube, 125 µl medium were mixed with 7.5 µl lipofectamine. The DNA-containing sample was then added to the lipofectamine-containing tube, samples were mixed, and incubated for 10 − 15 min at RT. Next, the mixture was added dropwise to the cells, the dish softly shaken to equally distribute the DNA, and the transfection mixture was incubated for one day. In a 24-well, 200 µl of fresh medium were used and the transfection mixture was distributed on four wells.

The next day, the medium was either exchanged by fresh medium or by fresh medium containing 1.5 mM Ca^{2+} to induce the formation of DSMs and 1 % antibiotics (penicillin and streptomycin, Sigma, P4333). Transiently transfected cells were imaged at least two days after transient transfection to allow sufficient time for construct expression.

3.3 Biochemical Methods

3.3.1 Cell Lysis

A 6-well plate with confluent monolayers was used to lyse the cells. The cells were kept on ice during the entire process. Cells were washed twice with with 2 ml PBS (Tab. 3.18) and incubated with 80 µl lysis buffer (Tab. 3.19) for 10 min. During the last minutes of the incubation, the cells were scratched and transferred into a precooled tube. The cell debris was separated by centrifugation in a precooled centrifuge for 15 min at 16,000 g at 4 °C and the supernatant was transferred in a fresh tube.

Component	Stock	Final	Used
NaCl	58.44 g/mol	137 mM	8 g
Potassium chloride (KCl)	75.55 g/mol	2.7 mM	0.2 g
Disodium hydrogen phosphate dihydrate ($Na_2HPO_4 \times H_2O$)	177.99 g/mol	10 mM	1.78 g
Potassium hydrogen phosphate (KH_2PO_4)	136.09 g/mol	1.75 mM	0.24 g
dH_2O			ad 1l

Table 3.18: Dulbecco's phosphate buffered saline (PBS)

Component	Stock	Final	Used
Tris-hydrogen chloride (HCl)	1 M	50 mM	50 µl
NaCl	1 M	150 mM	150 µl
Triton-X-100	100 %	1 %	10 µl
Phenylmethylsulfonylfluorid (PMSF)	1 tablet/2 ml	0.1 tablet	200 µl
ddH_2O			590 µl

PMSF tablets (Roche, 05892791001)

Table 3.19: Cell lysis buffer

The protein concentration of the cell lysate was determined by a bicinchoninic acid (BCA)-based assay (Merck, 71285) in comparison to bovine serum albumin (BSA) standards of $0-2$ mg/ml in lysis buffer. In a 96-well plate, 200 µl of the cell lysate or the BSA

standards were incubated with 40 µl of a BCA and cupric acid solution for 20−30 min. The intensities were measured at 562 nm with a plate reader (Tecan, Sunrise with magellan software version 7.2) and normalized to the BSA standard to determine the cell lysate concentration. The concentrations were adjusted to $c = 0.5\,\mu g/\mu l$ with lysis buffer and samples were denaturated with Laemmli buffer (Tab. 3.20) for 5 min at 95 °C. The cell lysates were stored at −20 °C.

Component	Stock	Final	Used
Tris, pH 7.6	1 M	250 mM	12.5 ml
Glycerol	100 %	20 %	10 ml
Sodium dodecyl sulphate (SDS)	20 %	4 %	10 ml
Bromphenol blue	669.96 g/mol	0.02 %	0.7 µg
β-Mercaptoethanol	100 %	4 %	2 ml
dH_2O			ad 50 ml

The buffer was stored without and with β-mercaptoethanol at 4 °C and −20 °C, respectively.

Table 3.20: Laemmli buffer (4×)

3.3.2 SDS-PAGE

In a SDS-polyacrylamide gel electrophoresis (PAGE), proteins are separated based on their size because SDS binds sequence-independent to the denatured protein. To efficiently separate desmosomal proteins, which are comparatively large, a separation gel with 8 % polyacrylamide (PAA) (Tab. 3.21) was used. The separation gel was poured, covered with isopropanol, and polymerized for 1.5 h at RT. To first assemble the proteins, a stacking gel with 6 % PAA (Tab. 3.22) was added on top of the separation gel. Therefore, the isopropanol covering the separation gel was discarded and the stacking gel polymerized around a comb for 30 min at RT.

Component	Stock	Final	Used
PAA	30 %	8 %	2.67 ml
Tris-HCl, pH 8.8	1.5 M	375 mM	2.5 ml
SDS	20 %	0.1 %	50 µl
Ammonium persulfate (APS)	10 %	0.1 %	100 µl
N,N,N′,N′-tetramethylethylenediamine (TEMED)	100 %	0.1 %	10 µl
ddH_2O			4.3 ml

PAA (Serva, 10688)

Table 3.21: Separation gel

Component	Stock	Final	Used
PAA	30 %	6 %	1 ml
Tris-HCl, pH 6.8	1.5 M	225 mM	750 µl
SDS	20 %	0.1 %	25 µl
APS	10 %	0.1 %	50 µl
TEMED	100 %	0.1 %	5 µl
ddH_2O			3.2 ml

Table 3.22: Stacking gel

The chambers were washed with running buffer (Tab. 3.23 and Tab. 3.24). Then, 5 µl of a prestained protein standard for $10-250$ kiloDalton(kDa) (Thermo Fisher, 26619) or 25 µl sample mixed with 5 µl loading buffer (NEB, B7021) were loaded. To separate the proteins according to their size, 120 V were applied for 15 min and then 170 V for 75 min or until the front line reached the end of the gel.

Component	Stock	Final	Used
Western blot (WB) running buffer (Tab. 3.24)	10×	1×	100 ml
SDS	20 %	0.1 %	5 ml
ddH_2O			3.2 ml

Table 3.23: Western blot running buffer

Component	Stock	Final	Used
Tris	121.14 g/mol	250 mM	30.3 g
Glycine	75.07 g/mol	2 M	144.1 g
dH_2O			ad 1 l

Table 3.24: Western blot buffer (10×)

3.3.3 Western Blot

The proteins were blotted from the PAA gel to a polyvinylidenfluorid (PVDF) membrane (Merck, IPVH00010), bound by antibodies, and detected with a horesradish peroxidase (HRP)-based reaction.

Transfer to the PVDF Membrane

The PVDF membrane was activated by a short methanol bath and then assembled together with the PAA gel, two filter papers and sponges to a sandwich, in which the gel and membrane were in direct contact to each other and surrounded by the filter papers and sponges. Already during assembly, all components were soaked with blotting buffer (Tab. 3.25). The blotting system also contained a cooling unit and blotting was performed with 25 V overnight while stirring at 4 °C to prevent heating.

Component	Stock	Final	Used
WB blot buffer (Tab. 3.24)	10×	1×	100 ml
Methanol	100 %	10 %	100 ml
dH_2O			ad 1 l

Table 3.25: Western blot blotting buffer

Detection of Protein Bands

After the protein bands were transferred to the membrane, the membrane was rinsed with Tris-buffered saline with Tween-20 (TBST) (Tab. 3.26 and Tab. 3.27) and then shaken at least three times with fresh TBST for at least 5 min at RT. To block unspecific binding sites, the membrane was shaken at least 1 h with TBST containing 5 % milk. The antibodies (Tab. 3.28) were diluted in TBST with milk and the first antibody was incubated overnight at 4 °C. Then, the membrane was again washed with TBST at least three times for 5 min and the secondary antibody was incubated for 1 − 2 h at RT.

Component	Stock	Final	Used
Tris-buffered saline (TBS) buffer (Tab. 3.27), pH = 7.6	10×	1×	100 ml
Tween-20	100 %	0.1 %	1 ml
ddH_2O			ad 1 l

Table 3.26: Tris-buffered saline (TBS) with Tween-20

Component	Stock	Final	Used
NaCl	58.44 g/mol	137 mM	80 g
Tris	121.14 g/mol	200 mM	24.4 g
ddH_2O			ad 1 l

pH = 7.6.

Table 3.27: Tris-buffered saline (10×)

Antigen	Clone	Species	Dilution	MW	Supplier
Desmoplakin I & II	DP2.15	mouse	1:50	332 kDa, 260 kDa	abcam, ab16434
Plakophilin 1	10B2	mouse	1:500	75 kDa	Santa Cruz, sc-33636
Plakophilin 2	PP2/62, PP2/86, PP2/150	mouse	1:500	100 kDa	Progen, 651101
Desmoglein 1 & 2	DG 3.10	mouse	1:500	165 kDa	Progen, 61002
Keratin 5	poly	rabbit	1:1,000	60 kDa	Hiss Diag., PRB-160P-100
E-Cadherin	ECCD-2	rat	1:500	60 kDa	Thermo Fisher, 13-1900
α-Tubulin	37B5	rat	1:1,000	50 kDa	Synaptic Systems, 302217
Integrin β1	MB1.2	rat	1:1,000	130 kDa	Millipore, MAB1997
Paxillin	349	mouse	1:5,000	68 kDa	BD Transduction L., 610051
Mouse IgG (H+L)		goat	1:20,000		Biorad, 170-6516
Rabbit IgG (H+L)		goat	1:20,000		Biorad, 170-6515
Rat IgG (H+L)		donkey	1:10,000		J. ImmunoR, 712-035-150

MW: molecular weight

Table 3.28: Antibodies used for Western blot

Next, the membrane was washed again with TBST at least three times for 5 min and then incubated with a 1:1 mixture of luminol and peroxide (Merck, WBKLS0500) to detect chemoluminescence with a flurorescence reader (GE Healthcare, ImageQuant 4000).

Stripping of the Membrane

To detect the loading control, the membrane was stripped by incubation with stripping buffer (ThermoFisher, 46430) for 15 min at RT. Then, the membrane was washed with TBST at least three times for 5 min and unspecific binding sites were blocked by incubation with TBST containing 5 % milk for 1 h at RT. The primary antibody for the loading control was again incubated overnight and the procedure was repeated as described above for the first detected protein.

3.4 Imaging of Desmosomes

3.4.1 Immunostaining

For immunostainings, confluent cells were transfected on cover slips (Menzel, 630-1847) in 24-well plates (Sec. 3.2.2), the medium was exchanged after one day to fresh medium

or to fresh medium containing 1.5 mM Ca^{2+} and 1 % antibiotics, and the immunostaining was performed after an additional incubation day. The cells were kept in the dark during the entire process to limit bleaching of the fluorophores. The samples were rinsed twice with ice-cold PBS (Tab. 3.18) and once with the cytoskeleton stabilizing buffer (Tab. 3.29). The cells were then fixed and permeabilized by incubation with precooled methanol for 8 min at −20 °C. Next, cells were washed subsequently with PBS, PBS with 0.02 % Tween-20 (PBST), and PBST with 1 % BSA (PBSTB) by shaking for at least 5 min at RT. Cells were then incubated with primary antibodies (Tab. 3.30) diluted in PBS with 3 % BSA (PBSB) overnight at 4 °C. Cells were washed with PBST and PBSTB by shaking for at least 5 min at RT to remove the primary antibody. Then, the cells were incubated with the secondary antibody for 1 h at RT. Next, cells were washed again with PBST and PBS by shaking for at least 5 min at RT. Finally, cells were mounted on object holders with a mounting solution to prevent fading of the fluorophores (ProLong Gold, ThermoFisher, P36934).

Component	Stock	Final	Used
EGTA	380.35 g/mol	1 mM	0.38 g
$MgCl_2 \cdot 6\,H_2O$	203.31 g/mol	1 mM	0.2 g
Glycerol	86 %	4 M	300 ml
PIPES	302.37 g/mol	25 mM	7.6 g
dH_2O			1 l
pH = 7.6			

Table 3.29: Cytoskeleton stabilizing buffer

Antigen	Clone	Species	Dilution	Label	Supplier
Desmoplakin I & II	DP2.15	mouse	1:50		abcam, ab16434
Keratin 14	poly	rabbit	1:1,000		Hiss Diag., PRB-155P-100
Keratin 5	poly	rabbit	1:1,000		Hiss Diag., PRB-160P-100
Desmoglein 1 & 2	DG 3.10	mouse	1:500		Progen, 61002
Plakoglobin	PG-11E4	mouse	1:250		Life Tech., 13-8500
Plakophilin 1	10B2	mouse	1:500		Santa Cruz, sc-33636
Rabbit IgG (H+L)		goat	1:500	Alexa-405	Thermo Fisher, A31556
Mouse IgG (H+L)		chicken	1:500	Alexa-488	Thermo Fisher, A21200
Mouse IgG (H+L)		donkey	1:500	Alexa-647	Thermo Fisher, A31571

Table 3.30: Antibodies used in immunostainings

The immunostainings were stored at 4 °C and imaged during the next days at a Zeiss LSM 780 confocal microscope with the ZEN 2.1 software (version 11.0, Zeiss). Images were taken with an α-plan-appochromat 100× oil objective with numerical aperture n_a =

1.46 (Zeiss, 420792-98009-720). A 2× zoom was used resulting in an image area of $42.51 \times 42.51\,\mu m^2$. The Alexa-405 dye, which was used to label the keratin IF, was excited with a 405 nm diode, the Alexa-488 dye and YPet labeling DP with the 488 nm band of the argon laser, and the Alexa-647 dye, which was used to label other desmosomal components, was excited with a 633 nm helium-neon laser line. The channels were excited separately and therefore detection windows could be broad, i.e. $410-507$ nm, $490-630$ nm, and $638-755$ nm. The power of the laser varied between experimental sessions and therefore laser intensities and gains were set individually to avoid overexposure. The settings were, however, preserved for the comparison of MEK-wt and MEK-KO. To maximize the collected signal, the images were averaged over four lines and collected with reduced scan speed, which resulted for an image size of $1024 \times 1024\,pixel^2$ in a frame time of approximately 12.5 s. With three colors per image and a z-stack with nine slices covering a total depth of 3.1 µm, the total acquisition time was slightly below 6 min per image. The final image was then saved in a 16 bit Carl Zeiss image (CZI) file format. All immunostainings shown in this thesis were repeated three to five times and a total of approximately $20-30$ images was taken. The only exception is the treatment with okadaic acid (OA), which was only performed once.

The images were imported into Fiji is just ImageJ (Fiji) [261, 262] and the signal of the different channels separately z-projected by summing all nine slices. From these projected images of the channels, a composite was made, color-coded, and saved as tagged image file format (TIF).

3.4.2 Transmission Electron Microscopy

For transmission electron microscopy (TEM) images, confluent keratinocytes were transfected in a 24-well plate (Sec. 3.2.2), the medium was exchanged after one day to medium with 1.5 mM Ca^{2+} and 1 % antibiotics, and incubated for another day to induce the formation of DSMs. Then, samples were brought to the group of Prof. Jens Waschke (Ludwig-Maximilians-Universität (LMU), Munich). Desalegn Tadesse Egu, Sabine Mühlsimer, and Dr. Hanna Ungewiß then prepared the samples and Dr. Hanna Ungewiß imaged the cells. In brief, transfected cells were fixed with 1 % glutaraldehyde for 1 h at 37 °C. Next, cells were rinsed three times with PBS and incubated with 2 % osmiumtetroxide solution for 1 h at 4 °C. The samples were then dehydrated through a series from $20-100$ % ethanol, embedded with Epon for 24 h at 80 °C, and cut with a diamond knife in ultra thin sections of $60-80$ nm. Finally, cells were stained with saturated solutions of uranyl acetate for 40 min and lead citrate for 5 min, respectively. Images were acquired with the transmission electron microscope Libra 120 (Zeiss). The images cover a size of $2048 \times 2048\,pixel^2 = 74.1 \times 74.1\,\mu m^2$. The images shown in this thesis are contrast-adjusted using the brightness- and contrast-tool of Fiji to better visualize the DSMs.

3.5 Fluorescence Lifetime Imaging Microscopy

Fluorescence lifetime imaging microscopy (FLIM) is used in this thesis to determine FRET efficiencies in tension sensor experiments. For most FLIM experiments, confluent keratinocytes were transiently transfected in a microscopy dish (Sec. 3.2.2). For the measurements on soft substrates, cells were seeded on hydrogels of defined stiffness (Matrigen, SV3520-EC-2/4/12/25 PK) instead of the microscopy dishes with glass bottom but transfected analogously. The medium was exchanged one day after transient transfection either to fresh medium or to medium containing 1.5 mM Ca^{2+} and 1 % antibiotics to induce DSM formation. Cells with Ca^{2+} were then imaged 1 day, i.e. after 22 − 27 h, or 3 days after induction of DSM formation. To image cells during the early formation of DSMs, the Ca^{2+}-depleted medium was exchanged to medium with 1.5 mM Ca^{2+} 3 h prior to the measurement.

FLIM images were acquired with a confocal laser scanning microscope (Leica TCS SP_5 X) equipped with a 63× water objective (HCX PL APO CS) and a pulsed white light laser (NKT Photonics) with 78 MHz repetition rate, which was used with 70 % laser intensity at 508 nm to excite YPet. The emitted fluorescence was filtered by a band-pass filter (Chroma, 545/30 nm) and the arrival of single photons was detected with a FLIM X16 TCSPC detector (LaVision Biotech). Cells on microscopy dishes were imaged in a heating chamber with 5 % CO_2 at 37 °C (Ibidi). The microscopy dishes with the hydrogels did not fit in the heating chamber and images were therefore taken at RT.

The FLIM images were acquired with the Leica Application Suite Advanced Fluorescence (version 2.7.3.9723) with 4× zoom covering 61.51 × 61.51 μm^2 in 512 × 512 $pixel^2$. With a scan speed of 400 Hz and a time of 2.586 s between subsequent image repeats, 20 image repeats required a total acquisition time of approximately 50 s and 100 image repeats of approximately 4.5 min. The additional dead time between image repeats was required to allow the detector software (Imspector Pro, LaVision) to save the current image repeat. Each image repeat consists of a stack of spatially-resolved images for each time bin. The temporal resolution was $\Delta t = 0.08$ ns and with the repetition rate of 78 MHz, 160 time bins were saved, of which only the first 155 contained signal (Sec. 4.3). The individual repeats of one image were saved into one folder. For donor-only controls 20 image repeats and for tension sensor and no-force control samples 100 image repeats were taken, respectively. The total measurement time of one experimental condition was therefore approximately 40 min for donor-only samples and 2 h for tension sensor and no-force control expressing cells.

For most experimental conditions, 15 − 20 images were taken on 3 − 5 experimental days resulting in 50 − 100 images. The exact numbers for the individual experiments are provided in the figures (Sec. 5). The FLIM images were analyzed using fluorescence lifetime analysis and merge software (FLAMES) (Sec. 4).

3.6 Micromanipulation Experiment

The micromanipulation experiments were performed together with Andrew J. Price, PhD, in Prof. Alexander R. Dunn's laboratory at the Stanford University. To apply external mechanical stress on the keratinocytes, confluent MEK-wt were transiently transfected in microscopy dishes (Sec. 3.2.2). After one day the medium was exchanged to medium containing 1.5 mM Ca^{2+} and 1 % antibiotics to induce the formation of DSMs and the pulling experiment was performed another day later. Cells were imaged with the epifluorescent microscope Nikon Ti-E controlled with the Micromanager (version 1.4.22) [263]. A heliophor light engine (89 North) was combined with a CFI Plan Apo Lambda 40× air objective with $n_a = 0.95$, an Andor sCMOS Neo camera, and band-pass and dichroic filters (Semrock) depending on the FRET pair and channel (Tab. 3.31). The power of the excitation was approximately 200 mW at 430 nm, 425 mW at 500 nm, and 350 mW at 530 nm. A heating chamber surrounded the entire setup and was heated to 37 °C.

FRET pair	Channel	Excitation	Excitation Filter	Dichroric Filter	Emission Filter
YPet/ mCherry	Donor	500/40	468/34; 553/24	515/40; 574	517/20
	FRET	500/40			609/57
	Acceptor	530/50			609/57
mTFP1/ EYFP	Donor	430/40	425/35; 527/42; 685/130	475/25; 523	475/28
	FRET	430/40			560/25
	Acceptor	500/40			560/25

The characteristic wavelength and width of the excitation light and employed filters are given in nm.

Table 3.31: Excitation wavelengths and filters used for sensitized emission FRET measurements at the epifluorescence microscope in Prof. Alexander R. Dunn's laboratory, Stanford University

For the micromanipulation, a glass micropipette was pulled from a glass capillary (Sutter instruments) and mounted with two manual single axis stages (ThorLabs, PT1) for $x-y$-translation and a motorized single axis stage (ThorLabs, MTS50) to control the height. A transfected cell was identified and a first set of images for SE-FRET was taken. Then the glass micropipette was lowered on the cell monolayer such that the neighboring cell was pinched between the micropipette and the glass surface. The micropipette was then moved in the y-axis, which dragged the pinched cell and thereby pulled on the cell–cell contact to the transfected cell. The displacement of the micropipette tip was chosen as large as possible without monolayer rupture. If the monolayer ruptured upon pulling, the respective data were excluded from further analysis. The displacement was typically below 20 µm. A second set of images for SE-FRET was taken at the maximal displacement. Then, the micropipette was lifted and the monolayer was allowed to relax.

A third set of images for SE-FRET was taken once cells stopped relaxation for at least 10 s, which typically took few minutes.

Next to pulling experiments with keratinocytes, also pulling on MDCK cells expressing DPI tension sensor constructs was performed. These cells were generated as a doxycycline-inducible cell line and prepared by Andrew J. Price [11]. The pulling experiment was performed analogously to the pulling on keratinocyte monolayers with two deviations. As more cells expressed tension sensor and no-force control constructs, areas with signal localized to cell–cell contacts were selected rather than individual cell–cell contacts for transiently transfected keratinocytes. Second, MDCK cells adhered less to the substrate and therefore pulling distances were considerably larger and in the order of $50-100\,\mu m$ instead of $< 20\,\mu m$.

Each set of images for SE-FRET comprised of imaging the donor emission after donor excitation D_{obs}, the acceptor emission after donor excitation F_{obs}, and the acceptor emission after acceptor excitation A_{obs}. In addition, a brightfield (BF) transmission image was taken to visualize the entire monolayer. The exposure times were $t_{exp} = 6\,s$ to excite YPet, $t_{exp} = 1.5\,s$ for mCherry, $t_{exp} = 4\,s$ for mTFP1, and $t_{exp} = 1\,s$ for EYFP.

3.7 Analysis of Sensitized-emission FRET Images

The sensitized emission (SE) ratiometric FRET analysis was developed by Andrew J. Price and only slightly modified during the course of the joined project.

3.7.1 Data Import

The individual images were saved as 16 bit TIF files with $2560 \times 2160\,pixels^2 = 414.21 \times 349.49\,\mu m^2$. The images were then imported in MATLAB version R2017b using `imread()` and for each image type, i.e. D_{obs}, F_{obs}, A_{obs}, and BF, a stack of all images taken in one experimental condition was saved as TIF. The associated meta-information was imported using `parse_json()`[1] and saved as matlab (MAT) file.

3.7.2 Intensity Correction Based on Individual Channels

The individual channels were then corrected for dark noise, the differential illumination throughout the image, and autofluorescence background. The correction for dark

[1] François Glineur, 2009; `https://de.mathworks.com/matlabcentral/fileexchange/23393-another-json-parser`

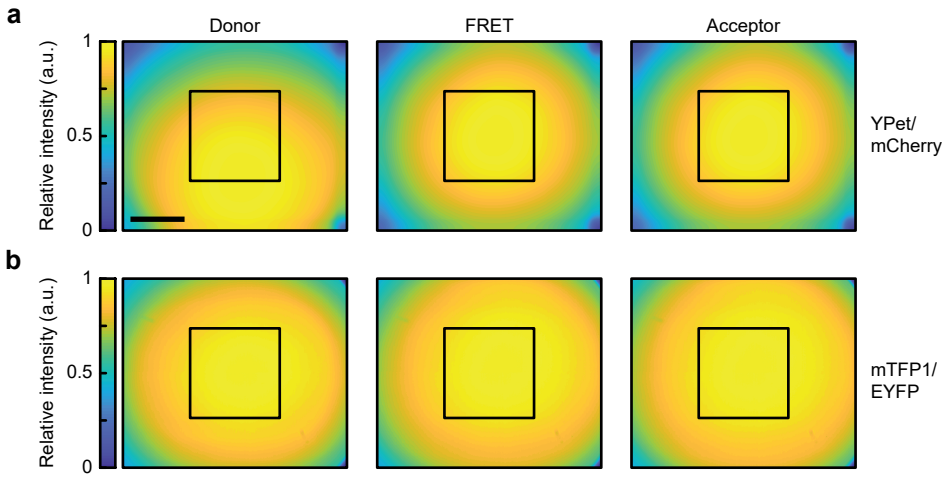

Figure 3.1: The relative illumination r_{illum} in the field of view was experimentally determined and normalized to the brightest signal. Fluorescent compounds, i.e. TRITC for mCherry excitation and riboflavin for all other cases, were dissolved in PBS to generate uniformly fluorescent samples. These samples were excited with the donor excitation and the emission was detected either in the donor (Donor) or acceptor (FRET) emission range. In addition, a uniformly fluorescent sample was excited with the acceptor excitation and emission was detected in the acceptor emission range (Acceptor). The illumination measurements used donor and acceptor channel settings matching YPet and mCherry (**a**) or mTFP1 and EYFP (**b**). The final data analysis was later limited to the central $1024 \times 1024\,\text{pixels}^2$ (black box) mainly to exclude areas strongly influenced by differential illumination. Scale bar: 100 µm.

noise I_{dark} is based on measurements of the intensity images without any sample, which could be described in dependence of the exposure time t_{exp} by

$$I_{\text{dark}} = 1.145 \cdot 10^{-3}\, t_{\text{exp}} + 99.18. \tag{3.3}$$

To correct the observed intensities I_{obs} for the non-homogeneous illumination within the image, the illumination was experimentally measured from uniformly fluorescent samples and normalized to a relative illumination correction term r_{illum} (Fig. 3.1). The autofluorescent background I_{auto} was estimated by a rolling ball filter, which was implemented using `imfilter(image, shape, 'symmetric')`, where `shape` is the normalized neighborhood determined with `getnhood()` of a round disk with $r = 25$ pixels radius generated by `strel('disk', 25)`. The observed intensities I_{obs} were then corrected for dark noise I_{dark}, relative inhomogeneity in illumination r_{illum}, and autofluorescent background I_{auto} by

$$I_{\text{corr, bkg}} = \frac{I_{\text{obs}} - I_{\text{dark}}}{r_{\text{illum}}} - I_{\text{auto}}, \tag{3.4}$$

where I_{obs} is D_{obs}, F_{obs}, and A_{obs}, respectively, and I_{dark}, r_{illum}, and I_{auto} are the correction terms determined for the respective channel.

3.7.3 Intensity Correction for Cross-talk between Channels

The observed intensities are not only affected by variations within one channel but also influenced by bleed-through between channels [264]. The corrected intensities I_{corr} are therefore related to the ideal intensities without any crosstalk I_{ideal} (Fig. 3.2a) by

$$\begin{pmatrix} D_{\text{corr}} \\ F_{\text{corr}} \\ A_{\text{corr}} \end{pmatrix} = \begin{pmatrix} 1 & \epsilon_{\text{FD}} & \epsilon_{\text{AD}} \\ \epsilon_{\text{DF}} & 1 & \epsilon_{\text{AF}} \\ \epsilon_{\text{DA}} & \epsilon_{\text{FA}} & 1 \end{pmatrix} \cdot \begin{pmatrix} D_{\text{ideal}} \\ F_{\text{ideal}} \\ A_{\text{ideal}} \end{pmatrix}, \tag{3.5}$$

where the individual correction coefficients ϵ_{ij} describe the bleed-through from i in j relative to the brightness in i (Fig. 3.2b), e.g. ϵ_{DF} is the bleed-through from donor emission into the FRET channel. For example, the contributions of direct donor and acceptor emission to the FRET channel can be determined by

$$\epsilon_{\text{DF}} = \frac{I_{\text{DF}}}{D_{\text{ideal}}} \tag{3.6}$$

$$\epsilon_{\text{AF}} = \frac{I_{\text{AF}}}{A_{\text{ideal}}}, \tag{3.7}$$

where I_{DF} and I_{AF} are the intensity of the donor and acceptor that is detected in the acceptor channel after donor excitation, respectively (Fig. 3.2c). These intensities were determined from cytosolic expression of the individual fluorophores. From the same fluorophore-only controls, also the contribution of the direct acceptor excitation and emission to the donor image and of the direct donor excitation and emission to the acceptor image (Fig. 3.2d) can be determined by

$$\epsilon_{\text{AD}} = \frac{I_{\text{AD}}}{A_{\text{ideal}}} \tag{3.8}$$

$$\epsilon_{\text{DA}} = \frac{I_{\text{DA}}}{D_{\text{ideal}}}. \tag{3.9}$$

The contribution of the FRET signal to donor and acceptor channels (Fig. 3.2e) is not directly accessible from fluorophore-only measurements but can be calculated if the excitation profile is the same as for the donor and the emission profile is the same as for the acceptor with

$$\epsilon_{\text{FA}} = \frac{I_{\text{DA}}}{I_{\text{DF}}} \tag{3.10}$$

$$\epsilon_{\text{FA}} = \frac{I_{\text{AD}}}{I_{\text{AF}}}. \tag{3.11}$$

The correction coefficients were determined from the slope of a linear fit from the intensities determined from cells with cytosolic expression of the individual fluorophores [265].

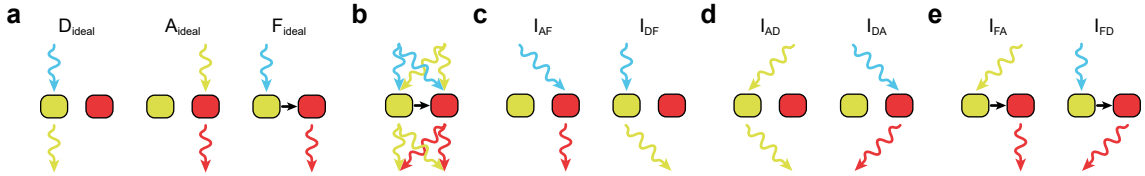

Figure 3.2: The crosstalk depends on excitation and emission. (**a**) The ideal donor intensity D_{ideal} depends on the excitation and emission of the donor. Analogously, the ideal acceptor intensity A_{ideal} depends on excitation and emission of the acceptor. In the FRET image F_{ideal}, the emission of the acceptor is measured after excitation of the donor. (**b**) In a real experiment, the measurement is complicated by crosstalk between the excitation and emission spectra. (**c**) The direct excitation of the acceptor by the donor excitation contributes to the signal detected in the FRET image with I_{AF}. The FRET image also contains the bleed-through from the donor emission I_{DF}. These parameters cause the majority of bleed-through and can be determined with fluorophore-only measurements. (**d**) The contributions of direct acceptor excitation to the donor channel I_{AD} and direct donor excitation to the acceptor channel I_{DA} are typically small but can also be directly determined from fluorophore-only measurements. (**e**) The contribution of FRET to the acceptor I_{FA} and donor I_{FD} channels are not directly accessible but have to be calculated from the other parameters.

The resulting correction coefficients were initially measured with different exposure times matching the exposure times of the SE-FRET images and then normalized to the same exposure across all images. These normalized correction coefficients were for YPet and mCherry approximately

$$\begin{pmatrix} 1 & \epsilon_{\text{FD}} & \epsilon_{\text{AD}} \\ \epsilon_{\text{DF}} & 1 & \epsilon_{\text{AF}} \\ \epsilon_{\text{DA}} & \epsilon_{\text{FA}} & 1 \end{pmatrix} = \begin{pmatrix} 1 & 2.4 \cdot 10^{-3} & 1.3 \cdot 10^{-3} \\ 0.287 & 1 & 0.056 \\ 0.038 & 0.132 & 1 \end{pmatrix} \tag{3.12}$$

and for mTFP1 and EYFP approximately

$$\begin{pmatrix} 1 & \epsilon_{\text{FD}} & \epsilon_{\text{AD}} \\ \epsilon_{\text{DF}} & 1 & \epsilon_{\text{AF}} \\ \epsilon_{\text{DA}} & \epsilon_{\text{FA}} & 1 \end{pmatrix} = \begin{pmatrix} 1 & 4.9 \cdot 10^{-3} & 1.1 \cdot 10^{-4} \\ 0.626 & 1 & 0.023 \\ 9.5 \cdot 10^{-3} & 0.015 & 1 \end{pmatrix}. \tag{3.13}$$

The correction coefficient was then also adjusted to the exposure times of the individual channels, i.e. each coefficient ϵ_{ij} was multiplied with the ratio of the respective exposure times $t_{\text{exp},i}/t_{\text{exp},j}$.

3.7.4 Isolation of the Desmosomal Puncta

To isolate desmosomal signal, images were first filtered to exclude background signal. Therefore, a bandpass filter was applied, which was implemented as `imfilter(image,`

`h, 'symmetric')` with `h = ones(s, s)/s`^{2} and $s = 3$ and 50. The positive pixel values were then rescaled to a range of zero to one using `imadjust(image, limit)`, where the `limit` was determined using `stretchlim()` on the positive values of the filtered image tolerating 0.01 % saturated pixels. These images were then saved as TIF stack and used to manually select regions of interest and generate binary masks using Fiji.

Furthermore, a region containing background signal was manually selected on the intensity-corrected image using `imrect` and `createMask()`. The pixel intensities within this background region I_{bkg} were then used to calculate a threshold intensity I_{thresh} for the signal of interest

$$I_{\mathrm{thresh}} = \overline{I_{\mathrm{bkg}}} + 4\,\sigma(I_{\mathrm{bkg}}), \tag{3.14}$$

where $\overline{I_{\mathrm{bkg}}}$ is the mean and $\sigma(I_{\mathrm{bkg}})$ is the standard deviation of the background signal. Note, during pulling analysis, the background was selected on a superimposed image of the individual images during and after pulling on a region containing no puncta in both conditions.

The individual desmosomal puncta were identified from the acceptor image in the area selected with the manual mask. First, the image was filtered with a bandpass filter as described above but using $s = 3$ and $s = 10$ and the outermost 10 pixels were cut in all directions. Then, pixels with values below I_{thresh} or outside the mask were excluded. Next, connected regions were identified using `regionprops()` and all pixels in connected areas of less than 9 pixels were excluded. The local maxima of the remaining pixels were identified using `imregionalmax()` and all pixels with desmosomal signal were assigned to the nearest local maximum, which was identified by `dsearchn()`.

3.7.5 Calculation of the FRET Index

The FRET index was calculated analogue to previous tension sensor experiments [225, 227] from the corrected intensities in the donor and FRET channel

$$\mathrm{FRET}_{\mathrm{index}} = 100\,\frac{F_{\mathrm{corr}}}{F_{\mathrm{corr}} + \gamma D_{\mathrm{corr}}}, \tag{3.15}$$

where γ describes the relative sensitivity of the detection of donor and FRET emission [266] and $\gamma = 1$ was assumed.

3.8 Analysis of the Micromanipulation Experiment

The analysis of the pulling data described in this section was developed in close collaboration with Andrew J. Price. The images were treated as described in Sec. 3.7 with the adjustment that the manual masks for the different time points were united and desmosomal puncta were isolated in the entire region.

3.8.1 Matching of Puncta across Time Points

To trace individual DSMs in a pulling experiment, the desmosomal puncta were matched between the images. To this end, puncta before and during pulling were matched to the puncta after pulling because matching of the shorter distances is more reliable. In a first step, a general transformation of the image was made. Therefore, six to ten points were manually selected in both images to be matched using `cpselect()` and a transformation was calculated using `fitgeotrans('projective')`.

The centroids of the puncta was determined using `regionprops()` and transformed using `tformfwd(maketform('projective'))` with the previously determined transformation, which roughly overlays the centroids of the two images. The distances between all centroids $d_{\text{c–c}}$ were then calculated; distances $d_{\text{c–c}} < d_{\min}$ were regarded as noise and set to $d_{\min} = 1\,\text{pixel}$, and $d_{\text{c–c}} > d_{\max}$ were regarded as unlikely for the relevant matches and set to $d_{\max} = 100\,\text{pixels}$. To match the centroids, a `bipartite_matching` function[2] was used that solves a maximum-weight bipartite matching problem. Therefore, all distances were subtracted from $d_{\max}$ to achieve highest values for shortest distances prior to the matching. The matched puncta were then saved as a structure and used for further analysis.

3.8.2 Determination of the Recoil Distance and the Recoil Angle

The recoil distance d_{r} is the length of the vector between the centroids of the matched puncta during and after pulling

$$d_{\text{r}} = \sqrt{\left(x_{\text{during}} - x_{\text{after}}\right)^2 + \left(y_{\text{during}} - y_{\text{after}}\right)^2}, \tag{3.16}$$

where x_{during}, y_{during} and x_{after}, y_{after} are the x- and y- coordinates of the punctum during and after pulling, respectively.

[2] David F. Gleich and Ying Wang, 2009; `https://de.mathworks.com/matlabcentral/fileexchange/24134-gaimc-graph-algorithms-in-matlab-code`

The recoil angle α_r is the acute angle between the recoil vector $\vec{r}$ and a tangential vector to the cell–cell contact $\vec{c}$. The angle between the two vectors can be calculated using the trigonometric relationship

$$\tan\alpha = \tan\left(\rho - \gamma\right) = \frac{\tan\rho - \tan\gamma}{1 + \tan\rho\tan\gamma}, \tag{3.17}$$

and the slopes of the vectors $m_\mathrm{r} = \tan\rho$ and $m_\mathrm{c} = \tan\gamma$, which results in

$$\alpha_\mathrm{r} = \tan^{-1}\left|\frac{m_\mathrm{r} - m_\mathrm{c}}{1 + m_\mathrm{r}\cdot m_\mathrm{c}}\right|. \tag{3.18}$$

The cell–cell contact slope was determined based on the centroids of the neighboring puncta in the during image. Therefore, puncta within $d_\mathrm{slope} = 25\,\mathrm{pixels} \approx 4.2\,\mu\mathrm{m}$ were identified using `rangesearch()` and if at least $N_\mathrm{min} = 3$ puncta were found in this range, a linear fit was made using `robustfit()`. Only if the slope was determined within $\sigma_{m_\mathrm{c}} \leq 9^\circ$ the cell–cell contact vector was used for the angle determination.

3.8.3 Exclusion of Puncta from the Analysis

To exclude puncta out-of-focus, manual masks were drawn on TIF images of the separate channels using Fiji. Similarly, to identify puncta at the pulled cell–cell contact in experiments with keratinocytes, another set of masks was drawn. Furthermore, isolated puncta were excluded. Therefore, the distances between the centroids of puncta after pulling were determined and for each punctum the distance to the nearest neighbor d_near was identified. A punctum i was excluded if

$$d_{\mathrm{near},i} > f\,\overline{d_\mathrm{near}}, \tag{3.19}$$

where $\overline{d_\mathrm{near}}$ is the mean of the distances to the nearest neighbor from all puncta within one image. The relative factors $f = 2$ and $f = 1.5$ were used for pulls in keratinocytes and MDCK monolayers, respectively.

Moreover, puncta that recoiled different than the average neighboring puncta were also identified as mismatches. To this end, the surrounding of the punctum i was defined by the $S = 7$ and $S = 11$ puncta with the shortest distance in the image after pulling of keratinocytes and MDCK cells, respectively. Within this surrounding S_i of the punctum i an average recoil direction $\vec{\overline{r}}_j^{(S)}$ was determined

$$\vec{\overline{r}}_j^{(S)} = \frac{\sum_{j\in S_i}\vec{r}_j\,e^{-d_{\mathrm{r},j}^2/(2\sigma^2)}}{\left|\sum_{j\in S_i}\vec{r}_j\,e^{-d_{\mathrm{r},j}^2/(2\sigma^2)}\right|}, \tag{3.20}$$

where $d_{\mathrm{r},j}$ is the recoil distance of the punctum j, i.e. the distance between the same punctum in the during and after image, $\vec{r}_j$ is the unit vector in the recoil direction, and

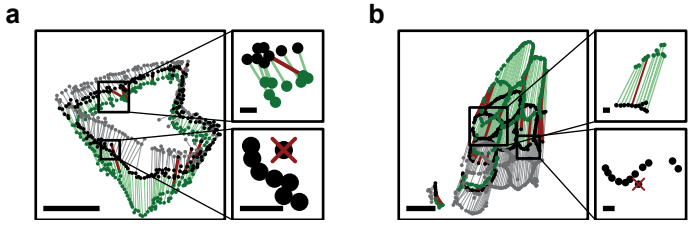

Figure 3.3: Mismatched puncta were excluded from the distance- and angle-dependent analysis. The centroids of puncta before (grey) and during (green) the pulling were matched to puncta after pulling (black). Mismatches were then identified in relation to the neighboring puncta. *Top* Puncta were excluded if the matched vector had a substantially different orientation than neighboring puncta (red line). *Bottom* Isolated puncta were also excluded (red cross). The surrounding comprised of a total of eight puncta in keratinocytes (**a**) and 12 puncta in MDCK cells (**b**). Scale bars: 20 µm and 2 µm.

σ is the width of the Gaussian distribution used to rescale the unit vectors. The scaling term was introduced to account for the smaller reliability of short unit vectors. For pulls in keratinocytes and MDCK cells $\sigma = 15$ and $\sigma = 30$ was used, respectively. The resulting average recoil direction was then used to calculate a score ξ_i for each punctum i

$$\xi_i = \left(1 - \left|\vec{r}_i \cdot \vec{\overline{r}}_i^{(S)}\right|\right) e^{-\overline{d_\mathrm{r}}/d_{\mathrm{r},i}}. \tag{3.21}$$

Here, the score is scaled with the recoil distance $d_{\mathrm{r},i}$ of an individual punctum i in relation to the average recoil distance $\overline{d_\mathrm{r}}$ of all puncta such that the score is reduced for shorter recoil distances because the recoil orientation is a better identification parameter for mismatches with longer distances. Puncta with a score $f\times$ larger than the average score $\overline{\xi}$ of all puncta in the image, $\xi_j > f\,\overline{\xi}$, were identified as mismatches. For pulls in keratinocytes and MDCK monolayers, $f = 2$ and $f = 1.5$ were used, respectively.

The puncta that should be excluded based on one of the criteria, i.e. focus, location towards tip, distance to the nearest neighbor and mismatch, were marked in a structure with logicals. All information was then saved in a comma-separated values (CSV) file for the import in R.

3.8.4 Assembly, Statistically Evaluation, and Fit of the Data

The data from individual desmosomal puncta were assembled using R (RStudio, version 1.1.442). First, puncta were excluded if they were out-of-focus, had recoil distances below one pixel, were isolated or mismatched or had a too low acceptor intensity, i.e. $A_\mathrm{corr} < 2,000$ for mCherry $A_\mathrm{corr} < 5,000$ for EYFP. Furthermore, for pulls in keratinocytes, only the puncta at the pulled cell–cell contact were included for most analysis with the exception being the explicit analysis of puncta at the opposite cell side (Sec. 5.8).

The statistical analysis is highly sensitive to outliers, and therefore also puncta with FRET indices $I_{\mathrm{FRET}} < 0$ or $I_{\mathrm{FRET}} > 100$ were excluded from the analysis.

Binning of the Data by the Recoil Distance or the Recoil Angle

The data were grouped in bins of equal size using the `bin(`N_{bin}`, 'length')` function from the library `OneR`[3], where N_{bin} is the number of bins. The distance-dependent data were binned based on the logarithm of the recoil distances. To best reflect the underlying data distribution, recoil distances below a minimal distance $d_{\mathrm{r,min}} = 2\,\mathrm{pixels}$ were assigned the logarithm of the minimal distance. Furthermore, pulls with extremely large recoil distances $d_{\mathrm{r,max}} > 10\,\mu\mathrm{m} > 61.805\,\mathrm{pixels}$ were excluded from the analysis. To ensure comparable binning between conditions, the same number of bins $N_{\mathrm{bin}} = 13$ was used. The binning was slightly adapted for two experiments. For the F40-based DPII expressed in MEK-wt only few large pulling distances were observed and therefore $50\,\mathrm{pixels} < d_{\mathrm{r}} \leq d_{\mathrm{r,max}}$ were assigned the logarithm of $d_{\mathrm{r,max}} = 61.805\,\mathrm{pixels}$ and $N_{\mathrm{bin}} = 12$ were used. Similarly, for DPI in MEK-wt only few short pulling distances were observed and $d_{\mathrm{r,min}} = 4.7155\,\mathrm{pixels}$ and $N_{\mathrm{bin}} = 12$ were used.

To assemble angle-dependent data, the binning was performed on the recoil angle α_{r} with $N_{\mathrm{bin}} = 12$. To split the distance-dependent data in parallel and perpendicular pulls, the data were filtered based on the recoil angle. Pulls were considered as parallel if $\alpha_{\mathrm{r}} \leq 45^{\circ}$ and as perpendicular if $\alpha_{\mathrm{r}} > 45^{\circ}$.

Statistical Comparison of Tension Sensor and No-force Control Samples

To statistically compare the tension sensor to the no-force control data, a linear-mixed effects model (lmer) implemented by `lme4` [268] was used to take the interdependence of the puncta from one image into account

$$I_{\mathrm{FRET}} \sim L_{\mathrm{Ctrl}} + \left(1|N_{\mathrm{image}}\right), \tag{3.22}$$

where I_{FRET} is the FRET index and L_{Ctrl} is a logical that is zero for the data to be compared and one for the reference data; typically, the tension sensor data are compared to the no-force control as reference. This model requires that the grouped error between images follows a normal distribution around zero. The normality of the data is not necessarily provided but the overall Gaussian shape of the histograms (Fig. 5.21 and Fig. 5.30) indicate that this prerequisite is met. The `lmer()` makes a linear fit through the two compared data sets and therefore the mean of the first data set ($L_{\mathrm{Ctrl}} = 0$) was accessed as

[3] Holger von Jouanne-Diedrich, 2017; `https://www.rdocumentation.org/packages/OneR/versions/2.2`; based on [267]

the intercept of the fit. The confidence intervals (CIs) were determined using `confint()` on the coefficients of the fit, either with a level of $1\,\sigma \approx 0.68$ or $2\,\sigma \approx 0.95$. The difference in FRET index was analogously accessible from the lmer as the end point of the linear fit. The p-values were derived from the same lmer using the `lmerTest` library [269].

The resulting data were then saved as an CSV file and displayed with MATLAB. The distance- and angle-dependent data are reported as mean with 68 % CI. The FRET index difference and the statistical comparison of the binned tension sensor data were calculated in relation to the non-binned no-force control data using lmer. This non-binned no-force control data are displayed as mean with 95 % CI along with the binned tension sensor and no-force control data. For the comparison of the non-binned tension sensor and no-force control data the FRET index difference is reported as mean with 95 % CI.

Fitting of the Distance- and Angle-binned Data

The binned data were fitted in MATLAB. Therefore, the lmer-determined mean was associated with the median of the corresponding axis value, i.e. angle or logarithmic recoil distance. The fit equation was either a constant value, a sine (Eq. 5.2) for the angle-dependent data or a model with contributions from a constant and a linear logarithmic behavior (Eq. 5.1) for the distance-dependent data. The fit function `lsqcurvefit()` was employed, which uses non-linear least square (NLSQ)-based optimization. To determine, the CI of the fit `nlparci()` was calculated with the fit result, residual, and jacobian of the fit. The used fit equations as well as the resulting fit values are reported with the experiments (Sec. 5.6 to Sec. 5.9).

4 Fluorescence Lifetime Analysis and Merge Software

The fluorescence lifetime analysis and merge software (FLAMES) is developed for the automated analysis of FLIM data collected during FRET-based tension sensor experiments. Such an automated data analysis is preferred over manual analysis not only because it saves time but also because it reduces bias and increases the reproducibility. The software thereby encompasses all steps from data import, signal extraction, and lifetime fits over merging and comparing results of different experimental days to the calculation of FRET efficiencies and their statistical comparison. Moreover, a range of additional data visualizations and meta-information can be generated to gain a better understanding of the data, or to analyze specific questions, e.g. the ratio of stretched molecules or spatially-resolved images. Next to performance improvements and new program features, an efficient workflow and user-friendliness for day-to-day use were main goals during software development. The software described in this chapter is written for MATLAB version R2017b.

4.1 Precursor Software

Dr. Carleen Kluger pioneered automated data analysis in the Grashoff group with a first data analysis software for FRET-based tension sensor experiments [270]. In FLIM analysis software version v03 and v04 (FLIMv03/v04), the spatial and temporal information of photon arrival times are treated separately. The spatial information is used to perform manual masking and subsequent automated signal extraction. During this signal extraction a binary mask is generated that contains all pixels from the brightest intensity class of a multi-Otsu threshold[1]. Multi-Otsu thresholding thereby maximizes the variance between intensity classes [271, 272]. The raw data of the photon arrival times are then reimported using MATLAB's `imread()` function and only the information of the signal within the binary mask is saved. The saved photon count is then fitted with a mono-exponential tail fit based on NLSQ using MATLAB's `fit()` function. The fit quality is judged by R^2. FRET efficiencies are calculated based on an average donor-only lifetime,

[1] Damien Garcia, 2010; `http://www.biomecardio.com/matlab/otsu.html`

which is determined from an associated donor-only control measurement. The lifetimes and FRET efficiencies can also be merged. Therefore, the grouped data sets are identified by their entry number in lists of paths to the data. Furthermore, merged lifetimes or FRET efficiencies can be statistically compared and boxplots are used to visualize the data. The statistical information can be included as significance stars in the boxplots or displayed separately.

4.2 FLAMES Workflow

The FLAMES workflow has two main parts (Fig. 4.1). First, the data are imported, the signal of interest is extracted, and the photon count is fitted. Second, the individual experiments are merged and the data are visualized, statistically compared and saved. After the initial data import, the photon arrival information is resaved as a sparse matrix, which preserves both, spatial and temporal information of the photon arrivals. The spatial information is then used to draw manual masks and to isolate the specific signal of interest via different automated signal extraction algorithms. These signal extraction algorithms are specifically designed for different subcellular structures, which account for the divergent shapes of e.g. FAs, DSMs, or muscle attachment sites. In a brief general outline, images are blurred using e.g. Gaussian or tophat filtering, binary masks are generated using intensity-based thresholding like multi-Otsu, and the binary masks are then refined using e.g. size exclusion or smoothing. Typically, one binary mask is generated, which covers the area with signal of interest. For spatially-resolved images, binary masks are generated for each substructure and collected in a sparse mask matrix. To determine the temporal information of individual masks, the binary mask, or binary mask sparse matrix, is multiplied with the sparse data matrix. Then, mono- and bi-exponential tail fits are used to determine lifetimes and stretch ratios, respectively.

In tension sensor experiments, a set of constructs is measured on different experimental days to reduce the influence of biological variability. During analysis, the data from these different experimental days are merged to achieve sufficient statistics and robust comparisons. To identify corresponding data sets, a *mergeInfo* file associates an individual experimental data set with its controls and defines a merge name. All data sets with the same merge name are combined and can be accessed by their merge name for subsequent analysis.

To calculate FRET efficiencies from lifetimes, an average donor-only lifetime is required, which critically influences the resulting FRET efficiency. To best match the requirements of different projects, FLAMES contains several methods to determine the average donor-only lifetime including, for instance, the median of the merged donor-only control measurements or a previously determined fixed value.

The main data visualizations in FLAMES are boxplots of merged or individual experiments. Additionally, a range of special plots for advanced data evaluation can be displayed, e.g. (area-normalized) photon counts versus lifetimes, FRET efficiencies or ratios. Moreover, FLAMES automatically saves plots, data values, and meta-information like average values and spread, numbers of masks, images, as well as experiments, and statistical comparisons.

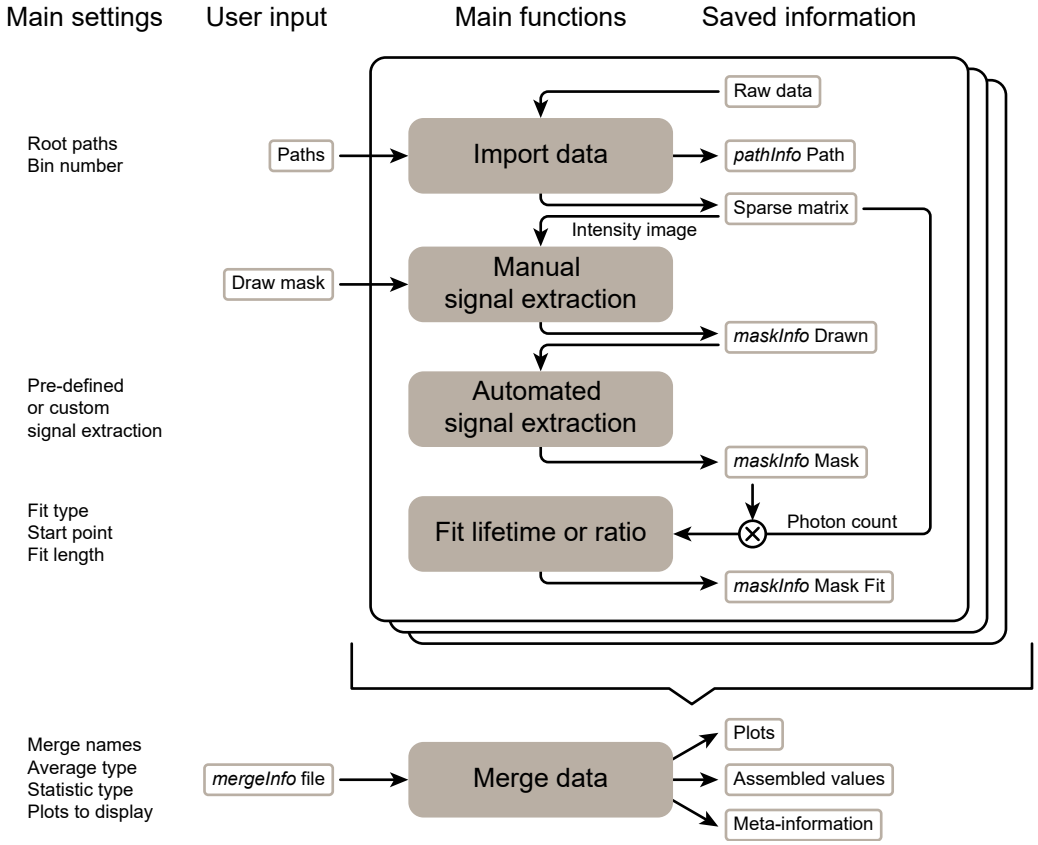

Figure 4.1: The fluorescence lifetime analysis and merge software (FLAMES) allows for an automated analysis of FLIM data. During analysis of individual experimental days, the user only needs to provide paths to the raw data and draw manual masks. Nevertheless, the software can be adjusted to the needs of specific projects by a range of settings. Furthermore, the data analysis pipeline is flexible as intermediate steps are saved. To merge the data, the user provides a *maskInfo* file that identifies the data sets based on the *pathInfo* and *maskInfo* files, which are saved by FLAMES during the analysis. Depending on the enabled settings, FLAMES can display a variety of plots, save the data values, and provide meta-information.

4.3 Import FLIM Data

Prior to the actual data import, a *pathInfo* file that contains paths to the raw data and save locations for the imported and analyzed data is generated. To this end, the user selects all folders containing the experimental data in a graphical user interface (GUI), which is based on `uipickfiles()`[2]. The folder structure of the raw data (Fig. 4.2a) is then rebuild at the save locations for the imported and analyzed data. Therefore, the root path of the raw data is replaced by user-provided root paths. The *pathInfo* file is then automatically saved. The parent folder name of the first entry is thereby used as identifying file name part, which is typically the measurement date. The user can, however, also choose a different save name, which is particularly helpful for a *pathInfo* that contains data from more than one parent folder.

The paths contained in the *pathInfo* file point to the folder with the FLIM raw data. FLIM data are saved by the used FLIM detector (Sec. 3.5) as image stacks in a TIF. Each image in the stack corresponds to an individual time bin, i.e. each image repeat contains spatially-resolved frames per time bin (Fig. 4.2b). These image stacks are imported with MATLAB using `imformats()`, which is about three times faster than `imread()` because it uses information on the data structure like the number of frames. Note that the raw data contains 160 frames, of which the first 155 frames contain photon counts and are imported. As individual photons are collected, each frame has only a few non-zero elements, which make the data ideal for sparse matrix representation. In sparse format, instead of a full matrix only the non-zero elements are saved. The photon arrival information has two spatial and one temporal dimension but MATLAB does not provide three-dimensional sparse matrices. Therefore, the spatial information of photon arrivals is represented by a single linear index, which is saved together with the temporal information into a two-dimensional sparse matrix without information loss. The sparse matrix representation reduces the required disk space largely compared to the raw data TIF files. For example, the FLIM data shown in Sec. 5 are more than 30 TB, while the imported FLIM data save the same information in approximately 60 GB. Due to the significant reduction in disk space, the data can even be saved twice. The first file contains all photon counts irrespective of the image repeat and is used for the analysis described in this chapter. The second file contains one sparse matrix per image repeat and is only used in FLAMES if image repeats are analyzed individually, e.g. to analyze the effect of photobleaching (Fig. 5.9).

[2] Douglas M. Schwarz, Version 1.15, 2012; `https://de.mathworks.com/matlabcentral/fileexchange/10867-uipickfiles-uigetfile-on-steroids`

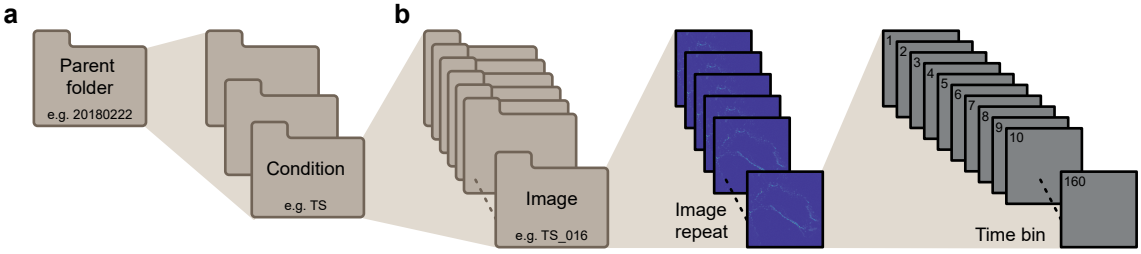

Figure 4.2: The fluorescence lifetime imaging microscopy (FLIM) raw data have spatially-resolved images per time bin. (**a**) The experimenter generates the top-level data structure, which is typically one folder with the measurement date and separate folders for each condition. This data structure is reproduced for the analyzed data. (**b**) The experimenter usually takes 15−20 images per condition. Each of the images contains multiple repeats, e.g. 20 or 100. The image repeats comprise of one spatially-resolved image per time bin. Note that only the first 155 time bins contain photon counts and are imported. During data import, a sparse data matrix is generated for each image repeat and a summed sparse data matrix contains the summed signal of all image repeats from one image.

4.4 Extract Signal of Interest

To isolate specific structures of interest, an intensity image is generated from the raw data by summing the temporal information of photon arrivals. On this intensity image, a manual mask is then drawn using MATLAB's `imfreehand` and `createMask()` functions (Fig. 4.3a). With this manual step signal from neighboring cells on one image is separated. Furthermore, the manual mask can be used to exclude off-target signal that might also be bright and therefore potentially be included during subsequent automated signal extraction. In principle, the number of manual masks is not limited and also smaller structures or areas can be masked, e.g. masking each cell–cell contact separately. To facilitate drawing of multiple, non-overlapping masks, the boundaries of already drawn masks are identified using `bwboundaries()` and displayed. With a separate function, these masks can later also be joined again to perform a common fit on the photon arrival times of all the extracted signal from one image. Another feature of FLAMES is that individual images and masks can be excluded from further analysis during the manual masking. During the masking process, intensity images are visually inspected and images out-of-focus or with samples of unwanted appearance can be identified. The user can thereby only use the intensity information and is therefore not biased during manual data exclusion by the resulting binary mask or lifetime.

The manual masking is followed by an automated signal extraction. Automated signal extraction can consist of blurring (Fig. 4.3b), morphology-based exclusion (Fig. 4.3c), thresholding (Fig. 4.3d), and refinement of the binary mask (Fig. 4.3e, f) to isolate the signal of interest (Fig. 4.3g). The intensity image is blurred to simplify the recognition

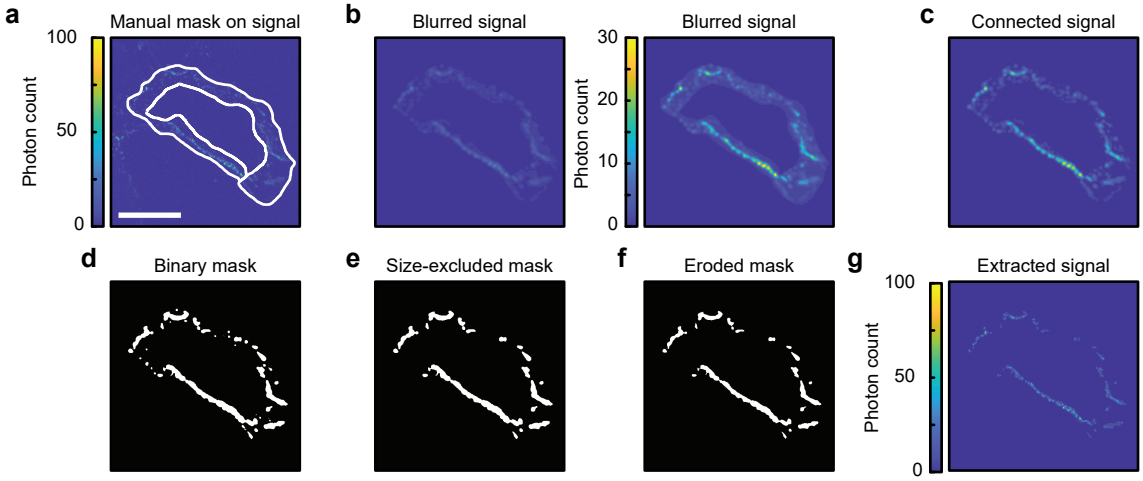

Figure 4.3: The signal of interest is isolated from an intensity image. (**a**) A manual mask is drawn around the structure of interest to exclude signal from other cells or bright background. (**b**) The intensity image is blurred to emphasize connected bright pixels. (**c**) The connected regions can then be identified, e.g. by tophat filtering. (**d**) A binary mask is generated, e.g. with a fixed level threshold. (**e, f**) This binary mask is refined, e.g. by size exclusion (**e**) and erosion (**f**). (**g**) The extracted signal typically covers only few pixels. The exemplary images show the signal extraction for DSMs. Scale bar: 20 µm.

of connected structures. A median filter `medfilt2(image, [`M`, `M`])` can be used, which averages a square neighborhood of M^2 pixels. Alternatively, a Gaussian filter `imgaussfilt(image, `σ`)` smooths based on a Gauss distribution of width σ. Gaussian filtering is additionally also implemented using `imfilter()` with a Gaussian lowpass filter of size h and standard deviation σ defined with `fspecial('gaussian',` h`, `σ`)`. For morphology-based exclusion with a tophat filter, a round disk of size d is used to probe structures and the morphological opened image `imopen(image, strel('disk',` d`))` is then subtracted from the intensity image. During morphological opening, the disk is first used to erode, which removes small structures, and then to dilate, which reverts the erosion for the remaining structures.

Next, a binary mask is generated with multi-Otsu thresholding or a fixed threshold level. In multi-Otsu thresholding using `otsu(image,` N_{class}`)`[3], the variance between N_{class} intensity classes is maximized [271, 272]. The signal within the brightest class is identified as the signal of interest. Alternatively, a binary image is generated using a fixed threshold level t and MATLAB's `im2bw(image,` t`)`. This binary mask can then be further refined with size exclusion based on a minimal pixel number N_{min} using `bwareaopen(mask,` N_{min}`)`. A morphological closing with a round disk of one pixel `bwmorph(mask, 'close')` can be used to smooth the mask. For the isolation of big connected structures, holes can be filled

[3]Damien Garcia, 2010; `http://www.biomecardio.com/matlab/otsu.html`

Structure	Steps for signal extraction
FA	Multi-Otsu ($N_{\text{class}} = 3$), minimal size ($N_{\text{min}} = 9$ pixels) Multi-Otsu ($N_{\text{class}} = 2$), minimal size ($N_{\text{min}} = 9$ pixels) Multi-Otsu ($N_{\text{class}} = 3$) Multi-Otsu ($N_{\text{class}} = 2$)
Cytosolic	Multi-Otsu ($N_{\text{class}} = 2$)
MA	Median filter ($M = 3$ pixels), multi-Otsu ($N_{\text{class}} = 3$), fill holes
HD	Gaussian filter ($h = 7$, $\sigma = 3$), tophat filter ($d = 15$), binary image ($t = 3.5 \cdot 10^{-5}$), minimal size ($N_{\text{min}} = 50$ pixels), morphological closing
DSM	Gaussian filter ($\sigma = 3$), tophat filter ($d = 12$), binary image ($t = 4 \cdot 10^{-5}$), minimal size ($N_{\text{min}} = 75$), morphological erosion ($d = 1$)

Table 4.1: Signal extraction settings are predefined for different biological structures. Four signal extraction methods are implemented to isolate focal adhesions (FAs), which are distinct elongated structures at the cell–matrix interface. Optimized signal extraction is also implemented for cytosolic signal and the muscle attachment sites (MAs) in *Drosophila*, which appear as lines at the muscle–tendon interface. In addition, hemidesmosomes (HDs), which are cauliflower-like extended structures covering large parts of the cell–matrix interface, and desmosomes (DSMs), which are puncta at the cell–cell borders, can be specifically isolated. The signal extraction algorithms are optimized for images of 512×512 pixel^2, which cover 123.02×123.02 µm^2 for all cases but DSMs, where images cover 61.51×61.51 µm^2.

using `imfill(mask, 'holes')`. Finally, masks can be slimmed by erosion with a round disk with defined diameter d using `imerode(mask, strel)` and `strel('disk', d)`.

FLAMES contains predefined signal extractions optimized for FAs, cytosolic expression, muscle-attachment sites in flies, HDs, and DSMs (Tab. 4.1) but also allows to define a custom thresholding without further programming. For custom signal extraction, the order of operations is predefined but all steps can be individually enabled and their parameters can be set.

The resulting binary mask is saved in a *maskInfo* structure and later reimported and multiplied with the sparse data matrix. This matrix multiplication abolishes the reimport of the raw data needed in the precursor software to get the photon count inside the mask. As an additional feature, masks can also be inverted, for example to analyze all discarded signal within a manual mask.

4.5 Fit Lifetime

4.5.1 Model Photon Count Histograms by Exponential Decays

To determine FRET efficiencies from FLIM data, the donor lifetime in the presence and absence of the acceptor is compared (Eq. 2.4). Therefore, the core piece of the data analysis is to robustly determine these lifetimes from the experimentally-determined photon count histograms. While each fluorophore alone emits photons according to an exponential decay, in a FLIM experiment not only the photons of an individual fluorophore are detected but the sum of all photons is assembled to the photon count histogram (Fig. 4.4). If all fluorophores contribute with a common lifetime τ, the overall photon count rate can be described by a mono-exponential function

$$P(t) = A\, e^{-t/\tau}, \tag{4.1}$$

where A is the amplitude. Similarly, if the fluorophores contribute with two lifetimes, τ_1 and τ_2, the photon count rate can be described by the sum of two exponentials, a bi-exponential function

$$P(t) = A_1\, e^{-t/\tau_1} + A_2\, e^{-t/\tau_2}, \tag{4.2}$$

where A_1 and A_2 are the amplitudes corresponding to the lifetimes τ_1 and τ_2, respectively. In principle, three-, four- or multi-exponential decays describe photon count histograms if the fluorophores contribute with more lifetimes. In practice, photon count numbers and observation times in experimental data are limited, which makes it difficult to fit multi-exponential models. The measured photon counts also vary substantially even within one experiment, e.g. almost by an order of magnitude between the desmosomal signal isolated from twenty cell–cell contacts imaged in the same experiment (Fig. 4.4a, b). As the fluorescence lifetime is intensity-independent, these differences do not affect the lifetime per se. In images with reduced photon counts, however, the contribution of the background signal to the overall photon count is typically larger, which increases the deviation from an ideal exponential decay (Fig. 4.4a) and thereby reduces the fit precision. Because the robustness of fits against deviations from the ideal decay reduces with increasingly complex models, FLAMES focuses on mono- and bi-exponential fits.

To estimate the lifetime from a photon count histogram, either an exponential tail fit or deconvolution with the instrument response function (IRF) can be used. The IRF at our setup is determined using the very fast decay of Rose Bengal [273]. This IRF is suitable to check for general microscopy alignment but Rose Bengal is excited at $\lambda_{ex} = 550\,\text{nm}$ and thus at a different wavelength than YPet during FLIM measurements, which is excited at $\lambda_{ex} = 508\,\text{nm}$. Therefore, the current version of FLAMES focuses on tail fits.

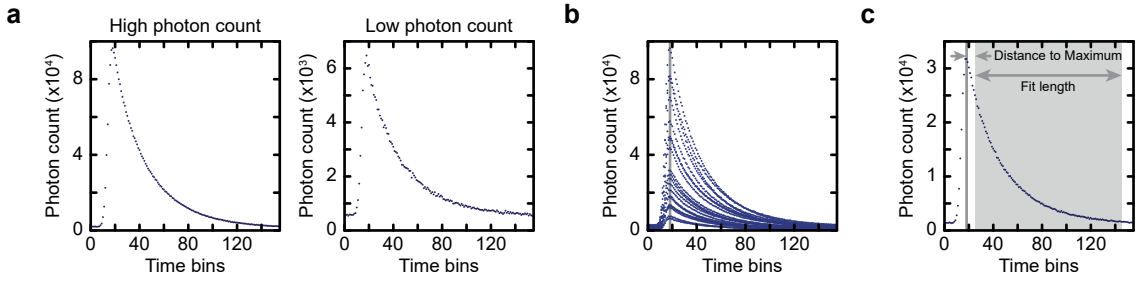

Figure 4.4: The limits for tail fits are standardized. (**a**) The photon count number varies by an order of magnitude even in the same experiment. The photon count histogram with less counts shows more spread, i.e. non-systematic differences between subsequent time bins. (**b**) The time bin with maximal photon count (grey line) is determined from the mean photon count of all images of one experimental condition. (**c**) The start point for tail fitting is chosen relative to the maximal photon count and the fit length is fixed, which defines the last time bin included in lifetime fitting. The photon count histograms belong to desmosomal signal of images measured in one experimental condition with an average of approximately 300,000 total photons.

4.5.2 Determine the Limits of a Tail Fit

The first step for a tail fit is to determine the fit range. To achieve fit stability even if the excitation shifts in relation to the detection window, the fit starting point is chosen in reference to the maximal photon count. To reliably determine the time bin of the maximal photon count, the mean of all photon count histograms within one experiment is used (Fig. 4.4b). The start of the fit is shifted with respect to the maximum of the mean photon count. This shift should be small to maximize the amount of photon arrivals used for fitting but big enough to exclude the initial time bins that are strongly affected by the IRF. To identify a suitable distance, the same data can be fitted with different starting points. The shortest distance after the maximum, for which the lifetime is converged is then used as the starting point for tail fits. For our setup, Dr. Carleen Kluger determined seven time bins after the maximal photon count as optimal starting point [270]. The fit length L is fixed so that the same number of time bins is fitted for all decays. The fit length is set to $L = 120$ time bins to ensure that the same fit length can be used also for small alignment changes between excitation and detection (Fig. 4.4c). Based on the typical maximum location, the fit length could be in principle extended to $L = 130$ time bins. In FLAMES, both parameters, time bins after the maximum and the fit length, are set once per project to ensure comparability of the lifetimes estimated from the photon arrival times.

4.5.3 Simulate Exponential Decay Data

To estimate the effect of individual parameters like the fit length on the lifetime estimation, photon arrival data are simulated. In contrast to experimental data, the underlying lifetime distribution of simulated data is known and can be varied. The simulated data with known properties can then be fitted with different fits to compare their behavior. Furthermore, simulated data with defined changes in individual parameters, e.g. the fit length or photon count, can be fitted with the same settings to estimate the effect of these parameters on the lifetime determination.

In the simulations, the mean number of photons s_i in the time bin i is modeled according to mono- or bi-exponential decay functions on top of an homogeneous background. To best mimic the experimental conditions during simulation, parameters are thereby based on experimental values. The amplitude A, however, is not known but instead the total photon count $\mathcal{N}_{\text{total}}$ within a defined observation time $L\,\Delta t$ with L the number of time bins and Δt the time bin width. In a first step towards a reformulation of the mono-exponential model function (Eq. 4.1) in dependence of the known parameters, the photon count N for an infinite observation time is calculated as the integral of the photon count rate $P(t)$

$$\begin{aligned} N &= \int_0^\infty P(t)\,\mathrm{d}t = \int_0^\infty A\,e^{-t/\tau}\,\mathrm{d}t \\ &= -A\,\tau\,e^{-t/\tau}\Big|_0^\infty \\ &= A\,\tau. \end{aligned} \tag{4.3}$$

Next, the photon count rate can be expressed in dependence of the photon count N

$$P(t) = \frac{N}{\tau}\,e^{-t/\tau}. \tag{4.4}$$

The photon count n_i within one time bin i is then described by

$$\begin{aligned} n_i &= \frac{N}{\tau}\int_{t_{i-1}}^{t_i} e^{-t/\tau}\,\mathrm{d}t \\ &= N\left(e^{-t_{i-1}/\tau} - e^{-t_i/\tau}\right), \end{aligned} \tag{4.5}$$

where $t_i = i\,\Delta t$ is the end time of the i^{th} time bin. The photon number $\mathcal{N}_L$ in a trace of L time bins is therefore

$$\mathcal{N}_L = \sum_{i=1}^{L} n_i = N\left(e^{-t_0/\tau} - e^{-t_L/\tau}\right). \tag{4.6}$$

This reformulation can be used to replace the photon count N in Eq. 4.5 by the total photon number in the trace $\mathcal{N}_L$, which results in

$$n_i = \mathcal{N}_L \frac{e^{-t_{i-1}/\tau} - e^{-t_i/\tau}}{e^{-t_0/\tau} - e^{-t_L/\tau}}. \tag{4.7}$$

However, in the experiment also background photons, which do not stem from the exponential decay are collected. The total photon count $\mathcal{N}_{\text{total}}$ observed in a time trace of L time bins is therefore

$$\mathcal{N}_{\text{total}} = \mathcal{N}_{\text{L}} + \mathcal{N}_{\text{b}}, \tag{4.8}$$

where $\mathcal{N}_{\text{b}}$ is the background photon count in a time trace of L time bins. With the relative contribution b of the background photon count $\mathcal{N}_{\text{b}}$ to the total photon count $\mathcal{N}_{\text{total}}$, this background photon count can be reformulated as $\mathcal{N}_{\text{b}} = b\,\mathcal{N}_{\text{total}}$. Analogously, the photon number that stems from the exponential decay can be expressed as $\mathcal{N}_L = (1-b)\,\mathcal{N}_{\text{total}}$. The photon count n_i per time bin i when tacking the background photon count into account is then described by

$$n_i = (1-b)\,\mathcal{N}_{\text{total}} \frac{e^{-t_{i-1}/\tau} - e^{-t_i/\tau}}{e^{-t_0/\tau} - e^{-t_L/\tau}} + \frac{b\,\mathcal{N}_{\text{total}}}{L} \tag{4.9}$$

with the implicit assumption that the background photons counts are homogeneously collected over the time bins. If the fit start point is the first time bin, i.e. $t_0 = 0$, the simulation equation for a mono-exponential decay simplifies to

$$s_i^{\text{mono}} = (1-b)\,\mathcal{N}_{\text{total}} \frac{e^{-t_{i-1}/\tau} - e^{-t_i/\tau}}{1 - e^{-t_L/\tau}} + \frac{b\,\mathcal{N}_{\text{total}}}{L}. \tag{4.10}$$

Analogously, to simulate a bi-exponential decay, the bi-exponential model function (Eq. 4.2) is expressed using Eq. 4.3 in terms of the individual photon counts N_1 and N_2

$$P(t) = \frac{N_1}{\tau_1} e^{-t/\tau_1} + \frac{N_2}{\tau_2} e^{-t/\tau_2}. \tag{4.11}$$

This equation can be reformulated in dependence of the total number of photons N. To this end, the number of photons coming from one population is defined as

$$N_1 = r_{\text{N}}\, N, \tag{4.12}$$

where r_{N} is the relative amount of photons from the first lifetime. As all photons come from either of the two lifetimes, the photon number of the second lifetime can be calculated as

$$N_2 = (1 - r_{\text{N}})\, N. \tag{4.13}$$

The bi-exponential model function is then

$$P(t) = N \left(\frac{r_N}{\tau_1}\, e^{-t/\tau_1} + \frac{1 - r_N}{\tau_2}\, e^{-t/\tau_2} \right). \tag{4.14}$$

The photon count n_i within one time bin i is described by

$$\begin{aligned} n_i &= \int_{t_{i-1}}^{t_i} N \left[\frac{r_N}{\tau_1} e^{-t/\tau_1} + \frac{1-r_N}{\tau_2} e^{-t/\tau_2} \right] \mathrm{d}t \\ &= N \left[-r_N e^{-t/\tau_1} - (1-r_N) e^{-t/\tau_2} \right] \Big|_{t_{i-1}}^{t_i} \\ &= N \left[r_N \left(e^{-t_{i-1}/\tau_1} - e^{-t_i/\tau_1} \right) + (1-r_N) \left(e^{-t_{i-1}/\tau_2} - e^{-t_i/\tau_2} \right) \right]. \end{aligned} \tag{4.15}$$

The total photon count N is replaced by the total photon count $\mathcal{N}_{\text{total}}$ in a time trace of L time bins analogue to the formulation for the mono-exponential function (Eq. 4.7). Furthermore, homogeneously-distributed background photons are included in the model by their relative contribution b to the total photon count and the fit start point is the first time bin, i.e. $t_0 = 0$. The simulation equation for a bi-exponential decay is then

$$s_i^{\text{bi}} = (1-b)\,\mathcal{N}_{\text{total}} \frac{r_N \left(e^{-t_{i-1}/\tau_1} - e^{-t_i/\tau_1} \right) + (1-r_N) \left(e^{-t_{i-1}/\tau_2} - e^{-t_i/\tau_2} \right)}{r_N \left(1 - e^{-t_L/\tau_1} \right) + (1-r_N) \left(1 - e^{-t_L/\tau_2} \right)} + \frac{b\,\mathcal{N}_{\text{total}}}{L}. \tag{4.16}$$

With these simulation equations, Eq. 4.10 and Eq. 4.16, the mean number of photons s_i detected in the time bin i is described based on a mono- or bi-exponential decay function and homogeneous background photon counts. To simulate data, next to the simulation equation also the distribution of the data has to be known. The emission of an individual photon is independent of the history, i.e. the emission time of other photons. Furthermore, photon count histograms have a discrete probability distribution as only a natural number of photons can be emitted. Therefore, TCSPC-FLIM data can be described by a Poisson distribution, which is simulated using `poissrnd(`s_i`)`.

The simulation parameters are chosen similar to the experimental values. The total photon count varies between experiments and upon measurement conditions between approximately 10^4 and 10^6 photons within the extracted signal of one image. The median photon counts for FAs is approximately 5×10^4 photons, for donor-only controls in DSMs 7×10^4 photons, and for DP tension sensor constructs more than 3×10^5 photons because these experiments are measured with more image repeats. The YPet lifetime in FAs is 3.2 ns, which corresponds to 40 time bins of width $\Delta t = 0.08$ ns. Furthermore, the ideal case of no background photons is assumed unless explicitly stated otherwise. To simulate bi-exponential data, a second lifetime of 18 time bins, which corresponds to 1.44 ns, is added in a 1 : 1 ratio ($r_N = 0.5$). These values are based on the ratio determination of experimental data (Sec. 4.8). For each condition, 10,000 photon counts are simulated and then fitted using FLAMES to either compare different fits or estimate the effect of changes in the simulation parameters on the lifetime estimation.

4.5.4 Determine Optimization Equation

The basic principle of fits is to find the best parameters to describe the measured data, here photon count, with a model equation, e.g. a mono-exponential decay function. Fitting is therefore an optimization problem how to identify the model parameters that minimize the residuals between model and data. The optimization equation thereby makes an assumption about the underlying data distribution, for example, MATLAB's `fit()` function assumes a normal distribution of the data. TCSPC-FLIM data, however, follows a Poisson distribution $\mathcal{P}_\mu(m)$, which describes the probability to observe a certain number of events m with the mean expected number of events μ in a given time

$$\mathcal{P}_\mu(m) = \frac{\mu^m}{m!} e^{-\mu}. \tag{4.17}$$

Note that for large event numbers, Poisson statistics develop into Gaussian statistics and therefore for large photon count numbers also Gaussian statistics can be used [274].

One method to estimate the best fit parameters is the maximum likelihood (MLH), which is based on information theory [274]. The likelihood $\mathcal{L}(n:m)$ is defined as the likelihood that the measured data m are observed when expecting n. In MLH point estimation, the fit parameters are optimized for highest likelihood that the expected values predict the measured data. For Poisson statistic (Eq. 4.17), the maximum likelihood $\mathcal{L}_\mathrm{P}$ is given by

$$\mathcal{L}_\mathrm{P}(n:m) = \prod_i \frac{e^{-n_i} n_i^{m_i}}{m_i!} \tag{4.18}$$

with i the bin. During optimization, the fit function is calculated for distinct parameter values and the function values n_i are compared to the measured data m_i using Eq. 4.18. The parameters that maximize $\mathcal{L}_\mathrm{P}(n:m)$ are chosen as optimal [274].

For better optimization, the MLH can be transformed to fulfill a χ^2 distribution [274], which is in the general form

$$\chi^2 = \sum_i \frac{(m_i - n_i)^2}{w_i}, \tag{4.19}$$

with m_i and n_i the measured and predicted number of events in the i^th bin, respectively, and w_i a weighting factor. The transformation uses the likelihood ratio

$$\lambda = \frac{\mathcal{L}(n:m)}{\mathcal{L}(m_\mathrm{ideal}:m)} \tag{4.20}$$

with m_ideal the true (unknown) value of m without any errors [274]. For Poisson statistics, the likelihood ratio is

$$\lambda_\mathrm{P} = \prod_i e^{-n_i+m_i} \left(\frac{n_i}{m_i}\right)^{m_i}, \tag{4.21}$$

replacing the unknown $m_{\text{ideal},i}$ by the model-independent MLH estimation m_i [274]. According to the MLH ratio test theorem, the logarithm of λ obeys a χ^2-statistic and the likelihood-χ^2 function for Poisson statistic is

$$\begin{aligned}\chi^2_{\lambda,\mathrm{P}} &= -2\ln\left[\lambda_{\mathrm{P}}\right] = -2\ln\left[\prod_i e^{-n_i+m_i}\left(\frac{n_i}{m_i}\right)^{m_i}\right] \\ &= -2\sum_i\left(\ln\left[e^{-n_i+m_i}\right] + \ln\left[\left(\frac{n_i}{m_i}\right)^{m_i}\right]\right) \\ &= 2\sum_i\left(n_i - m_i + m_i\ln m_i - m_i\ln n_i\right). \end{aligned} \tag{4.22}$$

The likelihood-χ^2 function needs to be minimized and the global minimum results in the best fit parameter estimate. Note, in principle terms that only depend on m_i can be omitted for the minimization but to use the resulting χ^2 also as goodness-of-fit parameter (Sec. 4.5.7) all terms are used. In FLAMES, `fmincon()` is used with the optimization equation Eq. 4.22 to estimate the fit parameters. The measured data m_i is thereby the detected photon count and the expected data n_i is the predicted photon count in the i^{th}-time bin by a mono- or bi-exponential fit function.

4.5.5 Define Fit Functions and Start Values

To estimate a lifetime from a photon count histogram, an exponential fit equation is required. The photon arrival rate of an individual fluorophore with a single decay time is thereby described by a mono-exponential function

$$P(t) = Ae^{-t/\tau} + P_{\mathrm{b}}, \tag{4.23}$$

where τ is the lifetime, A the amplitude, and P_{b} the background photon count rate.

In FLAMES, the initial parameters for fitting can be either set manually or determined from the data. To this end, the total number of photons $\mathcal{N}_{\text{total}}$ is estimated as the mean of the data multiplied with the fit length L and the background photon count rate P_{b} is based on the last five time bins. The lifetime is then estimated by

$$\tau = \frac{\mathcal{N}_{\text{total}} - P_{\mathrm{b}}\,L\,\Delta t}{P_{\text{start}} - P_{\mathrm{b}}} \tag{4.24}$$

and the amplitude A by

$$A = \left(P_{\text{start}} - P_{\mathrm{b}}\right)e^{t_{\text{start}}/\tau}, \tag{4.25}$$

where P_{start} is the photon count rate at the first time bin t_{start}.

The number of photons per time bin is $n_i \approx P(t_i)\,\Delta t$, where $t_i = i\,\Delta t$ is the time at the i^{th}-time bin and Δt the time bin width. The mono-exponential decay function for the number of photons n_i per time bin i is therefore

$$n_i = a\,e^{-t_i/\tau} + n_\text{b}, \tag{4.26}$$

where a is the amplitude and n_b the background photon count.

In tension sensor experiments, typically more than one lifetime contribute to the photon count histogram because individual FRET pairs can be in different states. The two predominant states are closed and open sensors. In the closed sensor, the donor lifetime is quenched by the presence of the acceptor, while in the open sensor, the acceptor is too far away for efficient FRET and the lifetime of the donor is increased. This situation can be described by a bi-exponential decay. Note, in general also a bi-exponential model does not fully reflect the underlying lifetime distribution because donor fluorophores experience different levels of quenching by FRET, especially in tension sensors with a linker that opens gradually. However, the bi-exponential decay is the simplest model that includes the coexistence of closed and open sensors. A bi-exponential decay can be described by

$$P(t) = A_1 e^{-t/\tau_1} + A_2 e^{-t/\tau_2} + P_\text{b} \tag{4.27}$$

where A_1, A_2 and τ_1, τ_2 are amplitudes and lifetimes of quenched and non-quenched donor, respectively, and P_b is the background photon count rate. This general bi-exponential fit equation can then be transformed to

$$P(t) = N\left(\frac{r_N}{\tau_1}\,e^{-t/\tau_1} + \frac{(1-r_N)}{\tau_2}\,e^{-t/\tau_2}\right) + P_\text{b}, \tag{4.28}$$

where N is the photon count and r_N is the relative contribution of the first lifetime to the photon count.

To determine the start parameters for a bi-exponential fit in FLAMES, either manual start values can be used or the values can be calculated based on the parameters of a mono-exponential fit. These mono-exponential parameters can be either calculated as described above or derived from a mono-exponential fit of the data. To estimate two lifetimes from one lifetime, a $1:1$ mixture ($r_N = 0.5$) of $\tau_1 = 1.5\,\tau$ and $\tau_2 = 0.5\,\tau$ is assumed.

Analogue to the mono-exponential decay function (Eq. 4.26), the bi-exponential decay function for the number of photons n_i per time bin i is

$$n_i = n\left(\frac{r_N}{\tau_1}\,e^{-t/\tau_1} + \frac{1-r_N}{\tau_2}\,e^{-t/\tau_2}\right) + n_\text{b}, \tag{4.29}$$

where n is the photon count, r_N the relative contribution of the first lifetime τ_1, and n_b the background photon count.

4.5.6 Estimate the Effect of the Fit Statistic on the Lifetime Estimate

To optimize the mono- or bi-exponential fit function, FLAMES uses the optimization equation based on Poisson statistics (Eq. 4.22). Note that an analogue optimization equation can also be derived with the assumption of normally distributed data [274], which leads to the well-known least-square optimization

$$\chi^2_{\lambda,\mathrm{G}} = \sum_i (n_i - m_i)^2 \,. \tag{4.30}$$

This least-square optimization equation combined with `fmincon()` makes point estimates that are indistinguishable from the point estimates of `fit()`, which inherently uses NLSQ, if the same fit function is used (Fig. 4.5a). This observation confirms that the change in the fit implementation from `fit()` to `fmincon()` itself does not influence the resulting lifetime but instead allows to also use Poisson statistics instead of Gaussian statistics during optimization. Poisson statistics better reflect the TCSPC-FLIM data distribution and fits using Poisson statistics also have a higher fit precision, i.e. smaller variance, on simulated data (Fig. 4.5b) and are therefore used in FLAMES for optimization. Note that the average lifetime determined from bi-exponential data depends on the used fit statistics. Lifetime estimates derived with different fit statistics therefore should not be compared because differences would then not necessarily reflect biological changes but could also be caused by the used fit statistics. Therefore, during standard analysis with FLAMES only Poisson statistics is used.

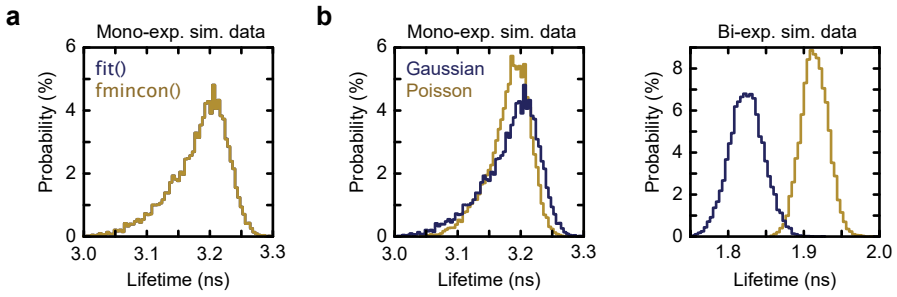

Figure 4.5: The fit precision improves if Poisson instead of Gaussian statistics is used. (**a**) Lifetime determination does not depend on the used fit implementation, i.e. mono-exponential fits using Gaussian statistics with MATLAB's `fit()` and `fmincon()` functions are indistinguishable. (**b**) Mono-exponential fits using Poisson and Gaussian statistics estimate the lifetime of mono-exponential data similarly but estimate different average lifetimes if the underlying data are bi-exponential. Using Poisson statistics thereby increases fit precision. The data are simulated with Eq. 4.10 (**a, b**) and Eq. 4.16 (**b**). The simulation parameters are $\mathcal{N}_{\mathrm{total}} = 50,000$ photons, $\tau = \tau_1 = 40$ time bins (3.2 ns), $\tau_2 = 18$ time bins (1.44 ns), $r_N = 0.5$, $b = 0$, and $L = 120$ time bins. For mono- (**a, b**) and bi-exponential (**b**) data 10,000 decay curves are simulated and fitted with mono-exponential tail fits using FLAMES with `fit()` (**a**) and `fmincon()` (**a, b**).

4.5.7 Determine the Goodness-of-fit

To describe how well a model, e.g. a mono- or bi-exponential fit, explains the measured data, goodness-of-fit measures are used. In principle, goodness-of-fit measures calculate the deviation of the measured data from the value that is expected based on the model.

One simple method to judge the goodness-of-fit is the R^2 value, which is defined as

$$R^2 = 1 - \frac{\sum_i (m_i - n_i)}{\sum_i (n_i - \overline{m})}, \tag{4.31}$$

where m_i and n_i are the measured and expected values in the i^{th} bin, respectively, and $\overline{m}$ is the mean of the measured data. Thus, R^2 judges whether the fit describes the data better than a simple mean. This method, however, is only applicable to linear models and fails to distinguish model quality for non-linear models such as exponential functions [275]. Therefore, R^2 is only contained in FLAMES in combination with the old fit function to allow comparable data analysis with the precursor software but is not implemented for the newer fit routines.

To estimate the goodness-of-fit of non-linear data, the χ^2 value can be used [274, 276]. There are several flavors of χ^2 functions, which differ in the weighting factor in the general χ^2 equation (Eq. 4.19). In Pearson's χ^2 form, the weights $w_i = n_i$ are the expected values

$$\chi^2_{\text{P}} = \sum_{i=1}^{k} \frac{(m_i - n_i)^2}{n_i} \tag{4.32}$$

and in Neyman's chi-square form, the weights $w_i = m_i$ are the measured values

$$\chi^2_{\text{N}} = \sum_{i=1}^{k} \frac{(m_i - n_i)^2}{m_i}. \tag{4.33}$$

If two models with the same number of data points and fit parameters are compared, the resulting χ^2 value can in principle be directly used. A smaller value for χ^2 thereby means that the data is better explained by the model. However, the χ^2 value depends on the number of data points k and the number of fit parameters in the model. Therefore an universal characterization is required to compare the goodness-of-fit of different model functions. To this end, the probability density function (pdf) of the χ^2 function is harnessed, which describes how likely certain χ^2 values arise. The χ^2 function that relates to the tested data and model is identified by the number of data points k, here the fit length L, minus the number of fit parameters in the model, which is three for a mono-exponential and five for a bi-exponential fit. With the help of the corresponding tabulated values, the upper integral is calculated, which describes the likelihood to observe this χ^2 value or any higher value. A perfect model without deviations is zero and the upper integral is one. χ^2 values are typically, and also in FLAMES, reported as this

upper integral. As a rule of thumb, values above 0.1 are in accordance with the model, values below 0.01 reject the model, and those in between are ambiguous [274, 276].

In FLAMES, χ^2 values are calculated based on Pearson and Neyman statistics and also the MLH-based χ^2 fit function (Eq. 4.22) is used to determine the upper integral. Median values are saved for all three χ^2 determination methods, but because Pearson's method is most widely used [276], plots of data versus χ^2 use this determination method.

Use the Goodness-of-fit to Decide between Models

To evaluate mono- and bi-exponential models on experimental data an example experiment measured by Dr. Pia Ringer [216] is used. The FA protein talin-1 connects the transmembrane integrins to the F-actin cytoskeleton and thereby experiences force [216, 217, 224]. Tension sensors at two different integration sites in talin-1 show a tension gradient with more tension at the first integration site between head and rod domains than at the second integration site between the two actin binding sites (ABSs) in the rod domain [216]. This additional tension depends on the presence of the adapter molecule vinculin, while the ground level of tension, which is also present at the second integration site, is independent of vinculin binding [216] (Fig. 4.6).

In simulated data, the χ^2 values clearly indicate that the bi-exponential fit better describes bi-exponential data because the mono-exponential fit is often rejected as a model to explain the data while the vast majority of bi-exponential fits has high χ^2 values (Fig. 4.7a). In measured data, however, the χ^2 values of mono-exponential fits do not allow to reject this model even though tension sensor data certainly has contributions from more than one lifetime (Fig. 4.7b). The goodness-of-fit can therefore not be used to decide between mono- and bi-exponential models to fit the experimental data.

4.5.8 Compare the Mono- and the Bi-exponential Fit Function

The main requirement for the fit function used to determine a lifetime for FRET efficiency calculations is to reproducible estimate the same lifetime if the data follow the same distribution. To estimate the fit precision and accuracy of both, mono- and bi-exponential fits, mono- and bi-exponential data are simulated with varying photon count numbers (Fig. 4.8). For all fit and data combinations, increasing photon counts lead to improved fit quality. Mono-exponential fits determine already for very low photon counts of a few hundred photons a reasonable lifetime for mono-exponential data (Fig. 4.8a) and the fit precision of the mono-exponential fit is also high if the simulated data follow a bi-exponential decay (Fig. 4.8b). Bi-exponential fits of the same data, however, require much more photons, in the order of several thousands, for a reliable lifetime determination

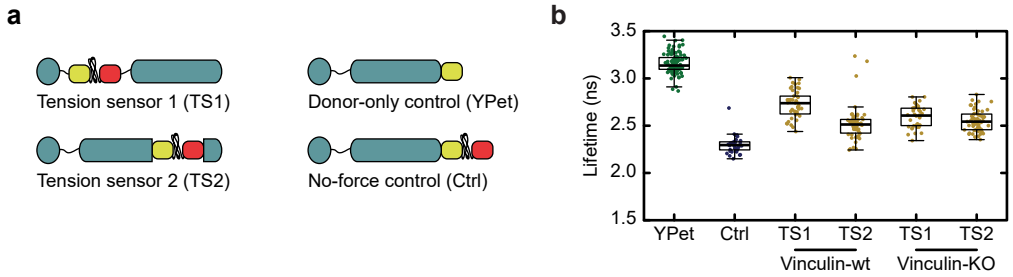

Figure 4.6: An exemplary data set shows tension across talin-1. (**a**) The focal adhesion (FA) protein talin-1 is targeted with a FL-based tension sensor module (TSM) at two different integration sites. The first integration site is between the talin head, which binds to integrins, and talin rod that binds to the F-actin cytoskeleton. The second integration site is between the two actin binding site (ABS) in the rod domain. Talin-1 is C-terminally tagged with YPet or the TSM to generate the donor-only and no-force control, respectively. (**b**) The lifetime of the no-force control is reduced as compared to the donor-only value due to FRET. All tension sensor constructs show values in between these two extremes, which demonstrates tension across talin-1. The tension at the first integration site is reduced in the absence of the adapter molecule vinculin, which establishes an additional connection between talin and the F-actin cytoskeleton. This reduced tension also reduces the tension gradient across talin-1, i.e. less forces act at the second integration site in the presence of vinculin but the level of tension is not further reduced upon vinculin depletion and therefore independent of vinculin binding. In the experiment, 106, 36, 46, 55, 40, 59 cells measured in 78, 33, 40, 53, 36, 54 images were merged from 11 experiments for the donor-only control and four experiments for all other conditions. The experiment was performed by Dr. Pia Ringer and corresponding FRET efficiencies, calculated with $\overline{\tau}_D = 3.2\,\text{ns}$, are published [216].

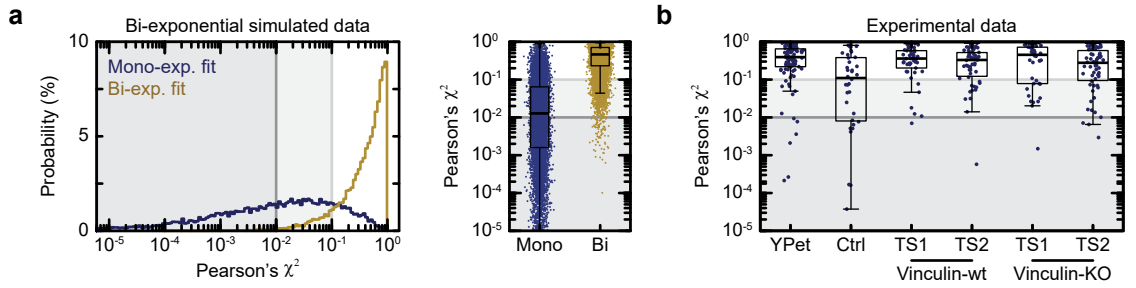

Figure 4.7: Mono-exponential fits are not rejected to model experimental data. (**a**) While a bi-exponential fit describes simulated bi-exponential data well, a mono-exponential fit results in low χ^2 values. However, the mono-exponential model cannot always be rejected based on the χ^2 values. (**b**) In experimental data, the underlying distributions are only for the donor-only control expected to be mono-exponential. The data quality, however, is not sufficiently good to reject the mono-exponential model. χ^2 values below 0.1 (light grey) are ambiguous and values below 0.01 (grey) allow to reject a model. The simulated data (**a**) shows the goodness-of-fit of mono- or bi-exponential fits of 10,000 bi-exponential decay curves simulated with Eq. 4.16. The simulation parameters are $\mathcal{N}_{\text{total}} = 50,000$ photons, $\tau_1 = 40$ time bins (3.2 ns), $\tau_2 = 18$ time bins (1.44 ns), $r_N = 0.5$, $b = 0$, and $L = 120$ time bins. The experimental raw data (**b**) are the same as in Fig. 4.6.

(Fig. 4.8c). The number of photons required for reliable fits is likely increased for bi-exponential fits compared to mono-exponential fits because five instead of three parameters are estimated. As photon counts are limited in the experimental data and the main requirement is to reproducible fit the same rather than the absolute lifetime, lifetimes to calculate FRET efficiencies are determined using mono-exponential fits in FLAMES. Note that bi-exponential fits can be used to determine the relative contribution of open and closed tension sensor molecules (Sec. 4.8).

4.5.9 Estimate the Effect of the Fit Length on the Lifetime Estimate

The fit length is determined by the used setup. However, state-of-the-art microscopes allow the experimenter to change the excitation frequency and thereby the size of the detection window. Furthermore, also with a given detection window, e.g. in the setup

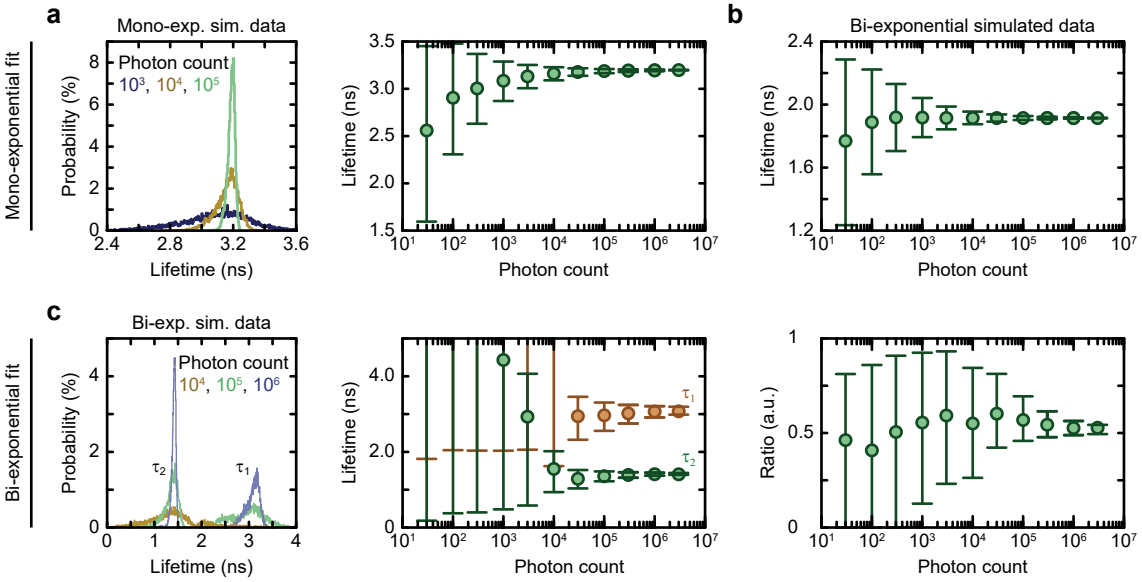

Figure 4.8: The lifetime determination is more precise with increasing photon counts. (**a**) The fit of the mono-exponential lifetime on mono-exponential data becomes increasingly more precise with increasing photon counts. (**b**) Similarly, the average mono-exponential lifetime for bi-exponential data is determined with higher precision for higher photon counts. (**c**) For the lifetime determination with a bi-exponential fit of bi-exponential data considerably more photons are required to reduce the variance in point estimates than for a mono-exponential fit of the same data. The data are simulated with Eq. 4.10 (**a**) and Eq. 4.16 (**b, c**). The simulation parameters are $\mathcal{N}_{\text{total}} = 30\text{–}3 \times 10^6$ photons, $\tau = \tau_1 = 40$ time bins (3.2 ns), $\tau_2 = 18$ time bins (1.44 ns), $r_N = 0.5$, $b = 0$, and $L = 120$ time bins. The data points with error bars are the median with 68 % CI of the lifetimes determined from 10,000 simulated decay curves with mono-exponential (**a, b**) or bi-exponential (**c**) tail fits using FLAMES.

used in this thesis with maximal 12 ns, the fit length can be changed by the selection of the fit limits (Sec. 4.5.2). For mono-exponential fits of mono-exponential data, a fit length of three to four times the lifetime is sufficient for high precision and accuracy and longer time traces only minimally improve the fit quality (Fig. 4.9a). For mono-exponential fits on bi-exponentially decaying photon counts, the same fit length is also required for maximal fit precision but the determined lifetime is biased towards smaller values until the fit length reaches about ten times the long lifetime. Shorter fit lengths lead to shorter average lifetimes because they underestimate the influence of the longer lifetime (Fig. 4.9b). Therefore, it is crucial that the same fit length is used in all experiments that are compared. Furthermore, longer fit lengths are beneficial because fits then better recapture the underlying lifetimes.

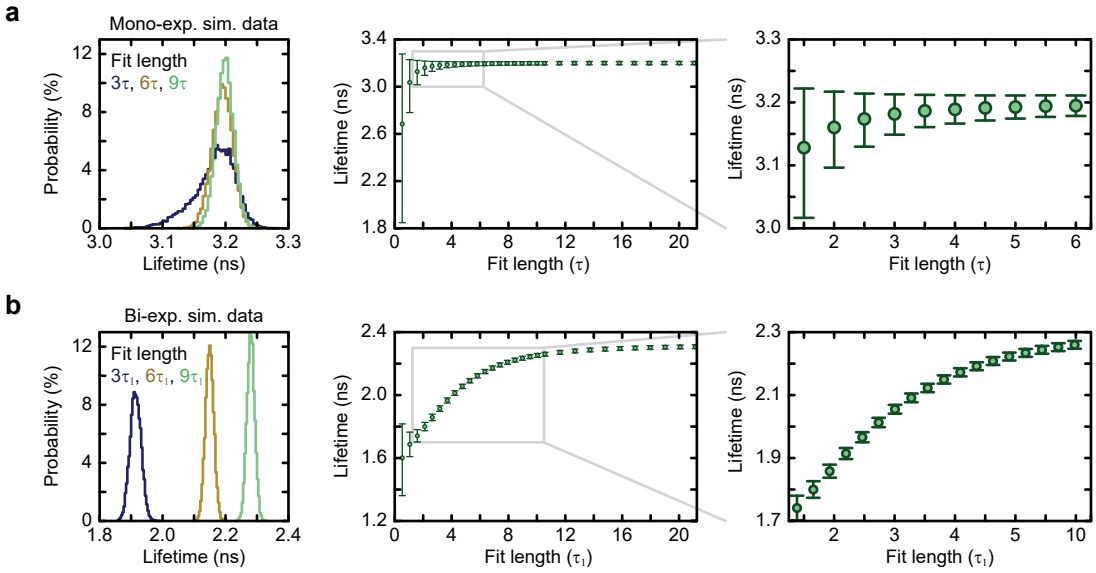

Figure 4.9: Longer time traces increase fit precision and accuracy. (**a**) For short fit lengths, the lifetime determination with a mono-exponential fit on mono-exponential data has increased variance. The lifetime estimate converges if the fit length is approximately four times the lifetime. (**b**) For bi-exponential data, short fit lengths not only lead to increased spread but also result in shorter lifetimes. While the spread is small already if the fit length is three times the long lifetime τ_1, the average lifetime is still strongly biased and converges at a fit length of approximately ten times the long lifetime, $L \approx 10\,\tau_1$. The data are simulated with Eq. 4.10 (**a**) and Eq. 4.16 (**b**). The simulation parameters are $\mathcal{N}_{\text{total}} = 50,000$ photons, $\tau = \tau_1 = 40$ time bins (3.2 ns), $\tau_2 = 18$ time bins (1.44 ns), $r_N = 0.5$, $b = 0$, and $L = 20-800$ time bins. The data points with error bars are the median with 68 % CI of the lifetimes determined from 10,000 simulated decay curves with mono-exponential tail fits using FLAMES.

4.5.10 Estimate the Effect of the Background on the Lifetime Estimate

So far simulations assume the ideal case of no background photons. In an experimental setting, however, some photon counts do not follow an exponential decay, e.g. because they stem from shot noise of the detection system. When these background photon counts are taken into account, the precision of the lifetime determination reduces, i.e. the variance of the estimation is increased (Fig. 4.10a). The background photons not only affect the fit precision but also the fit accuracy and for mono-exponential fits on bi-exponential data, the median of the fitted data is biased towards shorter lifetimes in the presence of background photons (Fig. 4.10b). Therefore, it is important that tension sensor and control samples have the same amount of background. As the background photon count is typically not caused by the sample itself but by the measurement system, e.g. shot noise of the detector, this requirement is likely fulfilled in tension sensor experiments that are performed in a standardized fashion if sample brightness's are on the same order of magnitude.

In summary, FLAMES mainly uses mono-exponential fits based on Poisson statistics to determine an average lifetime because mono-exponential fits robustly report lifetime changes. Bi-exponential fitting is also implemented in FLAMES but the main usage is the calculation of a stretch ratio (Sec. 4.8). The main settings made by the user are the fit type, e.g. mono-exponential, the fit range, and the mask that defines the signal to which the fitting should be applied.

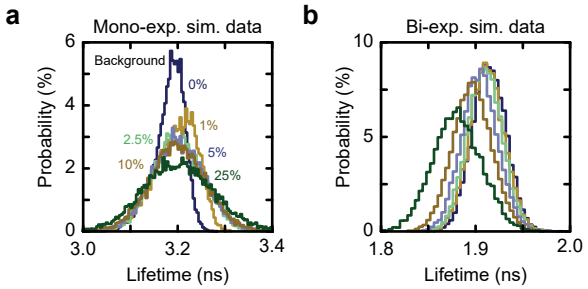

Figure 4.10: Background photon counts reduce the fit precision and accuracy. (**a**) The precision of the lifetime determination is impaired already by small amounts of background photons. (**b**) The average mono-exponential lifetime determined on bi-exponential data reduces with an increasing relative amount of background photon counts. The data are simulated with Eq. 4.10 (**a**) and Eq. 4.16 (**b**). The simulation parameters are $\mathcal{N}_{\text{total}} = 50,000$ photons, $\tau = \tau_1 = 40$ time bins (3.2 ns), $\tau_2 = 18$ time bins (1.44 ns), $r_N = 0.5$, $b = 0-0.25$, and $L = 120$ time bins. The histograms show lifetimes determined from 10,000 simulated decay curves fit with a mono-exponential tail fit using FLAMES.

4.6 Merge and Assemble Data

4.6.1 Merge Data

One key part of FLAMES is the ability to merge data of different experiments. To this end, the user provides an EXCEL sheet, or alternatively a MATLAB cell array, with one row per data set and the corresponding controls specified by four identifiers each (Tab. 4.2 and Fig. 4.11). In addition to this *mergeInfo* file, the user also provides a list of names that are defined as `MergeNames` in the *mergeInfo* file and FLAMES then assembles specifically the data grouped by these names.

The merge function first generates a list of all `MergeNames` listed in the *mergeInfo* file using `unique()`. Then, all `MergeNames` are identified that are not contained in the user-

Column name	Example	Obligate	Explanation
`Name`	Tension Sensor	no	Labeling of individual days
`DonorAcceptorPath`	20180215	yes	Identifies *pathInfo* file, typically by measurement date
`DonorAcceptorName`	DPII_TSi_1dCa_wt	yes	Folder name of the experimental data set
`DonorAcceptorMask`	DSM	yes	Mask for signal extraction
`DonorAcceptorFit`	monoexpchi2poisson0	yes	Fit for lifetime (or ratio) determination
`DonorOnlyPath`	20180215	no	Identifies corresponding donor-only control (`DonorOnly`)
`DonorOnlyName`	YF40dC_int_1d_wt		
`DonorOnlyMask`	DSM		
`DonorOnlyFit`	monoexpchi2poisson0		
`DonorOnlyList`	YF40dC	no	Name of additional file with a list of DonorOnly identifiers
`NoForceControlPath`		no	Identifies no-force control; used to rescale ratio determined with fitted lifetime (Sec. 4.8)
`NoForceControlName`			
`NoForceControlMask`			
`NoForceControlFit`			
`NoForceControlList`		no	
`MergeName`	TSi/1d	yes	Identifies data sets to be grouped in the merge

Table 4.2: Data sets and associated controls are identified in a *mergeInfo* file.

provided `MergeName` list by `setdiff()`. The data associated to these unused `MergeNames` are removed from the imported information. Note, the order of the `MergeNames` in the user input is preserved and for an empty `MergeName` list the data for all `MergeNames` are assembled in the order they are contained in the file. Furthermore, all `MergeNames` that are exclusively defined in the *mergeInfo* file or merge name list are displayed to facilitate the identification of typographical errors by the user.

For each `MergeName`, the corresponding data sets are assembled in a merge structure. The keys to identify a specific data set (Fig. 4.11a) have the prefix `DonorAcceptor`. The `Path` is the specific name part of a *pathInfo* file that contains paths to the analyzed data, the `Name` identifies the appropriate entry in the *pathInfo* file, which then points to the save location of *maskInfo* files containing fit results. The appropriate *maskInfo* file is identified using `Mask` and `Fit`, which reflect the signal extraction algorithm and fit procedure used, respectively. To prevent that multiple fits of the same raw data are assembled in a merge,

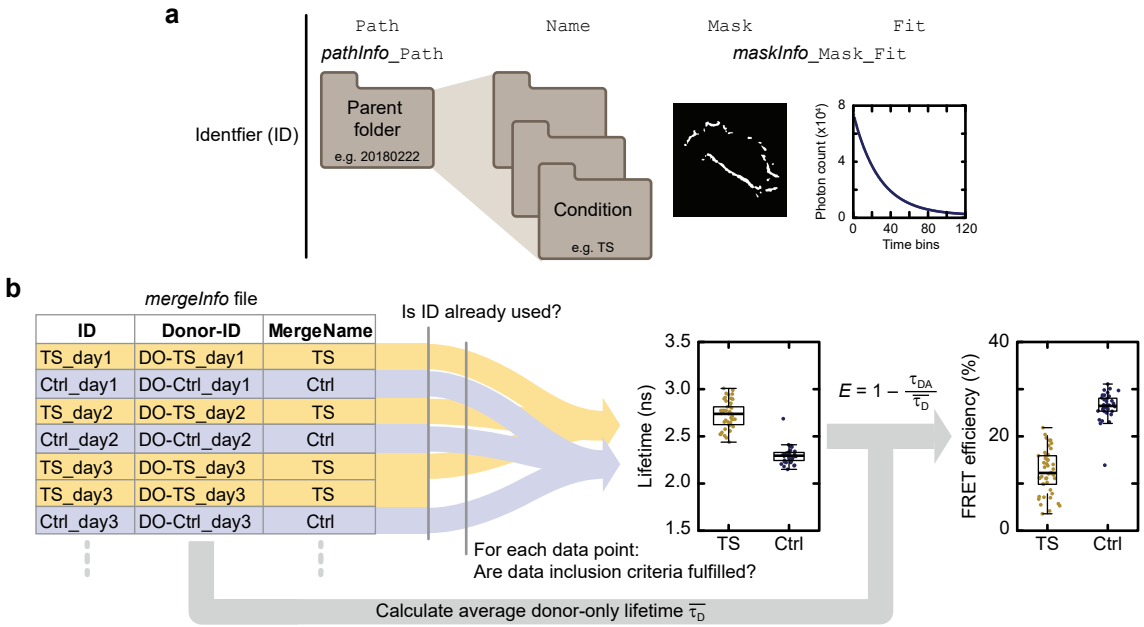

Figure 4.11: Individual experiments are merged based on their `MergeName`. (**a**) Each data set is identified by a set of four keys, which together form the identifier (ID). `Path` refers to the specific name part of a *pathInfo* file, which contains paths to the analyzed data. `Name` is used to identify the respective entry in the *pathInfo* file by the condition name. `Mask` and `Fit` are analysis-specific name parts of the *maskInfo* file that contains the fit results. (**b**) Each row in a *mergeInfo* Excel-sheet contains at least the ID for one sample and the `MergeName`, which is used to merge individual data sets. During assembly, a short version of the ID, i.e. `Path` and `Name`, is used to prevent duplication of data in the same merge. Furthermore, data inclusion criteria are applied to each data point. To calculate the FRET efficiencies from the lifetimes, an average donor-only lifetime $\overline{\tau_D}$ is required, which can, for example, be calculated from associated donor-only controls.

a string of `Path` and `Name` is compared to a continuous list of these short identifiers using `ismember()`. Note that a similar string containing all four keys can be used to label individual data sets in plots, which facilitates the identification of user errors in the assignment of individual experiments to a specific `MergeName`.

During the assembly of individual data, data inclusion criteria are applied on each data point (Sec. 4.6.3). Only data that fulfill these criteria are assembled in a merge structure. This merge structure contains fields for individual experiments, the merged data, and also a range of meta-information. For each data point of a single experiment, the lifetime or ratio, the goodness-of-fit parameter χ^2, as well as total and area-normalized photon counts are assembled. In addition, global information about the data in a merge is provided like median values for χ^2, global image numbers counting all images within one merge, and numbers of (sub)-masks. Particularly for spatially-resolved images, instead of the individual submasks also one median per image can be calculated during the assembly of individual data.

Next to the merged main data, also the corresponding donor-only controls are merged. The corresponding donor-only data set is identified by the same keys as the sample but with `DonorOnly` prefix instead of `DonorAcceptor` and the data are assembled as described for the main data set. In addition to one donor-only data set that can be directly associated with the sample, also a list of donor-only data sets can be provided. Therefore, the `DonorOnlyList` field contains the specific name part to identify a *DonorOnlyList* file, which contains a list of the keys to identify the donor-only data sets, i.e. `Path`, `Name`, `Mask`, and `Fit`.

Moreover, merging of ratios is implemented analogue to the merging of lifetimes and also uses the same function to assemble individual data. Similarly, the no-force control data for rescaling of the ratio plots is assembled analogue to the donor-only control data.

In summary, the merging of tension sensor experiments results in a merge structure containing the individual and merged data as well as associated data and meta-information. This merge structure is assembled new for each merge, because it contains the information as defined by the user, i.e. for specific `MergeNames` and data inclusion criteria. The assembly time for the merge structure is usually on the order of seconds rather than minutes, which further justifies the transient assembly of the merge. The merge structure is then used to generate the data visualizations and to save merged data depending on the user input, e.g. which comparisons are desired.

4.6.2 Calculate FRET Efficiencies

To calculate FRET efficiencies from lifetimes, an average donor-only lifetime $\overline{\tau_D}$ is required. FLAMES has four different methods to determine an average donor-only lifetime. First,

the donor-only control associated with the individual experiment can be used. Second, all donor-only controls corresponding to data grouped in one merge can be merged together. Third, a list of all donor-only controls that should be averaged can be provided separately. This list is then identified by its name in the `DonorOnlyList` column of the *mergeInfo* file. Finally, a fixed lifetime can be provided. The calculation of individual donor-only controls can be enabled, even if some experiments lack the corresponding control. For these individual entries, the donor-only list is used if provided; otherwise the merged data from all donor-only controls in the merge is used.

For the averaging method, the mean and median can be chosen. In general, both averaging methods result in similar values. The median is less affected by outliers, but if only very few data points are merged the median might be more variable. As default options, FLAMES uses the median of the merge of all donor-only lifetimes associated to the merged data.

4.6.3 Exclude Data

During generation of the merge structure (Sec. 4.6.1), only data are included that fulfill the data inclusion criteria. The current version of FLAMES contains three main measures to exclude data from the analysis. First, a minimal number of photons in the entire photon count or in the fit range can be required. Second, a minimal size of the included structures might be set, which is particularly useful for spatially-resolved images with small submasks. Finally, a relative error in the lifetime (or ratio) determination can be used. This relative error is calculated as the width of the 1σ-CI divided by the lifetime (or ratio). Using the CI of the fit more directly reports the fit accuracy than a threshold on the absolute photon count numbers. The CI is normalized to the data values because mono-exponential lifetimes differ up to 50 % between tension sensor and no-force control and comparing absolute values would therefore mean to apply different thresholds on different samples. In addition to these main data exclusion methods, the R^2 value can be used to exclude data in combination with the old fit method to preserve comparability with the precursor software (Sec. 4.1).

4.6.4 Calculate Statistics

With FLAMES, data can be pairwise statistically compared. The t-test, implemented with `ttest()`, requires normality of the data. Therefore, normality is checked for each data set with more than ten values with the Lilliefors test using `lillietest()` and the Kolmogorov-Smirnov (KS)-test using `kstest()`. Both test results are saved in a meta-information file so that the user can decide, whether the student's t-test is applicable and

then run the merge again with the correct statistical test. If the data are not normally-distributed, usually the KS-test using `kstest2()` is applicable. The KS-test requires that the compared data sets follow the same distribution. For bounded systems, e.g. if the ratio is determined (Sec. 4.8), this prerequisite is not necessarily fulfilled. For these cases, the Wilcoxon-Mann-Whitney-U (WMW) test is implemented using `ranksum()`. This test calculates statistics based on a ranked order of the data values and therefore does not require the same shape of compared distributions. Note that the significance level is $\alpha = 0.05$ for all statistical tests.

For more advanced statistical analysis, the saved data values can be imported into specialized software like R. A unique image number can be additionally saved to also take the image-dependency into account during statistical tests.

4.6.5 Generate Plots and Save Data

When performing a merge, the user can decide to generate a range of plots, which are all based on the information in the merge structure. The user sets logicals to enable plots to be generated, statistics to be calculated, and data and plots to be saved.

Plot Data

The main plot type are boxplots using `boxplot(data, symbol, '')`, without marking outliers because all data points are additionally plotted with a jitter in x using `plot()` (Fig. 4.12a). The box of the boxplot is the interquartile range (IQR), i.e. the 25^{th} and 75^{th} percentile, the line marks the median, and whiskers reach to the last data point within $1.5\times$ the IQR, which corresponds to $\pm 2.7\sigma$ for normally distributed data. Data can be displayed as merged according to the merge name or as individual experiments. The individual experiments can be sorted according to their measurement date or merge name (Fig. 4.12b, c). Lifetime plots can include the donor-only lifetimes used for the respective merge. Furthermore, the user can specify settings for the plot appearance, like plot limits, the amount of jitter, and whether grid lines should be displayed.

Simple, pairwise statistical comparisons using t-test, KS-test or WMW-test can be performed automatically in FLAMES (Sec. 4.6.4). All pairwise significance comparisons are made and saved but for the ease of visualization, individual comparisons can also be selected in a GUI based on `listdlg()`. Stars are then displayed in the figure using `sigstar()`[4].

[4]Rob Campbell, 2013; `https://www.github.com/raacampbell/sigstar`

In addition to boxplots, the main data values, i.e. lifetimes, FRET efficiencies or ratios, can also be visualized as histograms. These histograms are plotted and saved individually for each data set that would also be one boxplot. Next to the described data visualizations also the numbers of total photon count and area-normalized photon count can be used to generate boxplots for individual and merged data (Fig. 4.12d), which can be statistically compared as well. The photon counts can be shown together with the respective main data, i.e. lifetimes, FRET efficiencies or ratios. For this purpose, scatter plots with main data versus total or area-normalized photon count can be generated. From this scattered data the Pearson's correlation coefficient is calculated using `corrcoef()` and directly written with 95 % CI and the *p*-value on the scatter plot to visualize and statistically detect correlations between main data and photon counts. In addition to individual scatter plots, also a merged plot is generated, where the individual data are color-coded (Fig. 4.12e).

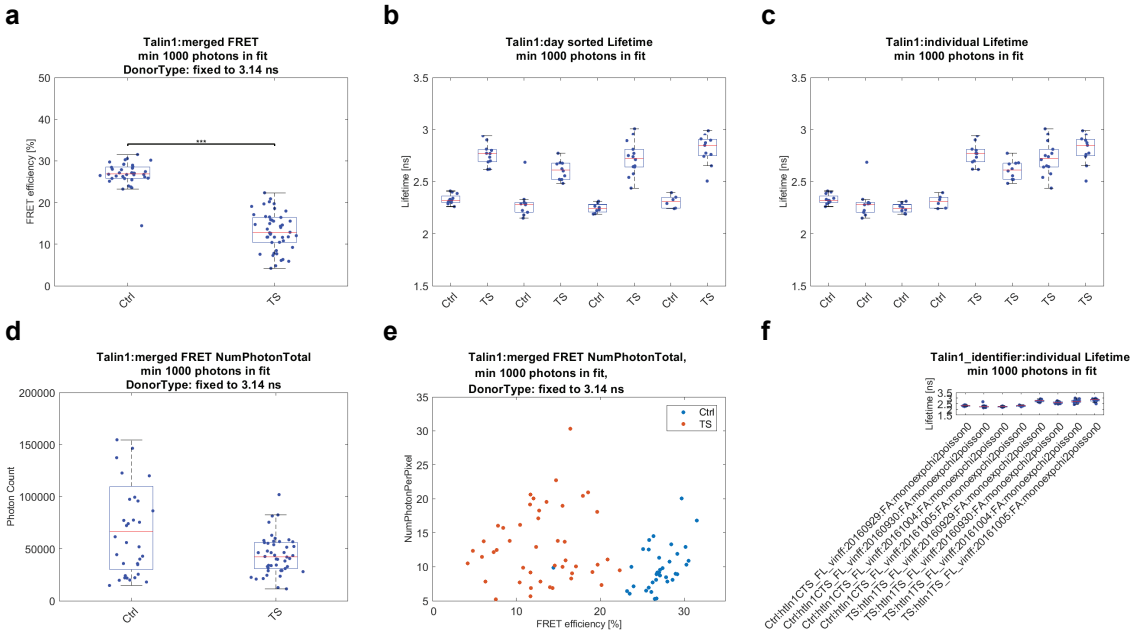

Figure 4.12: With fluorescence lifetime analysis and merge software (FLAMES) plots can be saved automatically. (**a**) The FRET efficiencies can be compared, e.g. by a Kolmogorov-Smirnov (KS)-test. (**b, c**) Individual experiments can be displayed according to their experimental day (**b**) or their merge name (**c**). (**d, e**) The overall photon count (**d**) and the area-normalized photon count (**e**) can be displayed as boxplots (**d**) or in a scatter plot in comparison to the main data value, e.g. FRET efficiencies (**e**). (**f**) To verify that the appropriate data sets are included, plots of individual data can also be labeled with the information used to identify the data set. The applied data inclusion criteria and the method to calculate the donor-only lifetime are included in all figure titles. The examples are unmodified plots as PNG but all plots can also be saved as EPSC for the modification with e.g. Adobe Illustrator. The raw data are the no-force control (Ctrl) and first tension sensor (TS) in vinculin wild type cells in Fig. 4.6.

As an additional feature, identifier labels can be used to label individual experiments (Fig. 4.12f). These identifiers are composed of the information required to load the data and facilitate to verify that the intended data are included in the merge. Finally, the time dependence of the data can be analyzed by plotting the values in dependence of their acquisition time. The acquisition time of the first image within one folder is thereby set to zero and the time in minutes after the first acquisition is calculated for subsequent images. Note that default settings for all plots exist, which are then replaced by project-specific preferences and for each merge the desired plots are enabled.

Save Data

Data values, i.e. lifetimes, FRET efficiencies, ratios, total photon numbers, area-normalized photon numbers, and χ^2 values, can be saved as MAT and text (TXT) files for all generated plots. The TXT files are thereby optimized for the import in ORIGIN or EXCEL and can be used to further analyze or plot data. Next to the data values, also the plots themselves can be saved in different file formats chosen by the user. Typical file formats for saving plots are MATLAB figure (FIG) for reimport in MATLAB, EPSC for modifications with ADOBE ILLUSTRATOR, and PNG for a quick view. Plots have automatically-generated names and titles that contain information used for the assembly to reduce the ambiguity about the plot generated, e.g. the averaging of the donor-only lifetime and the data inclusion criteria applied.

Importantly, meta-information is also saved for all plots as an EXCEL sheet. Note that TXT files are saved on UNIX systems because the servers used in the Grashoff group to analyze data do not support saving of EXCEL files from MATLAB. The meta-information files contain information about the data in each boxplot regarding values and spread, the goodness-of-fit, normality, and experimental numbers. Data values and spread are characterized by median, mean, standard deviation, 2.5 % and 97.5 % CI, and the IQR. For the goodness-of-fit, Pearson's χ^2 is given with median, mean, standard deviation, and IQR. In addition, the median of Neyman's χ^2 and MLH χ^2 are provided. Logicals inform whether the normal distribution is rejected based on Lilliefors and KS-test. For individual experiments, only the number of data points in the plot is given. For merged experiments, in addition to the number of data points also the numbers of manual masks, images, and experiments are provided.

4.7 Spatially-resolve Images

In the main analysis pipeline for FLIM images, the signal of interest is extracted and all specific signal within one manual mask is pooled and jointly analyzed to increase the photon counts. However, to investigate the spatial distribution of tension, also individual substructures can be analyzed. In FLAMES two methods are implemented to identify individual substructures. In the first approach, substructures are defined as the near neighborhood of local maxima, which is suited for punctate structures. Alternatively, substructures can be identified as connected areas, which is suited for well-separated structures. In both strategies, the input is restricted to the extracted signal.

The assignment of pixels to the nearest local maximum contained in FLAMES is developed with Andrew J. Price, PhD, in the group of Prof. Alexander R. Dunn (Stanford University) based on an assignment algorithm already used for FLIM and ratiometric FRET data of DSMs. The signal can be blurred with a Gaussian filter using `imgaussfilt(image, σ)`, e.g. with $\sigma = 3$ for individual DSMs. Next, local intensity maxima are identified with `imregionalmax()`. To assign non-zero pixels to the nearest local maximum, the shortest distance is then determined with `dsearchn()`. The pixel lists of the individual substructures are then saved in one sparse matrix, which contains the linear index of the pixels in one dimension and the number of substructures in the other dimension. With this sparse mask matrix, the photon count traces in each mask are identified by a matrix multiplication with the sparse data matrix containing all spatial and temporal information. During fitting, only the main information, i.e. lifetime, ratio, and photon numbers but no CIs are determined to reduce calculation time. The resulting small masks and fit values are saved in a new *maskInfo* file, which can then be used for merging. Note that during merging, also the median of all substructures from one image can be calculated.

Alternatively to the intensity also the connectivity of the binary mask can be used to identify substructures. Individual FAs inside a manual mask (Fig. 4.13a), for example, are typically well-separated and therefore connected components are identified in the mask using `bwconncomp(mask, 4)`. This algorithm identifies pixels as connected if they share an edge, i.e. the pixels are left, right, above or below each other (Fig. 4.13b). From these connected components and the intensity image, the properties of the substructures are extracted using `regionprops()`. These properties include a list of pixels but also contain additional information, e.g. about eccentricity, intensity, and orientation.

The masks for the individual substructures are transferred in a sparse mask matrix and the corresponding photon count is fitted as described above for the assignment to the nearest local maximum. In the example data set, the FRET efficiency of the spatially-resolved structures, i.e. individual FAs, are comparable to the globally-fitted FRET efficiencies (Fig. 4.13c). However, the variance increases largely, which is caused by

the reduced photon count per fit (Fig. 4.8). Consequently, the spread reduces if a minimal photon count is required during the merge (Fig. 4.13c).

The additional information about the properties of individual substructures can be harnessed to address more specific research questions. In FLAMES, for example, splitting in inner and outer substructures is implemented. To this end, the user draws an elliptic manual mask using `imellipse` and `createMask()` around the nucleus or the center of the cell. The centroid is identified using `regionprops(mask, 'Centroid')` and the pixel closest to the centroid is set as a reference point (Fig. 4.13d) with the coordinates x_0 and y_0. For each pixel j in the substructure with the coordinates x_j and y_j, the distance d_j to the reference point is calculated. Pixels with a smaller distance to the reference point are

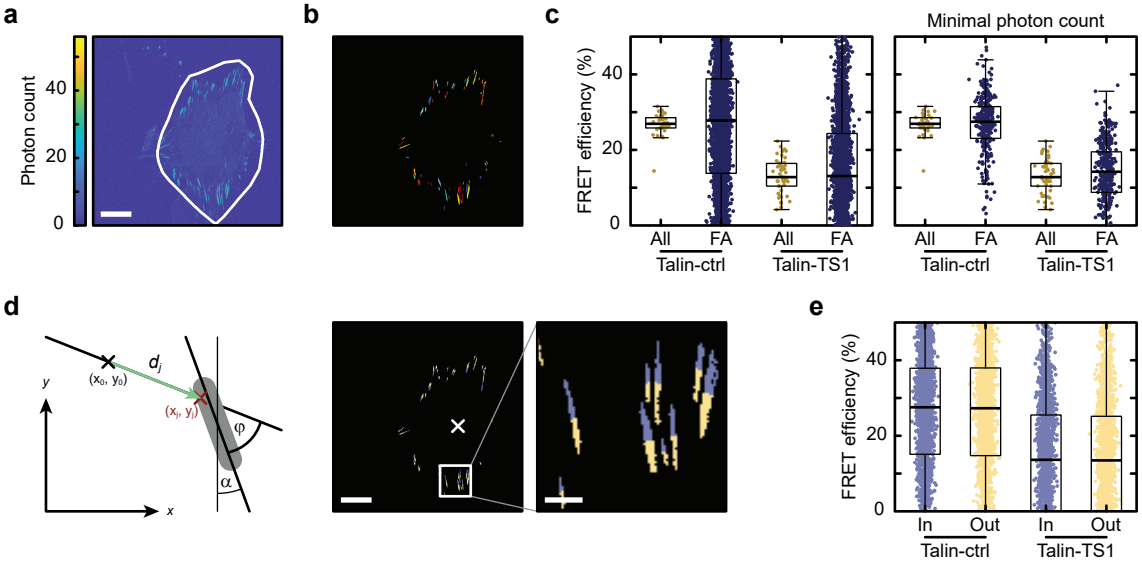

Figure 4.13: Substructures can be analyzed with respect to geometric properties. (**a**) The focal adhesion (FA) signal is extracted inside a manually-drawn mask by a multi-Otsu thresholding selecting the brightest of three intensity classes. (**b**) Individual FAs are identified as connected region of at least 9 pixels area. (**c**) The median FRET efficiency remains unaffected if individual FAs instead of the total extracted signal are fitted. The spread, however, increases considerably, which is caused by the reduced photon count number per fit. Consequently, the spread reduces, if FAs with less than 1,000 photons are excluded from the analysis. (**d**) To determine the projected distance of individual pixels j within a FA (grey shading), the distance to the reference point (x_0, y_0) is determined as well as the relative orientation φ between the distance vector and the major orientation axis of the FA, which is characterized by the angle α relative to the image axis. FAs with at least 18 pixels are then divided based on their orientation towards the manually-determined reference point (white cross) into inner (blue) and outer (yellow) parts. (**e**) The FRET efficiencies are indistinguishable for inner and outer FAs in the example data set. Scale bars: 20 µm and 4 µm. The raw data are the same as for the no-force control and the first talin tension sensor in vinculin wt cells in Fig. 4.6.

therefore closer to the center of the cell, which can be used to identify inner and outer regions. To split the substructure along its major axis, the distance of each pixel to the reference point is then scaled with the orientation angle φ between the major axis and the direction to the reference point

$$d_{\text{projected},j} = |d_j \cos\varphi| = \left| \left[\begin{pmatrix} x_j \\ y_j \end{pmatrix} - \begin{pmatrix} x_0 \\ y_0 \end{pmatrix} \right] \cdot \begin{pmatrix} \sin\alpha \\ -\cos\alpha \end{pmatrix} \right|, \tag{4.34}$$

where α is the orientation angle of the major axis of the substructure relative to the image axis. The pixels are then sorted according to their projected distance $d_{\text{projected},j}$, and split in a fixed number of parts, i.e. two parts to analyze inner and outer FAs. For the example data set, inner and outer FAs, however, do not show any FRET efficiency differences (Fig. 4.13e).

4.8 Determine the Molecular Stretch Ratio

The main method to analyze tension sensor experiments is to determine one lifetime per construct, calculate a FRET efficiency, and compare different constructs based on this average value. However, this average FRET efficiency does not contain information about the molecular distribution of forces (Sec. 2.3.3). In the two extreme cases, either all molecules experience the same average force or some molecules experience a sufficient force to fully open the tension-sensitive linker peptide while others remain closed (Fig. 2.9). If the latter situation is assumed, the relative amount of open tension sensors, i.e. the molecular stretch ratio, can be determined.

4.8.1 Determine the Fit Equation

A bi-exponential fit assumes that two lifetimes are mixed (Sec. 4.5.5). In a tension sensor experiment, the two lifetimes correspond to the the donor fluorophore with and without quenching by FRET. The ratio determination implemented in FLAMES uses the simplification to two lifetimes to determine the ratio of stretched molecules (Eq. 4.28) by

$$P(t) = N \left(\frac{r_\mathrm{N}}{\tau_1} e^{-t/\tau_1} + \frac{(1 - r_\mathrm{N})}{\tau_2} e^{-t/\tau_2} \right) + P_\mathrm{b}.$$

In this formulation, the fit parameters are the total photon count N, the two lifetimes τ_1 and τ_2, the relative contribution of the first lifetime to the photon count r_N, and the background photon count rate P_b.

The molecular ratio r_M, i.e. the relative amount of molecules that contribute with the first lifetime to the signal, is not identical to the relative amount of photons r_N related to the

first lifetime. The difference of these ratios stems from the loss in quantum efficiency caused by FRET, i.e. a donor undergoing FRET emits less photons. The number of molecules M can be assumed to be anti-proportional to the lifetime [277] according to

$$M \propto \frac{N}{\tau}, \tag{4.35}$$

where M is the number of molecules, N the photon count, and τ the lifetime. The molecular ratio can therefore be calculated from the photon number ratio with

$$\begin{aligned} r_\mathrm{M} &= \frac{M_1}{M_1 + M_2} \\ &= \frac{r_\mathrm{N}\frac{N}{\tau_1}}{r_\mathrm{N}\frac{N}{\tau_1} + (1 - r_\mathrm{N})\frac{N}{\tau_2}} \\ &= \frac{r_\mathrm{N}\tau_2}{r_\mathrm{N}\tau_2 + \tau_1 - r_\mathrm{N}\tau_1}. \end{aligned} \tag{4.36}$$

Note that analogue to the photon count ratio r_N also the ratio of the amplitudes could be determined with

$$P(t) = A\left(r_\mathrm{A} e^{-t/\tau_1} + (1 - r_\mathrm{A})\, e^{-t/\tau_2}\right) + P_\mathrm{b}. \tag{4.37}$$

The molecular ratio determination then simplifies to

$$\begin{aligned} r_\mathrm{M} &= \frac{M_1}{M_1 + M_2} \\ &= \frac{\frac{r_\mathrm{A} A \tau_1}{\tau_1}}{\frac{r_\mathrm{A} A \tau_1}{\tau_1} + \frac{(1-r_\mathrm{A}) A \tau_2}{\tau_2}} \\ &= r_\mathrm{A}. \end{aligned} \tag{4.38}$$

In FLAMES, the photon count ratio r_N is fitted using the optimization equation Eq. 4.29 and the molecular ratio r_M is then calculated using Eq. 4.36.

4.8.2 Limit the Fit Parameters

Bi-exponential fits with a fit length of only three-times the longer lifetime require large photon counts for reliable point estimates (Fig. 4.8c) and therefore bi-exponential fits are not used to determine lifetimes (Sec. 4.5). Similarly, the ratio determination on simulated data has a large spread for bi-exponential fits if both lifetimes contribute to the observed decay, while they are able to detect if the underlying decay is mono-exponential (blue histograms in Fig. 4.14). In a tension sensor experiment, however, information about the expected lifetimes exists. The ratio determination is based on the assumption that the

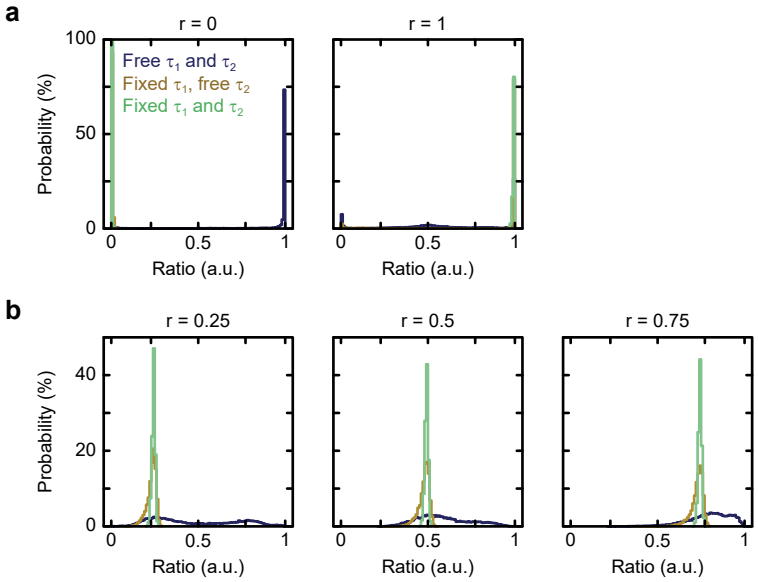

Figure 4.14: Reliable ratio determination requires fixed parameters. (**a**) Bi-exponential fits with five free parameters can identify that only one lifetime contributes to the data, i.e. $r_N = 0$ and $r_N = 1$. (**b**) For mixed ratios, however, reducing the free parameters (blue line) by using fixed lifetimes (yellow and green lines) greatly improves the ability to identify the underlying ratio. The data are simulated with Eq. 4.16. The simulation parameters are $\mathcal{N}_{\text{total}} = 50,000$ photons, $\tau_1 = 40$ time bins (3.2 ns), $\tau_2 = 18$ time bins (1.44 ns), $r = 0{-}1$, $b = 0$, and $L = 120$ time bins. Each histogram shows the ratio determined from 10,000 simulated decay curves by bi-exponential tail fits with five free parameters (blue), fixed long lifetime τ_1 (yellow), or additionally fixed short lifetime τ_2 (green) using FLAMES.

photon count histogram can be explained by two lifetimes, because the tension sensor is either stretched or closed. In the stretched tension sensor, the acceptor fluorophore is far apart from the donor fluorophore and no FRET occurs. The lifetime can therefore be measured in a donor-only control. The situation of a closed sensor is reflected in the no-force control (Fig. 4.15a). If these information are used and both lifetimes are fixed, only three parameters of the bi-exponential fit function (Eq. 4.29) are actually fitted, which are the total photon count $\mathcal{N}_{\text{total}}$, the photon number ratio from the stretched molecules r_{N}, and the background photon count rate P_{b}. This reduction in fit parameters, greatly improves the ability to determine the relative amount of the long lifetime (green histograms in Fig. 4.14).

The resulting photon count ratio (Fig. 4.15b) is then rescaled using Eq. 4.36 to get the relative amount of stretched molecules (Fig. 4.15c). From the example data set, one could learn e.g. that talin-1 experiences a tension gradient [216].

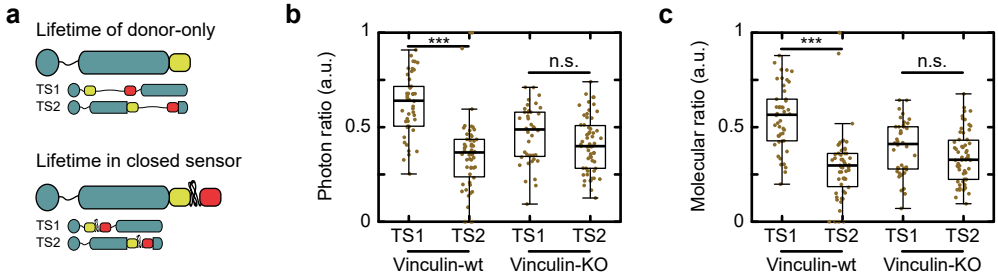

Figure 4.15: The stretch ratio describes how many molecules are mechanically engaged. (**a**) The FL-based TSM opens switch-like and has a long contour length increase. Thus, the donor in the stretched state has the non-quenched lifetime, while the donor in the non-stretched state undergoes FRET and intermediate states are negligible. The lifetime of the non-quenched donor is determined with a mono-exponential tail fit from talin-1 tagged only with YPet. The lifetime of the donor with FRET is determined with a mono-exponential tail fit from C-terminal tagged talin-1 data, where the TSM cannot sense tension. (**b**) The stretch ratio of the talin-1 tension sensors is determined by a bi-exponential fit using the lifetimes of the stretched and non-stretched states. The bi-exponential fit yields the relative photon counts of the two lifetimes with one and zero meaning that all photons come from stretched and closed molecules, respectively. (**c**) As FRET reduces the photon count, the photon count ratio r_N is rescaled to a molecular ratio r_M to determine the relative amount of stretched talin molecules, i.e. one means that all molecules are stretched while zero means that all molecules remain closed. The molecular stretch ratio shows, for example, that talin-1 experiences a tension gradient with more molecules loaded at the first integration site between head and rod domains than at the second integration site in the rod domain. WMW-test: *** $p < 0.001$, n.s. (not significant) $p > 0.05$. The raw data are the same as in Fig. 4.6.

4.8.3 Fit the Lifetime of the Donor Undergoing FRET

The ratio fit with the measured lifetimes for donor-only and no-force control assumes that these two lifetimes reflect the lifetimes also present in the tension sensor sample. This assumption is challenged by the observation that only about 40 % of mCherry is fluorescently-active in *in vitro* experiments [278]. If this incomplete acceptor chromophore maturation is taken into account, already in the no-force control only some donor fluorophores undergo FRET (Fig. 4.16a). Therefore, the experimentally-determined lifetime of the no-force control is an average of the donor lifetimes quenched and non-quenched by FRET and also the tension sensor has both populations, i.e. mCherry that can serve as an acceptor and the non-fluorescent version of mCherry (Fig. 4.16b).

To determine the quenched lifetime, a bi-exponential fit with four free parameters can be used, in which only the donor-only lifetime is fixed. The bi-exponential fit of the experimental data, however, results in lifetime values of several thousand nanoseconds, which clearly do not reflect the lifetime of the quenched donor that has to be shorter than the non-quenched lifetime (Fig. 4.17a). Therefore, the bi-exponential fit with four free

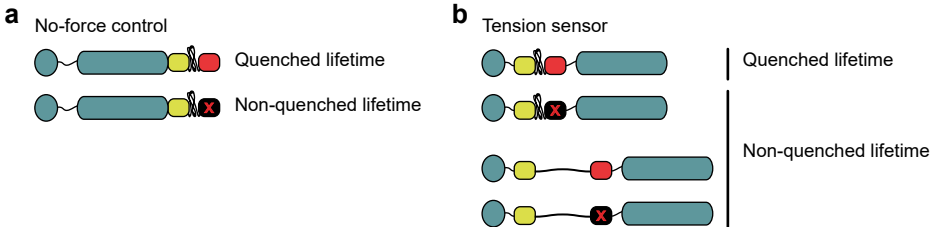

Figure 4.16: Two donor populations exist already without tension because of the incomplete acceptor chromophore maturation. (**a**) In the no-force control, some donor molecules undergo FRET while others emit with the non-quenched lifetime because the acceptor fluorophore is non-fluorescent. (**b**) Tension increases the population of non-quenched donor molecules because linker elongation prevents FRET. Tension sensors under force therefore always contribute with the non-quenched donor lifetime irrespective of the acceptor fluorophore state.

parameters requires a restriction to estimate the quenched donor lifetime. In principle, the fit can be constraint by limiting the fit ranges of individual parameters, which are by default unlimited in FLAMES. Limiting the fit range of the lifetime, however, requires prior knowledge that is typically not available for experimental data. One other straight forward restriction is that the ratio r_N should be limited between zero, i.e. all donor molecules are quenched, and one, i.e. all donor molecules emit with the non-quenched lifetime. Instead of using fixed fit boundaries, however, this constraint can also be implemented by reformulating the ratio r_N with a sine of ρ, which is inherently limited between minus and plus one [276]. Thus, the ratio is replaced in Eq. 4.28 by

$$r_\mathrm{N} = \frac{1 + \sin\rho}{2}, \tag{4.39}$$

which leads to the new fit equation for bi-exponential fitting with a bounded ratio of

$$P(t) = N\left(\frac{1+\sin\rho}{2\,\tau_1}\,e^{-t/\tau_1} + \frac{1-\sin\rho}{2\,\tau_2}\,e^{-t/\tau_2}\right) + P_\mathrm{b}. \tag{4.40}$$

From the estimated ρ, the ratio r_N can then be calculated using Eq. 4.39. Note that if the point estimates reach the boundaries, no CIs can be calculated [276]. The CI is used to determine the relative error, which then is the basis to exclude fit results with large uncertainties during merging (Sec. 4.6.3). Therefore, the fit equation with bounded ratio (Eq. 4.40) is only used when the additional restriction is required, i.e. if photon counts are relatively low. For higher photon counts, e.g. approximately 150,000 photons in *Drosophila* muscle attachment sites, already the unconstrained bi-exponential fit with four free parameters identifies the quenched donor lifetime [230].

Fitting the experimental data set with a bi-exponential fit with bounded ratio leads to values for the quenched donor lifetime that are in the expected range shorter than the non-quenched donor lifetime (Fig. 4.17b). Interestingly, the variance in lifetime

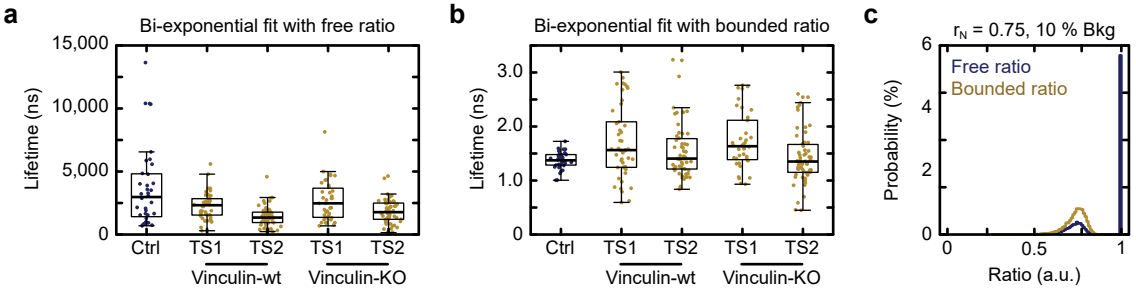

Figure 4.17: The lifetime of the donor undergoing FRET is determined with bi-exponential fitting using a bounded ratio. (**a**) Fitting the experimental data with a bi-exponential fit with four free parameters leads to very high lifetime values. (**b**) If the fit is rewritten such that the ratio is bounded between zero and one, a lifetime shorter than the non-quenched donor-only lifetime is found. Note that the bounded ratio does not limit the lifetime itself. (**c**) Also in simulated data, the ratio determination is impaired if some background photons are added but greatly improves if the ratio is bound between zero and one. The experimental raw data (**a, b**) is the same as in Fig. 4.6. The data are simulated (**c**) with Eq. 4.16. The simulation parameters are $\mathcal{N}_{\text{total}} = 50,000$ photons, $\tau_1 = 40$ time bins (3.2 ns), $\tau_2 = 18$ time bins (1.44 ns), $r_N = 0.75$, $b = 0.1$, and $L = 120$ time bins. The histograms show bi-exponential fits of 10,000 simulated decay curves with fixed τ_1 and free ratio (blue, Eq. 4.29) or bounded ratio (yellow, Eq. 4.40) using FLAMES.

determination is smaller for the no-force control than for the tension sensors, which is likely reflecting the higher variability in these samples caused by force. The resulting average lifetimes for all constructs, however, are similar. Note that in line with the observations on experimental data, also the addition of 10 % background to the simulated data impairs the ability of the bi-exponential fit to estimate the underlying ratio (Fig. 4.14 and Fig. 4.17c). Similar to the experimental result, also fits on the simulated data improve if the ratio is bounded by the sine implementation (Fig. 4.17c). Importantly, this bounds are specific for the ratio and do not limit the fit value range of the lifetimes.

4.8.4 Determine the Ratio with the Fitted Lifetime

The molecular ratio of donor molecules not quenched by FRET is determined by a bi-exponential fit with two fixed lifetimes. For the example data set, the lifetime of the non-quenched donor is determined by a mono-exponential fit of the donor-only sample and the quenched lifetime is determined by a bi-exponential fit with four free parameters (Sec. 4.8.3). The molecular ratio of the no-force control results in 58 % fluorophores without FRET, which means that only 42 % of the acceptor is fluorescently active (Fig. 4.18a). This values is in perfect agreement with the *in vitro* measurements of mCherry with fluorescence correlation spectroscopy (FCS) resulting in 43 ± 1 % flickering [278]. This *in vitro* measurement thereby provides an independent complementary measurement that confirms the results from the bi-exponential fit.

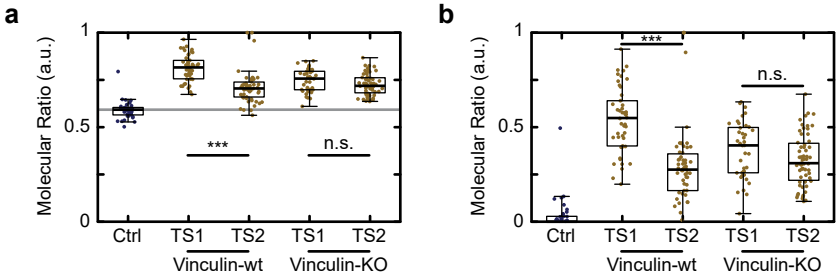

Figure 4.18: The incomplete acceptor chromophore maturation does not hinder ratio determination. (**a**) The molecular ratio of the no-force control (blue) describes the relative amount of the donor molecules that remains non-quenched even in the closed sensor because the acceptor chromophore is not fully matured. The median of the no-force control (grey line) can then be used to rescale the tension sensor (yellow) data. (**b**) The rescaled molecular ratio describes the relative amount of molecules that are exposed to sufficient tension to elongate the linker peptide with one indicating that all molecules are stretched. KS-test: *** $p < 0.001$, n.s. (not significant) $p > 0.05$. The raw data are the same as in Fig. 4.6.

In the biological context, however, the ratio of donor fluorophores undergoing FRET is only of minor interest. Instead, the relative amount of molecules that are stretched should be determined. With the assumption that the relative amount of fluorescently-active mCherry is the same in no-force control and tension sensor samples, the ratio can be rescaled (Fig. 4.18b). Therefore, the no-force control median is set as new zero and all data are scaled accordingly using

$$r_{\mathrm{M,\ rescaled}} = \frac{r_{\mathrm{M}} - \overline{r_{\mathrm{M}}}(\mathrm{Ctrl})}{1 - \overline{r_{\mathrm{M}}}(\mathrm{Ctrl})} \tag{4.41}$$

with r_{M} the molecular ratios and $\overline{r_{\mathrm{M}}}(\mathrm{Ctrl})$ the average molecular ratio of the no-force control. This average no-force control value can be determined analogue to the average donor-only control used for the FRET calculation (Sec. 4.6.2). In brief, either a fixed ratio is used or the mean or median is calculated of the individual corresponding no-force control values, of all no-force control values within one merge or of no-force control values manually-provided in a no-force control list.

This rescaled molecular ratio determined with a bi-exponentially fitted quenched donor lifetime takes the incomplete acceptor chromophore maturation into account (Fig. 4.18b). In contrast, the molecular ratio determined with a mono-exponentially fitted quenched donor lifetime uses an average lifetime were both donor populations contribute, i.e. donor molecules with and without fluorescently-active acceptors (Fig. 4.15c). Despite this fundamentally different approaches to determine the quenched donor lifetime, the resulting molecular stretch ratios are highly comparable. In the example data set, for instance, the bi-exponentially determined lifetime is 1.37 ± 0.16 ns (mean with standard deviation) and the mono-exponentially determined average lifetime is 2.30 ± 0.09 ns, but

the resulting (rescaled) molecular ratios differ only by approximately one percent. This observation that both ratio determination methods lead to comparable results underlines the robustness of these methods. In addition, this observation also confirms that mono-exponentially determined average lifetimes reflect the underlying data, which lends further support to the mono-exponential fit to determine lifetimes for the here presented FRET efficiency calculations.

In summary, the major assumption in ratio determination by bi-exponential fitting is that the tension sensor is either stretched or closed and all intermediate conformations can be neglected. The molecular ratio then reports on the relative amount of stretched molecules, i.e. molecules that experience sufficient tension to unfold the force-sensitive linker. The ratio determination thereby constitutes an alternative pathway compared to the determination of FRET efficiencies for the analysis of tension sensor experiments.

5 Desmoplakin Experiences Tension Upon External Stress

5.1 Desmoplakin Tension Sensor

DP is chosen as the target protein to measure molecular forces in DSMs because it establishes the major connection to the keratin IF, is an essential component of all DSMs, and has only two major splice isoforms (Sec. 1).

5.1.1 Tension Sensor Design

Integration Site

To determine the integration site of the TSM within DP, two major constraints were taken into account. First, the TSM should be placed between the N-terminal binding to the desmosomal plaque proteins and the C-terminal binding to the keratin IF. Second, the TSM integration should not interfere with protein functionality. Two different integration sites were tested to increase the likelihood of a functional tension sensor. A short N-terminal fragment of the first 584 aa localizes to DSMs, which demonstrates that the essential desmosomal binding capacities are contained within this sequence [90]. Therefore, integration after E584 in DP head domain was tested (Fig. 5.1a). The other integration site was chosen because of the tripartite structure of DP with globular N-terminal head, elongated coiled-coil rod and C-terminal keratin binding domains (1.7.1). As no crystal structure of the entire DP exists, the integration site is based on structural predictions, which indicate a 14 aa flexible region between coiled-coil rod and the first IF-binding domain [104]. The TSM is integrated in the middle of this stretch after E1952 for DPI and E1353 for DPII (Fig. 5.1a).

All tension sensor constructs localized in initial experiments in DP-deficient keratinocytes to cell–cell contacts after addition of Ca^{2+}, which induces DSM formation (data shown for selected constructs, Sec. 5.1.3). However, constructs harboring the TSM after E584 localize less efficient to cell–cell contacts. Furthermore, this integration site lies within

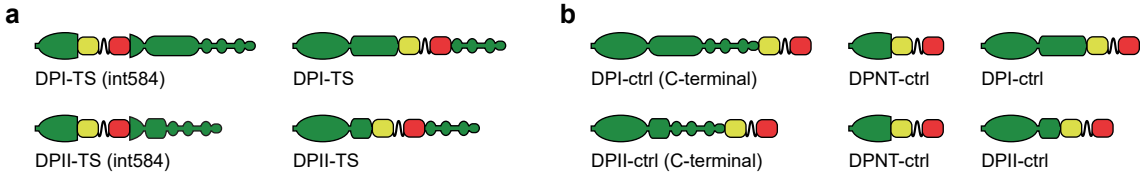

Figure 5.1: Different desmoplakin (DP) tension sensor and control constructs were tested. (**a**) The TSM is integrated in DPI and DPII either after E584 or in between central coiled-coil rod and C-terminus after E1952 and E1353 in DPI and DPII, respectively. (**b**) The no-force control either preserves protein integrity by terminal tagging or TSM environment by DP truncation. For a full list of all cloned constructs see Tab. 3.16 and Tab. 3.17. Note that for testing the DPNT construct, the HP35-based TSM was used.

the central SH3 domain of DP head [103] and potentially disturbs protein functionality. Therefore, only data for the second integration site is shown in this work.

Tension sensor constructs of both major splice isoforms, DPI and DPII, localized to cell–cell contacts in initial experiments. Because DPII seems more relevant for cell–cell adhesion in cultured human keratinocytes [119] and construct generation and cell transfection of the shorter isoform are more efficient, this work focuses on DPII data.

No-force Control

A matched no-force control is crucial to identify force-specific effects (Sec. 2.3). As FRET is highly sensitive to changes in the local environment or overall changes of the cells' state, e.g. pH-value, the no-force control reports these non-tension related changes. To place the TSM such that it does not experience any forces and resembles the situation in the tension sensor, C-terminal tagging of DP and truncated DP versions are compared. While C-terminal tagging preserves the protein integrity, a truncated protein preserves the TSM integration site (Fig. 5.1b). Initial FRET measurements revealed lower starting FRET efficiencies of the C-terminal no-force control as compared to the internal tension sensor (Fig. 5.2). In principle, the no-force control still could have been used as the essential function is to report on relative changes to FRET rather than absolute values. However, the truncated no-force control shows FRET efficiencies more comparable to the internal tension sensor and also localizes to cell–cell contacts (Sec. 5.1.3) and is therefore used in this work.

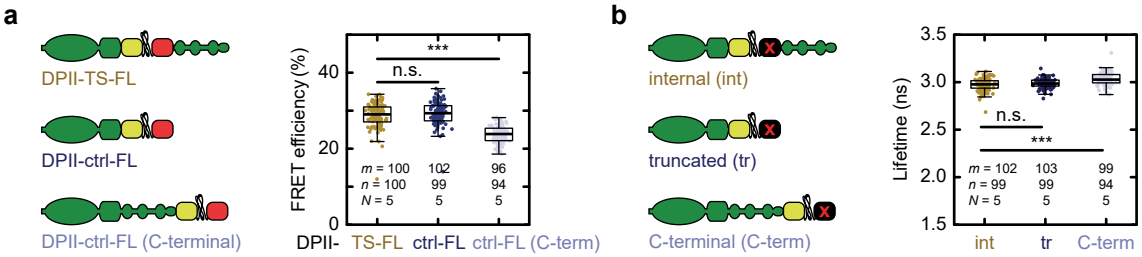

Figure 5.2: A truncated desmoplakin (DP)II construct is used as no-force control. (**a**) C-terminal tagging preserves the protein functionality, while truncation preserves the TSM integration site. The FRET efficiencies of tension sensor (yellow) and truncated no-force control (blue) are comparable but the C-terminal no-force control (light blue) shows considerably lower FRET. (**b**) The FRET efficiencies are calculated using donor-only lifetimes from the matched constructs harboring a Y72L mutation in mCherry resulting in $\overline{\tau_D} = 2.98\,\text{ns}$ for the tension sensor and $\overline{\tau_D} = 2.99\,\text{ns}$ and $\overline{\tau_D} = 3.03\,\text{ns}$ for truncated and C-terminal no-force control, respectively. FL-based constructs were measured in MEK-wt one day after induction of DSM formation. The numbers of masks m, images n, and experiments N are indicated in the figure. Two-sided KS-test: *** $p < 0.001$, n.s. (not significant) $p \geq 0.05$. The tension sensor and truncated control data are published [11].

Tension-sensitive Linker Peptide

The TSM defines the force sensitivity of the tension sensor (Sec. 2.3). At the time of initial construct design, the FRET pair in the TSM had already been optimized to YPet and mCherry (Sec. 2.4). Three calibrated tension-sensitive linker peptides with different force sensitivities were available, i.e. F40 sensitive to $1-6\,\text{pN}$, HP35 to $6-8\,\text{pN}$, and HP35st to $9-11\,\text{pN}$ [185, 217] (Fig. 2.7). The starting FRET efficiency of the HP35-based TSMs is with almost 30 % higher than that of F40-based TSM with approximately 25 %, so that less molecules under sufficient forces are required for a significant decrease in FRET efficiency. On the other hand, the force range across DSMs (and whether there are forces at all) was entirely unknown and the F40 linker peptide responds to the lowest forces. Therefore, most experiments were performed using the F40-based TSM. During the time of this project, the FL-based TSM was developed and calibrated, which shows a very high sensitivity to forces around 4 pN and a starting FRET efficiency of approximately 30 % [216] (Fig. 2.7). Furthermore, a tension-insensitive linker peptide became available that might serve as additional no-force control (Sec. 5.4.2). The stable seven aa linker (F7) peptide is not calibrated but insensitive to forces experienced by talin[1].

In summary, the desmoplakin tension sensor mainly used in this work is DPII with F40-based TSM integrated after E1353 prior to the IF-binding sites and the corresponding truncated no-force control.

[1]Personal communication by Lisa Fischer, Grashoff group

5.1.2 Model System

DSMs are prevalent in epithelial cells, heart and skin tissues (Sec. 1). Here, immortalized murine basal keratinocytes are used as the model system. These cells divide and proliferate because terminal differentiation is suppressed in the absence of Calcium. Prof. Kathleen J. Green (North Western University, Chicago) generously provided not only MEK-wt floxed for DP but also MEK-KO. These MEK-KO are valuable, for example, to evaluate protein functionality after TSM integration without endogenous protein (Sec. 5.1.3).

Both major DP isoforms are expressed to approximately the same level in MEK-wt (Fig. 5.3a). Depletion of DP in MEK-KO does not affect the expression of the armadillo family proteins Pkp1 and Pkp2 but the expression level of Dsg1 and 2 are reduced. This observation is in line with the reported skin-specific DP knockout [69]. Furthermore, the keratin IF and the AJ component E-cadherin are expressed to normal levels (Fig. 5.3a). In MEK-wt, the cytoskeletons of two neighboring cells seem interconnected one day after induction of DSM formation by addition of Ca^{2+} (Fig. 5.3b). In MEK-KO, however, the separation between the cytoskeletons of neighboring cells remains.

5.1.3 Protein Functionality After Tension Sensor Module Integration

To evaluate protein functionality after TSM integration, MEK-KO are rescued with C-terminal-tagged wild type DP (DPII-wt), tension sensor (DPII-TS), and truncated no-force control (DPII-ctrl) constructs. All constructs localize to cell–cell contacts one day after induction of DSM formation and co-localize with the desmosomal markers Dsg1 and 2, Pg, and Pkp1 (Fig. 5.4). In addition, the keratin cytoskeletons of neighboring cells seem interconnected in cells rescued with either wt or tension sensor constructs. Cells rescued with the truncated no-force control, however, preserve a visible separation between the keratin networks of neighboring cells. Of note, the truncated construct lacks the IF-binding repeats and therefore is not expected to rescue the keratin-binding defect but only the assembly of DSMs [107, 108, 279].

To confirm the ability of DP constructs to rescue the formation of *bona fide* DSMs in MEK-KO, ultrastructural images of keratinocytes one day after induction of DSM formation were acquired in collaboration with Dr. Hanna Ungewiß (Waschke group, LMU Munich) [Fig. 5.5]. MEK-wt show the expected disc-shaped structures with electron-dense layers at each side of the cell–cell contact connected to filamentous structures, probably the keratin IF (Fig. 5.5) [280]. In MEK-KO, no DSMs are detectable. In MEK-KO transiently rescued with DPII-wt or DPII-TS, individual cell–cell contacts show the characteristic DSM-like appearance. In contrast to MEK-KO rescued with constructs that comprise

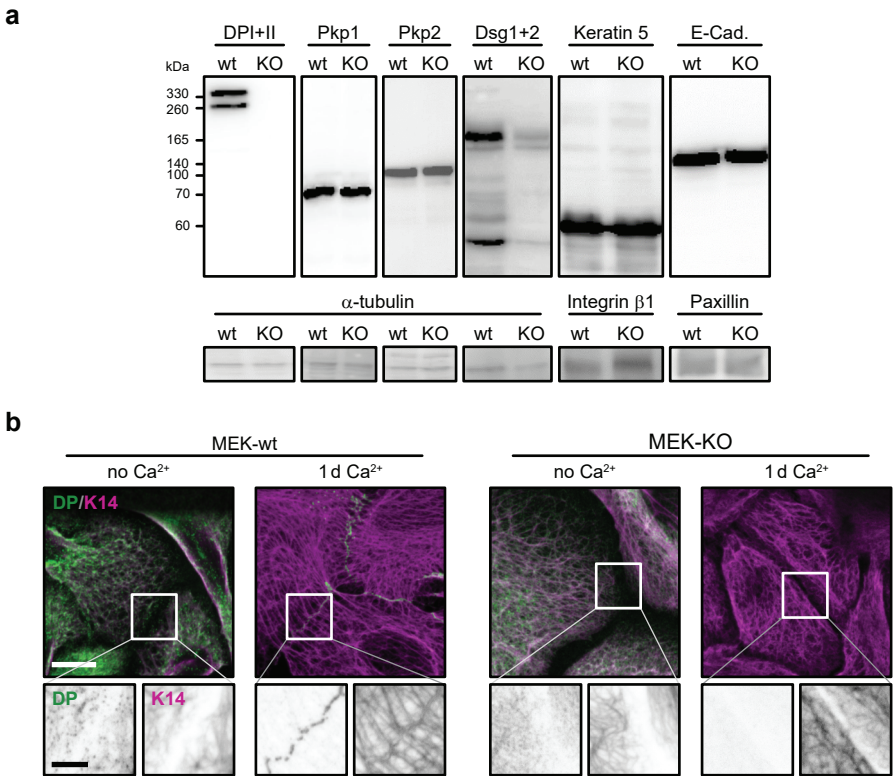

Figure 5.3: Desmoplakin (DP) knockout (KO) abolishes the desmosome (DSM)–intermediate filament (IF) connection. (**a**) In wild type (wt) keratinocytes, DPI and DPII are expressed to comparable levels. In MEK-KO no DP is detectable. In MEK-KO, the expression levels of the desmosomal components plakophilin (Pkp)1 and Pkp2 are unaffected, while desmoglein (Dsg)1 and 2 expression is reduced. Neither the expression of the keratin IF component keratin (K)5 nor of the adherens junction protein E-cadherin are affected by the depletion of DP. The microtubule protein α-tubulin or the focal adhesion proteins integrin β1 and paxillin serve as loading controls. The Western blot was performed by the Bachelor student Miriam Güra. (**b**) In MEK-wt, DP localizes to cell–cell contacts one day after induction of DSM formation by addition of Ca^{2+}. The keratin IF cytoskeletons of neighboring cells then seem connected in the keratin (K)14 stained IF. In MEK-KO, however, the IFs remain separated and only background staining of the DP antibody is seen. Scale bars: 20 µm and 5 µm. The immunostainings are summed projections of 9 slices covering 3.1 µm. The immunostainings of cells with Ca^{2+} are published [11].

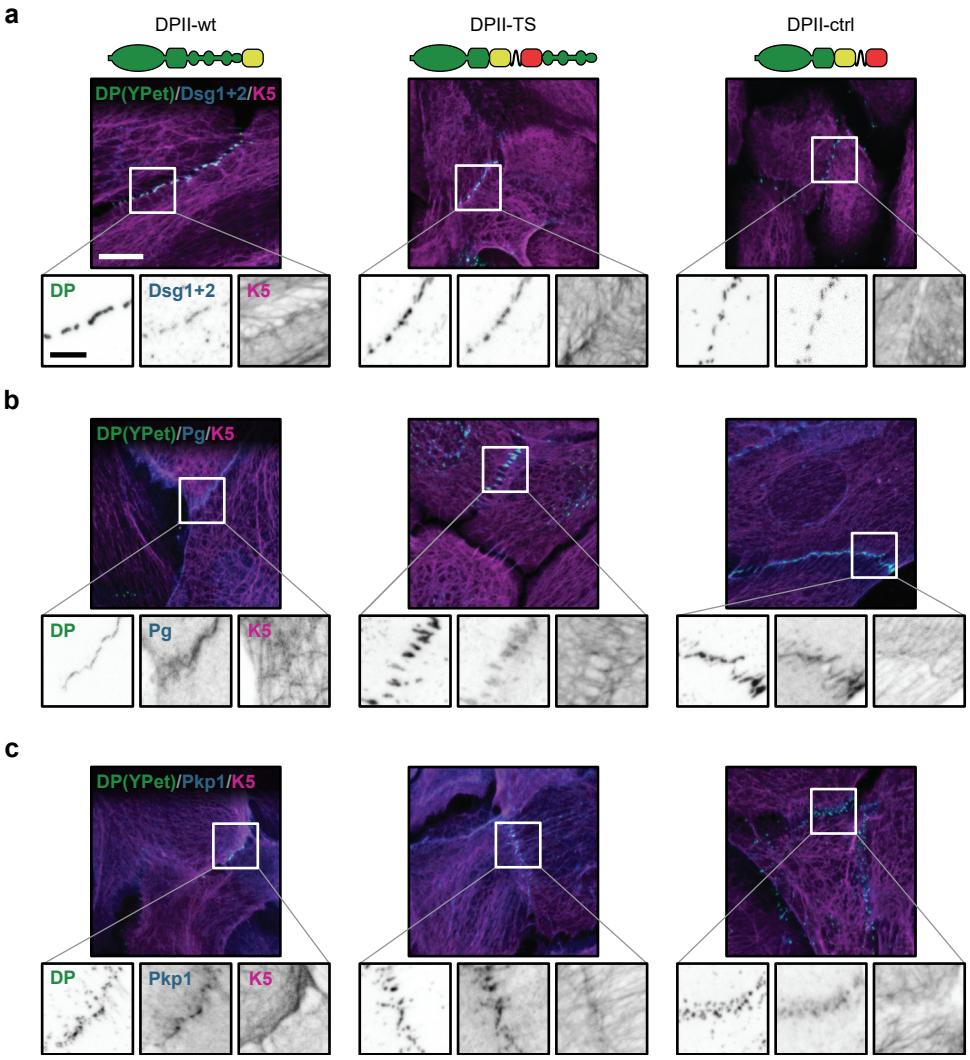

Figure 5.4: Tension sensor constructs rescue the desmosome (DSM) formation in MEKs depleted of desmoplakin (MEK-KO). All desmoplakin (DP) constructs co-localize with the desmosomal components desmoglein (Dsg)1+2 (**a**), plakoglobin (Pg) (**b**), and plakophilin (Pkp)1 (**c**). MEK-KO rescued with the full-length constructs, i.e. wild type (DPII-wt) and tension sensor (DPII-TS), have apparently connected keratin (K)5 stained intermediate filaments (IFs) between neighboring cells. In MEK-KO rescued with the truncated no-force control (DPII-ctrl), a visible separation remains. Scale bars: 20 µm and 5 µm. The immunostainings are summed projections of 9 slices covering 3.1 µm and are published [11].

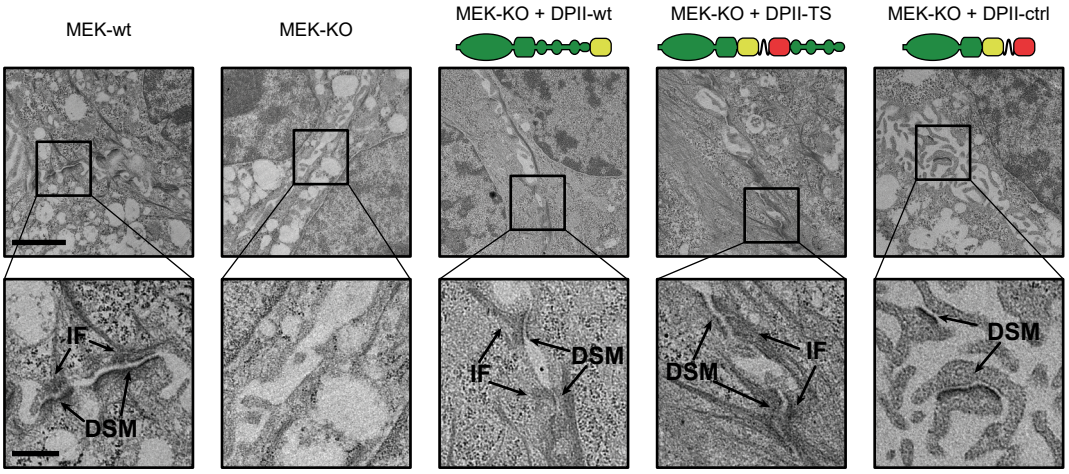

Figure 5.5: Transmission electron microscopy (TEM) images confirm rescue of desmosomes (DSMs) in MEKs depleted of desmoplakin (MEK-KO). MEKs wild type for desmoplakin (MEK-wt) form DSMs characterized by electron-dense layers at each side of the cell–cell contact and connection to the keratin intermediate filament (IF). DSMs are absent in MEK-KO and formation of DSMs is rescued by the expression of desmoplakin (DP) full-length constructs. The expression of the truncated no-force control, however, leads to the formation of electron-dense layers unconnected to the keratin IF. The TEM was prepared by Tadesse Desalegn Egu and Sabine Mühlsimer and images were taken by Dr. Hanna Ungewiß in the group of Prof. Jens Waschke (Ludwig-Maximilians-Universität, Munich). Scale bars: 2 µm and 0.5 µm. TEM images are contrast-adjusted and published [11].

the entire DP sequence, cells rescued with the truncated DPII-ctrl, show only the two electron-dense layers but lack the attachment to filamentous structures.

Taken together, immunostainings and ultrastructural images of rescued MEK-KO demonstrate that DP remains functional after TSM integration and can rescue the formation of *bona fide* DSMs.

5.2 Lifetime Controls

5.2.1 Donor-only Controls

Effect of the Donor-only Constructs

To calculate FRET efficiencies, lifetimes of the donor in presence and absence of the acceptor fluorophore are compared (Sec. 2.4). To this end, a donor-only control is required that closely mimics the environment within the tension sensor and no-force

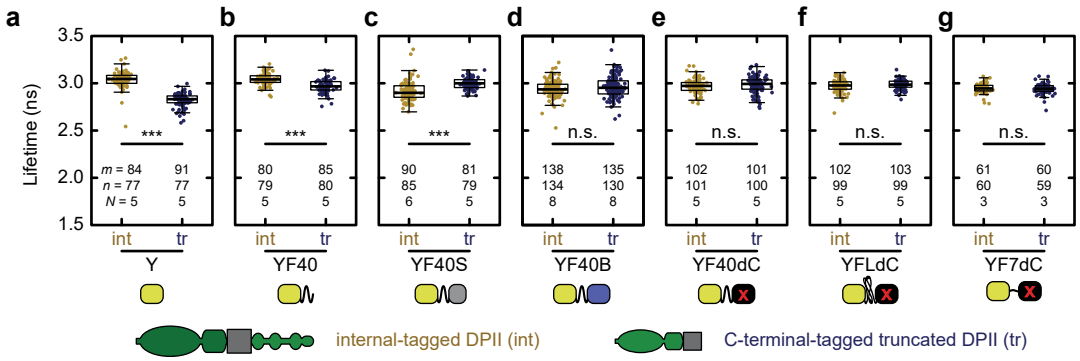

Figure 5.6: The donor lifetime depends on the local environment. The YPet lifetime differs between internal (int, yellow) and truncated (tr, blue) constructs if only YPet (**a**) or YPet and F40 (**b**) are integrated or if the acceptor in the tension sensor module (TSM) is replaced by a SNAP-tag, which is engineered for organic dye labeling but has no intrinsic fluorescence (**c**). The YPet lifetime, however, is indistinguishable for both constructs if the acceptor fluorophore in the TSM is replaced by a fluorophore that cannot serve as an acceptor, i.e. TagBFP (**d**) or mutated mCherry (Y72L) (**e**). The YPet lifetime remains indistinguishable between internal and truncated constructs also if the linker peptide is changed from F40 to FL (**f**) or F7 (**g**). MEK-wt expressing donor-only control constructs were measured one day after induction of desmosome formation. The numbers of masks m, images n, and experiments N are indicated in the figure. Two-sided KS test: *** $p < 0.001$, n.s. (not significant) $p \geq 0.05$. The lifetimes are published [11].

control constructs. Previous projects in the group used YPet-only constructs as donor-only control [216, 217, 270, 281]. The lifetime of YPet-only in DPII, however, differs between internal and truncated constructs (Fig. 5.6a). This difference could either reflect differences also present in the respective tension sensor and no-force control constructs or environmental differences that are not transferable. A non-transferable change could be caused by the different microenvironment. In the YPet-only construct corresponding to the no-force control, for example, YPet terminates the sequence, while in the no-force control YPet is followed by the linker and mCherry in the TSM. Therefore, the local environment of YPet is not necessarily comparable between these constructs and changes in YPet lifetime between the donor-only control constructs might not reflect changes between tension sensor and no-force control.

As the local environment affects fluorophore lifetimes [233], different donor-only control constructs were compared (Fig. 5.6). The addition of the F40 linker peptide alone reduces but does not abolish the lifetime difference between YPet integrated in full-length and truncated DP (Fig. 5.6b). Appending a SNAP-tag [253] as acceptor-mimetic even turns the relation between both lifetimes (Fig. 5.6c). The SNAP-tag is engineered for labeling with organic dyes and lacks intrinsic fluorescence. The structure of the SNAP-tag, however, is different from genetically-encoded fluorophores. To more closely mimic the shape of mCherry, a TSM with TagBFP was used (Fig. 5.6d), which could serve as donor

for YPet but cannot act as an acceptor. Finally, a single point mutation (Y72L) was introduced in mCherry (Fig. 5.6d). The point mutation disturbs chromophore formation but preserves overall protein structure, thereby generating a fluorescently-dead mCherry [282]. The lifetimes measured for YPet in these constructs, which contain a TSM with a fluorophore that cannot serve as an acceptor, are similar. Furthermore, the YPet lifetimes are indistinguishable between integration of the modified TSM in full-length or truncated DP. Note, the observed lifetime is higher than the lifetime in the truncated YPet-only construct, giving additional indication that the point-mutated mCherry has no remaining capabilities to serve as an acceptor.

Based on the constructs for the F40-based TSM, donor-only controls for other TSMs were generated with dead mCherry (Fig. 5.6f, g). These constructs show slightly different absolute YPet lifetimes but again no difference between full-length and truncated constructs.

In summary, the local environment of the YPet fluorophore affects its lifetime. For DP tension sensor experiments the use of YPet-only constructs therefore would result in misleading FRET efficiencies as artificial differences would be introduced from differences in the donor-only control that are not present in the TSM. Consequently, FRET efficiencies calculated in this work use one common donor-only lifetime for tension sensor and no-force control constructs averaged from measurements of constructs with fluorescently-dead mCherry (Fig. 5.6e–g).

Effect of the Cell State

Fluorophore lifetimes are not only influenced by the surrounding within the specific construct but also subjected to changes in the local cellular environment. To evaluate the influence of different cellular states on the YPet lifetime, donor-only constructs were measured in different conditions, which were also used for tension measurements (Sec. 5.3.1). Absolute changes of YPet lifetimes within one construct are small between different cellular states (Fig. 5.7a). However, some differences are significant (Fig. 5.7b). The effect of even slightly different donor-only lifetimes on the resulting FRET efficiency is substantial, so it is crucial to estimate whether the observed differences are systematic and likely to reflect differences also present in tension sensor and no-force control. If the differences were systematic, trends should be consistent across constructs, which is not the case (Fig. 5.7b). Therefore, the observed differences are likely caused by statistics and do not reflect systematic differences. In line with this hypothesis, the lifetimes between conditions are comparable in the other experimental settings, i.e. soft substrates (Fig. 5.8a) and disruption of the keratin–IF by okadaic acid (Fig. 5.8b) as well as measurements with constructs harboring different linker peptides, F7 (Fig. 5.8c) and FL (Fig. 5.8d).

Thus, in this work one average lifetime per experimental setting is calculated from all dead mCherry constructs and conditions. The resulting average lifetimes are $\overline{\tau_D} = 2.94\,\text{ns}$ for F40-based constructs on glass, $\overline{\tau_D} = 2.96\,\text{ns}$ for F40-based constructs treated with OA and F7-based constructs, and $\overline{\tau_D} = 2.98\,\text{ns}$ for F40-based constructs on soft substrates and FL-based constructs.

5.2.2 Effect of Photobleaching

Photobleaching of the donor fluorophore should not influence FRET efficiency measurements as bleached fluorophores do not emit any signal and therefore cannot influence the observed lifetime. Bleaching of the acceptor fluorophore, however, changes the

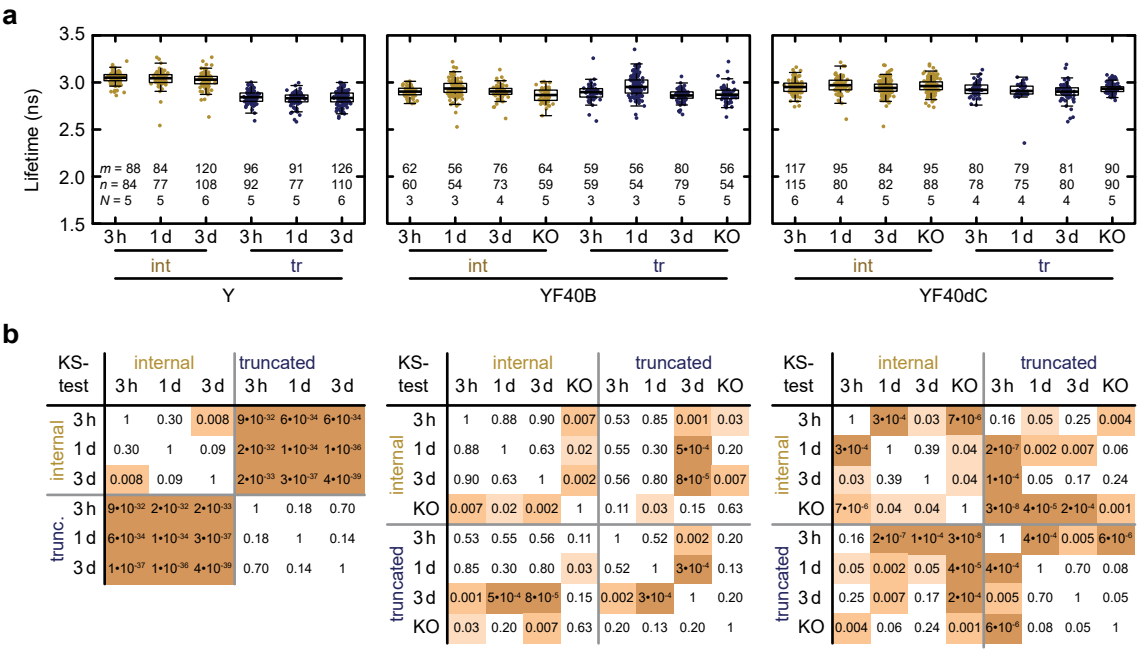

Figure 5.7: The donor lifetime is unaffected by the experimental condition. (**a**) The YPet lifetimes are measured in internal (int, yellow) and truncated (tr, blue) desmoplakin (DP)II constructs with YPet alone (Y) or the F40-based tension sensor module (TSM) with TagBFP (YF40B) or Y72L-mutated mCherry (YF40dC) as acceptor-mimetic. Lifetimes are similar in MEK-wt 3−5 h, 1 d or 3 d and in MEK-KO 1 d after induction of desmosome (DSM) formation. (**b**) Some pair-wise comparisons show significant differences. These differences are are not consistent for the different donor-only constructs indicating that they are not systematic and therefore likely not biologically relevant. Therefore, an average lifetime of $\overline{\tau_D} = 2.94\,\text{ns}$ is determined from all dead mCherry constructs to calculate FRET efficiencies. The numbers of masks m, images n, and experiments N are indicated in the figure. The p-values of pairwise two-sided KS tests are highlighted with light orange for $p < 0.05$, orange for $p < 0.01$ and dark orange for $p < 0.001$. The lifetimes and p-values are published [11].

observed lifetime as the corresponding donor is not anymore quenched due to FRET and therefore contributes with a longer lifetime. To estimate the effect of photobleaching on the observed lifetimes and resulting FRET efficiencies, the multiple subsequent image repeats that were taken during acquisition of one image (Sec. 4.3) were fitted individually. Fitting lifetimes to the individual repeats instead of the accumulated data leads to bigger uncertainties because less photons are fitted but still results in sufficient fit quality to compare lifetimes across repeats. For high statistics and a robust estimate of the effect of photobleaching, all data from DSM formation in MEK-wt and MEK-KO with the F40-based TSM were pooled (Sec. 5.3.1). The decrease in photon count over consecutive image repeats is a direct consequence of YPet photobleaching (Fig. 5.9a, b). The lifetime of YPet, however, is not affected by photobleaching and remains constant (Fig. 5.9c). In contrast, photobleaching of mCherry with the YPet excitation laser leads to an increase

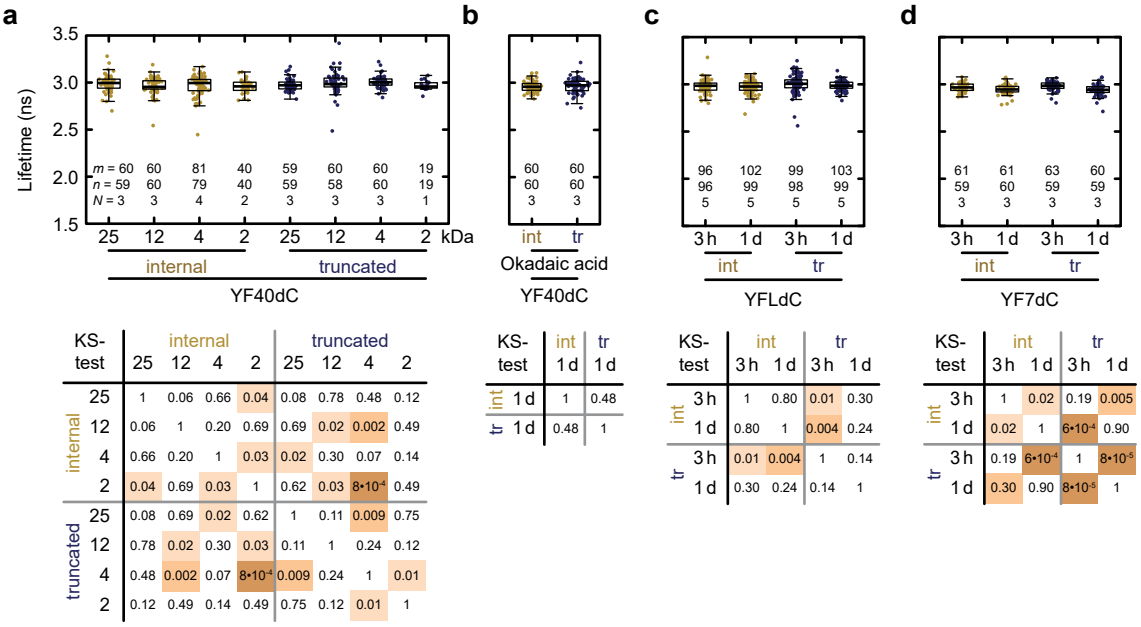

Figure 5.8: An average donor-only lifetime is used per experimental setting. The YPet lifetimes of internal (int, yellow) and truncated (tr, blue) desmoplakin (DP)II constructs with a Y72L-mutated mCherry as acceptor-mimetic in the tension sensor module (TSM) are similar. (**a, b**) Lifetimes of F40-based constructs (YF40dC) are similar on all soft substrates (**a**) and when treated with okadaic acid (**b**) in MEK-wt one day after induction of desmosome (DSM) formation. (**c, d**) Similarly, for constructs with the F7 (**c**) and FL (**d**) linker peptide, lifetimes are comparable for internal and truncated constructs in MEK-wt 3−5 h and 1 d after induction of DSM formation. Average lifetimes used to calculate FRET efficiencies are determined from all dead mCherry constructs in the same condition to $\overline{\tau_D} = 2.98\,\text{ns}$ (**a, d**) and $\overline{\tau_D} = 2.96\,\text{ns}$ (**b, c**), respectively. The numbers of masks m, images n, and experiments N are indicated in the figure. The p-values of pairwise two-sided KS tests are highlighted with light orange for $p < 0.05$, orange for $p < 0.01$ and dark orange for $p < 0.001$. The lifetimes and p-values are published [11].

in YPet lifetime (Fig. 5.9d). Consequently, absolute values for FRET efficiencies reported in this work are lower than the initial FRET efficiency without photobleaching because data from all image repeats is used to fit one lifetime. Importantly, this increase in lifetime is independent of the construct, so the relative difference between tension sensor and no-force control is not changed as long as the number of image repeats remains constant for both tension sensor and no-force control construct. In this work, FLIM measurements are standardized to 100 image repeats for tension sensor and no-force control measurements and 20 repeats for the corresponding donor-only controls. Thus, biological conclusions, which are based on the comparison of tension sensor and no-force control, are independent of photobleaching.

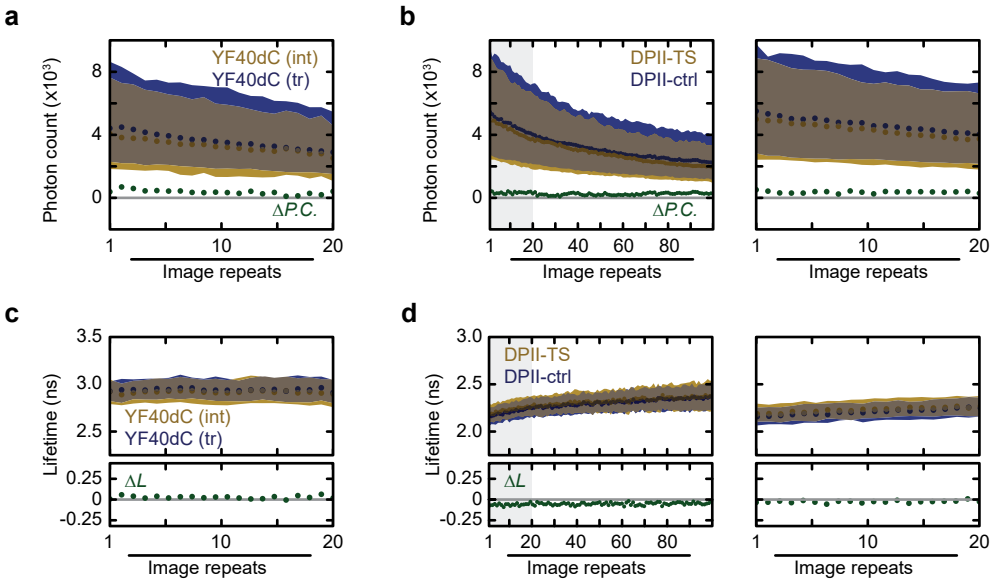

Figure 5.9: Photobleaching of the acceptor fluorophore changes FRET. (**a**) The photon count is reduced in subsequent image repeats due to photobleaching of YPet. The donor-only control measurements with internal (yellow) and truncated (blue) constructs using YPet-F40-mCherry(Y72L) have comparable photon counts, which results in a small photon count difference ($\Delta P.C.$, green). The data is pooled from Fig. 5.7 resulting in $m = 401,391$ masks. (**b**) Similarly, in tension sensor (DPII-TS, yellow) and no-force control (DPII-ctrl, blue) measurements with the F40-based TSM, the photon count reduces over repeats but the difference between both constructs remains constant ($\Delta P.C.$, green). The data is pooled from Fig. 5.13 resulting in $m = 406,332$ masks. (**c**) The lifetime of internal and truncated donor-only control is unaffected by photobleaching. The raw data is the same as in (**a**). (**d**) The YPet lifetime of DPII-TS and DPII-ctrl increases in subsequent repeats due to photobleaching of mCherry but the difference in lifetime ΔL remains unaffected. The raw data is the same as in (**b**). Median and interquartile range are shown. Mask numbers differ slightly from Fig. 5.7 and Fig. 5.13 because masks are only excluded if fits failed in a repeat due to insufficient photon counts but no general photon count threshold is applied. The tension sensor and no-force control data is published [11].

5.2.3 Intensity Dependence

The intensity independence of lifetime measurements is one of the major advantages of FLIM over intensity-based ratiometric approaches to determine FRET (Sec. 2.4.3). In FLIM measurements, the intensity is reflected in the photon count, which can vary by an order of magnitude between images (Fig. 5.10a). Tension sensor and no-force control are subjected to FRET, which reduces the expected photon count, but are also measured with 100 repeats per image, which is five times longer than the corresponding donor-only controls with 20 repeats. Indeed, total photon counts are higher for tension sensor and no-force control measurements (Fig. 5.10a). While total photon counts are important for fit quality, area-normalized photon counts reflect the underlying protein concentration. In fact, the normalized photon count is slightly but significantly decreased for tension sensor constructs (Fig. 5.10b). Lifetimes are, however, independent of the normalized photon count (Fig. 5.10c). Thus, differences in photon counts between constructs do not affect tension sensor experiments.

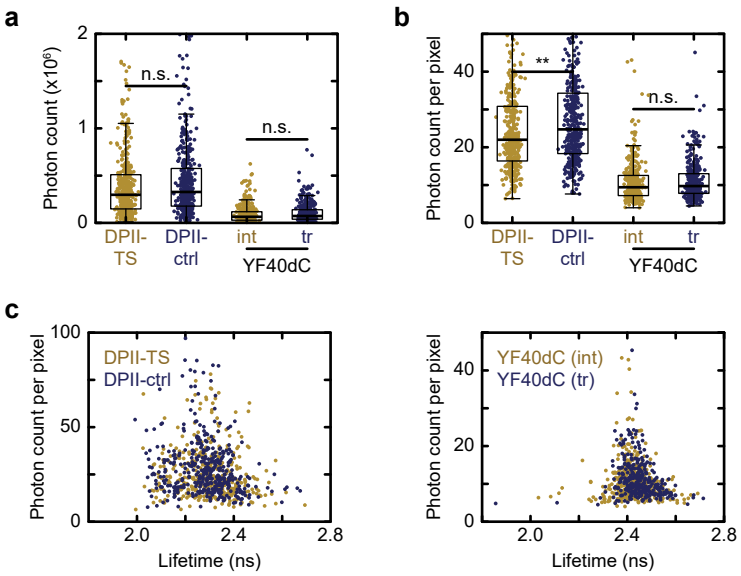

Figure 5.10: The lifetime determination is independent of the fluorescence intensity. (**a**) The total photon counts are higher for tension sensor (yellow) and no-force control (blue) measurements than for the corresponding donor-only controls because FRET samples were measured five times longer. (**b**) The normalized photon counts per pixel show similar tendencies. The photon count of the tension sensor constructs is reduced compared to the no-force control. (**c**) Intensity differences, however, do not affect tension measurements as lifetimes are independent of the intensity. The data is pooled from Fig. 5.13 and Fig. 5.7 resulting in $m = 398,401,391,330$ masks from $n = 364,363,365,323$ images taken at $N = 21,20,20,17$ experiments. KS-test: ** $p < 0.01$, n.s. (not significant) $p > 0.05$.

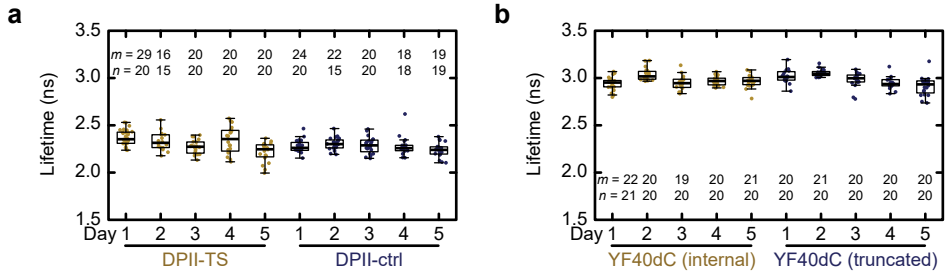

Figure 5.11: The experimental results are similar between experimental days. The day-to-day variability is small for tension sensor and no-force control (**a**) and the corresponding donor-only control constructs (**b**). The data shows individual experiments of the the F4o-based DPII MEK-wt one day after DSM induction. The raw data is the same as in Fig. 5.13 (**a**) and Fig. 5.6e (**b**). The numbers of masks m and images n are indicated in the figure. The tension sensor and no-force control data is published [11].

5.2.4 Stability Over Experimental Days

To minimize the effect of experimental variability on the biological conclusions, all experiments were replicated at least three to five times. Importantly, observed tendencies are consistent also across individual experimental preparations and variability is generally in the same order as the variance of data from one day (Fig. 5.11). A similar experimental stability is observed for most conditions (with the exception of 2 kPa soft substrates, Sec. 5.5) and therefore in this work only the merged results from all experiments are shown.

5.2.5 Robustness against the Fit Procedure

Two main different approaches are used in this work to determine the YPet lifetime of DP constructs. First, the signal is isolated and directly subjected to a mono-exponential fit, which yields one lifetime per mask. Second, the signal is attributed to distinct DSMs and then fit, which results in one lifetime per DSM and many lifetimes per image. The variance is much larger for the latter because less photons are used per fit. Note that the interdependence of the data points originating from the same image is taken into account for the statistical analysis (Sec. 3.8.4).

In this work, the donor-only controls are always determined from the entire mask but tension sensor and no-force control measurements contain sufficient signal to also allow the spatial-resolved analysis and results are similar for all lifetime determination methods (Fig. 5.12).

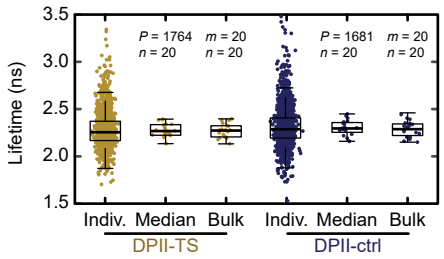

Figure 5.12: The resulting lifetime is independent of the specific fit procedure. The variance for fits of individual desmosomes (DSMs) (Indiv.) is high but reduces if the median per image is calculated (Median). Alternatively, all signal within one mask is fit collectively (Bulk). DPII-TS (yellow) and DPII-ctrl (blue) were measured in MEK-wt one day after DSM induction. The numbers of desmosomal puncta P, masks m, and images n are indicated in the figure. The raw data is the same as in Fig. 5.13. The fit comparison is published [11].

5.3 No Tension across DPII in Homeostatic Conditions

5.3.1 Formation of Desmosomes

DSM formation is suppressed during the cultivation of basal keratinocytes because cells are cultured with low levels of Ca^{2+} that are insufficient to induce DSM formation. To analyze tension across DP in early DSMs, FLIM was measured $3-5\,h$ after DSM induction. After one day, DSMs are matured but still depend on Ca^{2+} in the medium. In the course of several days more stable hyperadhesive DSMs form that are resistant to Ca^{2+}-chelators (Sec. 1.3.1 and Sec. 1.6) [25]. Overexpression of DP tension sensor constructs in MEK-wt reveals that DP does not experience substantial tension during these steps of DSM formation (Fig. 5.13).

At the very early time point, the observed FRET efficiency for the tension sensor is higher than for the no-force control, which could be explained by compression of the linker peptide or steric restrictions of the fluorophore orientation but not by tension or differences in intermolecular FRET (Sec. 5.4). In mature DSMs one day after induction of DSM formation, the FRET efficiency of the tension sensor is slightly decreased compared to the no-force control, so few molecules could experience tension. For this time point, fitting all DSMs in a mask with one lifetime led to a slightly different statistical result than analyzing the DSMs individually (Fig. 5.13c, d). However, both p-values are close to significance levels, so biological conclusions are independent from the details of the analysis procedure: no or very little tension is experienced by DP during the formation of DSMs in basal keratinocytes. Another hint to no or little tension across DPII one day after induction of DSM formation is that tension introduces additional spread in the observed lifetimes but the variances of tension sensor and no-force control data are comparable (Fig. 5.13).

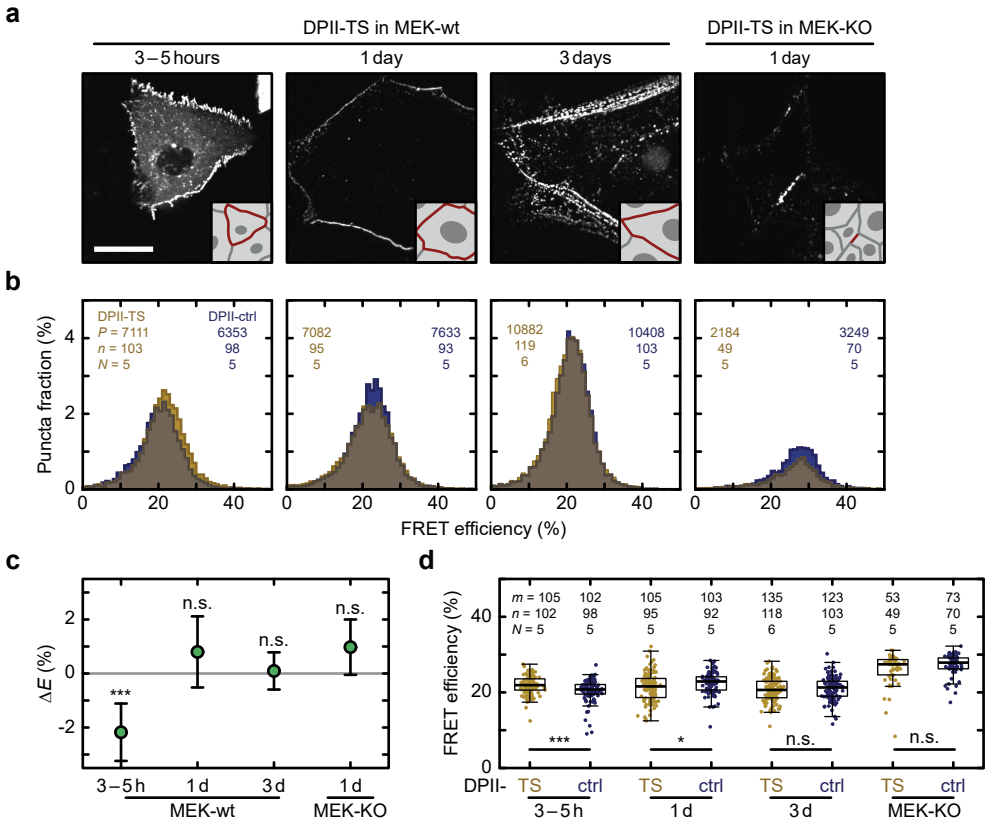

Figure 5.13: Desmoplakin (DP)II experiences no tension in homeostatic conditions. (**a**) FLIM was performed in confluent cell sheets of MEK-wt at distinct time points after DSM induction by addition of Ca^{2+} (3–5 h, 1 d, and 3 d) and in MEK-KO after 1 d. (**b**) The histograms of lifetime fits of individual DSMs are similar for F40-based DPII-TS (yellow) and DPII-ctrl (blue) expressed in MEK-wt or MEK-KO. (**c**) No or little tension is experienced by DPII with a positive FRET efficiency difference $\Delta E = E_{\mathrm{DPII-ctrl}} - E_{\mathrm{DPII-TS}}$ indicating tension. (**e**) Bulk fits of the same data confirm that no or little tension is experienced by DPII. Scale bar: 20 µm. The FRET efficiencies are calculated with $\overline{\tau_D} = 2.94$ ns. ΔE data points with errorbars are the lmer-determined mean with 95 % CI from puncta with $0 < E < 100$ %. Numbers of desmosomal puncta P, masks m, images n, and experiments N are indicated in the figure. Lmer-test (**c**) and two-sided KS-test (**d**): *** $p < 0.001$, * $p < 0.05$, n.s. (not significant) $p \geq 0.05$. The individual desmosomal fits and example images are published [11].

When measuring DP tension sensor constructs in MEK-wt, all cells also express the endogenous level of DP, which is beneficial because transfected cells are surrounded by an intact cell sheet and neighboring cells have the appropriate expression level. On the other hand, the presence of endogenous DP could reduce the tension experienced by the DP tension sensor molecules. Therefore, tension sensor measurements were performed also in rescued MEK-KO one day after induction of DSM formation at cell–cell contacts of neighboring transfected cells (Fig. 5.13a). The absolute FRET efficiencies are increased, which is likely caused by an increased level of intermolecular FRET (Sec. 5.4.1). Tension sensor and no-force control constructs, however, have highly comparable FRET efficiencies indicating no or very little tension across DP also in the absence of the endogenous protein.

5.3.2 Disruption of the Keratin IF

Attachment to the keratin IF is a likely prerequisite for tension transmission across the DSM. Therefore, disrupting the keratin IF serves as a biological no-force condition for the tension sensor experiment. Because no specific inhibitory factors for the keratin IF are known, the phosphatase inhibitor okadaic acid (OA) was used to induce a rapid collapse of the keratin IF [283]. Indeed, also after disruption of the keratin IF, FRET efficiencies of the tension sensor and no-force control constructs are comparable (Fig. 5.14). Thus, DPII experiences no tension in unstressed keratinocyte monolayers.

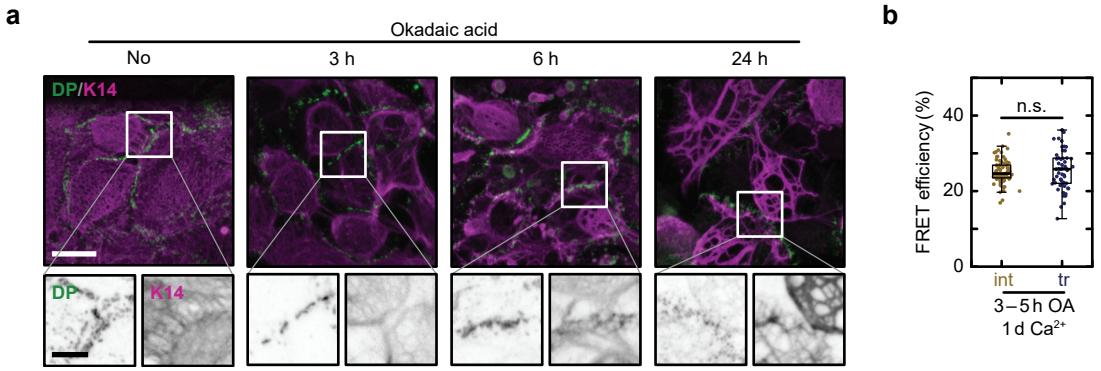

Figure 5.14: No tension is experienced by desmoplakin (DP) after disruption of the keratin intermediate filament (IF). (**a**) The keratin (K)14 IF in MEK-wt one day after induction of DSM formation is disturbed after treatment with 100 nM okadaic acid (OA). (**b**) FRET efficiencies of the tension sensor (DPII-TS, yellow) and no-force control (DPII-ctrl, blue) constructs in MEK-wt one day after induction of DSM formation are indistinguishable after 3 – 5 h OA treatment. Scale bars: 20 µm and 2 µm. The FRET efficiencies are calculated with $\overline{\tau_D} = 2.98$ ns and $m = 81, 55$ masks were analyzed from $n = 79, 55$ images taken at $N = 4, 4$ experimental days. Two-sided KS-test: n.s. (not significant) $p \geq 0.05$.

5.4 Potential Alternative Causes for FRET Changes

FRET is not only sensitive to changes in the fluorophore separation distance but is also influenced by a variety of other factors (Sec. 2.4). Comparing the tension sensor always with a matched no-force control excludes many of these influencing factors, e.g. changes in pH. However, even between tension sensor and no-force control, FRET differences could be caused by other reasons than tension. For example, the fluorophore separation distance can not only be increased by tension but also shortened by compression [284, 285]. Furthermore, differences in the rotational freedom that lead to construct-specific orientation of donor and acceptor fluorophore towards each other, change the κ^2-value and therefore FRET (Sec. 2.4.1). In addition, the observed FRET efficiency is not only caused by intramolecular FRET in the construct but also intermolecular FRET between neighboring molecules contributes to the overall FRET efficiency. While fluorophore anisotropy is difficult to determine experimentally, intermolecular FRET and compression were assessed as potential sources for differences in FRET.

5.4.1 Intermolecular FRET

The observed FRET efficiency in tension sensor measurements always comprises of *intramolecular* FRET within an individual tension sensor molecule that reports tension and *intermolecular* FRET between neighboring molecules that reflects molecular density. Intermolecular FRET does not influence the biological conclusions if tension sensor and no-force control experience comparable levels of intermolecular FRET. To verify this assumption, constructs with either fluorescently-dead donor or acceptor fluorophore were coexpressed, so that no intramolecular but only intermolecular FRET occurred (Fig. 5.15a). Indeed, in all conditions intermolecular FRET is indistinguishable for the tension sensor and no-force control constructs (Fig. 5.15b).

The intermolecular FRET is increased for expression in MEK-KO as compared to MEK-wt, which fits well with the notion that in wild type cells endogenous proteins are located next to tension sensor molecules, increase the distance between tension sensor molecules, and therefore reduce intermolecular FRET. Thus, the increased intermolecular FRET in MEK-KO explains the increased overall FRET efficiency observed in MEK-KO (Fig. 5.13).

Of note, the absolute values of intermolecular FRET within the DSM during tension measurements cannot be determined. One obvious difference between tension and intermolecular FRET measurements is that in a tension measurement most molecules have two intact fluorophores. The normalized photon count per pixel is consequently smaller in intermolecular FRET than tension measurements (Fig. 5.15c). However, the photon count per YPet is expected to be higher because less energy is transferred to

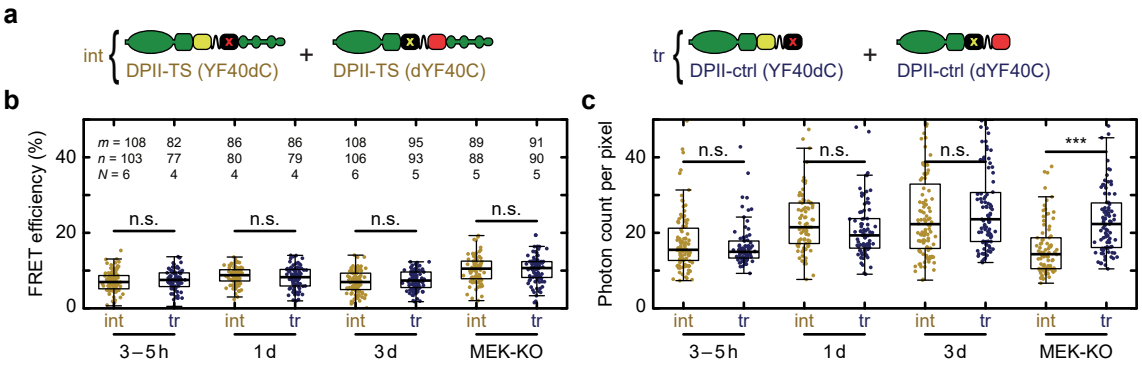

Figure 5.15: Intermolecular FRET is comparable between tension sensor and no-force control constructs. (**a**) Constructs with fluorescently-dead YPet(Y76G) and mCherry(Y72L) were coexpressed. (**b**) Intermolecular FRET is comparable at the internal (int, yellow) and truncated (tr, blue) integration sites corresponding to tension sensor and no-force control, respectively. Intermolecular FRET is higher in MEK-KO one day after induction of desmosome (DSM) formation than in MEK-wt after 3−5 h, 1 d, and 3 d. (**c**) Normalized photon counts are comparable for internal and truncated constructs in MEK-wt but reduced for the internal construct in MEK-KO. The F40-based TSM is used and FRET efficiencies are calculated with $\overline{\tau_D} = 2.94\,\text{ns}$. The numbers of masks m, images n, and experiments N are indicated in the figure. Two-sided KS-test: *** $p < 0.001$, n.s. (not significant) $p \geq 0.05$. The FRET efficiencies are published [11].

an acceptor via FRET. Therefore, the overall amount of transfected molecules might be similar between tension and intermolecular FRET measurements as judged by comparing the intensities, even though transient transfection variability and the assumptions made in these considerations prevent a definite statement.

During the formation of DSMs in MEK-wt, the photon count of internal and truncated intermolecular FRET constructs is comparable. In MEK-KO, however, the internal constructs emit significantly less photons, which means that more of the truncated construct is localized to cell–cell contacts (Fig. 5.15c).

In summary, intermolecular FRET is comparable between tension sensor and no-force control constructs. As biological conclusions are based on changes in FRET rather than on absolute values and intermolecular FRET does not introduce differences between constructs, conclusions from tension sensor measurements are unaffected by intermolecular FRET. Hypothetically, intermolecular FRET might even reduce specifically upon tension because DP molecules are aligned in parallel. Importantly, intermolecular FRET cannot explain differences in FRET between tension sensor and no-force control constructs, but it can explain the increased FRET efficiencies observed in MEK-KO compared to MEK-wt.

5.4.2 Compression of the Linker Peptide

The F40 linker peptide is predicted to be not only tension but also compression sensitive [284, 285]. Compression of the F40 peptide would reduce the fluorophore separation distance and therefore could explain the increased FRET efficiency for the tension sensor as compared to the no-force control construct early in DSM formation (Sec. 5.3.1). To test this hypothesis, alternative linker peptides were employed.

F7 Linker Peptide

The F7 peptide was cloned by Dr. Anna Chrostek-Grashoff and Lisa Fischer measured no FRET changes when integrating the F7-based TSM between head and rod of the FA protein talin (personal communication, Grashoff group). This observation indicates that the F7 peptide is insensitive to forces of at least 10 pN because a subpopulation of talin molecules is exposed to more than 10 pN [217]. The FRET efficiency for the F7-based DP tension sensor constructs are overall higher than for the F40-based constructs because of the shortened linker length (Fig. 5.16 and 5.13). The relative differences between tension sensor and no-force control constructs, however, recapitulate the behavior of the F40-based tension sensor constructs. Thus, the increased FRET efficiency early in the formation of DSMs is not specific to the F40-based TSM. However, despite the short linker length of 7 aa, compression is predicted also for short peptides [285]. Thus, compression of the linker peptide cannot be excluded with the F7-based tension measurements (Fig. 5.16) as explanation for the increased FRET in the F40-based tension measurements (Fig. 5.13).

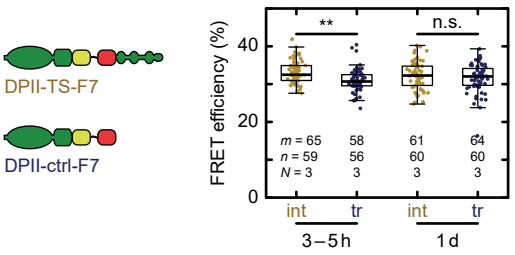

Figure 5.16: The stable seven aa linker (F7)-based desmoplakin (DP)II tension sensor has an elevated FRET efficiency compared to the no-force control construct early in DSM formation. The FRET efficiency of the tension sensor (DPII-TS-F7, yellow) is increased 3−5 h after induction of DSM formation in MEK-wt as compared to the corresponding no-force control (DPII-ctrl-F7, blue). One day after induction of DSM formation, both FRET efficiencies are comparable. The FRET efficiencies are calculated with $\overline{\tau_D} = 2.98$ ns. The numbers of masks m, images n, and experiments N are indicated in the figure. Two-sided KS-test: ** $p < 0.01$, n.s. (not significant) $p \geq 0.05$.

FL Linker Peptide

In contrast to the F40 and F7 peptides, which fold unstructured, the FL peptide has a well-defined conformation that unfolds almost digitally around 4 pN (Fig. 2.7). The absolute FRET efficiency is higher than for F40-based tension sensor constructs due to the shorter rest length [216]. For this TSM, FRET efficiencies for tension sensor and no-force control are comparable early in DSM formation and one day after induction of DSM formation (Fig. 5.17).

Thus, the increase in FRET efficiency of the tension sensor as compared to the no-force control construct depends on the linker peptide. Noteworthy, the measurements cannot distinguish between compression and a restriction in the rotational freedom of the fluorophores specifically in the F40- and F7- but not in the FL-based constructs. Compression of the unstructured linker peptides, F40 and F7 but not of the structured FL peptide, however, provides one reasonable explanation of the increased FRET efficiency for the tension sensor early in DSM formation. Irrespective of the specific reason for this FRET increase, the FL-based tension measurements confirm that no (or very little) tension is experienced by DPII in homeostatic conditions.

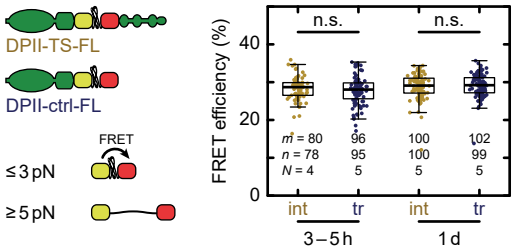

Figure 5.17: The ferredoxin-like fold (FL)-based desmoplakin (DP)II tension sensor shows comparable FRET to the no-force control construct. FRET efficiencies for the tension sensor (DP-TS-FL, yellow) and no-force control (DP-ctrl-FL, blue) are indistinguishable 3−5 h and one day after induction of DSM formation in MEK-wt; thereby confirming that no tension is experienced by DPII in homeostatic conditions. FRET efficiencies are calculated with $\overline{\tau_D} = 2.98$ ns. The numbers of masks m, images n, and experiments N are indicated in the figure. Two-sided KS-test: ** $p < 0.01$, n.s. (not significant) $p \geq 0.05$. The fits of individual desmosomal puncta of the same data are published [11].

5.5 Tension Across DPII on Very Soft Substrates

The measurements were performed on glass microscopy dishes, which are very stiff compared to the physiological environment (Fig. 2.1) and the stiffness of the underlying substrate greatly influences cell behavior (Sec. 2.1). For example, cells on a stiff substrates have a larger adhesive area and form stronger cell–matrix adhesions as reflected in increased overall traction force and tension across the FA protein talin [217]. Measurements of the epidermal stiffness that keratinocytes experience vary [286, 287] depending on study details but different stiffness's are also observed for different skin layers or body regions [287]. To better reflect the physiological environment of few kilo Pascal (kPa), tension measurements were performed in MEK-wt seeded on soft hydrogels with Young's moduli of 2, 4, 12, and 25 kPa (Fig. 5.18a, b).

In line with measurements on glass, DPII does not experience tension on soft substrates

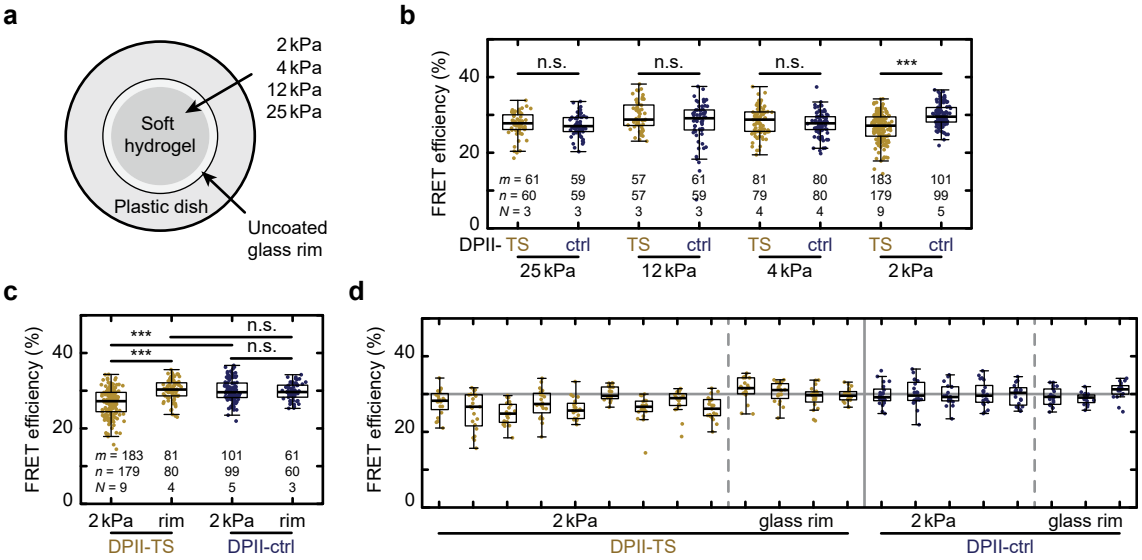

Figure 5.18: Desmoplakin (DP)II experiences forces on very soft substrates. (**a**) MEK-wt were seeded on microscopy dishes with a central hydrogel of defined stiffness. (**b**) FRET efficiencies of tension sensor (DPII-TS, yellow) and no-force control (DPII-ctrl) constructs are indistinguishable on 4, 12, and 25 kPa hydrogels showing that no tension is experienced by DPII. On 2 kPa hydrogels, however, the FRET efficiency is specifically reduced for DPII-TS indicating tension. (**c**) Tension across DPII is specific for very soft substrates and not an artifact of the used dishes as cells adhering to the outer glass rim of dishes with a central hydrogel of 2 kPa show no difference between DPII-TS and DPII-ctrl. (**d**) The FRET efficiencies for DPII-TS vary between experimental days but mostly remain below the average FRET efficiency of the no-force control (grey line). The FRET efficiencies are calculated with $\overline{\tau_D} = 2.98$ ns. The numbers of masks m, images n, and experiments N are indicated in the figure. Two-sided KS-test: *** $p < 0.001$, n.s. (not significant) $p \geq 0.05$. The schematic and merged FRET efficiencies are published [11].

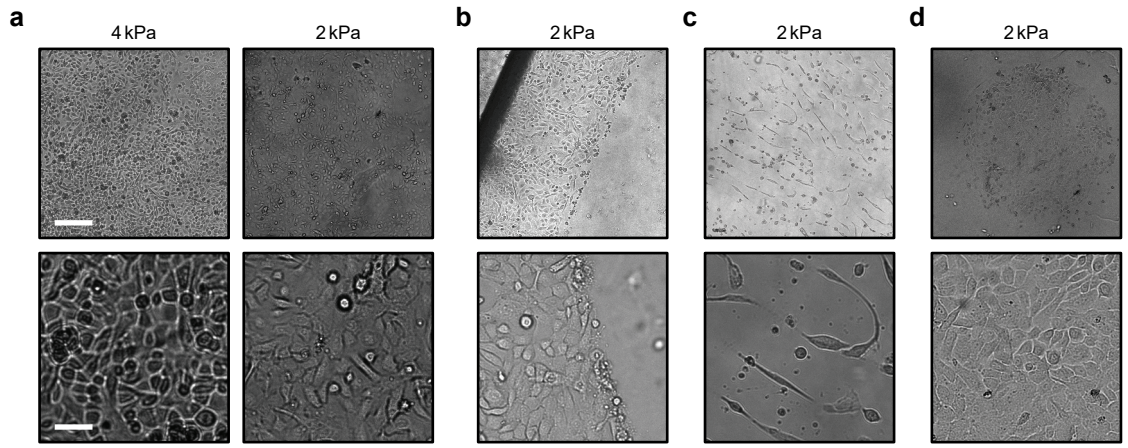

Figure 5.19: Keratinocytes hardly adhere to very soft substrates. (**a**) MEK-wt form confluent monolayers on most stiff substrates and in some cases also on 2 kPa. (**b**) Keratinocytes preferentially seed on the stiff glass rim surrounding the 2 kPa hydrogel. (**c**) The cells seem to sense patterns in some of these very soft dishes. (**d**) In other dishes, keratinocytes form roundish clusters. For FRET efficiency determination (Fig. 5.18) only cells surrounded by neighboring cells are imaged (**a, d**). Transmission images were contrast adjusted. Scale bars: 200 µm and 50 µm.

with 4−25 kPa stiffness. On the very soft 2 kPa substrates, however, the FRET efficiency of the tension sensor is specifically reduced. While cells on stiffer substrates always form a continuous monolayer (Fig. 5.19a), keratinocytes on 2 kPa dishes preferentially adhere to the outer glass rim surrounding the soft hydrogel (Fig. 5.19b). These cells are used as internal control demonstrating that DPII loading is indeed specific for very soft substrates (Fig. 5.18c). Of note, day-to-day variability of the DPII tension sensor is larger than in other experiments (Sec. 5.2.4) and for the matched control construct (Fig. 5.18d). This increased variance likely reflects changes in tension probably caused by small changes in substrate stiffness. This hypothesis is supported by the observation that MEK-wt seem to follow patterns in some of the soft hydrogels (Fig. 5.19c). For FRET efficiency determination, however, only cells surrounded by neighbors were measured (Fig. 5.19a, d).

In summary, DPII does not experience tension across a range of physiological relevant stiffness's similar to the experiments on glass (Sec. 5.3.1). On very soft substrates, however, DPII experiences tension.

5.6 Desmoplakin Experiences Tension Upon External Stress

5.6.1 DPII Experiences Transient Tension During Pulling

DSMs are particularly important in tissues exposed to external stress (Sec. 1). To test whether DP experiences tension when cells are exposed to external stress, I performed pulling experiments in Stanford together with Andrew J. Price, PhD, in the group of Prof. Alexander R. Dunn.

In a pulling experiment three subsequent ratiometric FRET images are taken (Fig. 5.20a). First, the unstressed monolayer is imaged (Pre). Then, a glass micropipette is positioned next to a transfected cell. The micropipette is lowered so that the cell underneath is pressed down. The glass micropipette is then laterally moved, which drags the squeezed cell away from the transfected cell. The cell–cell contact between squeezed and transfected cell is thereby pulled and the transfected cell deforms to preserve cell–cell adhesion. At the point of maximal displacement, a second FRET image is taken (Pull). The glass micropipette is then lifted and the monolayer is imaged a third time after a few minutes when cells stopped relaxation (Post).

From all three images, FRET indices of individual desmosomal puncta are determined (Fig. 5.20b) and compared between tension sensor and no-force control construct (Fig. 5.21).

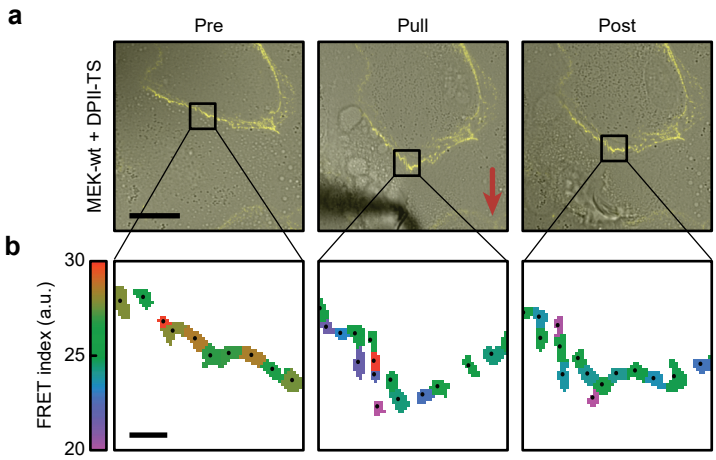

Figure 5.20: FRET is measured during application of external stress. (**a**) Confluent MEK-wt monolayers expressing desmoplakin (DP)II tension sensor (DPII-TS) or no-force control (DPII-ctrl) constructs are imaged unstressed (Pre), at the maximal displacement (Pull), and after relaxation (Post). The red arrow indicates the pulling direction. (**b**) The FRET indices are determined for individual desmosomal puncta. The black dots mark the centroids of the desmosomal puncta. The contrast-adjusted brightfield images are superimposed with YPet signal for DPII-TS. Scale bars: 20 µm and 2 µm. The example images are published [11].

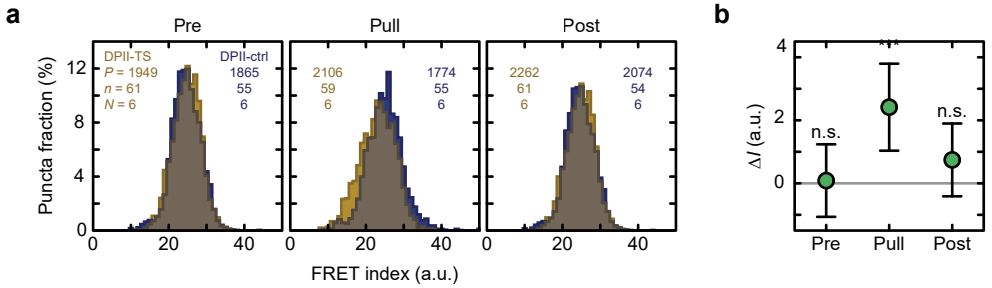

Figure 5.21: Desmoplakin (DP)II experiences tension specifically and transiently upon external stress. (**a**) FRET indices I for DPII tension sensor (DPII-TS, yellow) and no-force control (DPII-ctrl, blue) in MEK-wt one day after induction of DSM formation are indistinguishable before pulling. The FRET index is transiently reduced for DPII-TS compared to DPII-ctrl during pulling, which indicates tension specifically during pulling. (**b**) The FRET index difference $\Delta I = I_{\mathrm{DPII-ctrl}} - I_{\mathrm{DPII-TS}}$ confirms that only during pulling the FRET decrease of DPII-TS is statistically significant and tension is experienced by DPII. The data points with errorbars are the lmer-determined mean with 95 % CI. lmer-test: *** $p < 0.001$, n.s. (not significant) $p \geq 0.05$. The numbers of puncta P, images n, and experiments N are indicated in the figure. The pulling data is published [11].

Before pulling FRET indices of tension sensor and no-force control are comparable, which confirms the result of the unstressed MEK-wt monolayer when FRET efficiencies are determined using FLIM (Sec. 5.3.1). During external stress, the FRET index of the tension sensor specifically drops as compared to the no-force control. This decrease in FRET index is transient and FRET indices of tension sensor and no-force control are statistically not different after relaxation. Note, the FRET index of the no-force control also drops between subsequent images, which can be explained by the intensity-dependence of FRET indices. Photobleaching during imaging, however, affects tension sensor and no-force control to the same degree, so that the comparison between both constructs remains unaffected by photobleaching. In summary, DPII experiences tension in MEK-wt specifically and transiently during the application of external stress.

5.6.2 Tension Depends on the Magnitude and Orientation of External Stress

To evaluate the effects of magnitude and orientation of external stress, individual desmosomal puncta are matched between all three FRET images (Fig. 5.22). The distance between pull and post-pull position of an individual DSM is defined as *recoil distance* d_{r} and used as an estimator for the magnitude of external stress. To estimate the orientation of applied stress, the direction of the cell–cell contact is determined based on neighboring puncta and the acute angle between cell–cell contact and recoil vector is defined as *recoil angle* α_{r}.

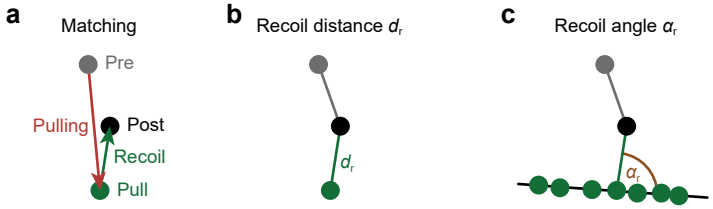

Figure 5.22: Recoil distance d_r and angle α_r are used to classify desmosomal puncta. (**a**) The centroids of individual desmosomal puncta before (Pre) and during (Pull) pulling are matched to the corresponding punctum after relaxation (Post). (**b**) The distance between pull- and post-puncta is defined as recoil distance d_r and serves as a proxy for the magnitude of external stress. (**c**) Similarly, the acute angle between recoil distance and cell–cell contact vector is defined as recoil angle α_r and serves as a proxy for the orientation of external stress. The schematic is published [11].

Magnitude Dependence

Desmosomal puncta are classified based on their recoil distance to estimate the effect of the magnitude of external stress (Fig. 5.23). As expected, puncta in the unstressed image before pulling show no difference between tension sensor and no-force control irrespective of the later recoil distance. This magnitude-independence confirms that no obvious artifacts are introduced by the matching of desmosomal puncta itself. During pulling, however, an increased recoil distance correlates with increased tension on DPII. After relaxation, no dependence of tension on the magnitude of external stress remains.

Looking at the behavior more closely, part of the response during pulling is independent of the recoil distance but once a distance threshold is surpassed the drop in tension sensor FRET index relative to the no-force control depends on the recoil distance. This behavior can be described using

$$\Delta I = a + \min\left(0, b \log \frac{d_r}{c}\right) \tag{5.1}$$

with the offset $a = 1.3(0.9, 1.6)$ (fit with 95 % CI), the steepness parameter $b = 1.6(1.0, 2.1)$ and the threshold distance that needs to be overcome of $c = 1.1(0.6, 1.6)$ µm. A fit of the pre-pull data with a constant value results in a FRET index difference close to zero, $\Delta I = 0.2(0.03, 0.4)$. After pulling, the FRET indices of tension sensor and no-force control are not statistically different (Fig. 5.21). Closely looking at the data, however, a small but not significant amount of tension seems to remain. Interestingly, the magnitude-dependent fraction of tension is entirely relaxed, while remainders of the magnitude-independent tension persist. The remaining tension is also reflected in the fit of the post-pull data with a constant value of $\Delta I = 0.6(0.4, 0.9)$.

In summary, the tension experienced by DPII increases with increasing external stress. In more detail, DP experiences a low amount of tension independent from the stress'

magnitude but also additional magnitude-dependent tension for recoil distances $d_r \gtrsim 1\,\mu m$. When cells stop relaxation after pulling, only the magnitude-dependent fraction entirely relaxes while some of the magnitude-independent tension seems to remain.

Orientation Dependence

Desmosomal puncta are classified based on their recoil angle to estimate the effect of the orientation of external stress (Fig. 5.24). In the unstressed monolayer none of the DSMs experiences tension, which is also reflected in a fit of the data with a constant value resulting in $\Delta I = 0.2(-0.06, 0.4)$. During pulling, DSMs experience increasingly more tension the closer the acute angle between cell–cell contact and recoil vector is to $\alpha_r = 90°$. As DP is oriented perpendicular to the cell–cell contact (Fig. 1.2), a recoil angle close to $\alpha_r = 90°$ indicates pulling along the major orientation axis of DP. To describe the simple hypothesis that tension is only experienced by DPII if external stress is applied

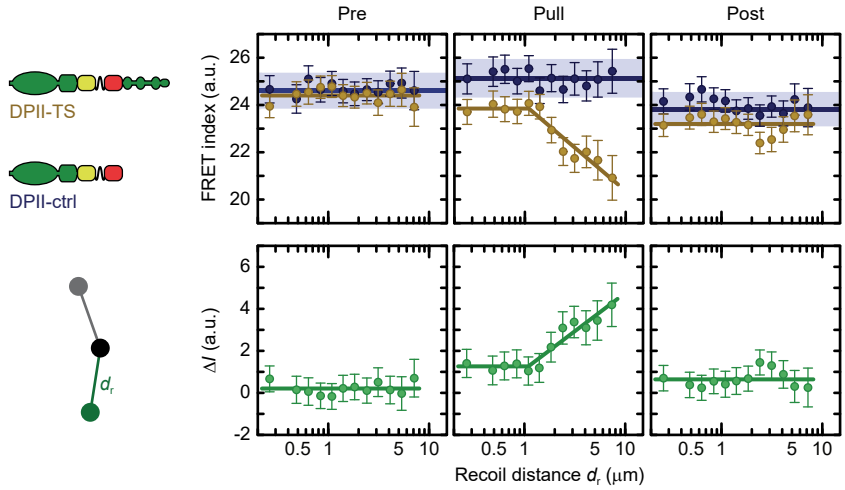

Figure 5.23: Tension across desmoplakin (DP)II depends on the magnitude of external stress. No tension is experienced by DPII before pulling (Pre). The tension during pulling (Pull) increases with increasing recoil distance, while no tension remains after cell sheet relaxation (Post). Puncta of DPII-ctrl (blue) and DPII-TS (yellow) are grouped based on their recoil distance. The FRET index difference $\Delta I = I_{\mathrm{DPII-ctrl}} - I_{\mathrm{DPII-TS}}$ (green) is calculated using lmer between distance-dependent DPII-TS data and the overall mean of DPII-ctrl. The data points with errorbars are the lmer-determined mean with 68 % CI. The blue lines and shadings are the lmer-determined mean with 95 % CI of all DPII-ctrl data. The yellow and green lines are fits to the data. Pre- and post-pull data is fitted with a constant value, while pull-data is fitted using Eq. 5.1 reflecting an initial magnitude-independent followed by a magnitude-dependent regime. A total of $P = 3198, 2449$ puncta before, $P = 3422, 2441$ during, and $P = 3664, 2826$ after pulling of DPII-TS and DPII-ctrl have a recoil distance below 10 μm. The raw data is the same as in Fig. 5.21. The magnitude-dependence is published [11].

along the major orientation axis of DP, pulling data is fitted using

$$\Delta I = a + b \sin\left(\frac{\alpha_r}{180\,\pi}\right). \tag{5.2}$$

The fit results in $a = -0.04(-0.6, 0.6)$, which is the FRET index difference for pulling with $\alpha_r = 0°$, and the scaling factor $b = 2.4(1.5, 3.2)$. Even though most of the tension is released after pulling (Fig. 5.21), some orientation-dependency seems to remain [$a = -0.6(-1.0, -0.1)$, $b = 0.8(1.0, 2.3)$].

In summary, the data can be described with the assumption that the DP tension sensor only reports tension along the major orientation axis of DP perpendicular to the cell–cell contact. This observation also directly implies that tension is not propagated through the keratin IF to neighboring DSMs with a different orientation towards the external stress.

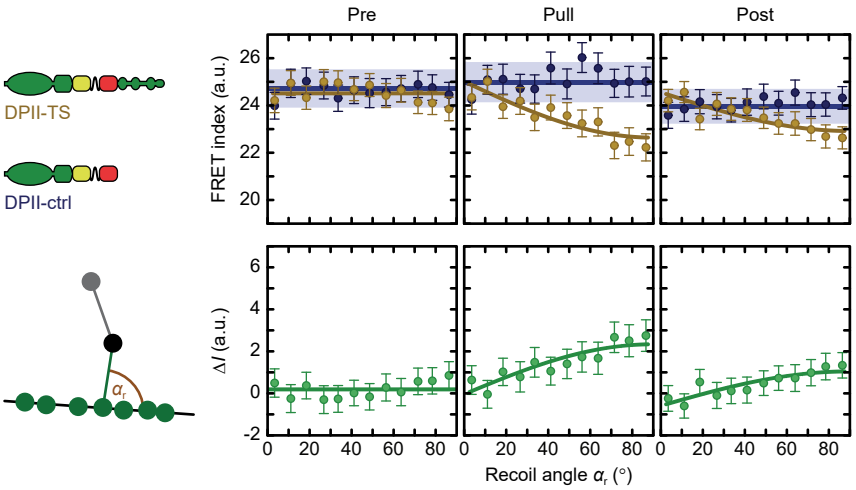

Figure 5.24: Tension across desmoplakin (DP)II depends on the orientation of external stress. Before pulling no tension is experienced by DPII (Pre). The tension during pulling increases with increasing recoil angle (Pull) and is partially released after cell sheet relaxation (Post). Puncta of DPII-ctrl (blue) and DPII-TS (yellow) are grouped based on their recoil angle. The FRET index difference $\Delta I = I_{\mathrm{DPII-ctrl}} - I_{\mathrm{DPII-TS}}$ (green) is calculated using lmer between angle-dependent DPII-TS data and the overall mean of DPII-ctrl. The data points with errorbars are the lmer-determined mean with 68 % CI. The blue lines with shadings are the lmer-determined mean with 95 % CI of all DPII-ctrl data. The yellow and green lines are fits to the data. Pre-pull data is fitted with a constant value, while pull- and post-pull data are fitted using Eq. 5.2 reflecting maximal tension for stress along the orientation of DP and no tension for orthogonal stress. For a total of $P = 1929, 1489$ puncta before, $P = 2164, 1550$ during, and $P = 2203, 1743$ after pulling of DPII-TS and DPII-ctrl recoil angles are determined with less than 9° uncertainty. The raw data is the same as in Fig. 5.21. The orientation-dependence is published [11].

Magnitude and Orientation Dependence

To test the interplay of magnitude and orientation dependence of tension, DSMs are classified based on their recoil angles as parallel, $\alpha_r \leq 45°$, or perpendicular, $\alpha_r > 45°$ (Fig. 5.25a). DSMs in cell–cell contacts parallel to the pulling direction experience no or only very little tension and no magnitude-dependency (Fig. 5.25b). Therefore, a fit with a constant value of $\Delta I = 0.7(0, 1.4)$ can be used to describe the data. DSMs in cell–cell contacts perpendicular to pulling direction, however, experience a strong magnitude-dependence of DPII tension. This dependence is also reflected in the fit using Eq. 5.1, which results in a magnitude-independent FRET index difference of $a = 0.7(-0.4, 1.8)$, a steepness factor of $b = 2.5(1.4, 3.6)$, and a minimal pulling distance that needs to be overcome of $c = 0.6(0.2, 1.1)$ µm. The confidence interval for the offset value a is considerably larger than if all puncta are fitted (Fig. 5.23). This increased uncertainty is caused by the reduced number of puncta in the fit. The steepness of the magnitude-dependence, however, clearly increases if only the perpendicular pulls are analyzed.

In summary, magnitude- and orientation-dependent effects are additive and DSMs that experience large external stress perpendicular to the cell–cell contact experience the highest tension across DPII.

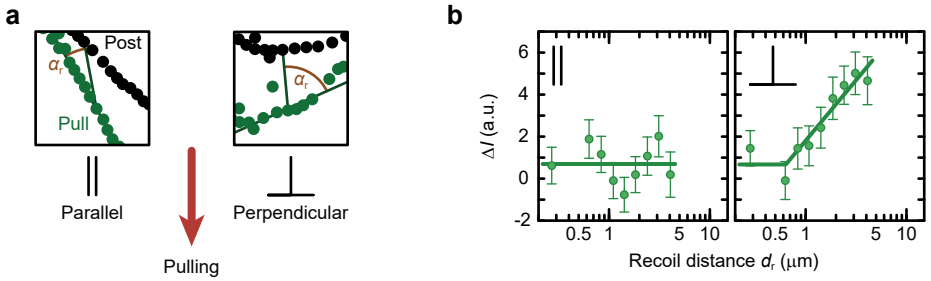

Figure 5.25: The magnitude and orientation dependence of desmoplakin (DP)II tension are additive. (**a**) Puncta are classified as parallel ($\alpha_r \leq 45°$) or perpendicular ($\alpha_r > 45°$). (**b**) Magnitude-dependent tension is only observed for perpendicular pulls. The FRET index difference $\Delta I = I_{\mathrm{DPII-ctrl}} - I_{\mathrm{DPII-TS}}$ is calculated using lmer between distance-dependent DPII-TS data and the overall mean of DPII-ctrl. The data points with errorbars are the lmer-determined mean with 68 % CI. The lines are fits to the data using a linear fit and Eq. 5.1 for puncta parallel and perpendicular to pulling direction, respectively. A total of $P = 1095,721$ and $P = 1057,738$ puncta of DPII-TS and DPII-ctrl from the same raw data as in Fig. 5.21 is assigned to parallel and perpendicular pulling direction, respectively. The magnitude and orientation dependence is published [11].

5.7 More Molecules Engage with Increasing External Stress

The pulling experiment with the F40-based TSM alone (Sec. 5.6) does not provide insights in the tension distribution across DPII molecules. The same decrease in FRET index could be caused if tension on engaged molecules increases or if more molecules are engaged (Sec. 2.3.3). The FL peptide opens switch-like and therefore allows to distinguish both effects (Sec. 2.3.1).

To learn more about the molecular distribution, pulling experiments in MEK-wt were repeated by Andrew J. Price with the FL-based DPII tension sensor constructs. Unexpectedly, the FRET index of the tension sensor is reduced compared to the no-force control

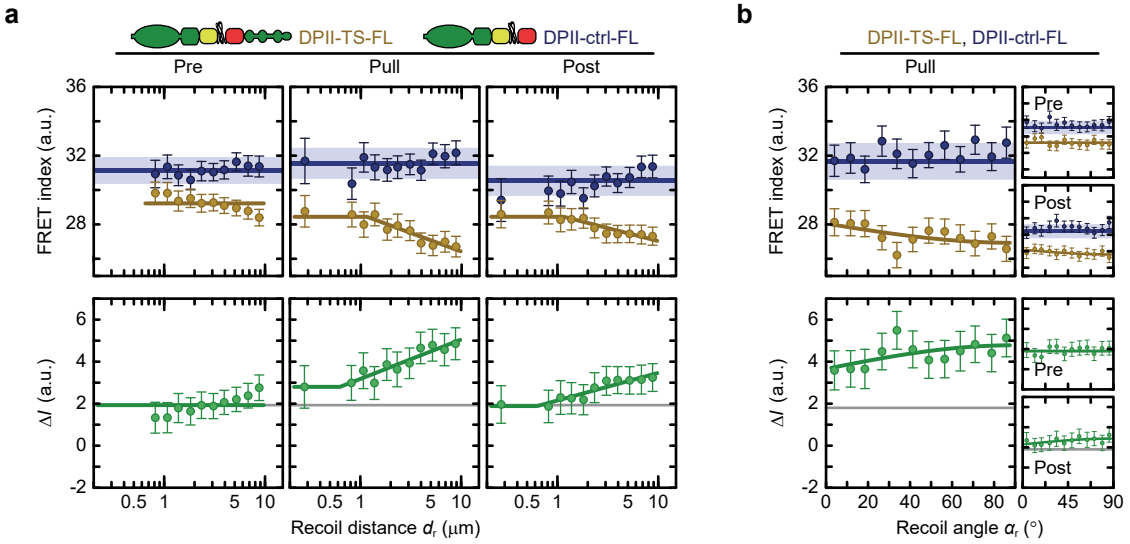

Figure 5.26: The tension across desmoplakin (DP)II exceeds 4 pN and more molecules are engaged during pulling. (**a, b**) Puncta of DPII-TS-FL (yellow) and DPII-ctrl-FL (blue) are grouped based on their recoil distance (**a**) or recoil angle (**b**). The FRET index difference $\Delta I = I_{\mathrm{DPII-ctrl-FL}} - I_{\mathrm{DPII-TS-FL}}$ (green) is calculated using lmer between distance- or angle-dependent DPII-TS-FL data and the overall mean of DPII-ctrl-FL. The data points with errorbars are the lmer-determined mean with 68 % CI. The blue lines with shadings are the lmer-determined mean with 95 % CI of all DPII-ctrl-FL data. The yellow and green lines are fits to the data. Pre-pull data is fitted with a constant value, while pull and post-pull data are fitted using Eq. 5.1 and Eq. 5.2 for distance- and angle-grouped data, respectively. The grey lines indicate the pre-pull linear fit result. A total of $P = 3118, 2163$ puncta before, $P = 3566, 2304$ during, and $P = 3525, 2247$ after pulling of DPII-TS-FL and DPII-ctrl-FL have a recoil distance below 10 μm. For a total of $P = 1143, 1042$ puncta before, $P = 1411, 1255$ during, and $P = 1360, 1183$ after pulling the recoil angles are determined with less than 9° uncertainty. Puncta are extracted from $n = 57, 57$ images before, $n = 58, 57$ during, and $n = 57, 57$ after pulling collected in $N = 6$ independent experiments performed on three experimental days by Andrew J. Price.

even in the unstressed monolayer (Fig. 5.26). This observation would indicate tension across DPII without external stress but FLIM measurements in the same condition reveal that no forces are experienced by DPII (Sec. 5.4.2). Therefore, the ratiometric FRET experiment described here should be considered as preliminary data because the reason for the discrepancy between ratiometric FRET and FLIM measurements remains unclear.

If the offset between tension sensor and no-force control prior to pulling is set as a new baseline, the magnitude-dependence of the FL-based tension sensor (Fig. 5.26a) resembles the F40-based tension sensor (Fig. 5.23). A fit of the pre-pull data with a constant value results in $\Delta I = 1.9(1.6, 2.3)$. All FRET index differences observed during pulling are considerably larger than this baseline. The data is fitted using Eq. 5.1 to reflect the initial magnitude-independent followed by a magnitude-dependent regime resulting in $a = 2.8(2.1, 3.5)$, $b = 0.8(0.5, 1.1)$, and $c = 0.6(0, 1.3)$ µm. After pulling, most of the tension is released but some magnitude-dependency remains. Therefore, Eq. 5.1 is used with the threshold distance $c = 0.6$ µm determined during pulling. The offset $a = 1.9(1.6, 2.1)$ reaches again the baseline level of the unstressed monolayer, while the steepness of $b = 0.6(0.4, 0.7)$ reflects some remaining magnitude-dependent tension even after cells stopped relaxing.

The baseline of angle-grouped data in the unstressed monolayer (Fig. 5.26b) recaptures the distance-grouped value with $\Delta I = 1.9(1.6, 2.1)$. Fitting the data during pulling using Eq. 5.2 results in a FRET index difference at $\alpha_r = 0°$ of $a = 3.7(2.9, 4.4)$, which is considerably above the baseline. The FRET index dependency from the angle is with $b = 1.1(0.1, 2.2)$ relatively small compared to the F40 data (Sec. 5.6.2). After pulling, tension across DPII relaxes largely to baseline values but the small angle dependency persists, which is also reflected in the fit results using Eq. 5.2, which are $a = 2.3(1.9, 2.7)$ and $b = 0.6(0, 1.2)$.

In summary, tension across DPII surpasses 4 pN as the FL-based tension sensor is opened. Furthermore, the FL peptide is either open or closed, so that the increasing tension with increasing external stress means that more DPII molecules are engaged and experience forces.

5.8 Tension Is Not Transduced across the Keratin IF

The analysis described above is focused on DSMs at the individual cell–cell contact that is pulled. Forces, however, are also transmitted further through the cell sheet. DSMs at the other side of the cell are not directly pulled and keratinocytes deform to cope with the external stress but still some DSMs at the opposite cell side move along the pulling direction. For pulling experiments with the FL-based tension sensor (Sec. 5.7), sufficient desmosomal puncta at the opposite cell side moved to analyze them

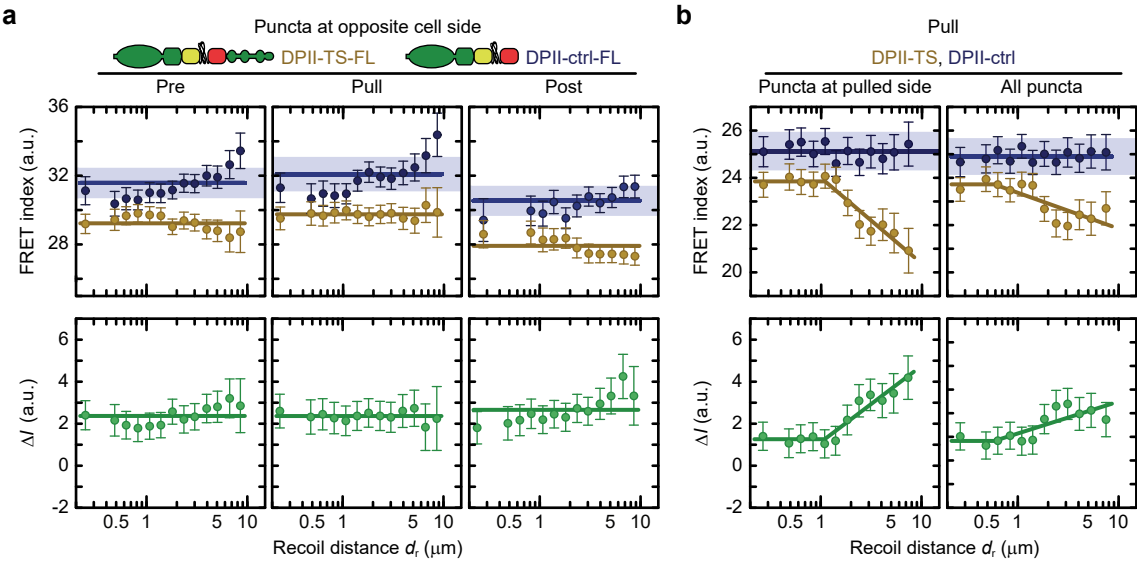

Figure 5.27: The tension is not transduced across the cell via the keratin intermediate filament (IF). (**a**) Desmosomal puncta at the cell side opposite of the pulling show a FRET index difference $\Delta I = I_{\mathrm{DPII-ctrl-FL}} - I_{\mathrm{DPII-TS-FL}}$ (green) between DPII-ctrl-FL (blue) and DPII-TS-FL (yellow) already before pulling (Pre). This difference, however, does not change during pulling (Pull) and is also similar after pulling (Post). (**b**) Desmosomal puncta at the pulled cell–cell contact in MEK-wt show a magnitude-dependent decrease in FRET index for the F40-based tension sensor (DPII-TS, yellow) as compared to the no-force control (DPII-ctrl, blue). The increase in the FRET index difference $\Delta I = I_{\mathrm{DPII-ctrl}} - I_{\mathrm{DPII-TS}}$ (green), however, is less pronounced if also puncta at the opposite cell side are included in the data analysis. Puncta of tension sensor and no-force control constructs are grouped based on their recoil distance. The FRET index difference is calculated using lmer between distance-dependent tension sensor and the overall mean of no-force control data. The data points with errorbars are the lmer-determined mean with 68 % CI. The blue lines with shadings are the lmer-determined mean with 95 % CI of all no-force control data. The yellow and green lines are fits to the data. FL-based data is fitted with a constant value, while F40-based pull-data is fitted using Eq. 5.1 reflecting an initial magnitude-independent followed by a magnitude-dependent regime. A total of $P = 4661, 4023$ puncta before, $P = 4952, 4533$ during, and $P = 4840, 4325$ after pulling of DPII-TS-FL and DPII-ctrl-FL at the opposite cell side have a recoil distance below 10 μm. For the F40-based constructs, puncta numbers increase from $P = 3422, 2441$ puncta at the pulled side to $P = 4031, 2751$ puncta if all puncta are taken into account. The raw data is the same as in Fig. 5.26 (**a**) and Fig. 5.21 (**b**).

separately (Fig. 5.27a). For the F40-based experiments (Sec. 5.6), however, not enough puncta are available and therefore the effect of these DSMs is regarded more indirectly: puncta at the pulled side only are compared to all desmosomal puncta irrespective of their location (Fig. 5.27b).

Remarkably, no tension seems to be experienced by DSMs that are not directly pulled. This is reflected in fits of the FL-based tension sensor data (Fig. 5.27a) with a constant value: Fit results are very similar before [$\Delta I = 2.4(2.1, 2.6)$], during [$\Delta I = 2.4(2.2, 2.5)$], and after [$\Delta I = 2.7(2.3, 3.0)$] pulling.

In line with the hypothesis that no tension is experienced by DSMs at the cell side opposite to the pulling direction, the strong magnitude-dependency observed for desmosomal puncta at the pulled side for the F40-based constructs is reduced if all puncta are analyzed (Fig. 5.27b). Consequently, the steepness of the magnitude dependence is reduced also in fits using Eq. 5.1 from $b = 1.6(1.0, 2.1)$ to $b = 0.7(0.2, 1.1)$. The offset is relatively unaffected by the additional puncta and changes from $a = 1.3(0.9, 1.6)$ to $a = 1.2(0.4, 1.9)$. Probably, due to the reduced steepness, the kink point that reflects the distance threshold has a larger uncertainty: while the threshold for pulled puncta is $c = 1.1(0.6, 1.6)$ µm, the kink point for all puncta is fitted with $c = 0.6(-0.3, 1.5)$.

Taken pulling experiments with both linker peptides together, no forces are experienced by DPII in desmosomal puncta at the cell side opposite to the pulling direction. This observation also implies that tension is not transduced through the cell via the keratin IF.

5.9 Complementary Measurements of DPI

5.9.1 Desmoplakin I Tension Sensor by Andrew J. Price

Independent of my development of a set of DP tension sensors, Andrew J. Price also developed a DPI tension sensor very similar to my construct (Fig. 5.28, Sec. 5.1.1). The TSM is also F40-based and integrated at the same structural integration site between central coiled-coil rod and C-terminus. The specific integration site, however, is chosen seven aa earlier after R1945 at the beginning instead of the middle of the unstructured 14 aa stretch. Furthermore, additional flexible linker regions of 25 and 24 aa, respectively, surround the TSM while my constructs have only two and three additional amino acids. The most striking difference between the tension sensors, however, is the FRET pair: Andrew's constructs harbor the blue/yellow FRET pair mTFP1/EYFP, while my constructs use the yellow/red combination YPet/mCherry (Sec. 2.4.2).

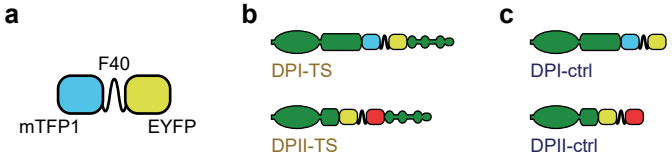

Figure 5.28: The desmoplakin (DP)I tension sensor by Andrew J. Price is similar to the DPII tension sensor. (**a**) The tension sensor module (TSM) comprises of the F40 linker peptide and the FRET pair mTFP1/EYFP. (**b**) The structural TSM integration site between central coiled-coil rod and C-terminus is the same for DPI and DPII tension sensors. (**c**) The no-force control lacks the C-terminal keratin binding domain. The construct schematics are published [11].

Andrew generated doxycline-inducible overexpression MDCK cell lines and performed tension sensor experiments using FLIM or SE-FRET. Similar to the results for DPII (Sec. 5.3), DPI in MDCK cells does not bear tension at different cell seeding densities, at the edge of migrating cell sheets and when the F-actin or keratin cytoskeletons are disrupted [11]. We therefore together analyzed tension in the case of external stress.

5.9.2 DPI Experiences No or Little Tension in Keratinocytes

Keratinocytes express both major DP isoforms to comparable levels (Fig. 5.3). To test whether both isoforms respond similar to tension, the pulling experiment was performed with DPI transiently overexpressed in MEK-wt. To preserve best comparability with the measurements of DPI in MDCK cells (Sec. 5.9.3), we used Andrew's DPI constructs.

Already before pulling, the FRET index of the tension sensor is reduced as compared to the no-force control (Fig. 5.29a), which indicates a low amount of tension already in the unstressed monolayer. However, a similar offset in the FL-based DPII constructs is an artifact (Sec. 5.7) and therefore care should be taken also when interpreting the pulling experiment of DPI in MEK-wt. The data before, during, and after pulling can be described using constant values of $\Delta I = 1.7(1.5, 2.0)$ before, $\Delta I = 2.5(1.9, 3.1)$ during, and $\Delta I = 1.2(0.4, 2.0)$ after pulling, which indicates a slight increase in the FRET index difference during pulling but the large data spread prevents a definite statement. Thus, even though no magnitude-dependent tension is experienced by DPI in keratinocytes, DPI might experience a small amount of magnitude-independent force in keratinocytes.

The binding of DP to the keratin IF is key to forces across the DSM. To test the effect of increased binding to the keratin IF, Andrew introduced the S2849G point mutation that also increases overall forces at the cell–cell interface (Sec. 1.8.5). Mutated DPI, however, is not loaded in a magnitude-dependent fashion upon the application of external stress (Fig. 5.29b). Instead, the data can be described with a constant value of $\Delta I = 1.5(1.1, 2.0)$ before, $\Delta I = 2.6(2.2, 2.9)$ during, and $\Delta I = 1.1(0.7, 1.6)$ after pulling.

Hence, increased binding to the keratin IF does not introduce any additional tension on DPI in keratinocytes.

In summary, the FRET index difference is transiently increased during pulling, which could indicate a small amount of magnitude-independent tension experienced by DPI upon external stress. In contrast to DPII in MEK-wt (Sec. 5.6), however, tension across DPI in MEK-wt does not depend on the magnitude of external stress. Furthermore, a mutant version with increased binding to the keratin IF does not change tension across DPI.

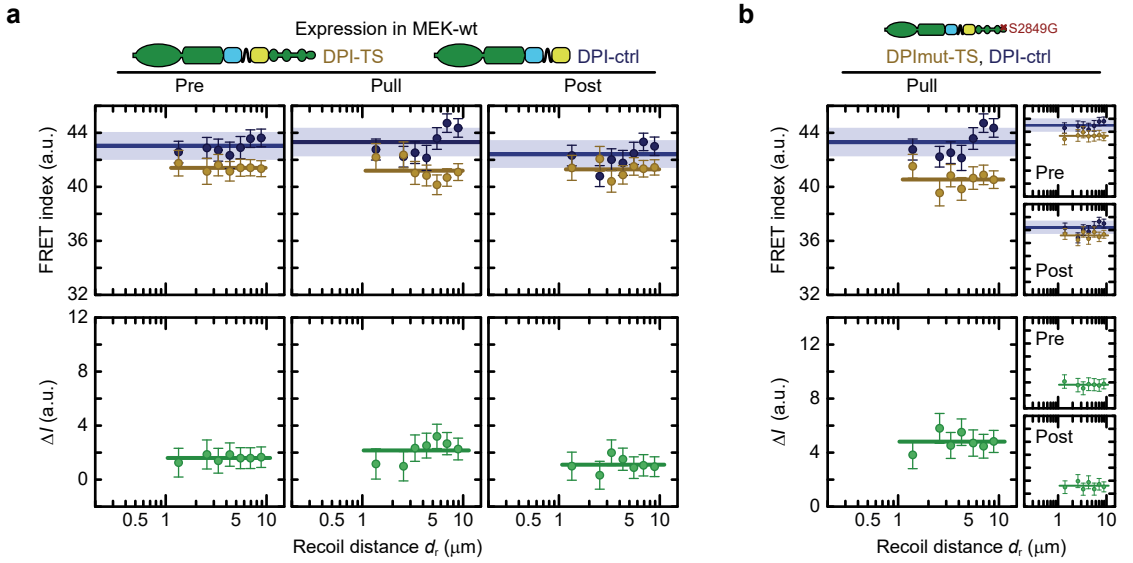

Figure 5.29: No or little tension is experienced by desmoplakin (DP)I in keratinocytes. (**a**) The tension sensor shows a reduced FRET index (DPI-TS, yellow) as compared to the no-force control (DPI-ctrl, blue) already before pulling in confluent MEK-wt one day after induction of DSM formation (Pre). This difference only slightly changes upon pulling (Pull) and subsequent relaxation (Post). (**b**) Enhancing the keratin binding by S2849G point mutation does not introduce recoil distance-dependent tension. The puncta are grouped based on their recoil distance. The FRET index difference $\Delta I = I_{\mathrm{DPI-ctrl}} - I_{\mathrm{DPI-TS}}$ (green) is calculated using lmer between distance-dependent DPI-TS data and the overall mean of DPI-ctrl. The data points with errorbars are the lmer-determined mean with 68 % CI. The blue lines with shadings are the lmer-determined mean with 95 % CI of all DPI-ctrl data. The yellow and green lines are fits to the data with a constant value. DPI-ctrl data is the same for (**a**) and (**b**). A total of $P = 1478, 1272, 2198$ puncta before, $P = 1669, 1535, 2785$ during, and $P = 1625, 1390, 2582$ after pulling of DPI-TS, DPImut-TS and DPI-ctrl puncta have a recoil distance below 10 μm. Puncta are extracted from $n = 36, 35, 41$ images before, $n = 38, 38, 43$ during, and $n = 36, 38, 40$ after pulling collected in $N = 6$ independent experiments performed on three experimental days by Andrew J. Price. The magnitude-dependent pulling data is published [11].

5.9.3 DPI Experiences Tension During Pulling in MDCK Cells

DPI is also expressed in simple epithelia and therefore MDCK monolayers expressing DPI tension sensor constructs were pulled similar to MEK-wt (Sec. 5.6). MDCK cells adhere less to the substrate, which leads to larger pulling distances before rupture (Fig. 5.30a). In line with FLIM measurements of unstressed monolayers [11], no tension is experienced by DPI before pulling (Fig. 5.30b, c). Upon pulling, tension is experienced by DPI and then reduced after cell sheet relaxation.

Similar to tension across DPII in keratinocytes (Sec. 5.6.2), tension across DPI in MDCK depends on the magnitude of external stress (Fig. 5.31a). Before pulling no tension is experienced by DPI and the magnitude-dependent data can be described with $\Delta I = 0.2(0, 0.4)$. During pulling, however, tension across DPI in MDCK monolayers depends on the magnitude of external stress and can be fit using Eq. 5.1. The magnitude-independent

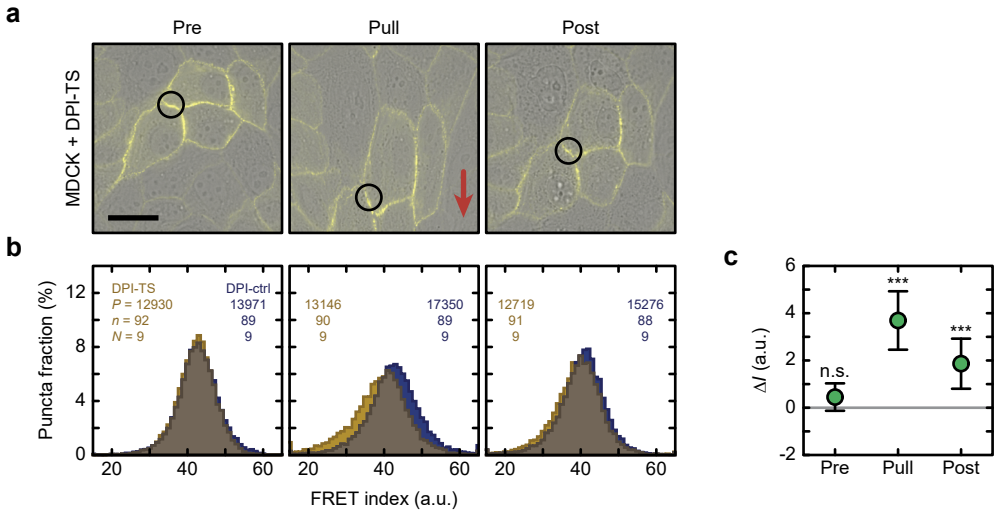

Figure 5.30: Desmoplakin (DP)I experiences tension during pulling in MDCK monolayers. (**a**) The FRET index is determined for individual desmosomal puncta in the unstressed monolayer (Pre), at the maximal displacement of pulling with a glass micropipette (Pull), and after cell sheet relaxation (Post). The red arrow indicates the pulling direction. The circles mark one cell–cell contact. (**b**) FRET indices for DPI tension sensor (DPI-TS, yellow) and no-force control (DPI-ctrl, blue) constructs in MDCK monolayers are indistinguishable before pulling. Tension is experienced by DPI during pulling as indicated by a lower FRET index for DPI-TS, which partially recovers after relaxation. (**c**) The FRET index difference $\Delta I = I_{\mathrm{DPI-ctrl}} - I_{\mathrm{DPI-TS}}$ shows that the decrease in FRET is statistically significant during and after pulling. The contrast-adjusted brightfield images are superimposed with EYFP signal for DPI-TS. Scale bar: 20 µm. The ΔI data points with errorbars are the lmer-determined mean with 95 % CI. The numbers of puncta P, images n, and experiments N are indicated in the figure. lmer-test: *** $p < 0.001$, n.s. (not significant) $p \geq 0.05$. The pulling example images and data are published [11].

offset is $a = 2.5(2.1, 2.8)$, the steepness $b = 6.1(4.8, 7.4)$, and the threshold distance after which tension depends on the recoil distance is $c = 2.9(2.4, 3.3)$ µm. After pulling, some of the magnitude-dependent tension remains, which is also reflected in a fit of the post-pull data using Eq. 5.1 with the threshold value $c = 2.9$ µm determined during pulling. Both magnitude-independent offset, $a = 1.3(0.9, 1.6)$, and the magnitude-dependent steepness, $b = 2.8(2.4, 3.9)$, reduce compared to the data during pulling, which reflects a partial tension release.

During pulling of MDCK monolayers, some cells are moved by more than a cell length and thereby also change their shape (Fig. 5.30a). Therefore, the angle determination based

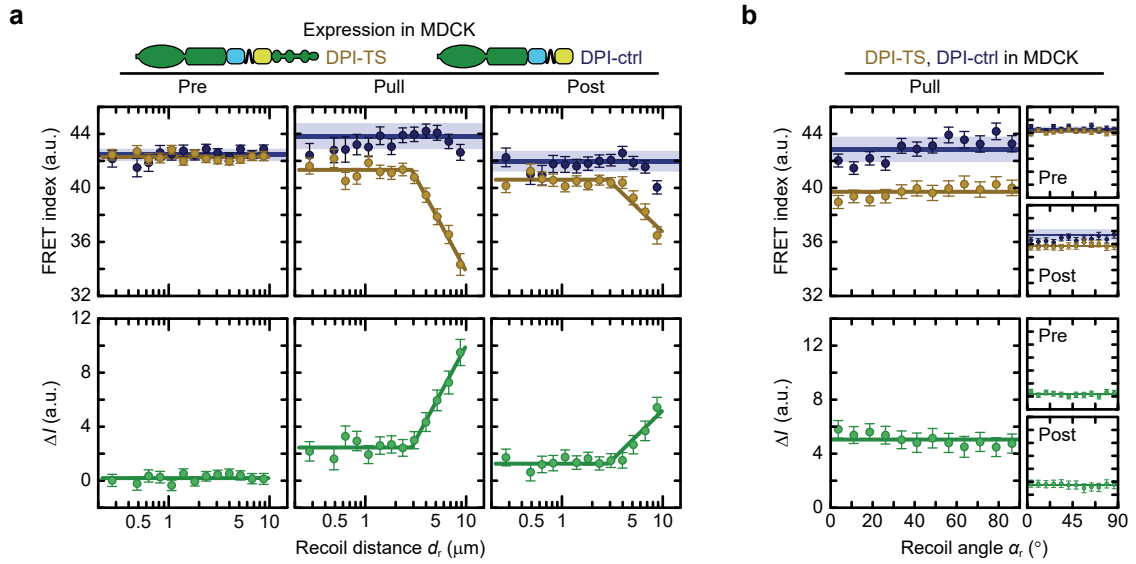

Figure 5.31: The tension across desmoplakin (DP)I depends on the magnitude of external stress but not on the recoil angle. (**a**) Before pulling no tension is experienced by DPI (Pre). The tension during pulling increases with increasing recoil distance (Pull), while tension is partially released after cell sheet relaxation (Post). (**b**) DPI tension does not depend on the recoil angle. Puncta of DPI-ctrl (blue) and DPI-TS (yellow) are grouped based on their recoil distance (**a**) or angle (**b**). The FRET index difference $\Delta I = I_{\mathrm{DPI-ctrl}} - I_{\mathrm{DPI-TS}}$ (green) is calculated using lmer between distance- or angle-dependent DPI-TS data and the overall mean of DPI-ctrl. The data points with errorbars are the lmer-determined mean with 68 % CI. The blue lines and shadings are the lmer-determined mean with 95 % CI of all DPI-ctrl data. The yellow and green lines are fits to the data. Pre-pull and angle-dependent data are fitted with a constant value, while pull- and post-pull distance-dependent data are fit using Eq. 5.1 reflecting an initial magnitude-independent followed by a magnitude-dependent regime. A total of $P = 13040, 9395$ puncta before, $P = 13669, 12231$ during, and $P = 13511, 11319$ after pulling of DPI-TS and DPII-ctrl have a recoil distance below 10 µm. For a total of $P = 9714, 8803$ puncta before, $P = 10192, 11436$ during, and $P = 9744, 9826$ after pulling recoil angles is determined with less than 9° uncertainty. The raw data is the same as in Fig. 5.30. The pulling data is published [11].

on the orientation of neighboring puncta during pulling (Fig. 5.22) might oversimplify the real orientation of the external stress. In fact, the orientation-dependent data distribution can be described with constant values of $\Delta I = 0.4(0.2, 0.5)$ before, $\Delta I = 3.1(2.8, 3.3)$ during, and $\Delta I = 1.5(1.3, 1.7)$ after pulling. The recoil angle independence of tension across DPI in MDCK cells is in contrast to the angle dependence of tension across DPII in keratinocytes (Sec. 5.6.2). Note, the recoil angle independence of DPI data can either reflect a biological difference in the orientation dependence of DP isoforms or model cell lines or result from a limitation of the orientation-determination method.

In summary, tension is experienced by DPI in confluent MDCK monolayers upon external mechanical stress. Similar to DPII in MEK-wt, tension also depends on the magnitude of external stress after a minimal distance threshold is surpassed but is independent of the recoil angle. Thus, the forces experienced by DP are cell-type and isoform-specific.

6 Discussion

6.1 Fluorescence Lifetime Analysis and Merge Software

The fluorescence lifetime analysis and merge software (FLAMES) is developed as part of this work and used to analyze FLIM data from tension sensor experiments. One design focus of the software was user-friendliness, which not only accelerates routine tasks and allows for more advanced analysis but also enables users without programming experience to analyze data in a standardized fashion. The focus on user-friendliness is, for example, reflected in the files required to analyze data with FLAMES. A MATLAB document with executable cells is used to perform the data analysis. Settings that are often changed, e.g. which merge names to display in the plot, can be defined directly in this document. All other settings are clearly presented in a second MATLAB document along with brief explanations, where they can also be changed from their default. In an EXCEL file, the data to be merged is identified. The merge file contains one row per experiment with the merge name and the information to identify a specific data set and its controls.

The software is also programmed to provide high flexibility for data evaluation and a range of characteristic properties. If multiple masks are drawn on one image, for instance, previous masks are displayed. The name of the *maskInfo* file can be changed, which allows to draw independent sets of masks, e.g. for different substructures. Different thresholding and fitting can be performed on the same set of manual masks and unambiguously referred to by their name in the continuous EXCEL sheet used to merge data. In addition, the lifetime, photon count, and FRET data are automatically saved and can therefore be easily imported in other programs, e.g. in R for advanced statistical analysis. Next to the data, also extensive meta-information is saved including the numbers of (sub)-masks, images, and experiments that indeed fulfilled the applied data inclusion criteria, the median and mean with standard deviation, and whether data sets are normally distributed. In addition, a range of plots is predefined and can be enabled with a logical. These plots allow easy access to many properties of the data such as intensity-dependence and day-to-day variability. To facilitate the identification of user errors in the critical step of merge name assignment, data sets can be labeled with their identification parameters.

In comparison to the precursor software, FLAMES not only improves user-friendliness but also encompasses a range of additional functions and improves performance. The initial data import is now faster but the gain in time is largely used to resave the raw data as a sparse matrix, so that the import takes approximately the same time. However, the sparse matrix contains all information in reduced disk space and reading the sparse matrix data is much faster than reimporting the raw data after manual masking. Therefore, FLAMES is responsive, i.e. is not impaired by slow data access. Furthermore, masking is now performed by a matrix multiplication of masks with the sparse matrix, which is a fast process. Therefore, spatially-resolved FLIM images can be generated from many small masks. Moreover, the average donor-only lifetime is now not necessarily determined from one experiment but can alternatively be calculated from the merge of the corresponding donor-only measurements, a list of donor-only experiments, or from a fixed value. Another major new function is bi-exponential fitting and the related ratio determination of stretched molecules. In addition, the merging function is new and replaces manual lists of entry numbers in manually loaded *pathInfos* by one Excel sheet. Finally, data and meta-information are now saved and supportive data visualization can be generated.

Commercial software from PicoQuant[1] and Leica[2] include next to tail fitting also the deconvolution with the IRF as an alternative to determine the lifetime. This approach uses the information from all photons, while in tail fitting the first time bins are excluded and only about 30 % of the total photon count are used for the fit. This improved photon usage, however, requires the knowledge of the IRF and IRF determination introduces a new error source. An advantage of the deconvolution method is that it can fit data with side maxima of the IRF. These commercial softwares, however, aim for a broad audience and are therefore not adapted to the specific needs of automated analysis. Start and end points of fits, for example, have to be manually set for each image and thresholding is largely based on recognition of similar brightness levels to a manually-selected reference within the image. This manual selection within each image prevents an automated signal extraction procedure. The main focus of the commercial software is the image acquisition and they also provide lifetime fits and data display of individual images. These softwares, however, cannot merge, exclude or plot data across experimental days or even multiple images.

FLAMES is still under development and therefore additional features remain to be implemented. These features include deconvolution with the IRF, advanced filter mechanisms based on submask properties, e.g. divide submasks in roundish versus elongated structures, and further data visualization. In addition, the software lacks import routines to allow compatibility with other microscope setups, e.g. an import routine for the per-

[1] SymPhoTime 64, PicoQuant, 2019
[2] LAS X in SP8 FALCON, Leica, 2019

former terrain utilities (PTU) file format. To further increase the outreach of the software, FLAMES could be transferred to an open-source programming language, e.g. PYTHON.

In summary, FLAMES facilitates and largely automates FLIM data analysis. The software has the potential to standardize live-cell FLIM data analysis in other laboratories, especially if it is accessible without the need for expensive MATLAB licenses and accompanied with a comprehensive documentation.

6.2 Molecular Stretch Ratio Determination

The classical method to analyze FRET-based tension sensor experiments is to determine an average FRET efficiency or index. This average FRET value is then used to compare tension sensor and no-force control constructs in different conditions [185, 213]. The relative changes in FRET thereby provide information about the relative forces. To relate these FRET values to forces, an assumption about the underlying molecular distribution has to be made. With the assumption of equal force distribution, an average force per molecule can be determined by relating the observed FRET efficiency to the single-molecule calibration of the tension-sensitive linker peptide. For the FA protein vinculin, for example, an average force per molecule of approximately 2.5 pN was determined with an F40-based vinculin tension sensor [185]. Similar average forces of approximately 1.5 pN and 2.0 pN were also observed for β-spectrin in the neuronal spectrin cortex of *Caenorhabditis elegans* (*C. elegans*) [227] and AJ cadherins in epithelial cells under shear flow [288], respectively. The underlying assumption that all molecules experience the same small amount of tension, however, is challenged by the observation that a considerable amount of vinculin molecules experiences forces above 6 pN [270]. A more conservative approach to translate the observed FRET values into forces is to only use the absolute information whether or not sufficient forces act on the molecule to open the linker peptide, i.e. when the FRET value of the tension sensor is below the no-force control, the force across some molecules exceeds the minimal force required to partially unfold the tension-sensitive linker peptide. To narrow the force range, linkers of different stiffness can be combined [217].

The determination of the molecular stretch ratio developed in the course of this thesis provides an alternative method to analyze tension sensor experiments. In contrast to the calculation of an average force, where the same gradual opened state is assumed for all molecules, the ratio determination is based on the assumption that tension sensor molecules only exist in two states, i.e. tension sensors are either fully open or remain closed. The assumption of two distinct states is particularly valid for FL-based TSMs because this linker peptide opens switch-like in a narrow force range [216] and intermediate states are therefore likely negligible. However, the stretch ratio can be

determined irrespective of the employed linker peptide with the assumption that tension across the protein of interest is either absent, i.e. too small to be detected by the tension sensor, or sufficiently large to fully open the linker. With this assumption, a bi-exponential fit is used to determine the relative contribution of stretched and non-stretched tension sensor molecules to the observed photon count. The ratio determination can thereby also take the incomplete acceptor chromophore maturation into account, which provides the unique opportunity to directly compare the fit result determined from measurements in living cells with an *in vitro* experiment. Indeed, the relative amount of fluorescently-active mCherry in the no-force control data is estimated to 42 %, which agrees well with the 43 ± 1 % of mCherry that flickers in *in vitro* FCS measurements [278], which lends further support to the reliability of the ratio determination. The ratio determination has already been applied to determine the relative amount of stretched talin molecules in FA of fibroblasts [216] and in the muscle attachment sites of developing *Drosophila* pupae [230].

In summary, the ratio determination opens another perspective on tension sensor experiments. The determination of the relative amount of stretched molecules thereby complements the determination of an average FRET efficiency.

6.3 Tension Sensor Development and Measurement

A number of insights were gained during the development of the DP tension sensor that might also help in future development of tension sensors for other proteins. First, the donor-only control construct has to be carefully selected. The donor lifetime depends on the microenvironment [233] and the microenvironment can differ between constructs. Typically, tension sensor constructs use a construct that only includes the donor fluorophore as donor-only control [185, 216, 217, 230, 281]. For DP, however, the YPet lifetime in the respective internal and truncated constructs are different. This difference is specific to the type of donor-only control used. In contrast, in constructs with non-fluorescent acceptor mimetics, i.e. TagBFP and mCherry(Y72L), the lifetime of YPet is indistinguishable between internal and truncated constructs. As differences in the donor-only lifetime are directly transferred into differences in the resulting FRET efficiency, using an inappropriate donor-only control hinders reliable interpretation of the tension sensor experiment. Importantly, for the biological interpretation of the FRET efficiency, the donor-only controls have to reliably report differences between tension sensor and no-force control constructs. On the other hand, the absolute lifetime values are only of minor interest. Based on the various DP constructs, rendering the acceptor non-fluorescent with a single point mutation, e.g. Y72L for mCherry [282], turned out to be the best suited donor-only control because these donor-only controls differ only minimally from the corresponding tension sensor and no-force control constructs.

Second, the averaging of the donor-only control deserves attention. The corresponding donor-only controls should be measured in all experiments alongside tension sensor and no-force control constructs to report on lifetime changes between experimental days. For the calculation of the FRET efficiency, however, all donor-only lifetimes should be merged that only differ by statistical variations. The distinction between both types of changes to the donor-only control, i.e. statistical and systematical variations, is inherently difficult. For DP, comparing changes in different donor-only controls, YPet alone and TSM with TagBFP or mCherry(Y72L), at the same experimental conditions, allowed to distinguish these effects. If the underlying biology caused a systematic difference in donor lifetime, the change should be reflected in all constructs. Of note, some differences of the pairwise comparisons are significant and would also cause differences in the resulting FRET efficiencies. The trends between the three different constructs, however, are inconsistent and therefore a single average lifetime for all conditions is used in this work. Similarly, donor-only controls for tension sensor and no-force control are averaged because differences are only rarely observed and therefore likely reflect statistic and not systematic changes. The donor lifetime might well differ between conditions in other settings, so averaging over all experimental conditions is not necessarily optimal to determine the donor-only lifetime. As even small lifetime differences might cause significant changes in the resulting FRET efficiencies, care should be taken how to average the donor-only control also in future projects.

Third, the FRET efficiency of the no-force control depends on its design. For DP, the FRET efficiency of the C-terminal tagged protein is considerably lower than the FRET efficiencies of the truncated or internal construct. This difference might be caused by the different microenvironment. The C-terminus binds to the keratin IF, which might change the local environment as compared to the internal integration before the IF binding sites. Thus, different no-force controls might need to be compared to identify the no-force control that best reflects the tension sensor.

Fourth, photobleaching of the acceptor during FLIM measurements increases the donor lifetime in subsequent repeats. The donor fluorophore that is paired with a bleached acceptor does not undergo FRET and therefore contributes with the non-quenched lifetime. In tension sensor experiments, the absolute FRET efficiency is only of minor interest but instead changes in FRET are interpreted. Therefore, the change in average FRET caused by photobleaching of the acceptor does not affect biological interpretations as long as tension sensor and no-force control are measured with the same acquisition parameters. In this work, all tension sensor and no-force control measurements comprise of 100 repeats to also allow spatially-resolved image processing.

Finally, the presence of intermolecular FRET per se does not prevent tension sensor experiments. The observed FRET efficiency in tension sensor experiments always comprises of both intra- and intermolecular FRET. In tension sensor experiments, the contribution

of intermolecular FRET is typically small and can be neglected, e.g. for the talin tension sensor [217]. DPII, however, has a considerable amount of intermolecular FRET, which changes the absolute value of the observed FRET efficiencies. Biological conclusions, however, are based on the comparison of tension sensor and no-force control and are therefore unaffected by intermolecular FRET as long as tension sensor and no-force control experience a comparable level. Indeed, DPII tension sensor and no-force control show comparable levels of intermolecular FRET. The effect of intermolecular FRET on the absolute FRET efficiency, however, can be seen in the comparison of constructs expressed in MEK-wt and MEK-KO. The level of intermolecular FRET is increased in the absence of endogenous proteins and also the FRET efficiency observed for the DPII tension sensor is elevated. Note that the FRET efficiencies determined in intermolecular FRET measurements cannot be directly transferred to the tension sensor experiment because only every other molecule contains donor and acceptor, and coexpression levels were judged by eye in cells cotransfected with donor- and acceptor-only constructs. Nevertheless, intermolecular FRET is comparable between tension sensor and no-force control and therefore differences in the tension sensor experiment cannot be attributed to differences in intermolecular FRET.

6.4 Desmosomes Act as Stress Absorbers

6.4.1 Unstressed Monolayers

While the importance of DSMs for the mechanical integrity of skin and heart tissues has long been recognized [22, 88], only recently the contribution of DSMs to cell–cell adhesion forces is analyzed [149, 152]. The DP tension sensor now allows for the first time to directly access forces at DSMs. Tension sensor measurements on stiff substrates show that no tension is experienced by DP in unstressed monolayers. The F-actin-bound AJs, however, experience tension also in homeostatic conditions [174, 226, 289]. Together, these observations imply that the actomyosin-generated tension is not transferred to DSMs, which is consistent with the pronounced elasticity of the IF network at low strain [50, 54] that might dissipate forces. In apparent conflict to the tension sensor experiment, measurements with the α-catenin conformation-specific antibody α18 indicate that tension across AJs increases if DSMs are disrupted [152] suggesting that DSMs share the load in the undisturbed situation. These different observations might indicate tension across DSMs that is not sensed by the DP tension sensor. An alternative explanation, however, is that the α18 antibody reflects increased clustering rather than increased tension in AJs when the DSM–IF linkage is disturbed [149, 153]. To learn more about the interdependence of tension across the two major cell–cell adhesion structures, a tension sensor

for an AJ protein, e.g. E-cadherin [225], might be measured simultaneously with the DP tension sensor if TSMs with separable fluorophore colors are employed [216, 249].

In unstressed monolayers, no forces are detectable with the DP tension sensor but the overall forces at the cell–cell interface depend on the strength of the DSM–IF linkage [149]. The modulation of the cell–cell adhesion strength thereby depends on the F-actin cytoskeleton, which could be explained by a model, in which DSMs counterbalance actomyosin-generated forces [149]. A stronger DSM–IF linkage then increases the ability of the system to resist tension, which leads to increased cell forces and stiffness [149]. The interplay of force-generating F-actin and resistance-providing keratin IF cytoskeletons would allow the cells to be in a prestressed state that might be important for the translation of mechanical forces into biochemical cues [149, 290]. This model is not only consistent with no tension across DP but would also be in line with compression of DP if the IF pushes towards the cell–cell contact. Even though, the tension sensor cannot directly measure compression, compression of the unstructured F40 and F7 linker peptides provides an appealing explanation for the increased FRET efficiency of the tension sensor as compared to the no-force control during the formation of DSMs, which could be potentially verified with a DP compression sensor analogue to the DP tension sensor.

On very soft substrates of about 2 kPa, tension is experienced by DPII. On these substrates, keratinocytes have difficulties to adhere and therefore likely form less stable cell–matrix adhesions. Furthermore, the substrate stiffness is in the range of the stiffness of the keratin IF, which is less than 1 kPa [291]. Therefore, the IF might be involved in stress propagation between neighboring cells similar as reported for the F-actin cytoskeleton [292]. The model of force transmission across the IF would also be consistent with the observation that the IF is involved in coordinating collective cell migration in the *Xenopus* mesendoderm [293, 294]. Moreover, disruption of desmosomal adhesion in mammary glands interferes with epithelial morphogenesis similar to the disruption of the E-cadherin adhesion [295]. The breast tissue is with a stiffness of about 1 kPa one of the softest human tissues [162], which supports the hypothesis that DSMs might experience forces if the surrounding stiffness matches the stiffness of the IF.

The range of the reported stiffness's for the epidermis is broad and depends on the measurement method [286, 287, 296]. Most values, however, are at least some kPa so that it is likely that the stiffer substrates used in this work with more than 4 kPa are reflective of the physiological environment of basal keratinocytes. The very soft substrates might, however, reflect softer environments that could occur, for example, during embryogenesis, in other tissues, and in suprabasal layers [162, 286]. Another situation, in which substrate stiffness changes, and potentially also the role of forces across DSMs, is wound healing [296]. Therefore, it would be interesting for future experiments to analyze tension across DP also in some of these conditions.

6.4.2 External Mechanical Stress

During the application of external mechanical stress, forces act transiently on DPII in keratinocytes and DPI in MDCK cells. Together with the absence of forces in unstressed monolayers, DSMs seem to be engineered to withstand acute mechanical stress. This hypothesis is supported by the epidermis-specific DP knockout mouse, which develops normally but is perinatal lethal because of skin blistering [69], and by relatively mild human diseases that show more blistering at mechanically stressed sites like palms and soles, which are even more severe if the patient performs manual labor [128, 129]. Furthermore, the keratin IF stiffens when deformed [55–57], which could explain, why tension can built up at the DSM during deformation and is not immediately dissipated through the IF. The keratin IF, however, still seems to remain flexible enough to dissipate forces as no forces are experienced by DPII in DSMs perpendicular to and at the cell side opposite to the pulling direction. This force dissipation would be in line with the large elasticity described for the IF [50, 54, 148].

Tension across DPII in keratinocytes and DPI in MDCK cells depends on the magnitude of external stress only after an initial distance threshold is surpassed. This threshold indicates that small levels of mechanical stress are processed differently than higher forces. This behavior could be explained if desmosomal proteins elongate in response to tension or their interaction interface shifts. One prime candidate for tension-dependent elongation is the SH3 domain in DP head [114].

The magnitude-dependent opening of the FL-based tension sensor provides a lower bound of 4 pN for the forces across the DSM. To further narrow the force range, also the HP35- and HP35st-based tension sensors and corresponding no-force controls could be used in a cell pulling experiment. These linkers are insensitive to forces below 6 pN and 8 pN, respectively [217]. Opening of the linker in pulling experiments would therefore show that tension across DP exceeds the respective minimal force.

External mechanical stress is applied in this work by squeezing and moving the neighboring cell. This method has the advantage that tension is directly transmitted to the cell–cell contact, while in methods that apply stress by substrate deformation, all external stress is primarily sensed by cell–matrix adhesions and just indirectly transferred to cell–cell contacts. One disadvantage of the pulling method is that the applied mechanical stress and strain rates are not calibrated but can only be inferred from the observed cell deformations, which are local deformations of an individual cell–cell contact in basal keratinocytes and larger rearrangements in MDCK cell sheets. Information on physiological stress and strain rates are sparse but forces are reported to be transmitted across $5-10$ cell diameters and strain in adult drosophila exceed 10 % [174]. Furthermore, cells surrounding a single-cell wound stiffen in up to three cell diameter distance [297]. The external mechanical stress applied in this work therefore seems to be in the physiological

range based on the observed cell deformations. To perform pulling in an automated and standardized fashion, a future setup could use a micromanipulator with programmable moving paths and speeds as well as pause times. Such a setup would not only facilitate imaging but also allow to compare different pulling conditions.

Combining the pulling experiment in future experiments with FLIM-based FRET determination would be particularly advantageous as ratiometric measurements are prone to artifacts caused by variations of the experimental setup, e.g. of the laser intensity. The ratiometric measurements of FRET in the unstressed monolayer of the FL-based tension sensor, for example, show a difference between tension sensor and no-force control that is absent in the FLIM-based measurements, which are less sensitive to experimental variations. Similarly, the difference between DPI tension sensor and no-force control in keratinocytes has likely the same cause as the difference in the FL-based data. This discrepancy prevents a definite statement about forces experienced by DPI in unstressed keratinocytes. The lack of the magnitude dependence during pulling, however, is striking and even the S2849G mutation for increased keratin binding does not induce magnitude-dependent tension experienced by DPI in keratinocytes. Therefore, it is likely that little or no tension is experienced by DPI in these conditions, but FLIM-based FRET measurements could strengthen these conclusions.

Further interesting aspects for future experiments could also be how force dissipates in visco-elastic tissues and how tension relaxes. These processes might be on the order of minutes to hours and could also involve more tension across AJs simultaneous to or after tension released across DSMs. Therefore, combining pulling experiments with tension measurements in both cell–cell adhesion sites would provide further insights in the interplay of the two main adhesive cell–cell contacts.

6.4.3 Mechanistic Insights

DP is the major linkage to the keratin IF and an essential desmosomal component but forces experienced by DP not necessarily reflect all forces acting on the DSM. The TSM is integrated just before the IF binding domains and therefore detects forces that are transmitted to the keratin IF, but no tension is measured if forces act on DSMs but dissipate earlier. Such a dissipation could be mediated by a connection to the F-actin cytoskeleton, which could be established, for example, by cortactin [298] or Pkp1 [34]. Indeed, tension is reported across Dsg2 even in the unstressed MDCK monolayer [299]. In this condition, no forces are experienced by DPI [11]. This discrepancy might be explained by the general property of FRET-based tension sensors to report on tension across individual proteins rather than the entire structure and reflect tension across the DSM that is not experienced by the DP tension sensor. It should be noted, however, that the measurements of tension across Dsg2 are only incompletely reported. Furthermore,

the FRET index differences, on which the interpretation that tension is experienced by Dsg2 is based, are shown only for one experimental day and are smaller than FRET index changes in the no-force control in cardiomyocytes that are regarded as small by the authors [299]. Therefore, the conclusion that Dsg2 is indeed exposed to tension in the unstressed monolayer should be treated with care. It remains, however, interesting to elucidate force transmission routes within DSMs and further tension sensors might help to identify them.

Next to targeting other desmosomal components, different integration sites in DP could be used to test for a tension gradient similar to the gradient talin-1 experiences in FAs [216]. Integrating the TSM after E584 and also after K1056 between the head and rod domain[3] leads to poorly localizing constructs indicating an impaired protein functionality. An alternative, promising integration site in the N-terminal region of DP might be the flexible linker in the DP head between SR6 and 7 (aa 630−660) [111, 112].

Already the existing DP tension sensors provide valuable tools to gain further insights into forces at the DSM. Epidermal layers, for example, express distinct cadherin isoforms [1] and *in vitro* measurements of their binding strengths showed that cadherins characteristic for suprabasal layers bind stronger [27]. Measuring tension across DP in 3D epidermis therefore might help to understand the differential function of DSMs in the epidermal layers.

Another interesting aspect is the difference in forces experienced by DPI and DPII in basal keratinocytes. Complementing these measurements from cells that express both isoforms to comparable levels with measurements in heart muscle cells, where DPII is not detectable [128], might help to better understand the isoform-dependency of forces. Furthermore, not only DP isoforms but also keratin isoforms might influence how mechanical forces propagate. To investigate individual keratins in keratinocytes, specific isoforms can be, for example, reexpressed in the KtyII$^{-/-}$ cells [58, 67]. Basal keratinocytes are, for instance, characterized by K5/K14, while suprabasal layers express K1/K10, and upon injury K6/K17 becomes upregulated [5]. In the context of mechanotransduction, also K9 might be particularly interesting because it is expressed specifically at sites of high mechanical stress [5]. Tension measurements in keratinocytes expressing only one type II keratin might therefore help to elucidate the influence of the IF on forces at the DSMs. These measurements could even be combined with measurements of both major DP isoforms to analyze the mutual isoform dependency.

To gain more mechanistic insights on the proteins and modifications influencing forces at the DSM, the DP tension sensor can be measured in cells depleted of individual desmosomal components, like Pkp1 [300] or Pkp3 [301] knockout cells. Moreover, mutations might be introduced into DP to learn more about the molecular regulation and

[3]Personal communication by Andrew J. Price, PhD, group of Prof. Alexander R. Dunn, Stanford University

protein parts required that DP experiences forces. The S2849G mutation already used in pulling of DPI in keratinocytes, for example, prevents a serine phosphorylation by GSK3 and enhances binding to the keratin IF [93]. Furthermore, the effect of PRMT-1-dependent methylation could be tested with a R2834H mutation [93]. In addition, mutations could be introduced that are associated with human diseases to identify the mutations that have an immediate mechanical impact as opposed to mutations primarily influencing the desmosomal signaling. Promising candidates could be S507F and S299R, which are associated with ARVD/C [103]. These serines are core residues contributing to the structural integrity of the DP head domain close to the central SH3 repeat and are also conserved in other plakins [103]. Furthermore, molecular dynamic (MD) simulations predict that these mutations reduce the mechanical stability of the DP head domain by increasing the flexibility of the SR4 to SR5 linkage [302], which could also affect the overall forces experienced by DP. Other mutations to be tested could include a double point mutation with Q664X and R2366C that causes symptoms in the skin but not in the heart [130] or G2475R, which causes heart and skin defects [303]. Complementary to tension measurements with mutated DP tension sensors, changes in the phosphoproteome could be analyzed to get indications about the signaling pathways involved.

In light of the observation that tension is experienced by DSMs, which are the cell–cell anchoring points of the IF, also potential forces at HDs, which anchor the IF at the cell–matrix interface, are of increasing interest. HDs are specifically formed in epithelial cells and in contrast to the hundreds of proteins identified in the F-actin-bound FAs [304], in mature HDs in the skin only six key proteins are identified [305–307]. From those proteins only the transmembrane integrin $\alpha 6\beta 4$ heterodimer, which binds with its head domain to laminins in the ECM, and the plakin-family protein member plectin, which connects the integrin $\beta 4$ tail to the IF, are also part of HDs in simple epithelia [306]. Therefore, a tension sensor to analyze forces at HDs might target one of these proteins. Integrin $\beta 4$ regulates integrin isoforms in the epidermis [308], is larger than all other integrin isoforms [309], and can be internally labeled with a fluorophore by substituting the non-functional calcium-sodium exchange (CalX) domain [310]. In initial experiments with an integrin $\beta 4$ tension sensor, in which the TSM replaces the CalX and is positioned between integrin's laminin- and plectin-binding sites, tension sensor and control constructs rescue the formation of HDs in integrin $\beta 4$-deficient keratinocytes, which indicate that protein functionality is preserved. These integrin $\beta 4$-deficient cells are isolated from a human patient suffering from junctional epidermolysis bullosa associated with pyloric atresia (PA-JEB)[4] [311]. The tension sensor and control constructs also show similar colocalization with other HD components as wt integrin $\beta 4$ [312]. Initial tension sensor measurements in unstressed keratinocytes showed not difference between tension sensor and no-force control, which could either mean that no tension is experienced by integrin $\beta 4$ or that forces are not sensed by the tension sensor. As tension is only

[4]PA-JEB keratinocytes are a gift from Prof. Arnoud Sonnenberg, Netherlands Cancer Institute, Amsterdam

transduced in some conditions across DSMs, future experiments using the described integrin $\beta 4$ tension sensor will be interesting especially in combination with external stress and soft substrates.

In summary, the DP tension sensor allows for the first time to directly measure tension across DSMs. DP tension sensor measurements presented in this work suggest that DSMs are engineered to withstand external mechanical stress and complement AJs in higher eukaryotes to preserve tissue integrity.

Acronyms

2D two-dimensional
3D three-dimensional

aa amino acid
ABS actin binding site
AC arrhythmogenic cardiomyopathy
AED acantholytic ectodermal dysplasia
AFM atomic force microscopy
AJ adherens junction
AP activator protein
APS ammonium persulfate
ARM autosomal recessive monilethrix
arm armadillo
ARVD/C arrythmogenic right ventricular dysplasia/cardiomyopathy

BC basal cell
BCA bicinchoninic acid
BF brightfield
bp basepair
BSA bovine serum albumin

Ca^{2+} calcium ions
CalX calcium-sodium exchange
CAP cardiomyopathy with alopecia and palmoplantar keratoderma
cDNA complementary deoxyribonucleic acid
C. elegans *Caenorhabditis elegans*
CI confidence interval
CIP contact inhibition of proliferation
CiP calf intestine alkaline phosphatase
CK casein kinase
cryo-ET cryoelectron tomography
CSV comma-separated values
CWP cardiomyopathy with woolly hair and palmoplantar keratoderma
CZI Carl Zeiss image

ddH$_2$O distilled and purified water
dH$_2$O distilled water
DM dense midline
DMSO dimethyl sulfoxide
DNA deoxyribonucleic acid
dNTP deoxyribonucleoside triphosphate
DP desmoplakin
DPNT N-terminal 584 aa of DP
Dsc desmocollin
Dsg desmoglein
DSM desmosome
DsRed Discosoma Red
dSTORM direct stochastical optical reconstruction microscopy
DTD desmoglein terminal domain

E embryonic day
EA extracellular anchor
EB epidermolysis bullosa
EB1 end-binding protein 1
EBS epidermolysis bullosa simplex
EC extracellular domain
Ecad E-cadherin
ECD extracellular core domain
ECM extracellular matrix
E. coli *Escherichia coli*
EDSFS ectodermal dysplasia skin fragility syndrome
EDTA ethlyenediaminetetraacetic acid
EGTA ethylene glycol-bis(β-aminoethyl ether)-N,N,N′,N′-tetraacetic acid
EM electron microscopy
EPSC encapsulated PostScript color
EYFP enhanced yellow fluorescent protein

F-actin filamentous actin
F40 flagelliform
F7 stable seven aa linker
FA focal adhesion
FAK focal adhesion kinase
FAM83H family with sequence similarity 8 member H
FCS fluorescence correlation spectroscopy
FIG figure
Fiji Fiji is just ImageJ

FL ferredoxin-like fold
FLAMES fluorescence lifetime analysis and merge software
FLIM fluorescence lifetime imaging microscopy
FLIMv03/v04 FLIM analysis software version v03 and v04
FRAP fluorescence recovery after photobleaching
FRET Förster resonance energy transfer

GFAP glial fibrillary acidic protein
GFP green fluorescent protein
GR granular layer
GSK3 glycogen synthase kinase 3
GUI graphical user interface

HaCaT human keratinocytes
HAI1 hepatocyte growth factor activator inhibitor type 1
HD hemidesmosome
HF high fidelity
HHS hereditary hypotrichosis simples
HP35 villin head piece
HP35st stable villin head piece
HRP horesradish peroxidase
HRSV hypotrichosis with recurrent skin vesicles

IA intracellular anchor
ICS intracellular cadherin-like sequence
ID identifier
IDP inner dense plaque
IF intermediate filament
Ig immunoglobulin
IPL intracellular proline-rich linker
IQR interquartile range
IRF instrument response function
ISC intersystem crossing

K keratin
kb kilobasepairs
kDa kilo Dalton
KEB-7 keratinocytes with keratin mutation in case of epidermolysis bullosa simplex
KF keratin filament
KG keratohyalin granules
KO knockout
kPa kilo Pascal

KS Kolmogorov-Smirnov
KtyII$^{-/-}$ keratinocyte depleted of type II keratins

LAEB lethal ancantholytic epidermolysis bullosa
LAH localized autosomal recessive hypotrichosis
LB lysogeny broth
LB$_{amp}$ LB containing 75 µg/µl ampicillin
LCEB lethal congenital epidermolysis bullosa
LINC linker of nucleoskeleton and cytoskeleton
lmer linear-mixed effects model
LMU Ludwig-Maximilians-Universität
LSSmOrange Large Stoke Shift monomeric Orange
LV DCM left ventricle dilated cardiomyopathy

MA muscle attachment site
MAPK mitogen-activated protein kinase
MAT matlab
mCherry monomeric Cherry
MD molecular dynamic
MDCK Madine Darby canine kidney
MEK murine epidermal keratinocyte
MEK-KO MEKs depleted of desmoplakin
MEK-wt MEKs wild type for desmoplakin
mKate2 monomeric Kate2
MLH maximum likelihood
MRTF myocardin-related transcription factor
MT microtubule
MTFM molecular tension-based fluorescence microscopy
mTFP1 monomeric teal fluorescent protein 1
mTOR mammalian target of rapamycin
MW molecular weight

N nucleus
NEB-1 keratinocytes from normal relative of epidermolysis bullosa simplex patient
NLSQ non-linear least square

OA okadaic acid
OD optical density
ODP outer dense plaque

PA-JEB junctional epidermolysis bullosa associated with pyloric atresia
PAA polyacrylamide

PAGE polyacrylamide gel electrophoresis
PBS Dulbecco's phosphate buffered saline
PBSB PBS with 3 % BSA
pBSK pBluescript II SK(+)
PBST PBS with 0.02 % Tween-20
PBSTB PBST with 1 % BSA
PCR polymerase chain reaction
pdf probability density function
PEG polyethylen glycol
Pg plakoglobin
PIPES piperazine-N,N′-bis(2-ethanesulfonic acid)
PKC protein kinase C
Pkp plakophilin
PM plasma membrane
PMSF phenylmethylsulfonylfluorid
PNG portable network graphics
POI protein of interest
PPK palmoplantar keratoderma
PRMT-1 protein arginin methyltransferase 1
PSS-B peeling skin syndrome type B
PTM post-translational modification
PTU performer terrain utilities
PVDF polyvinylidenfluorid

Rho Ras homologue
RNA ribonucleic acid
RT room temperature
RUD repeat unit domain

SAM skin dermatitis, multiple severe allergies and metabolic wasting
SC stratum corneum
SDS sodium dodecyl sulphate
SE sensitized emission
SEM standard error of the mean
SERCA2 sarcoendoplasmatic reticulum Ca^{2+}-ATPase isoform 2
SFWS skin fragility woolly hair syndrome
SH3 Scr-homology 3
siRNA small interfering ribonucleic acid
SP spinous layer
SPCA1 secretory pathway Ca^{2+}-ATPase isoform 1
SPPK striate palmoplantar keratoderma

SR spectrin repeat
SRF serum-response factor

TAE Tris-acetate-EDTA
TagBFP tagged blue fluorescent protein
TAZ transcriptional coactivator with PDZ-binding motif
TBS Tris-buffered saline
TBST Tris-buffered saline with Tween-20
TCSPC time-correlated single photon counting
TEAD transcription enhanced associate domain
TEM transmission electron microscopy
TEMED N,N,N′,N′-tetramethylethylenediamine
TFM traction force microscopy
TGT tension gauge tether
TIF tagged image file format
TJ tight junction
TM transmembrane domain
Tris 2-amino-2-hyroxymethyl-propane-1,3-diol
TRITC tetramethylrhodamine
TS tension sensor
TSM tension sensor module
TSS transformation and storage solution
TXT text

UV ultraviolet

VASP vasodilator-stimualted phosphoprotein
Vin Vinculin

WB Western blot
WMW Wilcoxon-Mann-Whitney-U
Wnt wingless/integrated
wt wild type

YAP Yes-associated protein
YPet yellow fluorescent protein engineered for efficient energy transfer

Bibliography

[1] M. D. Kottke, E. Delva, and A. P. Kowalczyk. "The desmosome: Cell science lessons from human diseases". *Journal of Cell Science* 119.5 (2006), pp. 797–806.

[2] G. Meşe, G. Richard, and T. W. White. "Gap junctions: Basic structure and function". *Journal of Investigative Dermatology* 127.11 (2007), pp. 2516–2524.

[3] E. Fuchs and S. Raghavan. "Getting under the skin of epidermal morphogenesis". *Nature Reviews Genetics* 3 (2002), pp. 199–209.

[4] E. Delva, D. K. Tucker, and A. P. Kowalczyk. "The desmosome". *Cold Spring Harbor Perspectives in Biology* 1.2 (2009), 1:a002543.

[5] M. Homberg and T. M. Magin. "Chapter Six – Beyond expectations: Novel insights into epidermal keratin function and regulation". *International Review of Cell and Molecular Biology* 311 (2014), pp. 265–306.

[6] K. D. Sumigray and T. Lechler. "Chapter twelve – Cell adhesion in epidermal development and barrier formation". *Current Topics in Developmental Biology* 112 (2015), pp. 383–414.

[7] M. Rübsam, A. F. Mertz, A. Kubo, S. Marg, C. Jüngst, G. Goranci-Buzhala, A. C. Schauss, V. Horsley, E. R. Dufresne, M. Moser, W. Ziegler, M. Amagai, S. A. Wickström, and C. M. Niessen. "E-cadherin integrates mechanotransduction and EGFR signaling to control junctional tissue polarization and tight junction positioning". *Nature Communications* 8.1 (2017), p. 1250.

[8] D. W. Fawcett. "Intercellular bridges". *Experimental Cell Research* 8 (1961), pp. 174–187.

[9] A. North, W. G. Bardsley, J. Hyam, E. A. Bornslaeger, H. C. Cordingley, B. Trinnaman, M. Hatzfeld, K. J. Green, A. I. Magee, and D. R. Garrod. "Molecular map of the desmosomal plaque". *Journal of Cell Science* 112.23 (1999), pp. 4325–4336.

[10] B. V. Desai, R. M. Harmon, and K. J. Green. "Desmosomes at a glance". *Journal of Cell Science* 122.24 (2009), pp. 4401–4407.

[11] A. J. Price, A.-L. Cost, H. Ungewiß, J. Waschke, A. R. Dunn, and C. Grashoff. "Mechanical loading of desmosomes depends on the magnitude and orientation of external stress". *Nature Communications* 9.1 (2018), p. 5284.

[12] C. J. Skerrow and A. G. Matoltsy. "Isolation of epidermal desmosomes". *The Journal of Cell Biology* 63.2 (1974), pp. 515–523.

[13] W. W. Franke, E. Schmid, C. Grund, H. Müller, I. Engelbrecht, R. Moll, J. Stadler, and E.-D. Jarasch. "Antibodies to high molecular weight polypeptides of desmosomes: Specific localization of a class of junctional proteins in cells and tissues". *Differentiation* 20.1 (1981), pp. 217–241.

[14] H. Müller and W. W. Franke. "Biochemical and immunological characterization of desmoplakins I and II, the major polypeptides of the desmosomal plaque". *Journal of Molecular Biology* 163.4 (1983), pp. 647–671.

[15] W. W. Franke, H.-P. Kapprell, and H. Müller. "Isolation and symmetrical splitting of desmosomal structures in 9 M urea". *European Journal of Cell Biology* 32.1 (1983), pp. 117–130.

[16] H.-P. Kapprell, P. Cowin, W. W. Franke, H. Ponstingl, and H.-J. Opferkuch. "Biochemical characterization of desmosomal proteins isolated from bovine muzzle epidermis: Amino acid and carbohydrate composition". *European Journal of Cell Biology* 36.2 (1985), pp. 217–229.

[17] G. Gorbsky and M. S. Steinberg. "Isolation of the intercellular glycoproteins of desmosomes." *The Journal of Cell Biology* 90.1 (1981), pp. 243–248.

[18] K. J. Green, D. A. D. Parry, P. M. Steinert, M. L. A. Virata, R. M. Wagner, B. D. Angst, and L. A. Nilles. "Structure of the human desmoplakins. Implications for function in the desmosomal plaque". *The Journal of Biological Chemistry* 265.5 (1990), pp. 2603–2612.

[19] A. Al-Amoudi, D. Castaño-Diez, D. P. Devos, R. B. Russell, G. T. Johnson, and A. S. Frangakis. "The three-dimensional molecular structure of the desmosomal plaque". *Proceedings of the National Academy of Sciences* 108.16 (2011), pp. 6480–6485.

[20] S. N. Stahley, E. I. Bartle, C. E. Atkinson, A. P. Kowalczyk, and A. L. Mattheyses. "Molecular organization of the desmosome as revealed by direct stochastic optical reconstruction microscopy". *Journal of Cell Science* 129.15 (2016), pp. 2897–2904.

[21] J. C. Jones, C. Y. Kam, R. M. Harmon, A. V. Woychek, S. B. Hopkinson, and K. J. Green. "Intermediate filaments and the plasma membrane". *Cold Spring Harbor Perspectives in Biology* 9.1 (2017).

[22] O. Nekrasova and K. J. Green. "Desmosome assembly and dynamics". *Trends in Cell Biology* 23.11 (2013), pp. 537–546.

[23] H. Hennings and K. A. Holbrook. "Calcium regulation of cell–cell contact and differentiation of epidermal cells in culture: An ultrastructural study". *Experimental Cell Research* 143.1 (1983), pp. 127–142.

[24] D. Garrod and T. E. Kimura. "Hyper-adhesion: A new concept in cell–cell adhesion". *Biochemical Society Transactions* 36.2 (2008), pp. 195–201.

[25] D. Garrod and L. Tabernero. "Hyper-adhesion: A unique property of desmosomes". *Cell Communication & Adhesion* 21.5 (2014), pp. 249–256.

[26] A. P. Kowalczyk and K. J. Green. "Chapter five – Structure, function, and regulation of desmosomes". *Progress in Molecular Biology and Translational Science* 116 (2013), pp. 95–118.

[27] O. J. Harrison, J. Brasch, G. Lasso, P. S. Katsamba, G. Ahlsen, B. Honig, and L. Shapiro. "Structural basis of adhesive binding by desmocollins and desmogleins". *Proceedings of the National Academy of Sciences* 113.26 (2016), pp. 7160–7165.

[28] H. Tariq, J. Bella, T. A. Jowitt, D. F. Holmes, M. Rouhi, Z. Nie, C. Baldock, D. Garrod, and L. Tabernero. "Cadherin flexibility provides a key difference between desmosomes and adherens junctions". *Proceedings of the National Academy of Sciences* 112.17 (2015), pp. 5395–5400.

[29] L. Eshkind, Q. Tian, A. Schmidt, W. W. Franke, R. Windoffer, and R. E. Leube. "Loss of desmoglein 2 suggests essential functions for early embryonic development and proliferation of embryonal stem cells". *European Journal of Cell Biology* 81.11 (2002), pp. 592–598.

[30] P. J. Koch, M. G. Mahoney, H. Ishikawa, L. Pulkkinen, J. Uitto, L. Shultz, G. F. Murphy, D. Whitaker-Menezes, and J. R. Stanley. "Targeted disruption of the pemphigus vulgaris antigen (desmoglein 3) gene in mice causes loss of keratinocyte cell adhesion with a phenotype similar to pemphigus vulgaris". *The Journal of Cell Biology* 137.5 (1997), pp. 1091–1102.

[31] A. Gross, L. A. P. Pack, G. M. Schacht, S. Kant, H. Ungewiß, M. Meir, N. Schlegel, C. Preisinger, P. Boor, N. Guldiken, C. A. Krusche, G. Sellge, C. Trautwein, J. Waschke, A. Heuser, R. E. Leube, and P. Strnad. "Desmoglein 2, but not desmocollin 2, protects intestinal epithelia from injury". *Mucosal Immunology* 11 (2018), pp. 1630–1639.

[32] P. M. Elias, N. Matsuyoshi, H. Wu, C. Lin, Z. H. Wang, B. E. Brown, and J. R. Stanley. "Desmoglein isoform distribution affects stratum corneum structure and function". *The Journal of Cell Biology* 153.2 (2001), pp. 243–249.

[33] M. Peifer, P. D. McCrea, K. J. Green, E. Wieschaus, and B. M. Gumbiner. "The vertebrate adhesive junction proteins β-catenin and plakoglobin and the *Drosophila* segment polarity gene *armadillo* form a multigene family with similar properties." *The Journal of Cell Biology* 118.3 (1992), pp. 681–691.

[34] M. Hatzfeld, C. Haffner, K. Schulze, and U. Vinzens. "The function of plakophilin 1 in desmosome assembly and actin filament organization". *The Journal of Cell Biology* 149.1 (2000), pp. 209–222.

[35] N. A. Chitaev, R. E. Leube, R. B. Troyanovsky, L. G. Eshkind, W. W. Franke, and S. M. Troyanovsky. "The binding of plakoglobin to desmosomal cadherins: Patterns of binding sites and topogenic potential." *The Journal of Cell Biology* 133.2 (1996), pp. 359–369.

[36] J. Zhurinsky, M. Shtutman, and A. Ben-Ze'ev. "Plakoglobin and β-catenin: Protein interactions, regulation and biological roles". *Journal of Cell Science* 113.18 (2000), pp. 3127–3139.

[37] J.-E. Bouameur, B. Favre, and L. Borradori. "Plakins, a versatile family of cytolinkers: Roles in skin integrity and in human diseases". *Journal of Investigative Dermatology* 134.4 (2014), pp. 885–894.

[38] M. Hesse, T. M. Magin, and K. Weber. "Genes for intermediate filament proteins and the draft sequence of the human genome". *Journal of Cell Science* 114.14 (2001), pp. 2569–2575.

[39] D. M. Toivola, G.-Z. Tao, A. Habtezion, J. Liao, and M. B. Omary. "Cellular integrity plus: Organelle-related and protein-targeting functions of intermediate filaments". *Trends in Cell Biology* 15.11 (2005), pp. 608–617.

[40] J. Block, V. Schroeder, P. Pawelzyk, N. Willenbacher, and S. Köster. "Physical properties of cytoplasmic intermediate filaments". *Biochimica et Biophysica Acta – Molecular Cell Research* 1853.11, Part B (2015), pp. 3053–3064.

[41] A. Robert, C. Hookway, and V. I. Gelfand. "Intermediate filament dynamics: What we can see now and why it matters". *BioEssays* 38.3 (2016), pp. 232–243.

[42] J. T. Jacob, P. A. Coulombe, R. Kwan, and M. B. Omary. "Types I and II keratin intermediate filaments". *Cold Spring Harbor Perspectives in Biology* 10.4 (2018).

[43] H. Herrmann and U. Aebi. "Intermediate filaments: Structure and assembly". *Cold Spring Harbor Perspectives in Biology* 8.11 (2016).

[44] H. Ishikawa, R. Bischoff, and H. Holtzer. "Mitosis and intermediate-sized filaments in developing skeletal muscle". *The Journal of Cell Biology* 38.3 (1968), pp. 538–555.

[45] E. Fuchs and K. Weber. "Intermediate filaments: Structure, dynamics, function and disease". *Annual Review of Biochemistry* 63.1 (1994), pp. 345–382.

[46] Y. Turgay, M. Eibauer, A. E. Goldman, T. Shimi, M. Khayat, K. Ben-Harush, A. Dubrovsky-Gaupp, K. T. Sapra, R. D. Goldman, and O. Medalia. "The molecular architecture of lamins in somatic cells". *Nature* 543 (2017), pp. 261–264.

[47] B.-M. Chung, J. D. Rotty, and P. A. Coulombe. "Networking galore: Intermediate filaments and cell migration". *Current Opinion in Cell Biology* 25.5 (2013), pp. 600–612.

[48] F. Gittes, B. Mickey, J. Nettleton, and J. Howard. "Flexural rigidity of microtubules and actin filaments measured from thermal fluctuations in shape." *The Journal of Cell Biology* 120.4 (1993), pp. 923–934.

[49] M. Hohenadl, T. Storz, H. Kirpal, K. Kroy, and R. Merkel. "Desmin filaments studied by quasi-elastic light scattering". *Biophysical Journal* 77.4 (1999), pp. 2199–2209.

[50] N. Mücke, L. Kreplak, R. Kirmse, T. Wedig, H. Herrmann, U. Aebi, and J. Langowski. "Assessing the flexibility of intermediate filaments by atomic force microscopy". *Journal of Molecular Biology* 335.5 (2004), pp. 1241–1250.

[51] L. Kreplak, H. Bär, J. Leterrier, H. Herrmann, and U. Aebi. "Exploring the mechanical behavior of single intermediate filaments". *Journal of Molecular Biology* 354.3 (2005), pp. 569–577.

[52] C. Guzmán, S. Jeney, L. Kreplak, S. Kasas, A. Kulik, U. Aebi, and L. Forró. "Exploring the mechanical properties of single vimentin intermediate filaments by atomic force microscopy". *Journal of Molecular Biology* 360.3 (2006), pp. 623–630.

[53] J. Block, H. Witt, A. Candelli, J. C. Danes, E. J. G. Peterman, G. J. L. Wuite, A. Janshoff, and S. Köster. "Viscoelastic properties of vimentin originate from nonequilibrium conformational changes". *Science Advances* 4.6 (2018), eaat1161.

[54] L. Ma, J. Xu, P. A. Coulombe, and D. Wirtz. "Keratin filament suspensions show unique micromechanical properties". *Journal of Biological Chemistry* 274.27 (1999), pp. 19145–19151.

[55] C. Storm, J. J. Pastore, F. C. MacKintosh, T. C. Lubensky, and P. A. Janmey. "Nonlinear elasticity in biological gels". *Nature* 435 (2005), pp. 191–194.

[56] P. Pawelzyk, N. Mücke, H. Herrmann, and N. Willenbacher. "Attractive interactions among intermediate filaments determine network mechanics in vitro". *PLOS ONE* (2014), e93194.

[57] O. Bousquet, L. Ma, S. Yamada, C. Gu, T. Idei, K. Takahashi, D. Wirtz, and P. A. Coulombe. "The nonhelical tail domain of keratin 14 promotes filament bundling and enhances the mechanical properties of keratin intermediate filaments in vitro". *The Journal of Cell Biology* 155.5 (2001), pp. 747–753.

[58] C. Kröger, F. Loschke, N. Schwarz, R. Windoffer, R. E. Leube, and T. M. Magin. "Keratins control intercellular adhesion involving PKC-α–mediated desmoplakin phosphorylation". *The Journal of Cell Biology* 201.5 (2013), pp. 681–692.

[59] L. Ramms, G. Fabris, R. Windoffer, N. Schwarz, R. Springer, C. Zhou, J. Lazar, S. Stiefel, N. Hersch, U. Schnakenberg, T. M. Magin, R. E. Leube, R. Merkel, and B. Hoffmann. "Keratins as the main component for the mechanical integrity of keratinocytes". *Proceedings of the National Academy of Sciences* 110.46 (2013), pp. 18513–18518.

[60] K. Seltmann, A. W. Fritsch, J. A. Käs, and T. M. Magin. "Keratins significantly contribute to cell stiffness and impact invasive behavior". *Proceedings of the National Academy of Sciences* 110.46 (2013), pp. 18507–18512.

[61] P. A. Coulombe, M. E. Hutton, R. Vassar, and E. Fuchs. "A function for keratins and a common thread among different types of epidermolysis bullosa simplex diseases." *The Journal of Cell Biology* 115.6 (1991), pp. 1661–1674.

[62] E. Fuchs and H. Green. "Changes in keratin gene expression during terminal differentiation of the keratinocyte". *Cell* 19.4 (1980), pp. 1033–1042.

[63] E. Candi, R. Schmidt, and G. Melino. "The cornified envelope: A model of cell death in the skin". *Nature Reviews Molecular Cell Biology* 6 (2005), pp. 328–340.

[64] J. Bär, V. Kumar, W. Roth, N. Schwarz, M. Richter, R. E. Leube, and T. M. Magin. "Skin fragility and impaired desmosomal adhesion in mice lacking all keratins". *Journal of Investigative Dermatology* 134.4 (2014), pp. 1012–1022.

[65] R. Windoffer, M. Beil, T. M. Magin, and R. E. Leube. "Cytoskeleton in motion: The dynamics of keratin intermediate filaments in epithelia". *The Journal of Cell Biology* 194.5 (2011), pp. 669–678.

[66] L. Wallace, L. Roberts-Thompson, and J. Reichelt. "Deletion of K1/K10 does not impair epidermal stratification but affects desmosomal structure and nuclear integrity". *Journal of Cell Science* 125.7 (2012), pp. 1750–1758.

[67] P. Vijayaraj, C. Kröger, U. Reuter, R. Windoffer, R. E. Leube, and T. M. Magin. "Keratins regulate protein biosynthesis through localization of GLUT1 and -3 upstream of AMP kinase and Raptor". *The Journal of Cell Biology* 187.2 (2009), pp. 175–184.

[68] G. I. Gallicano, P. Kouklis, C. Bauer, M. Yin, V. Vasioukhin, L. Degenstein, and E. Fuchs. "Desmoplakin is required early in development for assembly of desmosomes and cytoskeletal linkage". *The Journal of Cell Biology* 143.7 (1998), pp. 2009–2022.

[69] V. Vasioukhin, E. Bowers, C. Bauer, L. Degenstein, and E. Fuchs. "Desmoplakin is essential in epidermal sheet formation". *Nature Cell Biology* 3 (2001), pp. 1076–1085.

[70] B. Wehrle-Haller. "Structure and function of focal adhesions". *Current Opinion in Cell Biology* 24.1 (2012), pp. 116–124.

[71] O. Krylyshkina, K. I. Anderson, I. Kaverina, I. Upmann, D. J. Manstein, J. V. Small, and D. K. Toomre. "Nanometer targeting of microtubules to focal adhesions". *The Journal of Cell Biology* 161.5 (2003), pp. 853–859.

[72] S. Stehbens and T. Wittmann. "Targeting and transport: How microtubules control focal adhesion dynamics". *The Journal of Cell Biology* 198.4 (2012), pp. 481–489.

[73] R. Windoffer, A. Kölsch, S. Wöll, and R. E. Leube. "Focal adhesions are hotspots for keratin filament precursor formation". *The Journal of Cell Biology* 173.3 (2006), pp. 341–348.

[74] A. Kölsch, R. Windoffer, and R. E. Leube. "Actin-dependent dynamics of keratin filament precursors". *Cell Motility* 66.11 (2009), pp. 976–985.

[75] C.-H. Lee and P. A. Coulombe. "Self-organization of keratin intermediate filaments into cross-linked networks". *The Journal of Cell Biology* 186.3 (2009), pp. 409–421.

[76] N. Schwarz, R. Windoffer, T. M. Magin, and R. E. Leube. "Dissection of keratin network formation, turnover and reorganization in living murine embryos". *Scientific Reports* 5 (2015), p. 9007.

[77] S. Getsios, D. P. Kelsell, and A. Forge. "Junctions in human health and inherited disease". *Cell and Tissue Research* 360.3 (2015), pp. 435–438.

[78] M. G. Mahoney, Z. Wang, K. Rothenberger, P. J. Koch, M. Amagai, and J. R. Stanley. "Explanations for the clinical and microscopic localization of lesions in pemphigus foliaceus and vulgaris". *The Journal of Clinical Investigation* 103.4 (1999), pp. 461–468.

[79] M. Amagai, K. Tsunoda, H. Suzuki, K. Nishifuji, S. Koyasu, and T. Nishikawa. "Use of autoantigen-knockout mice in developing an active autoimmune disease model for pemphigus". *The Journal of Clinical Investigation* 105.5 (2000), pp. 625–631.

[80] S. Getsios, C. L. Simpson, S.-i. Kojima, R. Harmon, L. J. Sheu, R. L. Dusek, M. Cornwell, and K. J. Green. "Desmoglein 1–dependent suppression of EGFR signaling promotes epidermal differentiation and morphogenesis". *The Journal of Cell Biology* 185.7 (2009), pp. 1243–1258.

[81] R. Caldelari, A. de Bruin, D. Baumann, M. M. Suter, C. Bierkamp, V. Balmer, and E. Müller. "A central role for the armadillo protein plakoglobin in the autoimmune disease pemphigus vulgaris". *The Journal of Cell Biology* 153.4 (2001), pp. 823–834.

[82] D. I. Keller, D. Stepowski, C. Balmer, F. Simon, J. Guenthard, F. Bauer, P. Itin, N. David, V. Drouin-Garraud, and V. Fressart. "De novo heterozygous desmoplakin mutations leading to Naxos-Carvajal disease". *Swiss Medical Weekly* 142 (2012), w13670.

[83] J.-D. Fine. "Inherited epidermolysis bullosa: Past, present, and future". *Annals of the New York Academy of Sciences* 1194.1 (2010), pp. 213–222.

[84] J.-D. Fine. "Inherited epidermolysis bullosa". *Orphanet Journal of Rare Diseases* 5.1 (2010), p. 12.

[85] L. Samuelov and E. Sprecher. "Inherited desmosomal disorders". *Cell and Tissue Research* 360.3 (2015), pp. 457–475.

[86] J. Gomes, M. Finlay, A. K. Ahmed, E. J. Ciaccio, A. Asimaki, J. E. Saffitz, G. Quarta, M. Nobles, P. Syrris, S. Chaubey, W. J. McKenna, A. Tinker, and P. D. Lambiase. "Electrophysiological abnormalities precede overt structural changes in arrhythmogenic right ventricular cardiomyopathy due to mutations in desmoplakin – A combined murine and human study". *European Heart Journal* 33.15 (2012), pp. 1942–1953.

[87] H. P. Foote, K. D. Sumigray, and T. Lechler. "FRAP analysis reveals stabilization of adhesion structures in the epidermis compared to cultured keratinocytes". *PLOS ONE* 8.8 (2013), e71491.

[88] K. J. Green and C. A. Gaudry. "Are desmosomes more than tethers for intermediate filaments?" *Nature Reviews Molecular Cell Biology* 1 (2000), pp. 208–216.

[89] V. Vasioukhin, C. Bauer, M. Yin, and E. Fuchs. "Directed actin polymerization is the driving force for epithelial cell–cell adhesion". *Cell* 100.2 (2000), pp. 209–219.

[90] L. M. Godsel, S. N. Hsieh, E. V. Amargo, A. E. Bass, L. T. Pascoe-McGillicuddy, A. C. Huen, M. E. Thorne, C. A. Gaudry, J. K. Park, K. Myung, R. D. Goldman, T.-L. Chew, and K. J. Green. "Desmoplakin assembly dynamics in four dimensions: Multiple phases differently regulated by intermediate filaments and actin". *The Journal of Cell Biology* 171.6 (2005), pp. 1045–1059.

[91] S. Wallis, S. Lloyd, I. Wise, G. Ireland, T. P. Fleming, D. Garrod, and W. J. Nelson. "The α isoform of protein kinase C is involved in signaling the response of desmosomes to wounding in cultured epithelial cells". *Molecular Biology of the Cell* 11.3 (2000), pp. 1077–1092.

[92] R. Keil, K. Rietscher, and M. Hatzfeld. "Antagonistic regulation of intercellular cohesion by plakophilins 1 and 3". *Journal of Investigative Dermatology* 136.10 (2016), pp. 2022–2029.

[93] L. V. Albrecht, L. Zhang, J. Shabanowitz, E. Purevjav, J. A. Towbin, D. F. Hunt, and K. J. Green. "GSK3- and PRMT-1–dependent modifications of desmoplakin control desmoplakin–cytoskeleton dynamics". *The Journal of Cell Biology* 208.5 (2015), pp. 597–612.

[94] Z. Yang, N. E. Bowles, S. E. Scherer, M. D. Taylor, D. L. Kearney, S. Ge, V. V. Nadvoretskiy, G. DeFreitas, B. Carabello, L. I. Brandon, L. M. Godsel, K. J. Green, J. E. Saffitz, H. Li, G. A. Danieli, H. Calkins, F. Marcus, and J. A. Towbin. "Desmosomal dysfunction due to mutations in desmoplakin causes arrhythmogenic right ventricular dysplasia/cardiomyopathy". *Circulation Research* 99.6 (2006), pp. 646–655.

[95] M. Kawaguchi, A. Kanemaru, A. Sawaguchi, K. Yamamoto, T. Baba, C.-Y. Lin, M. D. Johnson, T. Fukushima, and H. Kataoka. "Hepatocyte growth factor activator inhibitor type 1 maintains the assembly of keratin into desmosomes in keratinocytes by regulating protease-activated receptor 2–dependent p38 signaling". *The American Journal of Pathology* 185.6 (2015), pp. 1610–1623.

[96] T. Kuga, M. Sasaki, T. Mikami, Y. Miake, J. Adachi, M. Shimizu, Y. Saito, M. Koura, Y. Takeda, J. Matsuda, T. Tomonaga, and Y. Nakayama. "FAM83H and Casein kinase I regulate the organization of the keratin cytoskeleton and formation of desmosomes". *Scientific Reports* 6 (2016), p. 26557.

[97] Y. Aoyama, Y. Yamamoto, F. Yamaguchi, and Y. Kitajima. "Low to high Ca^{2+}-switch causes phosphorylation and association of desmocollin 3 with plakoglobin and desmoglein 3 in cultured keratinocytes". *Experimental Dermatology* 18.4 (2009), pp. 404–408.

[98] K. Rietscher, R. Keil, A. Jordan, and M. Hatzfeld. "14-3-3 proteins regulate desmosomal adhesion via plakophilins". *Journal of Cell Science* 131.10 (2018).

[99] M. Hakuno, H. Shimizu, M. Akiyama, M. Amagai, J. K. Wahl, M. J. Wheelock, and T. Nishikawa. "Dissociation of intra- and extracellular domains of desmosomal cadherins and E-Cadherin in Hailey–Hailey disease and Darier's disease". *British Journal of Dermatology* 142.4 (2000), pp. 702–711.

[100] K. D. Sumigray and T. Lechler. "Control of cortical microtubule organization and desmosome stability by centrosomal proteins". *BioArchitecture* 1.5 (2011), pp. 221–224.

[101] T. Lechler and E. Fuchs. "Desmoplakin: An unexpected regulator of microtubule organization in the epidermis". *The Journal of Cell Biology* 176.2 (2007), pp. 147–154.

[102] E. J. O'Keefe, H. P. Erickson, and V. Bennett. "Desmoplakin I and desmoplakin II. Purification and characterization." *The Journal of Biological Chemistry* 264.14 (1989), pp. 8310–8318.

[103] H.-J. Choi and W. I. Weis. "Crystal structure of a rigid four-spectrin-repeat fragment of the human desmoplakin plakin domain". *Journal of Molecular Biology* 409.5 (2011), pp. 800–812.

[104] H.-J. Choi, S. Park-Snyder, L. T. Pascoe, K. J. Green, and W. I. Weis. "Structures of two intermediate filament-binding fragments of desmoplakin reveal a unique repeat motif structure". *Nature Structural Biology* 9.8 (2002), pp. 612–620.

[105] K. J. Green, T. S. Stappenbeck, D. A. Parry, and M. L. A. Virata. "Structure of desmoplakin and its association with intermediate filaments". *The Journal of Dermatology* 19.11 (1992), pp. 765–769.

[106] T. S. Stappenbeck and K. J. Green. "The desmoplakin carboxyl terminus coaligns with and specifically disrupts intermediate filament networks when expressed in cultured cells." *The Journal of Cell Biology* 116.5 (1992), pp. 1197–1209.

[107] T. S. Stappenbeck, E. A. Bornslaeger, C. M. Corcoran, H. H. Luu, M. L. Virata, and K. J. Green. "Functional analysis of desmoplakin domains: Specification of the interaction with keratin versus vimentin intermediate filament networks." *The Journal of Cell Biology* 123.3 (1993), pp. 691–705.

[108] E. A. Bornslaeger, C. M. Corcoran, T. S. Stappenbeck, and K. J. Green. "Breaking the connection: Displacement of the desmosomal plaque protein desmoplakin from cell–cell interfaces disrupts anchorage of intermediate filament bundles and alters intercellular junction assembly." *The Journal of Cell Biology* 134.4 (1996), pp. 985–1001.

[109] A. Sonnenberg and R. K. H. Liem. "Plakins in development and disease". *Experimental Cell Research* 313.10 (2007), pp. 2189–2203.

[110] C. Al-Jassar, H. Bikker, M. Overduin, and M. Chidgey. "Mechanistic basis of desmosome-targeted diseases". *Journal of Molecular Biology* 425.21 (2013), pp. 4006–4022.

[111] C. Al-Jassar, T. Knowles, M. Jeeves, K. Kami, E. Behr, H. Bikker, M. Overduin, and M. Chidgey. "The nonlinear structure of the desmoplakin plakin domain and the effects of cardiomyopathy-linked mutations". *Journal of Molecular Biology* 411.5 (2011), pp. 1049–1061.

[112] E. Ortega, J. A. Manso, R. M. Buey, A. M. Carballido, A. Carabias, A. Sonnenberg, and J. M. de Pereda. "The structure of the plakin domain of plectin reveals an extended rod-like shape". *The Journal of Biological Chemistry* 291.36 (2016), pp. 18643–18662.

[113] J. J. Jefferson, C. Ciatto, L. Shapiro, and R. K. H. Liem. "Structural analysis of the plakin domain of bullous pemphigoid antigen1 (BPAG1) suggests that plakins are members of the spectrin superfamily". *Journal of Molecular Biology* 366.1 (2007), pp. 244–257.

[114] C. Daday, K. Kolsek, and F. Gräter. "The mechano-sensing role of the unique SH3 insertion in plakin domains revealed by molecular dynamics simulations". *Scientific Reports* 7.1 (2017), p. 11669.

[115] C. J. Skerrow. "Selective extraction of desmosomal proteins by low ionic strength media". *Biochimica et Biophysica Acta – Protein Structure* 579.1 (1979), pp. 241–245.

[116] R. M. Cabral, H. Wan, C. L. Cole, D. J. Abrams, D. P. Kelsell, and A. P. South. "Identification and characterization of DSPIa, a novel isoform of human desmoplakin". *Cell and Tissue Research* 341.1 (2010), pp. 121–129.

[117] B. D. Angst, L. A. Nilles, and K. J. Green. "Desmoplakin II expression is not restricted to stratified epithelia". *Journal of Cell Science* 97.2 (1990), pp. 247–257.

[118] A. Uzumcu, E. E. Norgett, A. Dindar, O. Uyguner, K. Nisli, H. Kayserili, S. E. Sahin, E. Dupont, N. J. Severs, I. M. Leigh, M. Yuksel-Apak, D. P. Kelsell, and B. Wollnik. "Loss of desmoplakin isoform I causes early onset cardiomyopathy and heart failure in a Naxos-like syndrome". *Journal of Medical Genetics* 43.2 (2006), e05.

[119] R. M. Cabral, D. Tattersall, V. Patel, G. D. McPhail, E. Hatzimasoura, D. J. Abrams, A. P. South, and D. P. Kelsell. "The DSPII splice variant is crucial for desmosome-mediated adhesion in HaCaT keratinocytes". *Journal of Cell Science* 125.12 (2012), pp. 2853–2861.

[120] A. Arai, K. Yamamoto, and J. Toyama. "Murine cardiac progenitor cells require visceral embryonic endoderm and primitive streak for terminal differentiation". *Developmental Dynamics* 210.3 (1997), pp. 344–353.

[121] G. I. Gallicano, C. Bauer, and E. Fuchs. "Rescuing desmoplakin function in extra-embryonic ectoderm reveals the importance of this protein in embryonic heart, neuroepithelium, skin and vasculature". *Development* 128.6 (2001), pp. 929–941.

[122] R. C. Lyon, V. Mezzano, A. T. Wright, E. Pfeiffer, J. Chuang, K. Banares, A. Castaneda, K. Ouyang, L. Cui, R. Contu, Y. Gu, S. M. Evans, J. H. Omens, K. L. Peterson, A. D. McCulloch, and F. Sheikh. "Connexin defects underlie arrhythmogenic right ventricular cardiomyopathy in a novel mouse model". *Human Molecular Genetics* 23.5 (2013), pp. 1134–1150.

[123] V. Mezzano, Y. Liang, A. T. Wright, R. C. Lyon, E. Pfeiffer, M. Y. Song, Y. Gu, N. D. Dalton, M. Scheinman, K. L. Peterson, S. M. Evans, S. Fowler, M. Cerrone, A. D. McCulloch, and F. Sheikh. "Desmosomal junctions are necessary for adult sinus node function". *Cardiovascular Research* 111.3 (2016), pp. 274–286.

[124] D. M. Patel, A. D. Dubash, G. Kreitzer, and K. J. Green. "Disease mutations in desmoplakin inhibit Cx43 membrane targeting mediated by desmoplakin–EB1 interactions". *The Journal of Cell Biology* 206.6 (2014), pp. 779–797.

[125] M. Rübsam, J. A. Broussard, S. A. Wickström, O. Nekrasova, K. J. Green, and C. M. Niessen. "Adherens junctions and desmosomes coordinate mechanics and signaling to orchestrate tissue morphogenesis and function: An evolutionary perspective". *Cold Spring Harbor Perspectives in Biology* 10.11 (2018), a029207.

[126] K. D. Sumigray and T. Lechler. "Desmoplakin controls microvilli length but not cell adhesion or keratin organization in the intestinal epithelium". *Molecular Biology of the Cell* 23.5 (2012), pp. 792–799.

[127] J. D. Kapplinger, A. P. Landstrom, B. A. Salisbury, T. E. Callis, G. D. Pollevick, D. J. Tester, M. G. P. J. Cox, Z. Bhuiyan, H. Bikker, A. C. P. Wiesfeld, R. N. W. Hauer, J. P. van Tintelen, J. D. H. Jongbloed, H. Calkins, D. P. Judge, A. A. M. Wilde, and M. J. Ackerman. "Distinguishing arrhythmogenic right ventricular cardiomyopathy/dysplasia–associated mutations from background genetic noise". *Journal of the American College of Cardiology* 57.23 (2011), pp. 2317–2327.

[128] D. K. B. Armstrong, K. E. McKenna, P. E. Purkis, K. J. Green, R. A. J. Eady, I. M. Leigh, and A. E. Hughes. "Haploinsufficiency of desmoplakin causes a striate subtype of palmoplantar keratoderma". *Human Molecular Genetics* 8.1 (1999), pp. 143–148.

[129] N. V. Whittock, G. H. S. Ashton, P. J. C. Dopping-Hepenstal, M. J. Gratian, F. M. Keane, R. A. Eady, and J. A. McGrath. "Striate palmoplantar keratoderma resulting from desmoplakin haploinsufficiency". *Journal of Investigative Dermatology* 113.6 (1999), pp. 940–946.

[130] N. V. Whittock, H. Wan, R. A. J. Eady, S. M. Morley, M. C. Garzon, L. Kristal, P. Hyde, W. H. I. McLean, L. Pulkkinen, J. Uitto, A. M. Christiano, and J. A. McGrath. "Compound heterozygosity for non-sense and mis-sense mutations in desmoplakin underlies skin fragility/woolly hair syndrome". *Journal of Investigative Dermatology* 118.2 (2002), pp. 232–238.

[131] E. E. Norgett, S. J. Hatsell, L. Carvajal-Huerta, J.-C. Ruiz Cabezas, J. Common, P. E. Purkis, N. Whittock, I. M. Leigh, H. P. Stevens, and D. P. Kelsell. "Recessive mutation in desmoplakin disrupts desmoplakin–intermediate filament interactions and causes dilated cardiomyopathy, woolly hair and keratoderma". *Human Molecular Genetics* 9.18 (2000), pp. 2761–2766.

[132] M. F. Jonkman, A. M. G. Pasmooij, S. G. M. A. Pasmans, M. P. van den Berg, H. J. ter Horst, A. Timmer, and H. H. Pas. "Loss of desmoplakin tail causes lethal acantholytic epidermolysis bullosa". *The American Journal of Human Genetics* 77.4 (2005), pp. 653–660.

[133] M. Hatzfeld, R. Keil, and T. M. Magin. "Desmosomes and intermediate filaments: Their consequences for tissue mechanics". *Cold Spring Harbor Perspectives in Biology* 9.6 (2017), a029157.

[134] L. M. Godsel, A. D. Dubash, A. E. Bass-Zubek, E. V. Amargo, J. L. Klessner, R. P. Hobbs, X. Chen, and K. J. Green. "Plakophilin 2 couples actomyosin remodeling to desmosomal plaque assembly via RhoA". *Molecular Biology of the Cell* 21.16 (2010), pp. 2844–2859.

[135] M. Yang, Y. Liang, L. Sheng, G. Shen, K. Liu, B. Gu, F. Meng, and Q. Li. "A preliminary study of differentially expressed genes in expanded skin and normal skin: Implications for adult skin regeneration". *Archives of Dermatological Research* 303.2 (2011), pp. 125–133.

[136] T. Panciera, L. Azzolin, M. Cordenonsi, and S. Piccolo. "Mechanobiology of YAP and TAZ in physiology and disease". *Nature Reviews Molecular Cell Biology* 18 (2017), pp. 758–770.

[137] X. Liu, H. Li, M. Rajurkar, Q. Li, J. L. Cotton, J. Ou, L. J. Zhu, H. L. Goel, A. M. Mercurio, J.-S. Park, R. J. Davis, and J. Mao. "Tead and AP1 coordinate transcription and motility". *Cell Reports* 14.5 (2016), pp. 1169–1180.

[138] M. A. Hartman and J. A. Spudich. "The myosin superfamily at a glance". *Journal of Cell Science* 125.7 (2012), pp. 1627–1632.

[139] N. Hirokawa, Y. Noda, Y. Tanaka, and S. Niwa. "Kinesin superfamily motor proteins and intracellular transport". *Nature Reviews Molecular Cell Biology* 10 (2009), pp. 682–696.

[140] A. J. Roberts, T. Kon, P. J. Knight, K. Sutoh, and S. A. Burgess. "Functions and mechanics of dynein motor proteins". *Nature Reviews Molecular Cell Biology* 14 (2013), pp. 713–726.

[141] J.-F. Nolting and S. Köster. "Influence of microfluidic shear on keratin networks in living cells". *New Journal of Physics* 15.4 (2013), pp. 1–12.

[142] C. Lloyd, Q.-C. Yu, J. Cheng, K. Turksen, L. Degenstein, E. Hutton, and E. Fuchs. "The basal keratin network of stratified squamous epithelia: Defining K15 function in the absence of K14." *The Journal of Cell Biology* 129.5 (1995), pp. 1329–1344.

[143] H. Herrmann, T. Wedig, R. M. Porter, E. Lane, and U. Aebi. "Characterization of early assembly intermediates of recombinant human keratins". *Journal of Structural Biology* 137.1 (2002), pp. 82–96.

[144] D. Russell, P. D. Andrews, J. James, and E. B. Lane. "Mechanical stress induces profound remodelling of keratin filaments and cell junctions in *epidermolysis bullosa simplex* keratinocytes". *Journal of Cell Science* 117.22 (2004), pp. 5233–5243.

[145] X. Feng and P. A. Coulombe. "A role for disulfide bonding in keratin intermediate filament organization and dynamics in skin keratinocytes". *The Journal of Cell Biology* 209.1 (2015), pp. 59–72.

[146] R. Sanghvi-Shah and G. F. Weber. "Intermediate filaments at the junction of mechanotransduction, migration, and development". *Frontiers in Cell and Developmental Biology* 5 (2017), p. 81.

[147] J.-J. Meng, E. A. Bornslaeger, K. J. Green, P. M. Steinert, and W. Ip. "Two-hybrid analysis reveals fundamental differences in direct interactions between desmoplakin and cell type-specific intermediate filaments". *The Journal of Biological Chemistry* 272.34 (1997), pp. 21495–21503.

[148] P. A. Janmey, U. Euteneuer, P. Traub, and M. Schliwa. "Viscoelastic properties of vimentin compared with other filamentous biopolymer networks." *The Journal of Cell Biology* 113.1 (1991), pp. 155–160.

[149] J. A. Broussard, R. Yang, C. Huang, S. S. P. Nathamgari, A. M. Beese, L. M. Godsel, M. H. Hegazy, S. Lee, F. Zhou, N. J. Sniadecki, K. J. Green, and H. D. Espinosa. "The desmoplakin—intermediate filament linkage regulates cell mechanics". *Molecular Biology of the Cell* 28.23 (2017), pp. 3156–3164.

[150] V. Lulevich, H.-y. Yang, R. R. Isseroff, and G.-y. Liu. "Single cell mechanics of keratinocyte cells". *Ultramicroscopy* 110.12 (2010), pp. 1435–1442.

[151] A. R. Harris, A. Daeden, and G. T. Charras. "Formation of adherens junctions leads to the emergence of a tissue-level tension in epithelial monolayers". *Journal of Cell Science* 127.11 (2014), pp. 2507–2517.

[152] K. D. Sumigray, K. Zhou, and T. Lechler. "Cell–cell adhesions and cell contractility are upregulated upon desmosome disruption". *PLOS ONE* 7 (2014), e101824.

[153] K. H. Biswas, K. L. Hartman, R. Zaidel-Bar, and J. T. Groves. "Sustained α-catenin activation at E-cadherin junctions in the absence of mechanical force". *Biophysical Journal* 111.5 (2016), pp. 1044–1052.

[154] L. Puzzi, D. Borin, V. Martinelli, L. Mestroni, D. P. Kelsell, and O. Sbaizero. "Cellular biomechanics impairment in keratinocytes is associated with a C-terminal truncated desmoplakin: An atomic force microscopy investigation". *Micron* 106 (2018), pp. 27–33.

[155] B. L. Pruitt, A. R. Dunn, W. I. Weis, and W. J. Nelson. "Mechano-transduction: From molecules to tissues". *PLOS Biology* 12.11 (2014), e1001996.

[156] E. K. Paluch, C. M. Nelson, N. Biais, B. Fabry, J. Moeller, B. L. Pruitt, C. Wollnik, G. Kudryasheva, F. Rehfeldt, and W. Federle. "Mechanotransduction: Use the force(s)". *Biomed Central Biology* 13.1 (2015), p. 47.

[157] S. Kumar and V. M. Weaver. "Mechanics, malignancy, and metastasis: The force journey of a tumor cell". *Cancer and Metastasis Reviews* 28.1 (2009), pp. 113–127.

[158] J. I. Lopez, I. Kang, W.-K. You, D. M. McDonald, and V. M. Weaver. "*In situ* force mapping of mammary gland transformation". *Integrative Biology* 3.9 (2011), pp. 910–921.

[159] A. J. Engler, S. Sen, H. L. Sweeney, and D. E. Discher. "Matrix elasticity directs stem cell lineage specification". *Cell* 126.4 (2006), pp. 677–689.

[160] J. Swift, I. L. Ivanovska, A. Buxboim, T. Harada, P. C. D. P. Dingal, J. Pinter, J. D. Pajerowski, K. R. Spinler, J.-W. Shin, M. Tewari, F. Rehfeldt, D. W. Speicher, and D. E. Discher. "Nuclear lamin-A scales with tissue stiffness and enhances matrix-directed differentiation". *Science* 341.6149 (2013), p. 1240104.

[161] A. Buxboim, J. Irianto, J. Swift, A. Athirasala, J.-W. Shin, F. Rehfeldt, and D. E. Discher. "Coordinated increase of nuclear tension and lamin-A with matrix stiffness outcompetes lamin-B receptor that favors soft tissue phenotypes". *Molecular Biology of the Cell* 28.23 (2017), pp. 3333–3348.

[162] J. Irianto, C. R. Pfeifer, Y. Xia, and D. E. Discher. "SnapShot: Mechanosensing matrix". *Cell* 165.7 (2016), pp. 1820–1821.

[163] S. Majkut, T. Idema, J. Swift, C. Krieger, A. Liu, and D. E. Discher. "Heart-specific stiffening in early embryos parallels matrix and myosin expression to optimize beating". *Current Biology* 23.23 (2013), pp. 2434–2439.

[164] D. A. Fletcher and R. D. Mullins. "Cell mechanics and the cytoskeleton". *Nature* 463 (2010), pp. 485–492.

[165] D. E. Jaalouk and J. Lammerding. "Mechanotransduction gone awry". *Nature Reviews Molecular Cell Biology* 10 (2009), pp. 63–73.

[166] H. Clevers. "Wnt/β-catenin signaling in development and disease". *Cell* 127.3 (2006), pp. 469–480.

[167] A. Totaro, T. Panciera, and S. Piccolo. "YAP/TAZ upstream signals and downstream responses". *Nature Cell Biology* 20.8 (2018), pp. 888–899.

[168] V. Kanoldt, L. Fischer, and C. Grashoff. "Unforgettable force – crosstalk and memory of mechanosensitive structures". *Biological chemistry* (2018).

[169] S. S. Ranade, R. Syeda, and A. Patapoutian. "Mechanically activated ion channels". *Neuron* 87.6 (2015), pp. 1162–1179.

[170] J. Wu, A. H. Lewis, and J. Grandl. "Touch, tension, and transduction – The function and regulation of Piezo ion channels". *Trends in Biochemical Sciences* 42.1 (2017), pp. 57–71.

[171] T. J. Kirby and J. Lammerding. "Emerging views of the nucleus as a cellular mechanosensor". *Nature Cell Biology* 20.4 (2018), pp. 373–381.

[172] A. J. Maniotis, C. S. Chen, and D. E. Ingber. "Demonstration of mechanical connections between integrins, cytoskeletal filaments, and nucleoplasm that stabilize nuclear structure". *Proceedings of the National Academy of Sciences* 94.3 (1997), pp. 849–854.

[173] Z. Sun, S. S. Guo, and R. Fässler. "Integrin-mediated mechanotransduction". *The Journal of Cell Biology* 215.4 (2016), pp. 445–456.

[174] G. Charras and A. S. Yap. "Tensile forces and mechanotransduction at cell–cell junctions". *Current Biology* 28.8 (2018), R445–R457.

[175] P. Kanchanawong, G. Shtengel, A. M. Pasapera, E. B. Ramko, M. W. Davidson, H. F. Hess, and C. M. Waterman. "Nanoscale architecture of integrin-based cell adhesions". *Nature* 468 (2010), pp. 580–584.

[176] C. Bertocchi, Y. Wang, A. Ravasio, Y. Hara, Y. Wu, T. Sailov, M. A. Baird, M. W. Davidson, R. Zaidel-Bar, Y. Toyama, B. Ladoux, R.-M. Mege, and P. Kanchanawong. "Nanoscale architecture of cadherin-based cell adhesions". *Nature Cell Biology* 19 (2016), pp. 28–37.

[177] M. K. L. Han and J. de Rooij. "Converging and unique mechanisms of mechanotransduction at adhesion sites". *Trends in Cell Biology* 26.8 (2016), pp. 612–623.

[178] S. Yonemura, Y. Wada, T. Watanabe, A. Nagafuchi, and M. Shibata. "α-Catenin as a tension transducer that induces adherens junction development". *Nature Cell Biology* 12.6 (2010), pp. 533–542.

[179] J. M. Leerberg, G. A. Gomez, S. Verma, E. J. Moussa, S. K. Wu, R. Priya, B. D. Hoffman, C. Grashoff, M. A. Schwartz, and A. S. Yap. "Tension-sensitive actin assembly supports contractility at the epithelial zonula adherens". *Current Biology* 24.15 (2014), pp. 1689–1699.

[180] A. S. Yap, K. Duszyc, and V. Viasnoff. "Mechanosensing and mechanotransduction at cell-–cell junctions". *Cold Spring Harbor Perspectives in Biology* 10.8 (2018), a028761.

[181] C. D. Buckley, J. Tan, K. L. Anderson, D. Hanein, N. Volkmann, W. I. Weis, W. J. Nelson, and A. R. Dunn. "The minimal cadherin–catenin complex binds to actin filaments under force". *Science* 346.6209 (2014), p. 1254211.

[182] B. R. Acharya, S. K. Wu, Z. Z. Lieu, R. G. Parton, S. W. Grill, A. D. Bershadsky, G. A. Gomez, and A. S. Yap. "Mammalian Diaphanous 1 mediates a pathway for E-cadherin to stabilize epithelial barriers through junctional contractility". *Cell Reports* 18.12 (2017), pp. 2854–2867.

[183] M. Yao, W. Qiu, R. Liu, A. K. Efremov, P. Cong, R. Seddiki, M. Payre, C. T. Lim, B. Ladoux, R.-M. Mège, and J. Yan. "Force-dependent conformational switch of α-catenin controls vinculin binding". *Nature Communications* 5 (2014), p. 4525.

[184] J. T. Finer, R. M. Simmons, and J. A. Spudich. "Single myosin molecule mechanics: Piconewton forces and nanometre steps". *Nature* 368 (1994), pp. 113–119.

[185] C. Grashoff, B. D. Hoffman, M. D. Brenner, R. Zhou, M. Parsons, M. T. Yang, M. A. McLean, S. G. Sligar, C. S. Chen, T. Ha, and M. A. Schwartz. "Measuring mechanical tension across vinculin reveals regulation of focal adhesion dynamics". *Nature* 466 (2010), pp. 263–266.

[186] J. L. Bays, X. Peng, C. E. Tolbert, C. Guilluy, A. E. Angell, Y. Pan, R. Superfine, K. Burridge, and K. A. DeMali. "Vinculin phosphorylation differentially regulates mechanotransduction at cell–cell and cell–matrix adhesions". *The Journal of Cell Biology* 205.2 (2014), pp. 251–263.

[187] J. L. Bays and K. A. DeMali. "Vinculin in cell–cell and cell–matrix adhesions". *Cellular and Molecular Life Sciences* 74.16 (2017), pp. 2999–3009.

[188] E. S. Schiffhauer, T. Luo, K. Mohan, V. Srivastava, X. Qian, E. R. Griffis, P. A. Iglesias, and D. N. Robinson. "Mechanoaccumulative elements of the mammalian actin cytoskeleton". *Current Biology* 26.11 (2016), pp. 1473–1479.

[189] M. J. Greenberg, G. Arpağ, E. Tüzel, and E. M. Ostap. "A perspective on the role of myosins as mechanosensors". *Biophysical Journal* 110.12 (2016), pp. 2568–2576.

[190] K. Manibog, H. Li, S. Rakshit, and S. Sivasankar. "Resolving the molecular mechanism of cadherin catch bond formation". *Nature Communications* 5 (2014), p. 3941.

[191] D. L. Huang, N. A. Bax, C. D. Buckley, W. I. Weis, and A. R. Dunn. "Vinculin forms a directionally asymmetric catch bond with F-actin". *Science* 357.6352 (2017), pp. 703–706.

[192] K. Sugimura, P.-F. Lenne, and F. Graner. "Measuring forces and stresses *in situ* in living tissues". *Development* 143.2 (2016), pp. 186–196.

[193] O. Campàs, T. Mammoto, S. Hasso, R. A. Sperling, D. O'Connell, A. G. Bischof, R. Maas, D. A. Weitz, L. Mahadevan, and D. E. Ingber. "Quantifying cell-generated mechanical forces within living embryonic tissues". *Nature Methods* 11.2 (2014), pp. 183–189.

[194] W. J. Polacheck and C. S. Chen. "Measuring cell-generated forces: A guide to the available tools". *Nature Methods* 13.5 (2016), pp. 415–423.

[195] E. Bell, B. Ivarsson, and C. Merrill. "Production of a tissue-like structure by contraction of collagen lattices by human fibroblasts of different proliferative potential *in vitro*". *Proceedings of the National Academy of Sciences* 76.3 (1979), pp. 1274–1278.

[196] A. K. Harris, P. Wild, and D. Stopak. "Silicone rubber substrata: A new wrinkle in the study of cell locomotion". *Science* 208.4440 (1980), pp. 177–179.

[197] B. Sabass, M. L. Gardel, C. M. Waterman, and U. S. Schwarz. "High resolution traction force microscopy based on experimental and computational advances". *Biophysical Journal* 94.1 (2008), pp. 207–220.

[198] R. W. Style, R. Boltyanskiy, G. K. German, C. Hyland, C. W. MacMinn, A. F. Mertz, L. A. Wilen, Y. Xu, and E. R. Dufresne. "Traction force microscopy in physics and biology". *Soft Matter* 10.23 (2014), pp. 4047–4055.

[199] W. R. Legant, J. S. Miller, B. L. Blakely, D. M. Cohen, G. M. Genin, and C. S. Chen. "Measurement of mechanical tractions exerted by cells in three-dimensional matrices". *Nature Methods* 7.12 (2010), pp. 969–971.

[200] J. L. Tan, J. Tien, D. M. Pirone, D. S. Gray, K. Bhadriraju, and C. S. Chen. "Cells lying on a bed of microneedles: An approach to isolate mechanical force". *Proceedings of the National Academy of Sciences* 100.4 (2003), pp. 1484–1489.

[201] M. Ghibaudo, A. Saez, L. Trichet, A. Xayaphoummine, J. Browaeys, P. Silberzan, A. Buguin, and B. Ladoux. "Traction forces and rigidity sensing regulate cell functions". *Soft Matter* 4.9 (2008), pp. 1836–1843.

[202] J. Rajagopalan and M. T. A. Saif. "MEMS sensors and microsystems for cell mechanobiology". *Journal of Micromechanics and Microengineering* 21.5 (2011), p. 54002.

[203] Q. Luo, D. Kuang, B. Zhang, and G. Song. "Cell stiffness determined by atomic force microscopy and its correlation with cell motility". *Biochimica et Biophysica Acta – General Subjects* 1860.9 (2016), pp. 1953–1960.

[204] H. Zhang and K.-K. Liu. "Optical tweezers for single cells". *Journal of the Royal Society Interface* 5.24 (2008), pp. 671–690.

[205] A. Freikamp, A. Mehlich, C. Klingner, and C. Grashoff. "Investigating piconewton forces in cells by FRET-based molecular force microscopy". *Journal of Structural Biology* 197.1 (2017), pp. 37–42.

[206] K. C. Neuman and A. Nagy. "Single-molecule force spectroscopy: Optical tweezers, magnetic tweezers and atomic force microscopy". *Nature Methods* 5.6 (2008), pp. 491–505.

[207] G. Žoldák and M. Rief. "Force as a single molecule probe of multidimensional protein energy landscapes". *Current Opinion in Structural Biology* 23.1 (2013), pp. 48–57.

[208] M. J. Jacobs and K. Blank. "Joining forces: Integrating the mechanical and optical single molecule toolkits". *Chemical Science* 5.5 (2014), pp. 1680–1697.

[209] D. R. Stabley, C. Jurchenko, S. S. Marshall, and K. S. Salaita. "Visualizing mechanical tension across membrane receptors with a fluorescent sensor". *Nature Methods* 9.1 (2011), pp. 64–67.

[210] Y. Zhang, C. Ge, C. Zhu, and K. S. Salaita. "DNA-based digital tension probes reveal integrin forces during early cell adhesion". *Nature Communications* 5 (2014), p. 5167.

[211] M. Morimatsu, A. H. Mekhdjian, A. S. Adhikari, and A. R. Dunn. "Molecular tension sensors report forces generated by single integrin molecules in living cells". *Nano Letters* 13.9 (2013), pp. 3985–3989.

[212] X. Wang and T. Ha. "Defining single molecular forces required to activate integrin and Notch signaling". *Science* 340.6135 (2013), pp. 991–994.

[213] A.-L. Cost, P. Ringer, A. Chrostek-Grashoff, and C. Grashoff. "How to measure molecular forces in cells: A guide to evaluating genetically-encoded FRET-based tension sensors". *Cellular and Molecular Bioengineering* 8.1 (2015), pp. 96–105.

[214] A. Freikamp, A.-L. Cost, and C. Grashoff. "The piconewton force awakens: Quantifying mechanics in cells". *Trends in Cell Biology* 26.11 (2016), pp. 838–847.

[215] A.-L. Cost, S. Khalaji, and C. Grashoff. "Genetically encoded FRET-based tension sensors". *Current Protocols* (2019), e85.

[216] P. Ringer, A. Weißl, A.-L. Cost, A. Freikamp, B. Sabass, A. Mehlich, M. Tramier, M. Rief, and C. Grashoff. "Multiplexing molecular tension sensors reveals piconewton force gradient across talin-1". *Nature Methods* 14.11 (2017), pp. 1090–1096.

[217] K. Austen, P. Ringer, A. Mehlich, A. Chrostek-Grashoff, C. Kluger, C. Klingner, B. Sabass, R. Zent, M. Rief, and C. Grashoff. "Extracellular rigidity sensing by talin isoform-specific mechanical linkages". *Nature Cell Biology* 17.12 (2015), pp. 1597–1606.

[218] L. A. Kelley, S. Mezulis, C. M. Yates, M. N. Wass, and M. J. E. Sternberg. "The Phyre2 web portal for protein modeling, prediction and analysis". *Nature Protocols* 10.6 (2015), pp. 845–858.

[219] C. R. Reynolds, S. A. Islam, and M. J. Sternberg. "EzMol: A web server wizard for the rapid visualization and image production of protein and nucleic acid structures". *Journal of Molecular Biology* 430.15 (2018), pp. 2244–2248.

[220] C. Jurchenko and K. S. Salaita. "Lighting up the force: Investigating mechanisms of mechanotransduction using fluorescent tension probes". *Molecular and Cellular Biology* 35.15 (2015), pp. 2570–2582.

[221] C. Gayrard and N. Borghi. "FRET-based molecular tension microscopy". *Methods* 94 (2016), pp. 33–42.

[222] C.-W. Chang and S. Kumar. "Vinculin tension distributions of individual stress fibers within cell–matrix adhesions". *Journal of Cell Science* 126.14 (2013), pp. 3021–3030.

[223] S. Kuriyama, E. Theveneau, A. Benedetto, M. Parsons, M. Tanaka, G. Charras, A. Kabla, and R. Mayor. "In vivo collective cell migration requires an LPAR2-dependent increase in tissue fluidity". *The Journal of Cell Biology* 206.1 (2014), pp. 113–127.

[224] A. Kumar, M. Ouyang, K. Van den Dries, E. J. McGhee, K. Tanaka, M. D. Anderson, A. Groisman, B. T. Goult, K. I. Anderson, and M. A. Schwartz. "Talin tension sensor reveals novel features of focal adhesion force transmission and mechanosensitivity". *The Journal of Cell Biology* 213.3 (2016), pp. 371–383.

[225] N. Borghi, M. Sorokina, O. G. Shcherbakova, W. I. Weis, B. L. Pruitt, W. J. Nelson, and A. R. Dunn. "E-cadherin is under constitutive actomyosin-generated tension that is increased at cell–cell contacts upon externally applied stretch". *Proceedings of the National Academy of Sciences* 109.31 (2012), pp. 12568–12573.

[226] A. K. Lagendijk, G. A. Gomez, S. Baek, D. Hesselson, W. E. Hughes, S. Paterson, D. E. Conway, H.-G. Belting, M. Affolter, K. A. Smith, M. A. Schwartz, A. S. Yap, and B. M. Hogan. "Live imaging molecular changes in junctional tension upon VE-cadherin in zebrafish". *Nature Communications* 8 (2017), p. 1402.

[227] M. Krieg, A. R. Dunn, and M. B. Goodman. "Mechanical control of the sense of touch by β-spectrin". *Nature Cell Biology* 16.3 (2014), pp. 224–233.

[228] A. Suzuki, B. L. Badger, J. Haase, T. Ohashi, H. P. Erickson, E. D. Salmon, and K. Bloom. "How the kinetochore couples microtubule force and centromere stretch to move chromosomes". *Nature Cell Biology* 18.4 (2016), pp. 382–392.

[229] D. Cai, S.-C. Chen, M. Prasad, L. He, X. Wang, V. Choesmel-Cadamuro, J. K. Sawyer, G. Danuser, and D. J. Montell. "Mechanical feedback through E-cadherin promotes direction sensing during collective cell migration". *Cell* 157.5 (2014), pp. 1146–1159.

[230] S. B. Lemke, T. Weidemann, A.-L. Cost, C. Grashoff, and F. Schnorrer. "A small proportion of Talin molecules transmit forces at developing muscle attachments sites in vivo". *PLOS Biology* 17.3 (2019), e3000057.

[231] T. Förster. "Zwischenmolekulare Energiewanderung und Fluoreszenz". *Annalen der Physik* 437.1-2 (1948), pp. 55–75.

[232] R. Y. Tsien. *Spectra of various fluorescent proteins*. 2018. URL: `http://www.tsienlab.ucsd.edu/Documents.htm`.

[233] J. R. Lakowicz. *Principles of fluorescence spectroscopy*. 3rd ed. Springer, 2006.

[234] S. S. Vogel, T. A. Nguyen, B. W. van der Meer, and P. S. Blank. "The impact of heterogeneity and dark acceptor states on FRET: Implications for using fluorescent protein donors and acceptors". *PLOS ONE* 7.11 (2012), e49593.

[235] B. T. Bajar, E. S. Wang, S. Zhang, M. Z. Lin, and J. Chu. "A guide to fluorescent protein FRET pairs". *Sensors* 16.9 (2016), p. 1488.

[236] O. Shimomura, F. H. Johnson, and Y. Saiga. "Extraction, purification and properties of Aequorin, a bioluminescent protein from the luminous hydromedusan, *Aequorea*". *Journal of Cellular and Comparative Physiology* 59.3 (1962), pp. 223–239.

[237] M. Chalfie, Y. Tu, G. Euskirchen, W. W. Ward, and D. C. Prasher. "Green fluorescent protein as a marker for gene expression". *Science* 263.5148 (1994), pp. 802–805.

[238] D. A. Zacharias, J. D. Violin, A. C. Newton, and R. Y. Tsien. "Partitioning of lipid-modified monomeric GFPs into membrane microdomains of live cells". *Science* 296.5569 (2002), pp. 913–916.

[239] R. Heim, D. C. Prasher, and R. Y. Tsien. "Wavelength mutations and posttranslational autoxidation of green fluorescent protein". *Proceedings of the National Academy of Sciences* 91.26 (1994), pp. 12501–12504.

[240] R. N. Day and M. W. Davidson. "Fluorescent proteins for FRET microscopy: Monitoring protein interactions in living cells". *BioEssays* 34.5 (2012), pp. 341–350.

[241] D. W. Piston and G.-J. Kremers. "Fluorescent protein FRET: The good, the bad and the ugly". *Trends in Biochemical Sciences* 32.9 (2007), pp. 407–414.

[242] M. V. Matz, A. F. Fradkov, Y. A. Labas, A. P. Savitsky, A. G. Zaraisky, M. L. Markelov, and S. A. Lukyanov. "Fluorescent proteins from nonbioluminescent Anthozoa species". *Nature Biotechnology* 17 (1999), pp. 969–973.

[243] N. C. Shaner, R. E. Campbell, P. A. Steinbach, B. N. G. Giepmans, A. E. Palmer, and R. Y. Tsien. "Improved monomeric red, orange and yellow fluorescent proteins derived from *Discosoma* sp. red fluorescent protein". *Nature Biotechnology* 22.12 (2004), pp. 1567–1572.

[244] A. W. Nguyen and P. S. Daugherty. "Evolutionary optimization of fluorescent proteins for intracellular FRET". *Nature Biotechnology* 23 (2005), pp. 355–360.

[245] B. L. Scott and A. D. Hoppe. "Optimizing fluorescent protein trios for 3-Way FRET imaging of protein interactions in living cells". *Scientific Reports* 5 (2015), p. 10270.

[246] M. Ormö, A. B. Cubitt, K. Kallio, L. A. Gross, R. Y. Tsien, and S. J. Remington. "Crystal structure of the *Aequorea victoria* green fluorescent protein". *Science* 273.5280 (1996), pp. 1392–1395.

[247] F. Yang, L. G. Moss, and G. N. Phillips Jr. "The molecular structure of green fluorescent protein". *Nature Biotechnology* 14 (1996), pp. 1246–1521.

[248] H.-w. Ai, J. N. Henderson, S. J. Remington, and R. E. Campbell. "Directed evolution of a monomeric, bright and photostable version of *Clavularia* cyan fluorescent protein: Structural characterization and applications in fluorescence imaging". *Biochemical Journal* 400.3 (2006), pp. 531–540.

[249] C. Demeautis, F. Sipieter, J. Roul, C. Chapuis, S. Padilla-Parra, F. B. Riquet, and M. Tramier. "Multiplexing PKA and ERK1&2 kinases FRET biosensors in living cells using single excitation wavelength dual colour FLIM". *Scientific Reports* 7 (2017), p. 41026.

[250] D. M. Shcherbakova, M. A. Hink, L. Joosen, T. W. J. Gadella, and V. V. Verkhusha. "An orange fluorescent protein with a large stokes shift for single-excitation multicolor FCCS and FRET imaging". *Journal of the American Chemical Society* 134.18 (2012), pp. 7913–7923.

[251] H. Murakoshi, A. C. E. Shibata, Y. Nakahata, and J. Nabekura. "A dark green fluorescent protein as an acceptor for measurement of Förster resonance energy transfer". *Scientific Reports* 5 (2015), p. 15334.

[252] D. Shcherbo, C. S. Murphy, G. V. Ermakova, E. A. Solovieva, T. V. Chepurnykh, A. S. Shcheglov, V. V. Verkhusha, V. Z. Pletnev, K. L. Hazelwood, P. M. Roche, S. Lukyanov, A. G. Zaraisky, M. W. Davidson, and D. M. Chudakov. "Far-red fluorescent tags for protein imaging in living tissues". *Biochemical Journal* 418.3 (2009), pp. 567–574.

[253] A. Keppler, S. Gendreizig, T. Gronemeyer, H. Pick, H. Vogel, and K. Johnsson. "A general method for the covalent labeling of fusion proteins with small molecules *in vivo*". *Nature Biotechnology* 21 (2002), pp. 86–89.

[254] C. Berney and G. Danuser. "FRET or no FRET: A quantitative comparison". *Biophysical Journal* 84.6 (2003), pp. 3992–4010.

[255] T. Lambert. *tlamberto3/FPbase: mTFP1*. 2018. URL: `https://doi.org/10.5281/zenodo.1244328`.

[256] B. D. Venetta. "Microscope phase fluorometer for determining the fluorescence lifetimes of fluorochromes". *Review of Scientific Instruments* 30.6 (1959), pp. 450–457.

[257] K. Suhling, P. M. W. French, and D. Phillips. "Time-resolved fluorescence microscopy". *Photochemical & Photobiological Sciences* 4.1 (2005), pp. 13–22.

[258] W. Becker. "Fluorescence lifetime imaging – techniques and applications". *Journal of Microscopy* 247.2 (2012), pp. 119–136.

[259] M. A. Digman, V. R. Caiolfa, M. Zamai, and E. Gratton. "The phasor approach to fluorescence lifetime imaging analysis". *Biophysical Journal* 94.2 (2008), pp. L14–L16.

[260] D. G. Gibson, L. Young, R.-Y. Chuang, J. C. Venter, C. A. Hutchison III, and H. O. Smith. "Enzymatic assembly of DNA molecules up to several hundred kilobases". *Nature Methods* 6.5 (2009), pp. 343–345.

[261] J. Schindelin, I. Arganda-Carreras, E. Frise, V. Kaynig, M. Longair, T. Pietzsch, S. Preibisch, C. Rueden, S. Saalfeld, B. Schmid, J.-Y. Tinevez, D. J. White, V. Hartenstein, K. Eliceiri, P. Tomancak, and A. Cardona. "Fiji: An open-source platform for biological-image analysis". *Nature Methods* 9.7 (2012), pp. 676–682.

[262] M. D. Abràmoff, P. J. Magalhães, and S. J. Ram. "Image processing with ImageJ". *Biophotonics International* 11.7 (2004), pp. 36–42.

[263] A. D. Edelstein, M. A. Tsuchida, N. Amodaj, H. Pinkard, R. D. Vale, and N. Stuurman. "Advanced methods of microscope control using μManager software". *Journal of biological methods* 1.2 (2014), e10.

[264] G. W. Gordon, G. Berry, X. H. Liang, B. Levine, and B. Herman. "Quantitative fluorescence resonance energy transfer measurements using fluorescence microscopy". *Biophysical Journal* 74.5 (1998), pp. 2702–2713.

[265] A. J. Price. "Mechanics at the cadherin–keratin interface". PhD thesis. Stanford University, 2018.

[266] T. Zal and N. R. J. Gascoigne. "Photobleaching-corrected FRET efficiency imaging of live cells". *Biophysical Journal* 86.6 (2004), pp. 3923–3939.

[267] R. C. Holte. "Very simple classification rules perform well on most commonly used datasets". *Machine Learning* 11.1 (1993), pp. 63–90.

[268] D. Bates, M. Mächler, B. Bolker, and S. Walker. "Fitting linear mixed-effects models using lme4". *Journal of Statistical Software* 67.1 (2015), pp. 1–48.

[269] A. Kuznetsova, P. Brockhoff, and R. Christensen. "lmerTest package: Tests in linear mixed effects models". *Journal of Statistical Software* 82.13 (2017), pp. 1–26.

[270] C. M. Kluger. "The role of metavinculin in molecular mechanotransduction". PhD thesis. Ludwig-Maximilians-Universität München, 2016.

[271] N. Otsu. "A threshold selection method from gray-level histograms". *IEEE Transactions on Systems, Man, and Cybernetics* 9.1 (1979), pp. 62–66.

[272] P.-S. Liao, T.-S. Chen, and P.-C. Chung. "A fast algorithm for multilevel thresholding". *Journal of Information Science and Engineering* 17 (2001), pp. 713–727.

[273] M. Szabelski, R. Luchowski, Z. Gryczynski, P. Kapusta, U. Ortmann, and I. Gryczynski. "Evaluation of instrument response functions for lifetime imaging detectors using quenched Rose Bengal solutions". *Chemical Physics Letters* 471.1 (2009), pp. 153–159.

[274] S. Baker and R. D. Cousins. "Clarification of the use of CHI-Square and likelihood functions in fits to histograms". *Nuclear Instrumuments and Methods in Physics Research* 221 (1984), pp. 437–442.

[275] A.-N. Spiess and N. Neumeyer. "An evaluation of R^2 as an inadequate measure for nonlinear models in pharmacological and biochemical research: A Monte Carlo approach". *BioMed Central Pharmacology* 10.1 (2010), p. 6.

[276] F. James. *Statistical methods in experimental physics*. World Scientific Publishing Company, 2006.

[277] P. J. Verveer, A. Squire, and P. I. H. Bastiaens. "Global analysis of fluorescence lifetime imaging microscopy data". *Biophysical Journal* 78.4 (2000), pp. 2127–2137.

[278] J. Hendrix, C. Flors, P. Dedecker, J. Hofkens, and Y. Engelborghs. "Dark states in monomeric red fluorescent proteins studied by fluorescence correlation and single molecule spectroscopy". *Biophysical Journal* 94.10 (2008), pp. 4103–4113.

[279] A. C. Huen, J. K. Park, L. M. Godsel, X. Chen, L. J. Bannon, E. V. Amargo, T. Y. Hudson, A. K. Mongiu, I. M. Leigh, D. P. Kelsell, B. M. Gumbiner, and K. J. Green. "Intermediate filament–membrane attachments function synergistically with actin-dependent contacts to regulate intercellular adhesive strength". *The Journal of Cell Biology* 159.6 (2002), pp. 1005–1017.

[280] M. G. Farquhar and G. E. Palade. "Junctional complexes in various epithelia". *The Journal of Cell Biology* 17.2 (1963), pp. 375–412.

[281] A. K. Freikamp. "Molecular force analysis of the vertebrate kinetochore protein CENP-T". PhD thesis. Ludwig-Maximilians-Universität München, 2017.

[282] S. Yamashita, T. Tsuboi, N. Ishinabe, T. Kitaguchi, and T. Michiue. "Wide and high resolution tension measurement using FRET in embryo". *Scientific Reports* 6 (2016), p. 28535.

[283] K. Kasahara, T. Kartasova, X. Q. Ren, T. Ikuta, K. Chida, and T. Kuroki. "Hyperphosphorylation of keratins by treatment with okadaic acid of BALB/MK-2 mouse keratinocytes." *The Journal of Biological Chemistry* 268.31 (1993), pp. 23531–235837.

[284] M. J. Paszek, C. C. DuFort, O. Rossier, R. Bainer, J. K. Mouw, K. Godula, J. E. Hudak, J. N. Lakins, A. C. Wijekoon, L. Cassereau, M. G. Rubashkin, M. J. Magbanua, K. S. Thorn, M. W. Davidson, H. S. Rugo, J. W. Park, D. A. Hammer, G. Giannone, C. R. Bertozzi, and V. M. Weaver. "The cancer glycocalyx mechanically primes integrin-mediated growth and survival". *Nature* 511 (2014), pp. 319–325.

[285] K. E. Rothenberg, S. S. Neibart, A. S. LaCroix, and B. D. Hoffman. "Controlling cell geometry affects the spatial distribution of load across vinculin". *Cellular and Molecular Bioengineering* 8.3 (2015), pp. 364–382.

[286] F. M. Hendriks, D. Brokken, C. W. J. Oomens, D. L. Bader, and F. P. T. Baaijens. "The relative contributions of different skin layers to the mechanical behavior of human skin in vivo using suction experiments". *Medical Engineering & Physics* 28.3 (2006), pp. 259–266.

[287] X. Liang and S. A. Boppart. "Biomechanical properties of in vivo human skin from dynamic optical coherence elastography". *IEEE Transactions on Biomedical Engineering* 57.4 (2010), pp. 953–959.

[288] D. E. Conway, M. T. Breckenridge, E. Hinde, E. Gratton, C. S. Chen, and M. A. Schwartz. "Fluid shear stress on endothelial cells modulates mechanical tension across VE-cadherin and PECAM-1". *Current Biology* 23.11 (2013), pp. 1024–1030.

[289] C. Gayrard, C. Bernaudin, T. Déjardin, C. Seiler, and N. Borghi. "Src- and confinement-dependent FAK activation causes E-cadherin relaxation and β-catenin activity". *The Journal of Cell Biology* 217.3 (2018), pp. 1063–1077.

[290] D. E. Ingber. "Tensegrity-based mechanosensing from macro to micro". *Progress in Biophysics and Molecular Biology* 97.2 (2008), pp. 163–179.

[291] S. Sivaramakrishnan, J. V. DeGiulio, L. Lorand, R. D. Goldman, and K. M. Ridge. "Micromechanical properties of keratin intermediate filament networks". *Proceedings of the National Academy of Sciences* 105.3 (2008), pp. 889–894.

[292] R. Fernandez-Gonzalez, S. de Matos Simoes, J.-C. Röper, S. Eaton, and J. A. Zallen. "Myosin II dynamics are regulated by tension in intercalating cells". *Developmental Cell* 17.5 (2009), pp. 736–743.

[293] G. F. Weber, M. A. Bjerke, and D. W. DeSimone. "A mechanoresponsive cadherin-keratin complex directs polarized protrusive behavior and collective cell migration". *Developmental Cell* 22.1 (2012), pp. 104–115.

[294] P. R. Sonavane, C. Wang, B. Dzamba, G. F. Weber, A. Periasamy, and D. W. DeSimone. "Mechanical and signaling roles for keratin intermediate filaments in the assembly and morphogenesis of *Xenopus* mesendoderm tissue at gastrulation". *Development* 144.23 (2017), pp. 4363–4376.

[295] S. K. Runswick, M. J. O'Hare, L. Jones, C. H. Streuli, and D. R. Garrod. "Desmosomal adhesion regulates epithelial morphogenesis and cell positioning". *Nature Cell Biology* 3 (2001), pp. 823–830.

[296] N. D. Evans, R. O. C. Oreffo, E. Healy, P. J. Thurner, and Y. H. Man. "Epithelial mechanobiology, skin wound healing, and the stem cell niche". *Journal of the Mechanical Behavior of Biomedical Materials* 28 (2013), pp. 397–409.

[297] S. Karsch, D. Kong, J. Großhans, and A. Janshoff. "Single-cell defects cause a long-range mechanical response in a confluent epithelial cell layer". *Biophysical Journal* 113.12 (2017), pp. 2601–2608.

[298] O. Nekrasova, R. M. Harmon, J. A. Broussard, J. L. Koetsier, L. M. Godsel, G. N. Fitz, M. L. Gardel, and K. J. Green. "Desmosomal cadherin association with Tctex-1 and cortactin-Arp2/3 drives perijunctional actin polymerization to promote keratinocyte delamination". *Nature Communications* 9 (2018), p. 1053.

[299] S. R. Baddam, P. T. Arsenovic, V. Narayanan, N. R. Duggan, C. R. Mayer, S. T. Newman, D. A. Abutaleb, A. Mohan, A. P. Kowalczyk, and D. E. Conway. "The desmosomal cadherin desmoglein-2 experiences mechanical tension as demonstrated by a FRET-based tension biosensor expressed in living cells". *Cells* 7.7 (2018), p. 66.

[300] K. Rietscher, A. Wolf, G. Hause, A. Rother, R. Keil, T. M. Magin, M. Glass, C. M. Niessen, and M. Hatzfeld. "Growth retardation, loss of desmosomal adhesion, and impaired tight junction function identify a unique role of plakophilin 1 in vivo". *Journal of Investigative Dermatology* 136.7 (2016), pp. 1471–1478.

[301] T. Sklyarova, S. Bonné, P. D'hooge, G. Denecker, S. Goossens, R. De Rycke, G. Borgonie, M. Bösl, F. van Roy, and J. van Hengel. "Plakophilin-3-deficient mice develop hair coat abnormalities and are prone to cutaneous inflammation". *Journal of Investigative Dermatology* 128.6 (2008), pp. 1375–1385.

[302] C. Daday, L. M. Mateyka, and F. Gräter. "How ARVC-related mutations destabilize desmoplakin: An MD study". *Biophysical Journal* 116.5 (2019), pp. 831–835.

[303] R. Alcalai, S. Metzger, S. Rosenheck, V. Meiner, and T. Chajek-Shaul. "A recessive mutation in desmoplakin causes arrhythmogenic right ventricular dysplasia, skin disorder, and woolly hair". *Journal of the American College of Cardiology* 42.2 (2003), pp. 319–327.

[304] H. B. Schiller, C. C. Friedel, C. Boulegue, and R. Fässler. "Quantitative proteomics of the integrin adhesome show a myosin II-dependent recruitment of LIM domain proteins". *EMBO reports* 12.3 (2011), pp. 259–266.

[305] S. H. M. Litjens, J. M. de Pereda, and A. Sonnenberg. "Current insights into the formation and breakdown of hemidesmosomes". *Trends in Cell Biology* 16.7 (2006), pp. 376–383.

[306] C. Margadant, E. Frijns, K. Wilhelmsen, and A. Sonnenberg. "Regulation of hemidesmosome disassembly by growth factor receptors". *Current Opinion in Cell Biology* 20.5 (2008), pp. 589–596.

[307] G. Walko, M. J. Castañón, and G. Wiche. "Molecular architecture and function of the hemidesmosome". *Cell and Tissue Research* 360.2 (2015), pp. 363–378.

[308] A. L. Rippa, E. A. Vorotelyak, A. V. Vasiliev, and V. V. Terskikh. "The role of integrins in the development and homeostasis of the epidermis and skin appendages". *Acta Naturae* 5.4 (2013).

[309] M. Barczyk, S. Carracedo, and D. Gullberg. "Integrins". *Cell and Tissue Research* 339.1 (2009), pp. 269–280.

[310] E. Frijns, I. Kuikman, S. Litjens, M. Raspe, K. Jalink, M. Ports, K. Wilhelmsen, and A. Sonnenberg. "Phosphorylation of threonine 1736 in the C-terminal tail of integrin $\beta 4$ contributes to hemidesmosome disassembly". *Molecular Biology of the Cell* 23.8 (2012), pp. 1475–1485.

[311] R. Q. J. Schaapveld, L. Borradori, D. Geerts, M. R. van Leusden, I. Kuikman, M. G. Nievers, C. M. Niessen, R. D. M. Steenbergen, P. J. F. Snijders, and A. Sonnenberg. "Hemidesmosome formation is initiated by the $\beta 4$ integrin subunit, requires complex formation of $\beta 4$ and HD1/plectin, and involves a direct interaction between $\beta 4$ and the bullous pemphigoid antigen 180". *The Journal of Cell Biology* 142.1 (1998), pp. 271–284.

[312] C. A. W. Geuijen and A. Sonnenberg. "Dynamics of the $\alpha 6\beta 4$ integrin in keratinocytes". *Molecular Biology of the Cell* 13.11 (2002), pp. 3845–3858.

Acknowledgement

My PhD project as documented in this thesis would not have been possible without the help and support of many people. I'd like to start by thanking my supervisor Carsten Grashoff. His enthusiasm for science is inspiring and I'm grateful for his support but retrospective it were maybe even more the other phases that let me grow to an independent scientist.

I also like to thank my official supervisor and our department head Reinhard Fässler, who granted me access to his facilities and strengthened the project with critical comments. Furthermore, I'd like to thank Don Lamb for his continuous support as a thesis advisory committee member and the different perspective that he freely shared. I also like to thank Andreas Bausch for stepping in as the second examiner so uncomplicatedly and Klaus Förstemann and Dietmar Martin for being part of my thesis committee.

A special thanks goes to Andrew Price for our close collaboration. I very much enjoyed working together and I'm still sometimes missing our weekly Skype meetings to discuss the project. I'm also very grateful to Alex Dunn for the intense collaboration and hosting me in his lab for three weeks, where he and his group made me feel comfortable from the first day on. I'd especially like to thank Eva Huang, who was even sharing her flat with me for this time.

I'd like to thank all my current and former colleagues from the Grashoff group in the order they joined the lab: Anna Chrostek-Grashoff, Katharina Austen, Carleen Kluger, Andrea Freikamp, Michael Jawurek, Pia Ringer, Christoph Klingner, Verena Kanoldt, Christiane Barz, Lisa Fischer, Samira Khalaji, and also Sandra Lemke (though officially still in the Schnorrer group). I especially appreciated our critical and open discussion culture and that there was always someone stepping in to help if necessary. Furthermore, I'd like to particularly thank Andrea for showing me how to come to work for years even if experiments don't return usable results, Carleen for supervising my Master thesis and thereby introducing me to talin and vinculin, the two lab's favorite pet proteins, organic dye labeling and programming, Pia for trusting my data analysis skills and getting me involved in her project, and Verena for introducing Gibson cloning in our lab. Furthermore, I thank the Bachelor student Miriam Güra and the Master student Florian Simon for helping me to learn how to supervise and especially Miriam for her contribution to the desmoplakin project.

Being the first one to establish a new model system in the lab, requires even more external help than other projects might need. Therefore, I'm particularly grateful to Kathy Green, who freely shared her desmoplakin-deficient keratinocytes and her advice, and was even hosting me for a day in her lab. I also like to thank Josh Broussard for his highly-appreciated input. Furthermore, I thank Benedikt Sabass for checking and commenting on the ratio determination method.

The project was funded by SPP1782 (Epithelial junctions as dynamic hubs to integrate forces, signals and cell behaviour), which next to the funding also brought researchers with a shared interest together. In this context, I like to thank Fanny Büchau and Thomas Magin for sharing their knowledge on keratinocyte handling and experimental design and Dave Ahrens from Rudolf Merkel's group for the discussions about the application of external stress. The SPP1782 was also the platform that brought us together with Hanna Ungewiß in Jens Waschke's group, who then made the EM images. Furthermore, the SPP1782 paved the way for the collaboration with Matthias Rübsam and Plácido Pereira in the group of Carien Niessen to help their α-catenin tension sensor development.

I'd like to thank IMPRS, which provided a local forum for the exchange among PhD students. I thank Hans-Jörg Schäffer, Ingrid Wolf, Maxi Reif and the trainees especially for organizing the workshops, particularly those with Ruth Willmott, and for the travel allowance that gives me the chance to join the Gordon research conference for cell–cell contact and adhesion again this year, which two years ago marked the starting point for the intense collaboration with Andrew and Alex.

Next to the collaborations that turned into a paper, I'm also grateful to the people who helped me in other parts of my thesis. Thanks to Arnoud Sonnenberg for sharing the PA-JEB cells, Hildegard Reiter for retroviral transfecting them, Roy Zent for sharing integrin $\beta 1$ and $\beta 4$-deficient MDCK cells, Emmanuel Rognoni for showing me initially how to handle keratinocytes, Waldemar Schrimpf from Don Lamb's group for the discussions about and initial attempts to use phasor for FLIM analysis, and Katharina Austen, Raphael Ruppert, and Markus Moser for FACS sorting cells. The impact of some people one just really realizes when they are absent, so I'd also like to explicitly thank the department's secretary Ines Lach-Kusevich, the cleaning lady Lidia Wimmer, and Klaus Weber, who is taking care of everything technical.

I also like to thank my family and friends, who not always understood why I'm working that much but tolerated it and supported me in finding my path through the PhD.

Finally, I'm indebted and very grateful to Christian Schweizer, who is not only my beloved soul mate but also acted as my physics collaboration partner throughout the thesis. There is hardly any equation in this thesis or non-biological conclusion, which I not at least discussed with him and writing FLAMES would have been impossible without the countless evenings and weekends we spent together discussing and programming.